

Dissertation zur Erlangung des Doktorgrades
der Fakultät für Chemie und Pharmazie
der Ludwig-Maximilians-Universität München

Transition Metal Oxide Nanostructures for Electrochemical Energy Conversion

Ksenia Fominykh

aus

Glasow, Russland

2016

ERKLÄRUNG

Diese Dissertation wurde im Sinne von § 7 der Promotionsordnung vom 28. November 2011 von Frau PD Dr. habil. Dina Fattakhova-Rohlfing betreut.

EIDESSTATTLICHE VERSICHERUNG

Diese Dissertation wurde eigenständig und ohne unerlaubte Hilfe bearbeitet.

München, _____

Ksenia Fominykh

Dissertation eingereicht am 03.05.2016

1. Gutachterin: PD Dr. habil. Dina Fattakhova-Rohlfing

2. Gutachter: Prof. Dr. Thomas Bein

Mündliche Prüfung am 06.06.2016

ACKNOWLEDGEMENT

PREFACE

First and foremost I would like to express my sincere gratitude to my supervisor Dr. Dina Fattakhova-Rohlfing for her advice, motivation and continuous support throughout my doctoral research. Her immense knowledge inspired me to explore the exciting and challenging field of nanostructured water splitting electrocatalysts. I greatly appreciate her guidance giving me enough freedom to work independently and to realize my own ideas that motivated my creativity in the design of new synthesis pathways and helped me to become a better researcher in so many ways. I am particularly thankful for her guidance in writing and submission of manuscripts and for revising this thesis.

I would also like to express my greatest gratitude to my second supervisor Prof. Dr. Thomas Bein, who supported me throughout all my PhD studies. His encouragement, mentoring and interesting discussions during our group and subgroup meetings provided invaluable research experience and knowledge in the field of materials science. I wish to thank Dina and Thomas for providing optimum working conditions and for making all the facilities and analytical instruments available that were necessary to successfully complete my PhD thesis. Furthermore, I thank both for giving me the opportunity to participate in a large number of national and international conferences where I had the chance to present and discuss my work with experienced researchers helping me to extend my knowledge.

Very special thanks to all collaborators who were closely involved in my doctoral projects and performed key experiments for a successful publication of our work. I would like to thank Jiri Rathouský in Prague for krypton sorption analysis, Tina Scheu and her group in Düsseldorf for high resolution transmission electron microscopy, Goran Stefanic in Zagreb for Mössbauer analysis, Ivelina Zaharieva and Petko Chernev for extended X-ray absorption fine structure measurements at the BESSY synchrotron in Berlin, Rossitza Pentcheva and Hamid Reza Hajiyani in Duisburg for DFT calculations and Patrick Zeller in Munich for X-ray photoelectron spectroscopy analysis.

Thanks a lot to Steffen and Markus for transmission electron microscopy analysis of my ultrasmall nanoparticles and Alesja for many insightful scanning electron microscopy sessions. I thank Hans, Flo and Benni for introducing me to the installation, operation and maintenance of X-ray diffraction instruments and in situ XRD units. I am grateful to Tina for her lab organization, assistance in purchasing chemicals and office or lab equipment and performing different kinds of analysis of my nanopowders. I also highly appreciate Regina's

ACKNOWLEDGEMENT

support in all administrative issues and for her perfect organization and efficient management.

I greatly acknowledge my fellow colleagues Peter, Ilina, Chris, Daniel, Alex, Krissi und Jonathan for the many constructive discussions in the water splitting subgroup that often inspired me to consider things from another perspective and therefore substantially enriched my ideas.

Special thanks to all the students I had the pleasure to teach during my doctoral thesis: Ceren, Polina, Matthias, Karin, Johannes, Fabian, Maja and Aneil. Every one of them not only contributed their part to my research projects but also helped me to gain experience and improve my mentoring skills.

I would like to thank all my colleagues in the groups of Dina Fattakhova-Rohlfing and Thomas Bein for providing a pleasant working atmosphere. Thanks for the great time we had together celebrating Christmas, PhD defenses and during numerous conferences and BBQ evenings. I especially thank my office mates Daniel, Peter, Krissi and Chris for the entertaining office afternoons.

Many thanks to Alesja and Askhat for being such reliable friends and for the wonderful Russian evenings we spent that brought me a little piece of home and reminded me to remember Russian traditions and values.

Most of all, I would like to thank my family for loving and encouraging me throughout my dissertation journey. I am grateful to my Mom for her support and advice, Thorben for being so understanding and patient, especially during the time-consuming writing process, and Toni for being there for me at every stage of my life.

ABSTRACT

The development of sustainable and high performance energy conversion and storage systems is one of the most urgent goals of contemporary research. Electrochemical water splitting to hydrogen and oxygen is a viable technology to overcome our dependency on fossil fuels and help to establish a carbon-neutral hydrogen economy. However, the total efficiency of this process is rather low without the catalysis of both half-reactions and in particular water oxidation because of its slow kinetics. Therefore a significant challenge lies in finding stable and inexpensive high performance catalysts for the water oxidation reaction.

The development of electrocatalytic materials with minimized water splitting overpotentials, high available currents and improved stability was the main objective of this thesis. We pursued nanoscaling as a key strategy to achieve this goal due to the possibility of manipulating bulk and surface defect chemistry in nanosized materials together with a greatly increased surface area beneficial for electrocatalytic activity. Moreover, novel non-equilibrium mixed phases with extremely high miscibility of the elements open a new class of materials with tunable characteristics that only exist on the nanoscale. Understanding and control of these mixed structures along with the control of bulk and surface defect chemistry enables the development of superior functional materials for energy conversion applications.

First-row transition metal oxides are known to be among the most efficient catalysts for electrochemical and photoelectrochemical water splitting. Therefore, the main materials developed in this thesis are nickel oxide, cobalt oxide and iron oxide based nanostructures with various composition and structural properties. We established a non-aqueous solvothermal synthesis based on *tert*-butanol as reaction medium. The crystalline metal oxide nanoparticles are formed already in solution by a chemical reaction with the solvent, without the need for a further high temperature treatment leading to irreversible particle agglomeration. The particles prepared in this way are perfectly dispersible in different solvents without additional stabilizing agents. This enables a controlled distribution of the as-prepared crystals on different types of substrates for the application in electrochemical, photoelectrochemical or photovoltaic devices.

Chapters 3 to 5 describe the nanosized nickel oxide NiO and the mixed phases $\text{Ni}_x\text{Fe}_{1-x}\text{O}$ and $\text{Ni}_x\text{Co}_{1-x}\text{O}$. Ultrasmall crystalline nanoparticles of phase pure nickel oxide synthesized with the *tert*-butanol route demonstrate exceptionally high electrocatalytic efficiency in electrochemical water splitting, which is attributed to the partially oxidized surface resulting

from the diminishing crystal size. The high catalytic activity of NiO even outperforms expensive iridium oxide catalysts. Moreover, it can be further enhanced by doping with Fe atoms in concentrations of up to 20 at%. In combination with the decreased particle size and high crystallinity, substitutional incorporation of iron results in a significantly increased electrocatalytic activity, which is by far the highest among all the reported Ni/Fe oxide compounds and in fact among all reported water oxidation catalysts. Using optimized synthesis conditions we were also able to obtain ultrasmall $\text{Ni}_x\text{Co}_{1-x}\text{O}$ nanocrystals, which demonstrate complete element miscibility in the whole composition range. The unusually high solubility of Co and Fe in the rock salt NiO structure is attributed to the kinetic control of the phase formation during the *tert*-butanol synthesis as well as to the stabilizing effect for metastable defect phases on the nanoscale. The exceptionally high catalytic activity of our $\text{Fe}_x\text{Ni}_{1-x}\text{O}$ nanoparticles and the unusually high solubility of the elements in the $\text{Ni}_x\text{Co}_{1-x}\text{O}$ lattice demonstrate the high impact of synthesis strategy and nanomorphology on the properties of resulting materials.

Chapters 5 and 6 cover the cobalt oxide based nanoparticles of CoO and Co_3O_4 . Both structures are thermodynamically stable cobalt oxide phases and could be obtained using the solvothermal *tert*-butanol route by adjusting the reaction conditions. In both cases crystalline non-agglomerated spherical particles with an average size of 3 nm are formed. Among the two oxides, CoO was found to be a better electrocatalyst for both oxygen and hydrogen evolution reaction, in line with the activity trend reported for cobalt oxides. In spite of the lower dark electrocatalytic performance, nanocrystals of Co_3O_4 were found to act as efficient co-catalysts in photoelectrochemical water oxidation and lead to drastically enhanced photocurrents upon homogeneous distribution on the high surface area of mesoporous hematite.

The synthesis of nanostructured materials of the iron oxide family, akaganeite ($\beta\text{-FeOOH}$) and hematite ($\alpha\text{-Fe}_2\text{O}_3$), is summarized in chapters 7 and 8, respectively. These processes demonstrate that metal oxide nanoparticles with non-cubic crystal structure and an anisotropic shape such as akaganeite can be obtained using the *tert*-butanol synthesis as well. These particles are able to incorporate a variety of divalent to pentavalent dopant elements in extraordinary high concentrations of up to 40 at%, providing yet another example of nanoscale controlled formation of metastable phases. The particle shapes are strongly

dependent on the doping element and can be tuned from anisotropic to spherical particles of 4 nm in size. Films prepared *in situ* during the solvothermal reaction result in a unique hierarchical porous morphology that is particularly interesting for the thermal fabrication of highly efficient doped hematite photoanodes for photoelectrochemical oxygen evolution.

In the last part of this thesis porous hematite nanostructures were prepared *via* the sol-gel reaction of molecular precursors combined with the shape-persistent template nanocrystalline cellulose. The highly porous α -Fe₂O₃ morphologies exhibit a well-defined anisotropic porosity that can be varied by the choice of the iron precursor and the calcination procedure. Moreover, a post-synthetic hydrothermal treatment strongly affects the crystal growth as well as the porous nanomorphology of the obtained hematite scaffolds leading to highly tunable porous hematite nanostructures.

The nanostructuring concepts developed in this thesis provide an attractive pathway to greatly enhance the efficiency of electrochemical energy conversion systems. The tunable ultrasmall nanoparticle dimensions, their crystallinity and excellent dispersibility have great influence on the electrocatalytic activity. Furthermore, novel nanoscale stabilized metastable phases with increased solubility of dopant elements and assembly of nanosized building blocks into complex porous architectures open new perspectives in the design of advanced energy conversion devices.

TABLE OF CONTENTS

Acknowledgement.....	V
Abstract	IX
Table of contents	XIII
1 Introduction	1
1.1 Electrochemical water splitting	2
1.2 Overview of selected metal oxide electrocatalysts for alkaline water oxidation	4
1.3 Synthesis of metal oxide nanoparticles	10
1.4 Water electrocatalysis: figures of merit and benchmarking	15
1.5 References	18
2 Synthesis and Characterization	27
2.1 Solvothermal reactions	28
2.2 X-Ray diffraction (XRD).....	29
2.3 Raman spectroscopy	31
2.4 Dynamic light scattering (DLS)	32
2.5 Thermogravimetric analysis (TGA)	33
2.6 Electron microscopy (EM)	34
2.7 Quartz crystal microbalance (QCM)	36
2.8 Electrochemical water splitting setup.....	38
2.9 References	40
3 Ultrasmall dispersible crystalline nickel oxide nanoparticles as high performance catalysts for electrochemical water splitting	43
3.1 Abstract.....	45
3.2 Introduction	46
3.3 Results and discussion	47
3.4 Conclusion	55
3.5 Experimental section	56
3.5.1 Synthesis of NiO nanoparticles	56
3.5.2 Characterization	57

PREFACE

3.5.3	Electrode preparation	59
3.5.4	Electrochemical measurements	59
3.6	References	61
3.7	Supporting information.....	64
4	Iron-doped nickel oxide nanocrystals as highly efficient electrocatalysts for alkaline water splitting.....	69
4.1	Abstract.....	71
4.2	Introduction	72
4.3	Results and discussion	73
4.4	Conclusion	83
4.5	Experimental section	83
4.5.1	Synthesis of iron-doped nickel oxide nanoparticles.....	83
4.5.2	Characterization	84
4.5.3	Electrode preparation	86
4.5.4	Electrochemical measurements	87
4.6	References	88
4.7	Supporting information.....	92
4.7.1	References	105
5	Rock salt Ni/Co oxides with unusual nanoscale-stabilized composition as water splitting electrocatalysts	107
5.1	Abstract.....	108
5.2	Introduction	109
5.3	Results and discussion	111
5.4	Conclusion	123
5.5	Experimental section	124
5.5.1	Synthesis of $\text{Ni}_x\text{Co}_{1-x}\text{O}$ nanoparticles	124
5.5.2	Characterization	125
5.5.3	Electrode preparation	127
5.5.4	Electrochemical measurements	127
1.1.1	Computational details.....	128
5.6	References	129

TABLE OF CONTENTS

5.7	Supporting information.....	134
1.1.2	References	143
6	Ultrasmall CO_3O_4 Nanocrystals Strongly Enhance Solar Water Splitting on Mesoporous Hematite	145
6.1	Abstract.....	147
6.2	Introduction	148
6.3	Results and discussion	149
6.4	Conclusion	158
6.5	Experimental section	158
6.5.1	Synthesis of cobalt oxide nanoparticles	158
6.5.2	Electrode preparation	159
6.5.3	Photoelectrode preparation.....	160
6.5.4	Characterization	161
6.5.5	Electrochemical measurements	162
6.5.6	Photoelectrochemical measurements	163
6.5.7	Transient absorption spectroscopy (TAS).....	164
6.6	References	164
6.7	Supporting information.....	169
7	Single phase doped iron oxyhydroxide nanocrystals incorporating extraordinary high amounts of different elements	175
7.1	Abstract.....	176
7.2	Introduction	177
7.3	Results and discussion	178
7.4	Conclusion	191
7.5	Experimental section	192
7.5.1	Synthesis of doped iron oxyhydroxide nanoparticles	192
7.5.2	Characterization	193
7.5.3	Film preparation	194
7.6	References	194
7.7	Supporting information.....	198
7.7.1	References	205

PREFACE

8	Nanocellulose-assisted formation of porous hematite morphologies	207
8.1	Abstract.....	208
8.2	Introduction	209
8.3	Results and discussion	211
8.4	Conclusions	219
8.5	Experimental section	220
8.5.1	Extraction of cellulose nanocrystals.....	220
8.5.2	Preparation of precursor solutions.....	220
8.5.3	Film preparation	220
8.5.4	Characterization	221
8.6	References	222
8.7	Supporting information.....	226
9	Conclusion and outlook.....	231
10	Curriculum vitae	235
11	Publications and presentations	239
11.1	Publications	240
11.2	Oral presentations	241
11.3	Poster presentations	243

1 INTRODUCTION

With increasing demand for clean and sustainable environmental technologies, the design of high performance energy conversion and storage systems becomes exceptionally important.^{1,2} Electrochemical water splitting provides a viable strategy to generate hydrogen fuel from renewable energy sources delivering a clean and efficient energy carrier.³⁻⁶ A substantial challenge lies in finding stable, inexpensive and active electrocatalysts for the water splitting reaction.^{4,7} The performance of electrocatalysts depends not only on intrinsic materials properties defined by the chemical structure, phase composition and crystallinity, but to a great extent also on the morphology and surface-related structural characteristics.^{8,9} Nanostructuring is an important tool to maximize the performance of materials in electrochemical applications.¹⁰⁻¹⁴ The obvious advantages of nanostructuring are diminishing dimensions of the bulk resulting in shortened charge transport pathways, and a greatly increased surface area beneficial for the interface charge transfer processes.^{15,16} Using the nanoscaling effect, the performance of even established materials systems can be significantly improved. Furthermore, nanostructuring often gives access to unique structures that are thermodynamically unstable in the bulk and only exist on the nanoscale, thus extending the already existing material classes.¹⁷⁻²¹ Development of novel functional materials on the nanoscale requires a full understanding and controlled manipulation of size, shape and phase composition along with the control of bulk and surface chemistry. This includes the design of novel synthesis protocols for nano building blocks and their assembly into more complex nanostructures enabling the preparation of superior water splitting electrocatalysts.^{22,23}

1.1 ELECTROCHEMICAL WATER SPLITTING

The overall electrochemical water splitting (water electrolysis) reaction proceeds according to

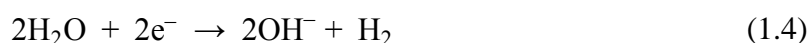


The electrochemical process comprises the reduction of water to hydrogen at the cathode (hydrogen evolution reaction, HER) and oxidation of water to oxygen at the anode (oxygen evolution reaction, OER).^{24,25} The change in free energy for the generation of one mole H₂ under standard conditions is $\Delta G = 237.2 \text{ kJ mol}^{-1}$ corresponding to $\Delta E^0 = 1.23 \text{ V}$.²⁶

In acidic conditions the electron transfer steps are coupled with proton transfer as described by equations (1.2) and (1.3) for the HER and OER, respectively.^{9,24}



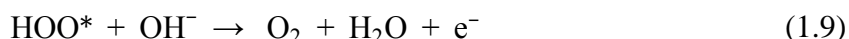
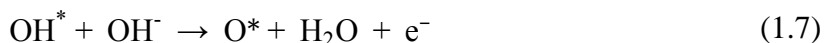
In alkaline environment the HER and the OER are balanced by the transfer of hydroxide ions and are expressed by the following equations.⁹



Water electrolysis at neutral pH is rather uneconomical, as the low concentrations of H^+ and OH^- at neutral conditions lead to potential losses associated with solution resistance and require the addition of water-soluble electrolytes to increase the conductivity.²⁷ Large-scale industrial water electrolysis is therefore preferably performed in strong acids such as H_2SO_4 or strong bases such as KOH or NaOH due to their high ionic conductivity.²⁸ Acidic water electrolysis is generally pursued because of available proton exchange membranes (PEM) such as Nafion commonly used for ionic transport and gas separation in integrated water splitting systems.²⁸⁻³¹ However the selection of catalyst materials stable under acidic and particularly under oxidative OER conditions is limited mostly to expensive noble metals.^{28,32} Cheap and earth-abundant non-noble catalysts are economically more attractive but are stable in alkaline rather than in acidic environment.^{28,33} Therefore alkaline water electrolysis is increasingly studied and is also the main objective of this thesis.

Both water splitting half-reactions have to be catalyzed with maximum efficiency to achieve maximum hydrogen production rate. The hydrogen evolution following a simple two electron reaction mechanism^{9,24} is kinetically fast and is catalyzed typically by noble metal electrodes such as Au, Pd and Pt with almost no overpotential.³⁴⁻³⁶ The overall process, however, is limited by the sluggish kinetics of the oxygen evolution reaction that requires a large overpotential to overcome several activation barriers in a four electron reaction.^{9,24,25,37} The development of economical and efficient OER electrocatalysts is therefore essential for improving the overall water splitting efficiency. A benchmarking overview of available OER catalysts is given in section 1.4.

The alkaline OER reaction proceeds through a series of elementary steps involving surface adsorbed intermediates according to following equations where the asterisk indicates the surface adsorbed species.³⁷



The electrocatalytic activity is determined by the binding strength of the reaction intermediates to the electrode surface. This general mechanism was proposed by Norskov, Rossmeisl *et al.* for metal oxide catalysts.³⁷ Their DFT calculations have shown that practically all OER electrocatalysts have a minimum theoretical overpotential caused by the scaling relationships between binding energies of the intermediate surface hydroxide HO* and surface hydroperoxy HOO* (universal scaling relation). To overcome this limitation the authors suggest to stabilize the HOO* intermediate compared to HO*, which can be expected for atomically rough surface structures or doped surfaces.^{37,38}

First-row transition metal oxides based on inexpensive and abundant elements nickel, cobalt and iron are attractive candidates for the application as oxygen evolution electrocatalysts.^{33,39} The crystal structures along with the most important characteristics of the investigated oxides are introduced in the following section.

1.2 OVERVIEW OF SELECTED METAL OXIDE ELECTROCATALYSTS FOR ALKALINE WATER OXIDATION

Nickel(II) oxide (NiO) is a stable transition metal oxide that is formed naturally as the mineral bunsenite. The color of NiO depends on the particle dimensions and is usually grey/green for large crystals whereas ultrasmall nanoparticles appear as brown/yellow powders.⁴⁰ Black color indicates that nickel is partially oxidized to Ni(III).⁴¹ NiO crystallizes in the cubic rock

salt type structure where the nickel atoms are octahedrally surrounded by six oxygen atoms as illustrated in Figure 1.1.⁴²

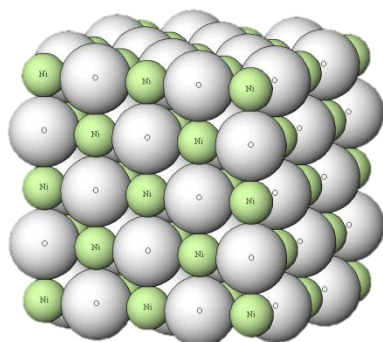


Figure 1.1 Crystal structure of rock salt type NiO.⁴³

The lattice of bulk nickel oxide shows a slight rhombohedral distortion which results from the antiferromagnetic ordering within the crystal.⁴⁴ Stoichiometric nickel oxide is an insulator at room temperature (RT) with a wide band gap of 3.6 – 4.0 eV.^{44,45} However it converts to a p-type semiconductor due to holes generated by Ni vacancies or by the presence of interstitial oxygen atoms.⁴⁶ Bulk stoichiometric NiO is antiferromagnetic, but some reported studies suggest that NiO nanoparticles show weak ferromagnetic or superparamagnetic behavior.⁴⁷⁻⁴⁹ Furthermore NiO shows electrochromic behavior which is the ability to reversibly and persistently change its optical properties due to the change in oxidation state in an electrochemical process.⁴⁶ Nickel oxide demonstrates high efficiencies as electrocatalyst for the OER in alkaline media combined with high corrosion stability in the oxidative environment.^{39,50-52} The OER activity is attributed to the β -NiOOH phase formed at the accessible NiO surface during continuous cycling. This activation of the catalyst surface can significantly enhance the catalytic performance.^{39,50,53,54}

The synthesis of ultrasmall NiO nanocrystals and their application as highly efficient electrocatalysts in water splitting is described in chapter 3. Furthermore the great impact of nanoscaling on the solubility of Fe(III) and Co(II) atoms in the NiO lattice and the influence of doping on the water splitting performance is investigated in chapters 4 and 5.

Cobalt(II) oxide adopts the rock salt crystal structure as well, corresponding to the mineral periclase with the chemical formula CoO.⁵⁵ The structure can be described as a crystalline network build up by CoO_6 or OCo_6 octahedra, respectively, as illustrated in Figure 1.2.

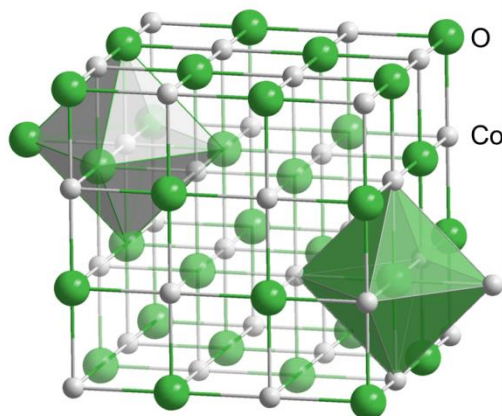


Figure 1.2 Illustration of the CoO rock salt type crystal structure with the corresponding coordination polyhedra.⁵⁶

The color of CoO powders ranges from greyish green to red or black crystals.⁵⁷ Similar to nickel oxide, CoO nanocrystals are superparamagnetic or weakly ferromagnetic at RT whereas bulk CoO exhibits antiferromagnetism.⁵⁸ Under anodic potentials the Co(II) is gradually oxidized to Co(III) forming a layered structure of CoOOH which is the catalytically active Co species for the OER.^{25,59} Cobalt oxide based electrocatalysts demonstrate reasonable efficiencies in both OER and HER and are therefore promising electrode materials for the design of overall water splitting devices.^{4,60,61} The synthesis of ultras-small dispersible CoO nanocrystals and their application as catalysts in the electrochemical oxygen evolution and hydrogen evolution reaction is described in chapter 5.

Cobalt(II,III) oxide with the chemical composition Co_3O_4 is a black solid that crystallizes in the spinel structure of the type AB_2O_4 .⁶² The crystal lattice consists of a face centered cubic (fcc) arrangement of O^{2-} anions where one eighth of the tetrahedral sites are occupied by high-spin Co^{2+} (A) and one half of the octahedral sites by low-spin Co^{3+} (B) (Figure 1.3).⁶³

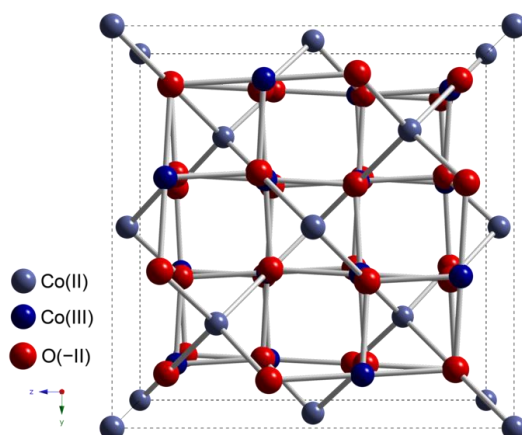


Figure 1.3 Crystal structure of the spinel type Co_3O_4 .⁶⁴

Co_3O_4 shows paramagnetic behavior at room temperature (RT) since its magnetic moment is dominated by the three unpaired electrons of Co^{2+} .⁶⁵⁻⁶⁷ The cobalt oxide indirect band gap of 1.60 – 1.65 eV is induced by d-d electron transitions between Co^{2+} and Co^{3+} and the direct band gap of 2.10 – 2.40 eV by 2p-d transfer between O^{2-} and Co^{2+} indicating charge transfer insulator properties.^{63,68} However, an increased conductivity induced by p-doping and other intrinsic effects was reported at different temperatures as well.⁶⁹ In recent years Co_3O_4 attracted attention as oxygen evolution catalyst in electrochemical water splitting and was also applied as co-catalyst in photoelectrochemical oxygen generation.⁷⁰⁻⁷² Deposition of Co_3O_4 on hematite,⁷³ bismuth vanadate,⁷⁴ or tungsten oxide⁷⁵ photoanodes was reported to enhance the catalytic efficiency in the OER by suppressing the recombination at the photocatalyst/cocatalyst interface and therefore increasing the charge separation efficiency.^{72,76} The synthesis of ultrasmall Co_3O_4 nanoparticles developed in our studies and their performance in electrochemical water splitting is described in chapter 6.

Hematite is a non-toxic, earth-abundant and the most thermodynamically stable isomorph of iron oxide with hexagonal symmetry and the chemical formula $\alpha\text{-Fe}_2\text{O}_3$. The crystal lattice of hematite is isostructural with the trigonal corundum $\alpha\text{-Al}_2\text{O}_3$ and consists of trigonally distorted Fe(III)O_6 octahedra building up a three-dimensional hexagonal closest packing (hcp) framework.⁷⁷ The hematite unit cell consists of octahedral face-sharing Fe_2O_9 dimers forming chains in the c direction (Figure 1.4).⁷⁸ Oxygen vacancies in the crystal lattice make hematite an n-type semiconductor.⁷⁹

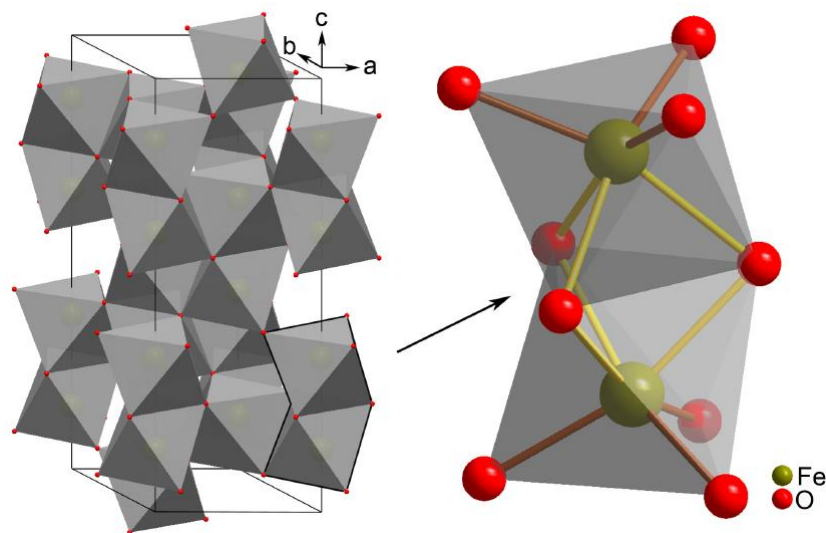


Figure 1.4 Illustration of the hematite unit cell (left) and a detailed view on one of the Fe_2O_3 dimer (right).⁸⁰

The weak ferromagnetic properties of bulk hematite (at RT) are mostly dictated by the atomic arrangement within the lattice and therefore the orientation of the spin magnetic moment of Fe^{3+} .⁸¹ Additionally, the iron spin configuration has influence on the optoelectronic and charge carrier transport properties of hematite.⁷⁸ The absorption in the visible range leading to the characteristic red color is caused by the small band gap of 2.0 – 2.1 eV.^{80,82} The combination of magnetic and electronic properties and stability in aqueous media make hematite a promising candidate for the application as photoanode material in photoelectrochemical (PEC) water splitting.^{80,82,83} The fabrication of porous hematite films with tunable morphologies obtained by three different synthesis routes is described in chapters 6 to 8.

Iron oxyhydroxide $\beta\text{-FeOOH}$ is a compound of the iron oxide family that occurs naturally as the rare mineral akaganeite with monoclinic structure.⁸⁴ The three-dimensional framework of akaganeite is built up by four double chains of edge-linked corner-sharing Fe(III)(O,OH)_3 octahedra forming a large tunnel-type structure (Figure 1.5).⁸⁵ Cl^- and other halogenide ions were found to stabilize the network by occupying sites within the channels and are therefore essential for the formation of akaganeite.^{86,87}

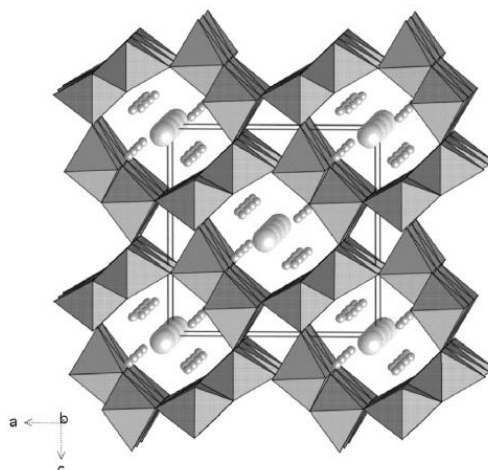


Figure 1.5 Illustration of the akaganeite crystal structure demonstrating the tunnel type arrangement of octahedral double chains with chloride ions occupying the center of the tunnels.⁸⁸

The tunnel structure of β -FeOOH along with the paramagnetic behavior leads to unique sorption and ion exchange properties and applications as catalysts.⁸⁹ Additionally akaganeite is easily transformed to the thermodynamically more stable hematite at rather low temperatures of 300 °C and is therefore used as a starting material for the preparation of hematite nanostructures with different morphologies that can also be applied as photoanodes in PEC.⁹⁰⁻⁹³ The synthesis route to ultrasmall β -FeOOH nanocrystals developed in this thesis and the influence of various dopants on particle structure and morphology is described in detail in chapter 7.

The iron, cobalt and nickel based metal oxides described above show promising efficiencies in the electrocatalytic oxygen generation.^{25,28,33} However, not only the choice of the material but also its morphology is essential for the development of a high performance electrocatalyst. Besides structural properties such as the defect chemistry, the catalytic efficiency is strongly influenced by the number of catalytically active sites dependent on the accessible surface area of the material.⁹ Uniform and monodisperse crystals of only a few nanometers in size are among the morphologies with the highest surface area and are therefore particularly interesting for catalytic applications. However the fabrication of metal oxide nanocrystals combining all the properties beneficial for water splitting electrocatalysis is challenging. The

next chapter gives an overview of the main preparation methods giving access to ultrasmall metal oxide nanoparticles.

1.3 SYNTHESIS OF METAL OXIDE NANOPARTICLES

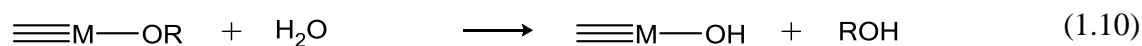
Metal oxide nanoparticles can be obtained by a broad range of physical and chemical methods that can be roughly divided into top-down and bottom-up approaches. Top-down approaches are based on physical processes such as attrition or ball milling. Nanopowders produced in this way usually exhibit broad size distributions and their size, shape and morphology are difficult to control. In addition possible structural and surface impurities can have a significant impact on the surface chemistry and therefore the catalytic properties of nanomaterials.²²

Bottom-up approaches generally offer better control of crystallinity, size distribution, shape and chemical composition of the nanoparticles. They are based on the self-assembly of atoms, molecules or clusters that build up nanomaterials in chemical reactions from the bottom including gas phase or aerosol and liquid phase processes.^{22,94,95} Typical examples of the gas phase synthesis are spray pyrolysis and chemical vapor deposition where nanoparticles are formed in the vapor phase by homogeneous nucleation at high temperatures. Depending on the synthesis conditions, a variety of particle shapes and morphologies can be produced. However, these methods often lead to large aggregates and offer insufficient control over the particle size distribution.⁹⁶ More important for the synthesis of small, uniform and monodisperse metal oxide nanoparticles are liquid phase processes conducted in aqueous or non-aqueous solvents with an optional addition of surfactants or structure directing agents such as oleylamine or trioctylphosphine oxide.^{23,95} These include coprecipitation, microemulsion, hot injection, polyol-mediated, microwave-assisted, solvothermal and sol-gel synthesis methods.^{23,58,95,97} Aqueous and non-aqueous sol-gel routes are particularly interesting for the fabrication of metal oxide nanoparticles. In a broad term the sol-gel process can be described as transformation of molecular precursors in solution into an integrated network by polycondensation reactions.⁹⁸

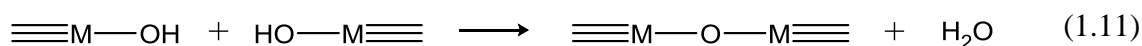
The main steps of an aqueous sol-gel process are hydrolysis of (typically) metal halides or alkoxides forming stable colloidal solutions (the sol) and subsequent polycondensation

leading to discrete particles gradually evolving to a more rigid porous inorganic network (the gel) consisting of both a liquid and a solid phase. This transformation is referred to as sol-gel transition. The hydrolysis step is initiated by a nucleophilic attack of the H₂O oxygen atom leading to the formation of a metal hydroxide and an alcohol in case of an alkoxide precursor according to equation (1.10). The metal-oxygen-metal (M–O–M) bonds are formed by condensation reactions between two metal hydroxides (oxolation) or between a hydroxide and an alkoxide (alkoxolation) as demonstrated in equations (1.11) and (1.12), respectively.²³

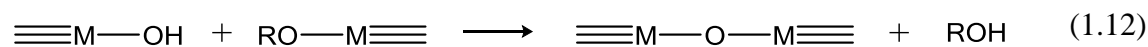
Hydrolysis



Condensation (oxolation)



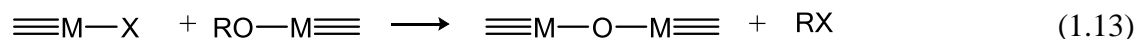
Condensation (alkoxolation)



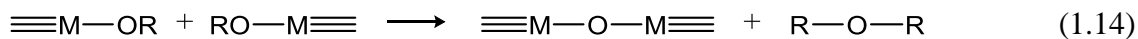
Scheme 1.1 Main synthesis steps of the aqueous sol-gel process using metal alkoxides as precursors.

In non-aqueous (non-hydrolytic) sol-gel processes the oxygen for the formation of metal oxides is provided by the solvent or by the organic ligand of the precursor, for example alkoxide, acetate or acetylacetonate. Depending on the applied solvent, for example ether, alcohol, ketone or aldehyde, the M–O–M bond formation proceeds *via* different mechanisms summarized in Scheme 1.2.^{23,99,100}

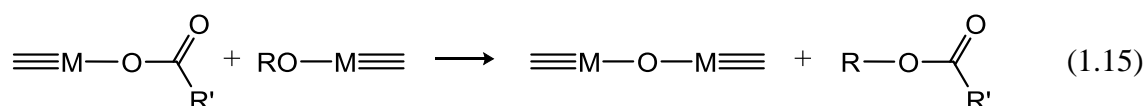
Alkyl halide elimination



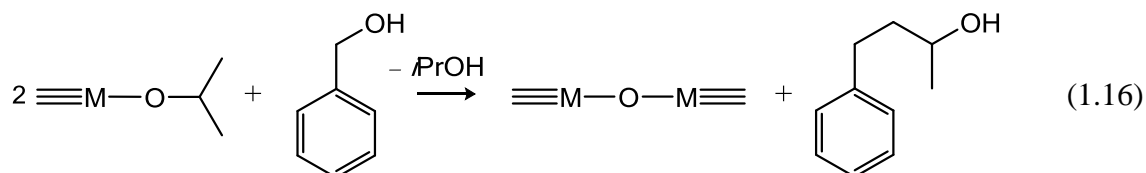
Ether elimination



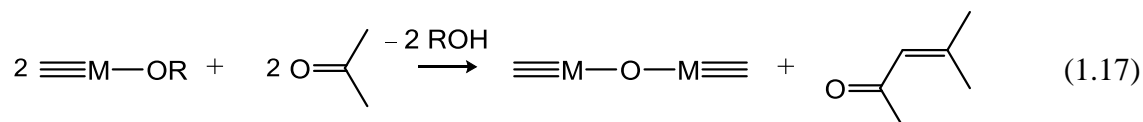
Condensation of carboxylate groups (ester and amide eliminations)



C-C coupling of benzylic alcohols and alkoxide molecules



Aldol condensation



Scheme 1.2 Different types of condensation steps in non-aqueous reactions in different solvents.

The final morphology of the metal oxide products can be controlled by the condensation progress and the type of processing. The dimensions of the resulting materials can range from molecular nanoclusters to highly crosslinked polymer-like networks obtained by aging of the gel. Further stages of the sol-gel method involve drying by removing the solvent under ambient or supercritical conditions forming xerogels or aerogels, respectively, or annealing at high temperatures to densify the material or to induce its crystallization (Figure 1.6).²³

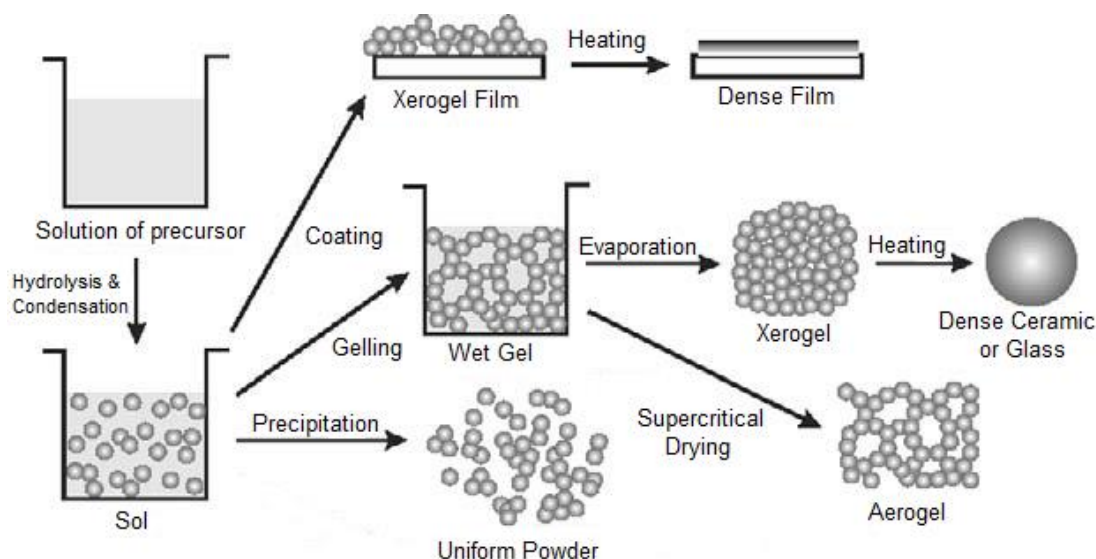


Figure 1.6 Different morphologies of resulting products depending on the steps of the sol-gel process.²³

One fundamental issue of the aqueous sol-gel chemistry is the high reactivity of the transition metal precursors towards water, leading to very fast hydrolysis and condensation rates.¹⁰¹ Generally, reactions proceeding too fast are less controllable resulting in the formation of amorphous phases and large agglomerates with a broad size distribution. Amorphous precipitates require additional postsynthetic annealing steps for crystallization, limiting the control over size and shape of the final product. This makes the reaction suitable rather for the fabrication of nanostructured films than for defined small nanocrystals.²³

These limitations can be overcome in non-aqueous sol-gel syntheses, which are performed in organic solvents at relatively low temperatures. These reactions offer greatly enhanced control over the particle morphology, dispersibility and crystallinity due to much slower reaction rates of metal ions with less polar organic solvents compared to water.^{100,102} However, the reduced solubility of some precursors in organic solvents limits the variability of nanoparticle phase composition. Therefore, sol-gel reactions can be performed under solvothermal conditions in a controlled atmosphere to increase the reactivity. The so-called solvothermal synthesis combines the moderate reaction rates of the non-aqueous route beneficial for the formation of ultrasmall particles and metastable phases with elevated temperatures and pressures to initiate the reaction. The preparation of nanoparticles using this method is facile

and is conducted by simple mixing of the precursors with the solvents that are non-toxic alcohols in most cases. The reactions take place at relatively low temperatures ranging from 70 to 200 °C.²³

A well-known solvothermal route to metal oxide nanoparticles was established by Niederberger *et al.* where dry benzyl alcohol simultaneously acts as solvent, capping agent and oxide source.¹⁰² Typically metal halides, acetylacetonates and alkoxides are used as precursors to produce very small crystalline nanoparticles of 2 – 80 nm in size, with uniform shape, narrow size distribution and in large quantities. Using the benzyl alcohol route, a broad selection of binary, ternary and mixed metal oxides can be produced.¹⁰³⁻¹⁰⁵ The mechanism of the M–O–M bond formation was investigated for example for zinc oxide nanorods prepared from zinc acetylacetonate hydrate. It is suggested that the reaction is initiated by a nucleophilic attack of the hydroxy group of the solvent on one of the carbonyl groups of the ligand leading to the formation of R–Zn–OH species under release of acetone and benzyl acetate.¹⁰⁶

Nanoparticles prepared *via* the benzyl alcohol method can be assembled into more complex nanomorphologies such as crystalline mesoporous metal oxide films.¹⁰⁷ However, a major issue of the benzyl alcohol synthesis is the particle dispersibility. Often additional stabilizers are required to redisperse the as-prepared nanocrystals. In some cases stabilization can be achieved spontaneously by ligands formed by the solvent. The benzyl alcohol ligands, however, are rather stable and are difficult to remove from the surface making them less suitable for electrocatalytic applications. An additional issue that has to be addressed is the different reactivity of the transition metal precursors, making the control of phase composition and homogeneity of complex mixed oxide phases rather problematic.²³ To overcome this problem, the reactivity of the metal compounds has to be modified and adjusted by the addition of chelating ligands or a slow *in situ* release of water.^{101,108-110}

The above listed limitations of the benzyl alcohol route have inspired us to search for alternative solvents. This project mainly focuses on the development of the *tert*-butanol solvothermal route for the synthesis of nanosized metal oxides. The tertiary alcohol *tert*-butanol is non-aromatic and the *tert*-butoxide residues can be removed more easily from the particle surface. At the same time the *tert*-butyl groups offer sufficient steric control to hinder the particle growth and aggregation. This route was successfully applied by us for the

solvothermal fabrication of ultrasmall and highly dispersible transition metal based oxide nanoparticles described in this thesis.¹¹¹⁻¹¹³

1.4 WATER ELECTROCATALYSIS: FIGURES OF MERIT AND BENCHMARKING

Objective comparison of electrocatalyst efficiency and stability is necessary to evaluate their viability for the application in water splitting devices as well as for the development of innovative electrocatalytic systems.³³ The overall electrocatalytic performance highly depends on intrinsic parameters such as structure and phase composition and extrinsic characteristics including catalytically active surface area, number and accessibility of active sites and mass transport properties.⁹ An accurate quantitative comparison of the catalytic performance is therefore only possible when the properties of the catalyst are known and the resulting currents are corrected for these parameters.

The most common figures of merit are the current density at a given overpotential, the overpotential at a given current density, the Tafel slope and the turnover frequency (TOF).⁹ Current densities are typically measured at $\eta = 300$ mV in OER and $\eta = 100$ mV in HER.^{28,33} Overpotentials are typically specified at the current density of $|j| = 10$ mA cm⁻², which is expected for an economically sustainable integrated solar water splitting device operating at 10 % solar-to-fuel conversion efficiency under 1 sun illumination.^{26,33,114} The Tafel slope provides information about the kinetics of the OER or HER reaction, relating the reaction rate to the overpotential.^{115,116} For a precise comparison of different catalysts with different morphology, current densities have to be corrected additionally for the roughness factor R_f , since films with the same geometric area can have a significantly different real surface area. The commonly accepted figure of merit for comparison of different OER electrocatalysts is the turnover frequency corresponding to the number of O₂ molecules that an active site can produce per second. TOF values are commonly given at a defined overpotential, assuming for an active site to be equal to one metal ion.^{9,39} Equation (1.18) represents a general formula for the calculation of TOF.

$$\text{TOF} = \frac{i}{4 F N_{\text{cat}}} \quad (1.18)$$

Where i is the current, F is Faraday's constant and N_{cat} is the number of catalytically active sites. The current has to be divided by 4 because four electrons are needed to generate one O_2 molecule.

Determination of the exact amount of active sites is challenging because their accessibility is not always clearly identified, especially in nanostructured porous electrodes. Additionally, the interatomic distances in materials with a tunnel or layer structure are larger than in compact materials such as cubic structures leading to a much higher fraction of available atoms. Therefore it is most likely that all atoms of a layered material but only the surface atoms of a cubic material are accessible. To be accurate, both TOF values should be reported as TOF_{min} (assuming all atoms are active) and TOF_{max} (assuming only surface atoms are active).^{112,117}

One of the most accurate methods to determine the mass loading of an electrocatalyst on the electrode is the quartz crystal microbalance (QCM). From the mass loading the total number of electroactive atoms can be derived.¹¹⁸ The surface atoms are usually estimated from the electrode surface area, the fraction of catalytic metal ions on the surface and the computed number of metal ions per unit area.^{39,117} The electrode surface area can be obtained from gas-sorption measurements or can be calculated from the electrode capacitance. The latter method is widely used but is often imprecise and shows large variations.^{9,119} Not only the number of active sites must be determined accurately, but also the current that has to be corrected for the uncompensated electrolyte resistance R_s . To reduce this resistance, the distance between the working and reference electrodes in the electrochemical setup is usually kept as small as possible. R_s is determined as minimum total impedance at open circuit conditions at potentials where no faradaic processes take place.⁹ The OER overpotential is then calculated as follows.

$$\eta = E - E_{\text{OER}} - iR_s \quad (1.19)$$

where E is the recorded potential, E_{OER} is the reversible potential of the OER and i is the current. The challenges associated with the correct calculation of TOF values along with a comparison of electrocatalysts are described in greater detail in chapter 4.

A variety of heterogeneous catalysts for water splitting was reported in the last decades.^{4,28,33,36,120,121} In 2015 McCrory *et al.* published a comprehensive benchmarking

overview of the state-of-the-art electrocatalysts for OER and HER by testing them at exactly identical conditions in basic and acidic media.³³ The authors confirmed the already existing literature findings that metal oxides and especially mixed metal oxides are among the most efficient water splitting materials. Iridium oxide and ruthenium oxide are considered the most efficient oxygen evolution electrocatalysts showing the lowest overpotentials below 300 mV and an excellent corrosion resistance in different environments.^{122,123} However Ir and Ru are among the least abundant elements making the production of their oxides extremely expensive. The search for cheap OER electrocatalysts has therefore greatly increased in recent years. Materials containing abundant non-noble transition metals such as Fe, Co and Ni offer a successful alternative showing high catalytic efficiencies at low overpotentials comparable to those of IrO_x and RuO_x. Mixed oxides such as NiCoO_x, CoFeO_x and NiFeO_x are of particular interest since they have shown much higher catalytic properties than the corresponding binary oxides.^{28,33,39,124} It should be noted that basic electrolytes are more suitable for non-noble transition metal oxides that are generally instable in acids especially under oxidative OER conditions. The long-term stability of catalysts is an additional important issue that has to be addressed in the development of economically viable devices. Non-noble mixed metal oxides were found to be excellent HER electrocatalysts as well showing activities comparable to classic Pt-based materials. Interestingly, the most efficient catalysts were again based on Co, Ni, Mo and Fe oxides in the combinations NiMoO_x, NiMoCoO_x, NiFeO_x and NiMoFeO_x reaching negative HER overpotentials as low as 10 mV in both acidic and basic electrolytes.³³

Water splitting catalysts are often prepared as thin films by electrodeposition on conductive surfaces.^{33,39,120} This method is very convenient since it is fast and does not require any special equipment. However, the structure and morphology of the resulting products remains widely uncontrolled. In contrast, crystalline single nanoparticles offer an exceedingly increased surface area showing a higher amount of surface defects that can additionally enhance the electrocatalytic performance. Furthermore, the structure and phase composition is highly controlled, which is particularly important for the fabrication of mixed oxides that contain two or more metal ions. The synthesis of defined Co-, Ni- and Fe-based nanostructures for water splitting has therefore attracted great interest in materials science. Various shapes and morphologies have been reported ranging from nanowires to nanoplates

and sizes of several nanometers to micrometers along with promising electrocatalytic performance.^{4,28,70,125,126}

1.5 REFERENCES

1. Ho, M. Y.; Khiew, P. S.; Isa, D.; Tan, T. K.; Chiu, W. S.; Chia, C. H. *Nano* **2014**, *09*, 1430002.
2. Zhang, Y.; Li, L.; Su, H.; Huang, W.; Dong, X. *J. Mater. Chem. A* **2015**, *3*, 43.
3. Turner, J. *Science* **2004**, *35*, 972.
4. Wang, J.; Cui, W.; Liu, Q.; Xing, Z.; Asiri, A. M.; Sun, X. *Adv. Mater.* **2016**, *28*, 215.
5. Morales-Guio, C. G.; Stern, L. A.; Hu, X. *Chem. Soc. Rev.* **2014**, *43*, 6555.
6. Zheng, Y.; Jiao, Y.; Jaroniec, M.; Qiao, S. Z. *Angew. Chem.* **2015**, *54*, 52.
7. Zhao, H.; Zhu, Y.-P.; Yuan, Z.-Y. *Eur. J. Inorg. Chem.* **2016**, DOI: 10.1002/ejic.201501181.
8. Rydzek, G.; Ji, Q.; Li, M.; Schaaf, P.; Hill, J. P.; Boulmedais, F.; Ariga, K. *Nano Today* **2015**, *10*, 138.
9. Trotochaud, L.; Boettcher, S. W. *Scr. Mater.* **2014**, *74*, 25.
10. Arico, A. S.; Bruce, P.; Scrosati, B.; Tarascon, J.-M.; van Schalkwijk, W. *Nat. Mater.* **2005**, *4*, 366.
11. Gao, M.; Sheng, W.; Zhuang, Z.; Fang, Q.; Gu, S.; Jiang, J.; Yan, Y. *J. Am. Chem. Soc.* **2014**, *136*, 7077.
12. Vignesh, A.; Prabu, M.; Shanmugam, S. *ACS Appl. Mater. Interfaces* **2016**, *8*, 6019.
13. Faber, M. S.; Jin, S. *Energy Environ. Sci.* **2014**, *7*, 3519.
14. Rao, C. N. R.; Müller, A.; Cheetham, A. K. *The Chemistry of Nanomaterials: Synthesis, Properties and Applications*; John Wiley & Sons, **2006**.

1.5 REFERENCES

15. Chen, H.; Yang, S. *Nanoscale Horiz.* **2016**, *1*, 96.
16. Lin, Y.-Y.; Chen, C.-W.; Chu, T.-H.; Su, W.-F.; Lin, C.-C.; Ku, C.-H.; Wu, J.-J.; Chen, C.-H. *J. Mater. Chem.* **2007**, *17*, 4571.
17. Bau, J. A.; Li, P.; Marenco, A. J.; Trudel, S.; Olsen, B. C.; Lubner, E. J.; Buriak, J. M. *Chem. Mater.* **2014**, *26*, 4796.
18. Bau, J. A.; Lubner, E. J.; Buriak, J. M. *ACS Appl. Mater. Interfaces* **2015**, *7*, 19755.
19. Bondi, J. F.; Misra, R.; Ke, X.; Sines, I. T.; Schiffer, P.; Schaak, R. E. *Chem. Mater.* **2010**, *22*, 3988.
20. Soriano, R. B.; Wu, J.; Kanatzidis, M. G. *J. Am. Chem. Soc.* **2015**, *137*, 9937.
21. Vasques, Y.; Luo, Z.; Schaak R. E. *J. Am. Chem. Soc.* **2008**, *130*, 11866.
22. Cao, G. Z.; Wang, Y. *Nanostructures and Nanomaterials: Synthesis, Properties, and Applications (2nd Edition)*; World Scientific, **2011**.
23. Niederberger, M.; Pinna, N. *Metal Oxide Nanoparticles in Organic Solvents: Synthesis, Formation, Assembly and Application*; Springer London, **2009**.
24. Dau, H.; Limberg, C.; Reier, T.; Risch, M.; Roggan, S.; Strasser, P. *ChemCatChem* **2010**, *2*, 724.
25. Fabbri, E.; Haberer, A.; Waltar, K.; Kötz, R.; Schmidt, T. J. *Catal. Sci. Technol.* **2014**, *4*, 3800.
26. Walter, M. G.; Warren, E. L.; McKone, J. R.; Boettcher, S. W.; Mi, Q.; Santori, E. A.; Lewis, N. S. *Chem.Rev.* **2010**, *110*, 6446.
27. Hernández-Pagán, E. A.; Vargas-Barbosa, N. M.; Wang, T.; Zhao, Y.; Smotkin, E. S.; Mallouk, T. E. *Energy Environ. Sci.* **2012**, *5*, 7582.
28. Burke, M. S.; Enman, L. J.; Batchellor, A. S.; Zou, S.; Boettcher, S. W. *Chem. Mater.* **2015**, *27*, 7549.
29. Ursua, A.; Gandia, L. M.; Sanchis, P. *Proc. IEEE* **2012**, *2*, 410.

30. Ayers, K. E.; Anderson, E. B.; Capuano, C. B.; Carter, B. D.; Dalton, L. T.; Hanlon, G.; Manco, J.; Niedzwiecki, M. *ECS Trans.*, **2010**, *33*, 3.
31. Carmo, M.; Fritz, D. L.; Mergel, J.; Stolten, D. *Int. J. Hydrogen Energy* **2013**, *38*, 4901.
32. Vargas-Barbosa, N. M.; Geise, G. M.; Hickner, M. A.; Mallouk, T. E. *ChemSusChem* **2014**, *7*, 3017.
33. McCrory, C. C.; Jung, S.; Ferrer, I. M.; Chatman, S. M.; Peters, J. C.; Jaramillo, T. F. *J. Am. Chem. Soc.* **2015**, *137*, 4347.
34. Safizadeh, F.; Ghali, E.; Houlachi, G. *Int. J. Hydrogen Energy* **2015**, *40*, 256.
35. Vesborg, P. C.; Seger, B.; Chorkendorff, I. *J. Phys. Chem. Lett.* **2015**, *6*, 951.
36. Zeng, M.; Li, Y. *J. Mater. Chem. A* **2015**, *3*, 14942.
37. Man, I. C.; Su, H.-Y.; Calle-Vallejo, F.; Hansen, H. A.; Martínez, J. I.; Inoglu, N. G.; Kitchin, J.; Jaramillo, T. F.; Nørskov, J. K.; Rossmeisl, J. *ChemCatChem* **2011**, *3*, 1159.
38. Halck, N. B.; Petrykin, V.; Krtil, P.; Rossmeisl, J. *Phys. Chem. Chem. Phys.* **2014**, *16*, 13682.
39. Trotochaud, L.; Ranney, J. K.; Williams, K. N.; Boettcher, S. W. *J. Am. Chem. Soc.* **2012**, *134*, 17253.
40. Ghosh, M.; Biswas, K.; Sundaresan, A.; Rao, C. N. R. *J. Mater. Chem.* **2006**, *16*, 106.
41. Greenwood, N. N.; Earnshaw, A. *Chemistry of the Elements*; Pergamon: Oxford, 1984.
42. Mironova-Ulmane, N.; Kuzmin, A.; Steins, I.; Grabis, J.; Sildos, I.; Pärs, M. *J. Phys.: Conf. Ser.* **2007**, *93*, 012039.
43. <https://staff.aist.go.jp/nomura-k/common/STRUCIMAGES/NiO.gif>, 22.04.2016
44. Liu, W. K.; Santos, M. B. *Thin Films: Heteroepitaxial Systems*; World Scientific, **1999**.

1.5 REFERENCES

45. He, J.; Lindström, H; Hagfeld, A; Lindquist, S.-E. *J. Phys. Chem. B* **1999**, *103*, 8940.
46. Avasthi, D. K.; Mehta, G. K. *Swift Heavy Ions for Materials Engineering and Nanostructuring*, Springer Netherlands, **2011**.
47. Ahmad, T.; Ramanujachary, K. V.; Lofland, S. E.; Ganguli, A. K. *Solid State Sci.* **2006**, *8*, 425.
48. Kodama, R. H.; Makhlof, S. A.; Berkowitz A. E. *Phys. Rev. Lett.* **1997**, *79*, 1393.
49. Makhlof, S. A.; Parker, F. T.; Spada, F. E.; Berkowitz, A. E. *J. Appl. Phys.* **1997**, *81*, 5561.
50. Sadiek, I. M.; Mohammad, A. M.; El-Shakre, M. E.; El-Deab, M. S. *Int. J. Hydrogen Energy* **2012**, *37*, 68.
51. Lyons, M. E. G.; Brandon, M. P. *J. Electroanal. Chem.* **2010**, *641*, 119.
52. Wang, X. *Int. J. Hydrogen Energy* **2004**, *29*, 967.
53. Wehrens-Dijksma, M.; Notten, P. H. L. *Electrochim. Acta* **2006**, *51*, 3609.
54. Lyons, M. E. G.; Brandon, M. P. *Int. J. Electrochem. Sci.* **2008**, *3*, 1386.
55. Silinsky, P. S.; Seehra, M. S. *Phys. Rev. B* **1981**, *24*, 419.
56. https://upload.wikimedia.org/wikipedia/commons/c/c0/NaCl_polyhedra.png, 22.04.2016
57. Patnaik, P. *Handbook of Inorganic Chemicals*, McGraw-Hill, **2003**.
58. Sinkó, K.; Szabó, G.; Zrínyi, M. *J. Nanosci. Nanotechnol.* **2011**, *11*, 4127.
59. Lyons, M.G. E.; Brandon, M. P. *Int. J. Electrochem. Sci.* **2008**, *3*, 1425.
60. Jin, H.; Wang, J.; Su, D.; Wei, Z.; Pang, Z.; Wang, Y. *J. Am. Chem. Soc.* **2015**, *137*, 2688.
61. Wang, H.; Lee, H. W.; Deng, Y.; Lu, Z.; Hsu, P. C.; Liu, Y.; Lin, D.; Cui, Y. *Nat. Commun.* **2015**, *6*, 7261.

62. Smith, W. L.; Hobson, A. D. *Acta Cryst.* **1973**, *29*, 362.
63. Kim, K. J.; Park, Y. R. *Solid State Commun.* **2003**, *127*, 25.
64. [https://upload.wikimedia.org/wikipedia/commons/8/8e/Cobalt\(II,III\)-oxide-unit-cell-2006-CM-perspective-3D-balls.png](https://upload.wikimedia.org/wikipedia/commons/8/8e/Cobalt(II,III)-oxide-unit-cell-2006-CM-perspective-3D-balls.png), 22.04.2016.
65. Dutta, P.; Seehra, M. S.; Thota, S.; Kumar, J. *J. Phys.: Condens. Matter* **2008**, *20*, 015218.
66. Kündig, W; Kobelt, M; Appel, H; Constabaris, G; Lindquist, R.H. *J. Phys. Chem. Solids* **1969**, *30*, 819.
67. Roth, W. L. *J. Phys. Chem. Solids* **1964**, *25*, 1.
68. Shinde, V. R.; Mahadik, S. B.; Gujar, T. P.; Lokhande, C. D. *Appl. Surf. Sci.* **2006**, *252*, 7487.
69. Kaczmarek, A.; Grzesik, Z.; Mrowec, S. *High Temp. Mater. Processes* **2012**, *31*.
70. Deng, X.; Tüysüz, H. *ACS Catal.* **2014**, *4*, 3701.
71. Chou, N. H.; Ross, P. N.; Bell, A. T.; Tilley, T. D. *ChemSusChem* **2011**, *4*, 1566.
72. Chua, C. S.; Ansovini, D.; Lee, C. J.; Teng, Y. T.; Ong, L. T.; Chi, D.; Hor, T. S.; Raja, R.; Lim, Y. F. *Phys. Chem. Chem. Phys.* **2016**, *18*, 5172.
73. Xi, L.; Tran, P. D.; Chiam, S. Y.; Bassi, P. S.; Mak, W. F.; Mulmudi, H. K.; Batabyal, S. K.; Barber, J.; Loo, J. S. C.; Wong, L. H. *J. Phys. Chem. C* **2012**, *116*, 13884.
74. Chang, X.; Wang, T.; Zhang, P.; Zhang, J.; Li, A.; Gong, J. *J. Am. Chem. Soc.* **2015**, *137*, 8356.
75. Chakraborty, A. K.; Shanjeda Akter, M.; Ahsanul Haque, M.; Arifuzzaman Khan, G. M.; Shamsul Alam, M. *J. Cluster Sci.* **2013**, *24*, 701.
76. Gan, J.; Lu, X.; Tong, Y. *Nanoscale* **2014**, *6*, 7142.
77. Faivre, D.; Frankel, R. B. *Iron Oxides: From Nature to Applications*, Wiley-vch, **2016**.

1.5 REFERENCES

78. van de Krol, R; Grätzel, M. *Photoelectrochemical Hydrogen Production*, Springer, **2012**.
79. Ahmed, S. M.; Leduc, J.; Haller, S. F. *J. Phys. Chem.* **1988**, *92*, 6655.
80. Sivula, K.; Le Formal, F.; Gratzel, M. *ChemSusChem* **2011**, *4*, 432.
81. Cornell, R. M. S. **2003**. 1. Cornell, R. M.; Schwertmann, U. *The iron oxides: structure, properties, reactions, occurrences and uses*; Wiley-vch, **2003**.
82. Yu, Q.; Meng, X.; Wang, T.; Li, P.; Ye, J. *Adv. Funct. Mater.* **2015**, *25*, 2686.
83. Zong, X.; Thaweesak, S.; Xu, H.; Xing, Z.; Zou, J.; Lu, G. M.; Wang, L. *Phys. Chem. Chem. Phys.* **2013**, *15*, 12314.
84. Mohapatra, M.; Anand, S. *Int. J. Engin. Sci. Technol.* **2010**, *2*, 127.
85. Chitrakar, R.; Tezuka, S; Sonoda, A; Sakane, K; Hirotsu, T. *Ind. Eng. Chem. Res.* **2009**, *48*, 2107.
86. Tufo, A. E.; García, K. E.; Barrero, C. A.; Sileo, E. E. *Hyperfine Interact.* **2013**, *224*, 239.
87. Ishikawa, T.; Motoki, T.; Katoh, R.; Yasukawa, A.; Kandori, K.; Nakayama, T.; Yuse, F. *J. Colloid Interface Sci.* **2002**, *250*, 74.
88. <http://ammin.geoscienceworld.org/content/gsammin/88/5-6/782/F1.large.jpg>, 22.04.2016.
89. Wei, C.; Wang, X.; Nan, Z.; Tan, Z. *J. Chem. Eng. Data* **2010**, *55*, 366.
90. Song, Y.; Bac, B. H.; Lee, Y.-B.; Kim, M. H.; Kang, I. M. *CrystEngComm* **2011**, *13*, 287.
91. Suresh, R.; Prabu, R.; Vijayaraj, A.; Giribabu, K.; Stephen, A.; Narayanan, V. *Mater. Chem. Phys.* **2012**, *134*, 590.
92. Kim, J. Y.; Magesh, G.; Youn, D. H.; Jang, J. W.; Kubota, J.; Domen, K.; Lee, J. S. *Sci. Rep.* **2013**, *3*, 2681.

93. Post, J. E.; Heaney, P. J.; von Dreele, R. B.; Hanson, J. C. *Am. Mineral.* **2003**, *88*, 782.
94. Cushing, B. L.; Kolesnichenko, V. L.; O'Connor, C. J. *Chem. Rev.* **2004**, *104*, 3893.
95. Park, J.; Joo, J.; Kwon, S. G.; Jang, Y.; Hyeon, T. *Angew. Chem.* **2007**, *46*, 4630.
96. Swihart, M. T. *Curr. Opin. Colloid Interface Sci.* **2003**, *8*, 127.
97. Caruntu, G.; Caruntu, D.; O'Connor, C. J. *Encycl. Inorg. Chem.* **2009**, DOI: 10.1002/0470862106.ia370.
98. Hench, L. L.; West, J. K. *Chem. Rev.* **1990**, *90*, 33.
99. Niederberger, M.; Garnweitner, G. *Chem. –Eur. J.* **2006**, *12*, 7282.
100. Niederberger, M. *Acc. Chem. Res.* **2007**, *40*, 793.
101. Livage, J. *J. Sol-Gel Sci. Technol.* **1989**, 103.
102. Debecker, D. P.; Mutin, P. H. *Chem. Soc. Rev.* **2012**, *41*, 3624.
103. Niederberger, M.; Garnweitner, G.; Buha, J.; Polleux, J.; Ba, J.; Pinna, N. *J. Sol-Gel Sci. Technol.* **2006**, *40*, 259.
104. Pinna, N.; Antonietti, M.; Niederberger, M. *Colloids Surf. A* **2004**, *250*, 211.
105. Pinna, N.; Karmaoui, M.; Willinger, M.-G. *J. Sol-Gel Sci. Technol.* **2010**, *57*, 323.
106. Ludi, B.; Suess, M. J.; Werner, I. A.; Niederberger, M. *Nanoscale* **2012**, *4*, 1982.
107. Szeifert, J. M.; Fattakhova-Rohlfing, D.; Georgiadou, D.; Kalousek, V.; Rathouský, J.; Kuang, D.; Wenger, S.; Zakeeruddin, S. M.; Grätzel, M.; Bein, T. *Chem. Mater.* **2009**, *21*, 1260.
108. Hubert-Pfalzgraf, L. G. *J. Mat. Chem.* **2004**, *14*, 3113.
109. In, M.; Sanchez, C. *J. Phys. Chem. B* **2005**, *109*, 23870.
110. Sanchez, C.; Livage, J.; Henry, M.; Babonneau, F. *J. Non-Cryst. Solids* **1988**, *100*, 65.

1.5 REFERENCES

111. Feckl, J. M.; Dunn, H. K.; Zehetmaier, P. M.; Müller, A.; Pendlebury, S. R.; Zeller, P.; Fominykh, K.; Kondofersky, I.; Döblinger, M.; Durrant, J. R.; Scheu, C.; Peter, L.; Fattakhova-Rohlfing, D.; Bein, T. *Adv. Mater. Interfaces* **2015**, *2*, 1500358.
 112. Fominykh, K.; Cernev, P.; Zaharieva, I.; Sicklinger, J.; Stefanic, G.; Doeblinger, M.; Müller, A.; Pokharel, A.; Böcklein, S.; Scheu, C.; Bein, T.; Fattakhova-Rohlfing, D. *ACS Nano* **2015**, *9*, 5180.
 113. Fominykh, K.; Feckl, J. M.; Sicklinger, J.; Döblinger, M.; Böcklein, S.; Ziegler, J.; Peter, L.; Rathousky, J.; Scheidt, E.-W.; Bein, T.; Fattakhova-Rohlfing, D. *Adv. Funct. Mater.* **2014**, *24*, 3123.
 114. Weber, M. F.; Dignam, M. J. *J. Electrochem. Soc.: Electrochem. Sci. Technol.* **1984**, *131*, 1259.
 115. Bard, A. J.; Faulkner, L. R. *Electrochemical Methods. Fundamentals and Applications*, Wiley, **2001**.
 116. Shinagawa, T.; Garcia-Esparza, A. T.; Takanabe, K. *Scientific reports* **2015**, *5*, 13801.
 117. Louie, M. W.; Bell, A. T. *J. Am. Chem. Soc.* **2013**, *135*, 12329.
 118. Marx, K. A. *Biomacromolecules* **2003**, *4*, 1099.
 119. Trasatti, S.; Petrii, O. A. *J. Electroanal. Chem.* **1992**, *321*, 353.
 120. McCrory, C. C.; Jung, S.; Peters, J. C.; Jaramillo, T. F. *J. Am. Chem. Soc.* **2013**, *135*, 16977.
 121. Mette, K.; Bergmann, A.; Tessonier, J.-P.; Hävecker, M.; Yao, L.; Ressler, T.; Schlögl, R.; Strasser, P.; Behrens, M. *ChemCatChem* **2012**, *4*, 851.
 122. Trasatti, S.; Lodi, G. *Electrodes of Conductive Metallic Oxides*, Elsevier Amsterdam, **1981**.
 123. Reier, T.; Oezaslan, M.; Strasser, P. *ACS Catal.* **2012**, *2*, 1765.
 124. Yuan, C.; Wu, H. B.; Xie, Y.; Lou, X. W. *Angew. Chem.* **2014**, *53*, 1488.
-

125. Gong, M.; Zhou, W.; Tsai, M. C.; Zhou, J.; Guan, M.; Lin, M. C.; Zhang, B.; Hu, Y.; Wang, D. Y.; Yang, J.; Pennycook, S. J.; Hwang, B. J.; Dai, H. *Nat. commun.* **2014**, *5*, 4695.
126. Gong, M.; Dai, H. *Nano Res.* **2014**, *8*, 23.

2 SYNTHESIS AND CHARACTERIZATION

The structure and morphology of nanocrystalline materials obtained in this work were analyzed by a variety of analytical methods commonly used in materials science. The phase composition, crystallinity, domain size and dispersibility of nanoparticles were determined by powder X-ray diffraction (XRD), dynamic light scattering (DLS), thermogravimetric analysis (TGA) and Raman spectroscopy. The morphology and structural properties including lattice parameters of the crystals were visualized by electron microscopy (EM). Additionally, the elemental composition of mixed phases was analyzed by energy dispersive X-ray spectroscopy (EDX). Furthermore, the electrocatalytic performance of nanomaterials in water splitting was investigated using electrochemical methods. The theoretical background and practical implementation of the most important characterization methods along with the solvothermal synthesis used in this thesis are briefly described in the following section.

2.1 SOLVOTHERMAL REACTIONS

Solvothermal reactions are mainly conducted in autoclaves beyond the boiling point of the solvent in hermetically sealed vessels (Figure 2.1a).¹ Typically the steel reactors are provided with additional Teflon liners protecting the reaction mixture from corrosion. However, due to the high porosity of Teflon ultrasmall nanoparticles can contaminate the walls of the liner reducing the quality of further reactions. Therefore glass liners were used to achieve high reproducibility. The sealed autoclaves were put in programmable laboratory ovens to provide a control over the temperature and duration of the reaction.



Figure 2.1 Illustration of a commercial (a) autoclave and (b) microwave reactor commonly used for solvothermal syntheses.

In addition to conventional heating, the solvothermal reactions can also be performed at microwave-assisted conditions in specially designed autoclaves. The advantages of microwave irradiation provided by commercial reactors (Figure 2.1b) comprise the ability to stir the reaction mixture during the synthesis ensuring homogeneity and the precise control of the temperature, pressure and the applied power, maximizing the reproducibility. Furthermore the efficient rapid heating and cooling allows for setting of fast temperature ramps. Combined with the microwave irradiation it can lead to extremely short reaction times down to only a few minutes.¹

2.2 X-RAY DIFFRACTION (XRD)

X-ray diffraction is a common technique in materials science that is widely used for phase identification of crystalline materials, providing information on unit cell dimensions, lattice parameters and size of crystalline domains.^{2,3} X-ray diffraction is based on constructive interference of a monochromatic X-ray beam scattered at specific angles from each set of lattice planes in a crystalline sample. In X-ray diffractometers X-rays are generated in a cathode ray tube by heating a filament to produce electrons. High voltage is applied to accelerate these electrons towards a target anode which is typically Cu, Mo or Co. When the electrons collide with the target material, X-rays are created by two different processes that lead to the emission of a continuous radiation (Bremsstrahlung) and characteristic X-ray radiation. The characteristic X-ray photons are emitted when the electrons have sufficient energy to knock out inner shell electrons from the anode atoms and electrons from higher energy levels fill up the vacancies. Usually these are transitions from upper shells into the K shell or L shell, the so-called K and L lines. For diffraction the X-ray beam is filtered to produce monochromatic X-rays that are collimated and directed onto the sample. Copper is the most common target material with the wavelength of Cu K_α radiation of $\lambda(\text{Cu K}_\alpha) = 1.5418 \text{ \AA}$. Constructive interference occurs when the interaction of the incident X-rays with the sample satisfies the Bragg equation:

$$n \lambda = 2d \sin \theta \quad (2.1)$$

This equation relates the wavelength of the electromagnetic radiation λ to the diffraction angle θ and the lattice spacing d in a crystalline sample. Figure 2.2 shows a graphic illustration of the Bragg relation.

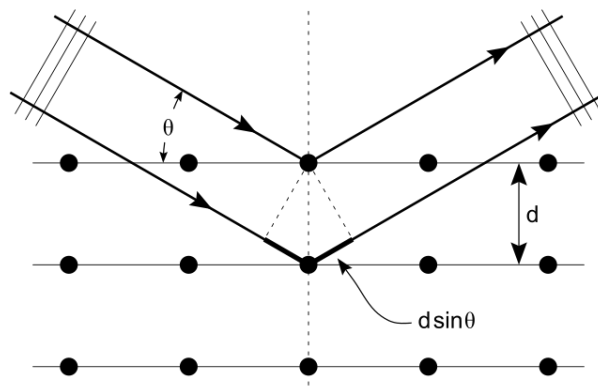


Figure 2.2 Constructive interference of X-ray radiation and a crystalline lattice.⁴

The diffracted X-rays are detected and result in characteristic patterns where the X-ray intensity is recorded as a function of 2θ .

In polycrystalline samples the crystallite size is related to the line broadening in a diffraction pattern. The particle size can be then calculated using the Scherrer equation:

$$D = \frac{K \lambda}{\beta \cos \theta} \quad (2.2)$$

where D is the mean size of the crystalline domains, K is a dimensionless shape factor with a typical value of around 0.9 for spherical particles, λ is the X-ray wavelength, β is the full width at half maximum (FWHM) of the reflection corrected for the intrinsic instrumental broadening, and θ is the diffraction angle.²

X-ray diffraction analysis was carried out in reflection mode using a Bruker D8 Discover with Ni-filtered $\text{Cu K}\alpha$ radiation and a position-sensitive LynxEye semiconductor detector. Measurements in transmission mode were carried out on a STOE powder diffractometer in transmission geometry ($\text{Cu K}\alpha_1$, $\lambda = 1.5406 \text{ \AA}$) equipped with a position-sensitive Mythen 1K detector.

2.3 RAMAN SPECTROSCOPY

Raman spectroscopy is a spectroscopic method based on inelastic scattering of monochromatic light, which can be used to characterize and identify materials and to determine their chemical and phase composition. With this technique vibrational, rotational and other low-frequency modes of a system can be analyzed.²

Raman-active molecules have bonds with varying polarizability as a function of the interatomic distance. Laser light interacts with these bonds and excites the molecule from the ground state into a more energetic virtual level. Subsequent relaxation leads to a simultaneous re-emission of a photon that can have a different wavelength than the incident photon corresponding to the frequency of the vibrational mode. Thus the molecule returns into a more energetic vibrational state and the photon is therefore emitted at a lower frequency. This shift in energy caused by inelastic Raman scattering is termed Stokes-shift. In the opposite case the molecule is already in an excited vibrational state and returns to the ground state upon interacting with the laser light. The final state is therefore less energetic than the initial state resulting in a shorter wavelength of the emitted light. This process is termed anti-Stokes Raman scattering. Elastic or Rayleigh scattering leads to relaxation into the initial ground state emitting a photon with the same frequency as the incident light, showing no Raman effect. All excitation processes are illustrated in Figure 2.3.

Not only molecules but also solid-state materials such as metal oxides can be analyzed *via* Raman spectroscopy. The special feature of crystalline structures is their periodicity. This allows for the formation of standing elastic waves induced by vibration of the atoms in the lattice with a phonon as a quantum of a crystal vibrational energy. A phonon mode in a solid is therefore equivalent to the vibrational mode in a molecule.⁵

The intensity of Raman scattering is several orders of magnitude lower than the Rayleigh scattering. Stokes scattering is much more frequent than anti-Stokes scattering because the initial energy level which is the ground state is more occupied than excited vibrational states. Therefore, commonly the Stokes-shift is recorded in a typical Raman measurement. Being directly related to the vibrational and rotational energies of a material, it provides characteristic Raman spectra.²

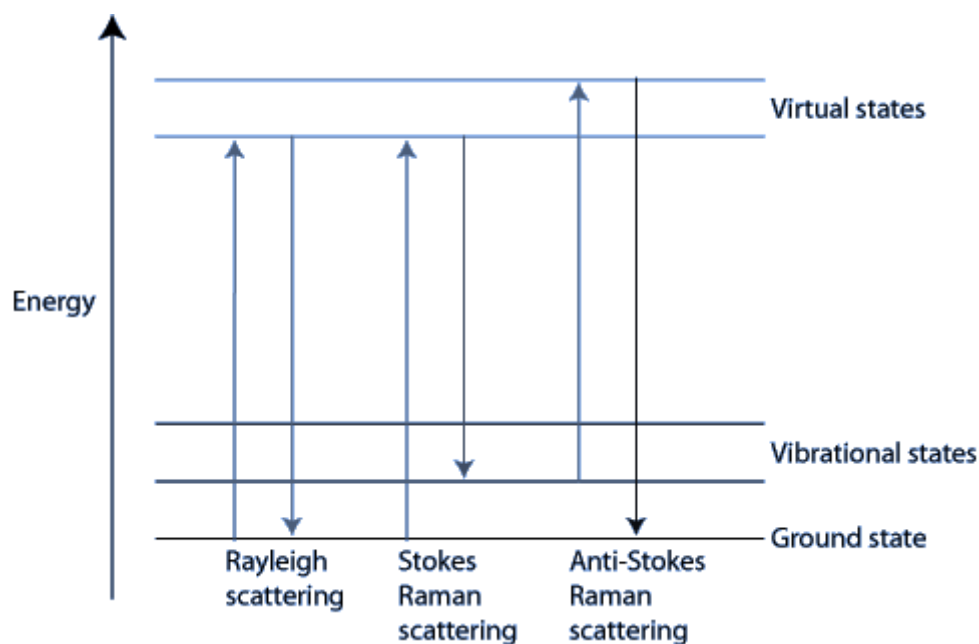


Figure 2.3 Energy transitions in Raman spectroscopy.⁶

Raman spectra were recorded with a LabRAM HR UV-VIS (Horiba Jobin Yvon) Raman microscope (Olympus BX41) with a Symphony CCD detection system using a HeNe laser at 632.8 nm.

2.4 DYNAMIC LIGHT SCATTERING (DLS)

Dynamic light scattering is a common method for the determination of the size distribution of small particles in colloidal suspensions.⁷ The technique uses monochromatic laser light to measure the speed of the particles that move randomly in the analyzed medium. The movement is called Brownian motion and is caused by collisions with the surrounding solvent molecules and other particles. The incident light is scattered in all directions by the small particles in a sample leading to fluctuations of the scattering intensity based on constructive or destructive interference of the scattered light. The recorded intensity variations depend on the speed of the Brownian motion that is influenced by several factors such as temperature, viscosity of the medium and particle size. These parameters are related according to the Stokes-Einstein equation.

$$d_H = \frac{kT}{3\pi\eta D} \quad (2.3)$$

where d_H is the hydrodynamic radius of the particles, k is the Boltzmann-constant, T is the temperature, η is the viscosity and D is the translational diffusion coefficient which defines the velocity of the Brownian motion. The hydrodynamic radius describes the actual particle diameter as well as any kind of surface structure including organic ligands and hydration and ionic shells. For all calculations spherical particle shape is assumed.

DLS measurements were performed on a MALVERN Zetasizer-Nano instrument equipped with a 4 mW He-Ne laser (633 nm) and an avalanche photodiode detector.

2.5 THERMOGRAVIMETRIC ANALYSIS (TGA)

Thermogravimetric analysis is used for the characterization of materials properties as an effect of thermal treatment. The key factor is the determination of the amount and rate of mass change in relation to the temperature or time. TGA is used primarily to characterize the composition of multicomponent organic/inorganic systems, oxidative and thermal stability or moisture and volatiles content of materials.^{8,9} This method requires high accuracy in determination of weight and temperature change to achieve optimum results. TGA measurements are carried out at constant heating rates at temperatures up to 1000 °C or more in a controlled atmosphere (synthetic air was typically used throughout this project). Subsequently, the relative weight change (in percent) is plotted as a function of temperature. The data provide information about chemical and physical processes such as redox reactions, desolvation, decomposition, phase transitions and sorption processes.

More detailed information on the thermodynamic processes is gained by additional application of differential scanning calorimetry (DSC). This technique measures the heat flow in the material compared to a reference and allows statements about the endothermic or exothermic character of the process and possible phase transitions such as melting, crystallization or degradation, which are not necessarily accompanied by weight loss.

Thermogravimetric analysis and differential scanning calorimetry were performed on a NETZSCH STA 440 C TG/DSC instrument applying a heating rate of 10 K min^{-1} in a synthetic air stream with a constant flow of 25 mL min^{-1} .

2.6 ELECTRON MICROSCOPY (EM)

Imaging of microstructural parameters such as particle size and size distribution, lattice planes in crystal structures and presence and composition of mixed and/or defect-rich phases comprised an essential part in the characterization of the nanostructures developed in this thesis. Structural and morphological analysis of nanocrystalline materials is demanding and requires instruments of high precision and extremely high resolution, especially when the crystallite dimensions are reduced to only a few nanometers. The features that have to be resolved are in the range of $0.3 \mu\text{m}$ to 0.1 nm . This cannot be reached by common light microscopes that are limited in their resolution to around 200 nm . Electron microscopy however provides a powerful tool enabling imaging on the atomic scale because of the shorter electron wavelength in the picometer range.¹⁰ The primary electron beam is generated by a heated tungsten filament or by a field emission gun and is typically accelerated by an applied voltage of $5 - 1000 \text{ keV}$. Further arrangement of electromagnetic lenses leads to focusing of the beam on a specimen to a spot size in the nanometer range (Figure 2.4). When the electron beam penetrates the sample several absorption, scattering and emission processes can be detected. Secondary electrons are generated when electrons in the sample are hit by the incident beam with sufficiently high energy and excited above the vacuum level. The energy of secondary electrons ($< 50 \text{ eV}$) rather low and therefore only electrons produced near the surface can escape and be detected. Backscattered and diffracted electrons are both produced by elastic scattering (losing only $20 - 40 \%$ of their energy), however they are detected at different diffraction angles. Auger electrons are created when sample electrons are knocked out from the inner shells and higher shell electrons fill the resulting vacancies. The produced energy is then transferred to outer shell electrons that are ejected from the sample. Alternatively, the excess energy can be balanced by emitting characteristic X-rays that are used in energy dispersive X-ray spectroscopy (EDX). The electrons are detected by a CCD camera or on a fluorescent screen.

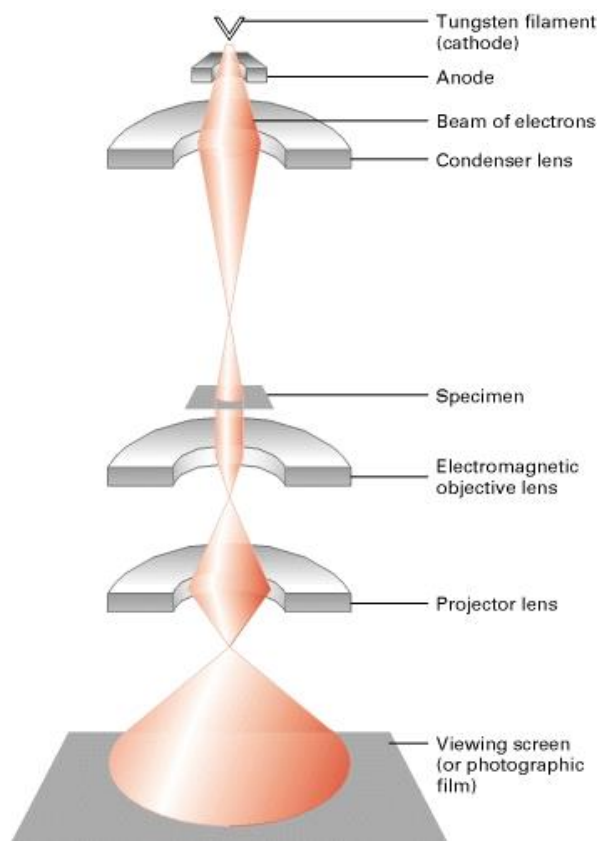


Figure 2.4 Illustration of the optical pathway in a transmission electron microscope.¹⁰

Scanning electron microscopy (SEM) operates at acceleration voltages typically in the range of 5 – 30 kV and provides information about the surface morphology of a sample. Being created at and near the surface, secondary electrons are commonly used in SEM imaging. By scanning the specimen with the electron beam and recording the output intensity for each position a precise image of the sample surface is generated.¹¹

Transmission Electron Microscopy (TEM) was used in this work for the identification of crystal structure, phase composition and presence and position of defects of crystalline samples. Usually acceleration voltages in the range of 80 – 300 kV are applied and the transmitted electrons are detected with a contrast caused by thickness variation in the specimen, the elemental composition and the density of the sample (mass contrast).¹⁰ In TEM diffraction mode electron diffraction (ED) patterns can be generated that correspond to the crystal structure of the analyzed material. In scanning transmission electron microscopy (STEM) the primary beam is highly focused forming a very small probe and scanned over the sample, thus enabling imaging of morphology like in SEM but with a much higher resolution.

High angle scattered electrons are then recorded by a ring detector located around the optical axis enabling imaging with a high mass contrast in the so-called high angle annular dark field mode (HAADF).

Scanning electron microscopy (SEM) was performed on a JEOL JSM-6500F scanning electron microscope equipped with a field emission gun operated at 4 – 10 kV depending on the sample. High Resolution Transmission Electron Microscopy (HRTEM) and Scanning Transmission Electron Microscopy in High Angle Annular Dark Field mode (STEM-HAADF) were performed using a FEI Titan 80-300 equipped with a field emission gun operated at 300 kV.

2.7 QUARTZ CRYSTAL MICROBALANCE (QCM)

For an accurate calculation of turnover frequencies of electrocatalytic materials it is important to determine the exact mass loading of the catalyst on the electrode. Very small amounts in the range of a few micrograms can be measured using a quartz crystal microbalance (QCM). This method uses the change in frequency of a quartz crystal resonator to compute the mass variation before and after loading with the catalyst (Figure 2.5a). The mechanism is based on the piezoelectric properties of the quartz crystal and uses the inverse piezoelectric effect to generate oscillations.¹² Depending on the polarization, the application of an electric field causes a contraction or elongation and induces a pure shear mode oscillation that propagates through the crystal (Figure 2.5b) Oscillation at the resonant frequency of a pure shear mode makes the device very sensitive for mass deviations caused by a thin film. The nominal frequency depends on the size and thickness of the quartz crystal and is typically $f_0 = 5$ or 10 MHz.¹³

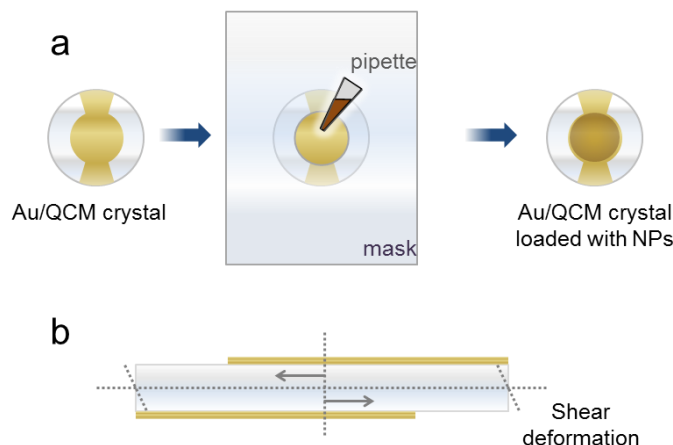


Figure 2.5 Illustration of an Au coated QCM crystal. (a) Top view of the crystal and catalyst loading procedure where a tape mask is used to deposit a catalyst layer only on the electrode. (b) Side view of the crystal demonstrating the shear deformation.

The relation between the change in resonant frequency and mass loading is given by the Sauerbrey equation.¹⁴

$$\Delta f = \frac{-2f_0^2 m n}{\sqrt{\rho \mu}} = -C_f m \quad (2.4)$$

where $\Delta f = f - f_0$ is the frequency change in Hz with f_0 being the nominal oscillation frequency and f being the frequency of the loaded crystal, m is the change in mass per unit area in g cm^{-2} , n is the harmonic number ($n = 1$ for crystals operated at the nominal frequency), ρ is the density of the quartz crystal (2.648 g cm^{-3}) and μ is the shear modulus of quartz ($2.947 \cdot 10^{11} \text{ g cm}^{-1} \text{ s}^{-2}$). The combination of all constants gives the sensitivity factor C_f which is $232.6 \text{ Hz cm}^2 \mu\text{g}^{-1}$ for a 10 MHz crystal in air.

According to the Sauerbrey equation a frequency change of 1 Hz for a 10 MHz crystal corresponds to a variation in mass loading of 4.4 ng, showing the great sensitivity of a QCM. However the Sauerbrey equation applies only for very low mass loadings and is limited to a maximum mass loading of $\Delta f \leq 2\% f_0$.¹³

2.8 ELECTROCHEMICAL WATER SPLITTING SETUP

The performance of catalysts in electrochemical water splitting was characterized using an electrochemical cell in a three-electrode setup containing a working electrode (WE), Ag/AgCl reference electrode (RE) and a Pt counter electrode (CE) immersed into an electrolyte as shown in Figure 2.6a. The Au/QCM crystals loaded with the catalyst film were directly used as WE after attaching a silver wire by fixing it with Ag varnish as electrical contact. The wire was isolated by a protective epoxy resin coating to avoid its direct contact with the electrolyte. (Figure 2.6b).

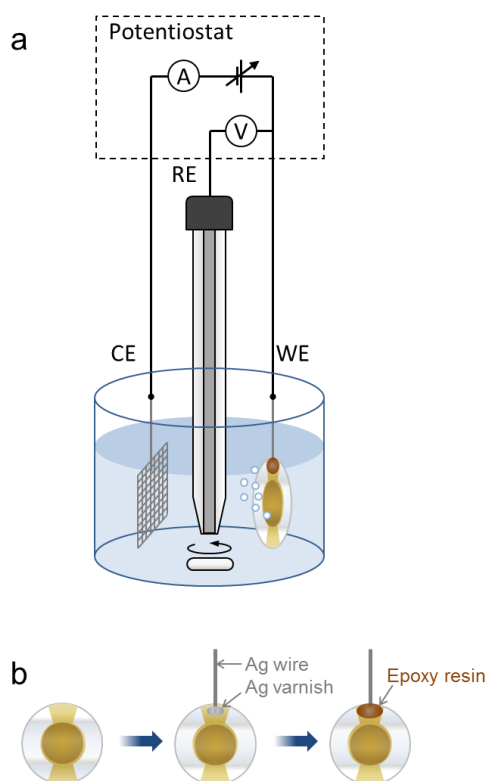


Figure 2.6 (a) Illustration of a common water splitting cell in a three-electrode setup. (b) Preparation of Au/QCM catalyst loaded electrodes for electrochemical measurements by attaching a silver wire and a subsequent protection with epoxy resin.

Cyclic voltammetry (CV) was used as the basic method for the electrode characterization. By applying an external power supply using a potentiostat the potential E of the WE was cycled linearly in a specified range with a constant scan rate, typically 20 mV s^{-1} . All electrochemical measurements in this thesis were performed using an Autolab

potentiostat/galvanostat PGSTAT302N with FRA32M module in a 0.5 M KOH aqueous electrolyte at pH 13.43 and a Pt mesh (2 cm²) counter electrode. All potentials were measured vs. Ag/AgCl/KCl (sat.) reference electrode with a potential $E_{\text{RHE}}(\text{Ag/AgCl})$ of +0.989 V vs. the reversible hydrogen electrode (RHE) at pH 13.43 calculated according to the following equation.

$$E_{\text{RHE}}(\text{Ag/AgCl}) = E_{\text{NHE}}(\text{Ag/AgCl}) + 0.059 \cdot \text{pH} \quad (2.5)$$

where $E_{\text{NHE}}(\text{Ag/AgCl})$ is the potential of the Ag/AgCl electrode vs. the normal hydrogen electrode (NHE) corresponding to +0.197 V. The potential stability of the Ag/AgCl electrode was regularly monitored by measuring the potential of a known redox couple.^{12,15}

Figure 2.7 shows a cyclic voltammogram of NiO as a typical example of a water splitting electrocatalyst studied in this thesis. In alkaline electrolyte at pH 13.43 NiO-based electrocatalysts usually show a pair of redox peaks corresponding to the reversible oxidative hydroxylation of NiO according to¹⁶



The peak shapes contain information about the electrode kinetics and allow for the investigation of structural composition in mixed phases which is especially important for mixed oxide electrocatalysts. The area under the anodic or cathodic peaks, respectively, corresponds to the charge transferred in this process and directly correlates to the number of catalytically active sites. At pH 13.43, the currents at potentials more positive than 0.47 V vs. Ag/AgCl correspond to the OER, and negative currents at potentials below -1.25 V vs. Ag/AgCl to the HER. The onset potentials of these processes along with current values reached at definite potentials are important figures of merit in benchmarking of electrocatalysts.

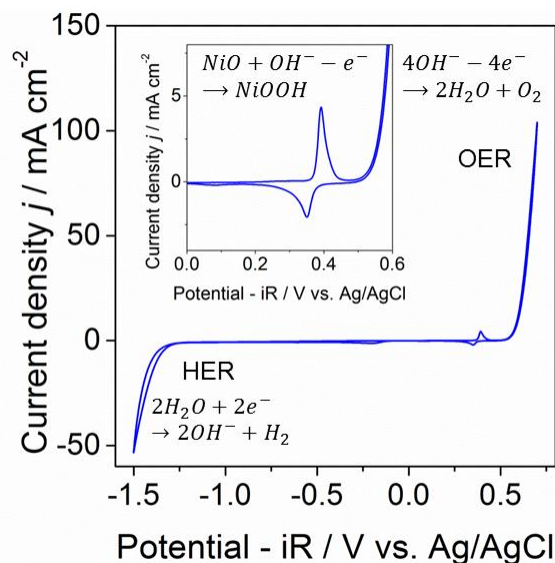


Figure 2.7 Cyclic voltammogram of NiO water splitting electrocatalyst. The inset shows a potential range at which oxidative hydroxylation of NiO is observed.

The stability of electrocatalysts was investigated using either multiple cycling in cyclic voltammetry (typically 200 cycles at the scan rate of 20 mV s^{-1}), or prolonged galvanostatic electrolysis using the same setup. In galvanostatic experiments a constant current is applied on the electrode and the potential is recorded as a function of time.

2.9 REFERENCES

1. Niederberger, M.; Pinna, N. *Metal Oxide Nanoparticles in Organic Solvents: Synthesis, Formation, Assembly and Application*; Springer London, **2009**.
2. Cao, G. Z.; Wang, Y. *Nanostructures and Nanomaterials: Synthesis, Properties, and Applications*, World Scientific, **2011**.
3. Bunaciu, A. A.; Udristioiu, E. G.; Aboul-Enein, H. Y. *Crit. Rev. Anal. Chem.* **2015**, *45*, 289.
4. <https://figures.boundless-cdn.com/17493/large/640px-bragg-diffraction-2.png>, 22.04.2016

2.9 REFERENCES

5. Kumar, C. S. S. R. *Raman Spectroscopy for Nanomaterials Characterization*, Springer London, **2012**.
6. <http://www.doitpoms.ac.uk/tlplib/raman/images/transitions.gif>, 22.04.2016.
7. Pecora, R. *J. Nanoparticle Res.* **2000**, 2, 123.
8. Pang, L. S. K.; Saxby, J. D.; Chatfield, S. P. *J. Phys. Chem.* **1993**, 97, 6941.
9. Pang, L. S. K.; Saxby, J. D.; Chatfield, S. P. *J. Phys. Chem.* **1993**, 97, 6941.
10. Williams, D. B.; Carter, C. B. *The Transmission Electron Microscope*; Springer, **1996**.
11. Goodhew, P. J.; Humphreys, J.; Beanland, R. *Electron Microscopy and Analysis*, Taylor & Francis, **2001**.
12. Bard, A. J.; Faulkner, L. R. *Electrochemical Methods. Fundamentals and Applications*, Wiley, **2001**.
13. SRS-Stanford-Research-Systems Quartz Crystal Microbalance-Operation and Service Manual, **2004**.
14. Sauerbrey, G. Verwendung von Schwingquarzen zur Wägung Dünner Schichten und zur Mikrowägung. *Z. Phys A: Hadrons Nucl.* **1959**, 155, 206.
15. Hamann, C. H.; Vielstich, W. *Elektrochemie*, Wiley-vch, 2005.
16. Corrigan, D. A. *J. Electrochem. Soc.* **1989**, 136, 723.

3 ULTRASMALL DISPERSIBLE CRYSTALLINE NICKEL OXIDE NANOPARTICLES AS HIGH PERFORMANCE CATALYSTS FOR ELECTROCHEMICAL WATER SPLITTING

This chapter is based on the following publication:

Ksenia Fominykh*, Johann M. Feckl*, Johannes Sicklinger, Markus Döblinger, Sebastian Böcklein, Jürgen Ziegler, Laurence Peter, Jiri Rathousky, Ernst-Wilhelm Scheidt, Thomas Bein and Dina Fattakhova-Rohlfing *Adv. Funct. Mater.* **2014**, *24*, 3123.

* These authors contributed equally

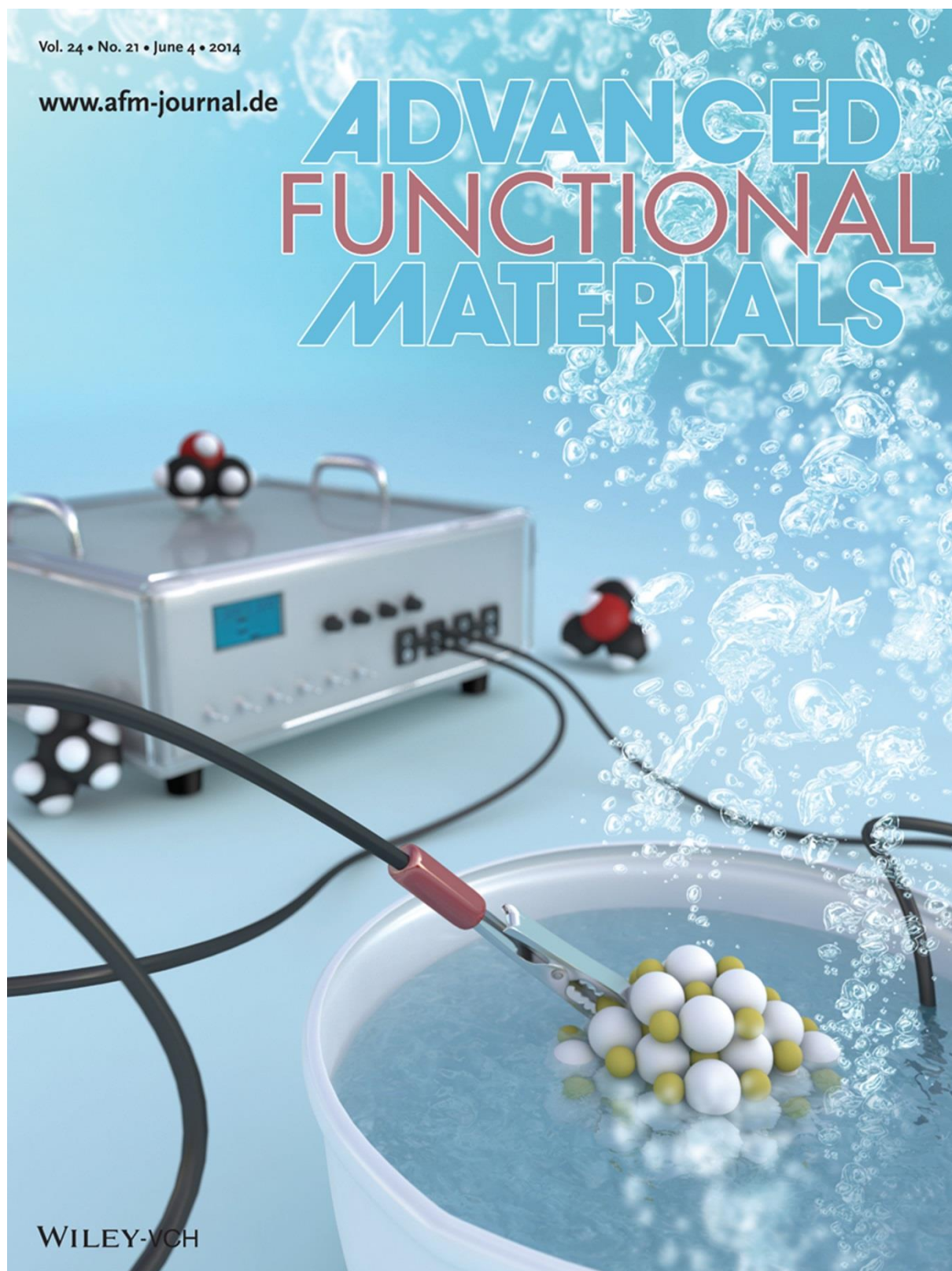


Figure 3.1 Image created by Christoph Hohmann (Nanosystems Initiative Munich, NIM) published as front cover in Adv. Funct. Mater. 21/2014 (used with permission from the publisher).

3.1 ABSTRACT

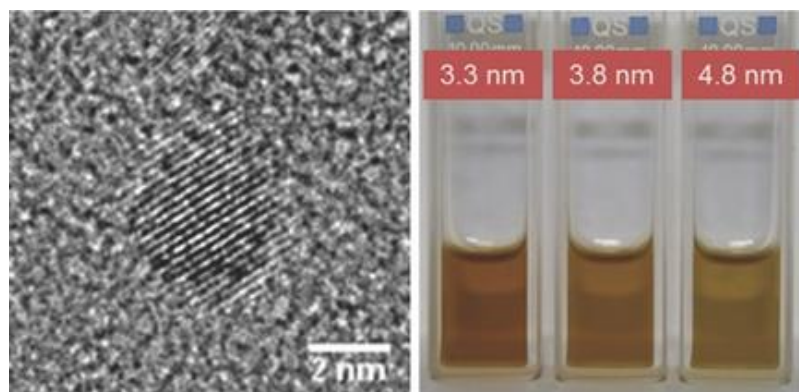


Figure 3.2 Table of contents (ToC) image: Ultrasmall, crystalline, and dispersible NiO nanoparticles are prepared for the first time using a solvothermal reaction in *tert*-butanol. These nanocrystals can be prepared with sizes tunable from 2.5 to 5 nm and are highly efficient catalysts for electrochemical oxygen generation.

Ultrasmall, crystalline and dispersible NiO nanoparticles, are prepared for the first time, and it is shown that they are promising candidates as catalysts for electrochemical water oxidation. Using a solvothermal reaction in *tert*-butanol, very small nickel oxide nanocrystals can be made with sizes tunable from 2.5 to 5 nm and a narrow particle size distribution. The crystals are perfectly dispersible in ethanol even after drying, giving stable transparent colloidal dispersions. The structure of the nanocrystals corresponds to phase-pure stoichiometric nickel(II) oxide with a partially oxidized surface exhibiting Ni(III) states. The 3.3 nm nanoparticles demonstrate remarkably high turnover frequencies of 0.29 s^{-1} at an overpotential of $\eta = 300 \text{ mV}$ for electrochemical water oxidation, even outperforming rare and expensive iridium oxide catalysts. The unique features of these NiO nanocrystals provide great potential for the preparation of novel composite materials with applications in the field of (photo)electrochemical water splitting. The dispersed colloidal solutions may also find other applications, such as the preparation of uniform hole-conducting layers for organic solar cells.

3.2 INTRODUCTION

Nickel(II) oxide (NiO) is an abundant and technologically important semiconducting oxide. The main applications of nickel oxide, such as catalysis,^{1,2} batteries,^{3,4} supercapacitors,^{5,6} electrochromics,⁷ sensors⁸ and many others can often benefit from nanostructuring and from reducing the crystal size down to the nanometer scale. Due to a greatly increased interface and drastically reduced dimensions relative to the bulk, the reported nickel oxide nanomorphologies such as nanoflowers,^{9,10} porous spheres,¹¹ nanowires¹² or nanotubes¹³ generally demonstrate superior performance in applications involving charge transfer and charge transport processes.¹⁴ Crystalline non-agglomerated dispersible nanoparticles of NiO are attractive because colloidal nanocrystal dispersions can be used for the controlled deposition of crystalline nickel oxide at room temperature, or for the fabrication of hole transporting layers in polymer solar cells.¹⁵ Furthermore, a reduction in the crystal size to only a few nanometers is expected to modify the electronic, optical and magnetic characteristics of the nanocrystals as well as their surface properties.

Although colloidal non-agglomerated nanocrystals can be obtained for several other metal oxides,¹⁶ nickel oxide in this form has not been available so far. NiO can be easily prepared by a range of chemical and physical methods.¹⁷⁻²⁰ However, practically all the existing approaches require a thermal treatment at elevated temperatures to obtain a crystalline material, and this generally results in an irreversible agglomeration of the nanoparticles. Sol-gel,^{21,22} hydrothermal,²³ and solvothermal²⁴ routes provide better control over the size, shape and agglomeration of nanoparticles, enabling fabrication of smaller nanoparticles down to 4 – 5 nm in size. Nevertheless, the reported NiO nanoparticles exhibit a broad particle size distribution, formation of intergrown or agglomerated crystals and a lack of dispersibility.

Here we report for the first time the preparation of ultrasmall, crystalline and dispersible NiO nanoparticles, using a solvothermal reaction in *tert*-butanol. The size of the nanocrystals can be tuned from 2.5 to 5 nm and electrochemical studies show that they are remarkably efficient electrocatalysts for electrochemical oxygen generation.

3.3 RESULTS AND DISCUSSION

In order to overcome the previous limitations and to obtain dispersible ultrasmall colloidal NiO nanocrystals, we have developed a solvothermal approach in *tert*-butanol that involves the direct formation of crystalline nanoparticles *via* a chemical reaction of the precursor with the solvent. We have previously demonstrated the suitability of this reaction pathway for the fabrication of ultrasmall dispersible nanocrystals for several titanate systems,²⁵⁻²⁷ but the *tert* butanol approach had not been explored yet for other metal oxide systems. The choice of appropriate NiO precursors is decisive for the formation of nanoparticles. Nickel(II) acetylacetonate (Ni(acac)₂) is the most suitable precursor for dispersible crystalline NiO nanoparticles in this reaction. Formation of NiO from Ni(acac)₂ in *tert*-butanol requires a reaction temperature of 200 °C and a reaction time of 12 h; no product formation was observed at lower temperatures and shorter times. (Figure S3.1 in the supporting information). For reaction times longer than 16 h NiO reflections are exclusively observed in the X-ray diffraction (XRD) patterns (Figure 3.3a).

The size of the phase-pure NiO nanocrystals calculated from the line broadening in the XRD corresponds to 2.5 nm after 16 h reaction time at 200 °C. For further discussion in the text the sample labeling NP-X will be used where X is the average particle size in nm determined from XRD. The particle size increases almost linearly from 3.3 ± 0.1 nm (NP-3.3) to 4.8 ± 0.1 nm (NP-4.8) with reaction times between 17 h and 33 h, respectively (Figure 3.3a and b). Dried NiO nanoparticles are perfectly dispersible in ethanol after the addition of very small amounts of acetic acid. Dynamic light scattering (DLS) measurements of these transparent colloidal dispersions reveal narrow size distributions centered at 2.5 nm (NP-2.5), 3.3 nm (NP-3.3) and 4.7 nm (NP-4.8), respectively (Figure 3.3c). The particle size in DLS agrees well with the particle size calculated from the XRD patterns and determined from TEM images (see below). The dispersions proved to be stable, as DLS measurements showed the same particle size distribution after several weeks.

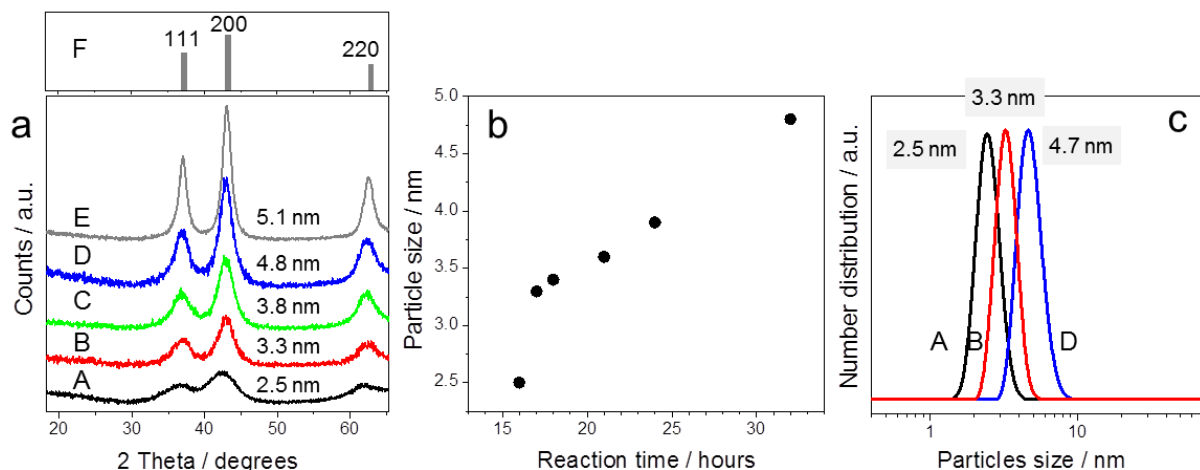


Figure 3.3 Characterization of NiO nanoparticles prepared from the reaction of Ni(acac)₂ in *tert*-BuOH at 200 °C after different reaction times: 16 h (A; sample code for further discussion in the text: NP-2.5), 17 h (B; NP-3.3), 24 h (C; NP-3.8) and 33 h (D, NP-4.8): (a) Powder XRD patterns of the dried NiO nanoparticles (E corresponds to the ICDD card number 01-071-1179, referring to NiO with rock salt structure), (b) crystalline domain size after different reaction times calculated from the XRD patterns for the most intensive NiO signal at $2\theta = 43^\circ$ using the Scherrer equation, (c) dynamic light scattering (DLS) analysis of ethanolic dispersions of NiO nanoparticles (sample codes see above).

Transmission electron microscopy (TEM) images of the NiO nanoparticles NP-3.3 show non-agglomerated, defined particles with a narrow particle size distribution (Figures 3.4a, b). The lattice fringe distances (Figure 3.4b) in high resolution TEM images and the electron diffraction patterns (Figure 3.4c) are in agreement with the cubic rock salt structure of NiO deduced from XRD patterns. The average particle size obtained from the TEM images, measured and calculated over 30 particles, is 3.3 nm which is also in good agreement with the size calculated from the XRD pattern (3.3 nm, NP-3.3). When more concentrated dispersions of NiO nanoparticles were used for TEM sample preparation, we observed the formation of hexagonal supercrystals assembled from nanoparticles (Figure S3.2 in the supporting information). The presence of such supercrystalline assemblies is indicative for the monodisperse shape and size of the nanoparticles.²⁸

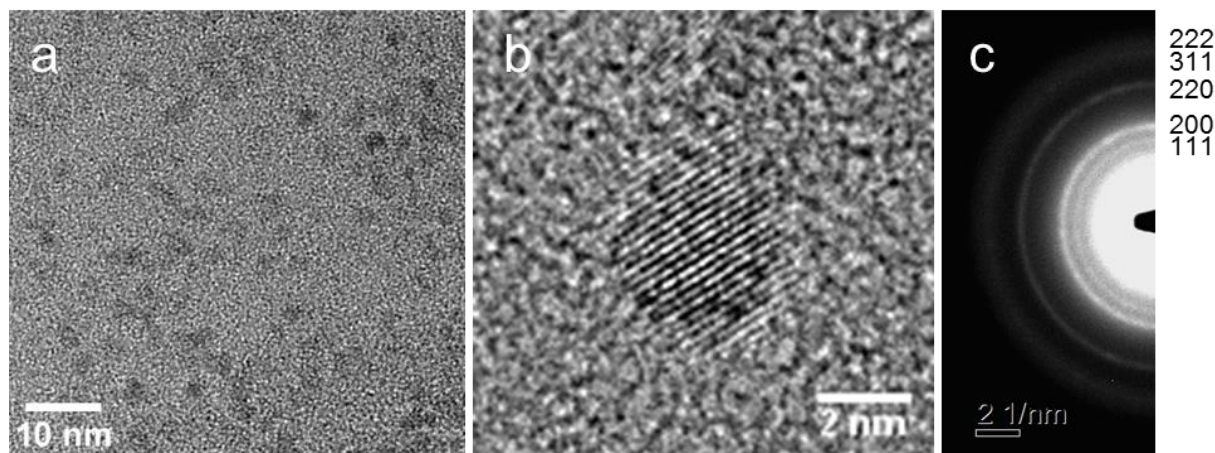


Figure 3.4 TEM images of the NiO nanoparticles NP-3.3. (a) Overview of the nanoparticles dispersed on the TEM grid. (b) HRTEM image of a single NiO nanoparticle. (c) Electron diffraction pattern of the NiO nanoparticles. The corresponding d-values are 2.4 (111), 2.08 (200), 1.47 (220) 1.26 (311) and 1.2 Å (222), respectively.

Raman spectra of the as-prepared dry NiO powders (NP-3.3) show the presence of aliphatic organic groups corresponding to *tert*-BuOH solvent residues, which practically vanish after heating the samples to 100 °C. The Raman spectra of NiO powders heated to 100–240 °C show only one broad phonon vibration peak at 500 – 600 cm^{-1} typical for NiO²⁹ and similar to the spectrum of commercial NiO nanopowder (Figure S3.3 in the supporting information). Heating up to 300 °C does not influence the size of the NiO nanoparticles; they only start to grow at temperatures above 350 °C (Figure S3.3b in the supporting information).

Figure 3.5 shows the UV-visible spectra of nickel oxide nanocrystals of various sizes dispersed in ethanol with the same concentration for each sample. The distinct absorption peak around 375 nm in the UV region, as well as the weaker absorption features around 425 and 480 nm are attributed to d-d transitions of Ni(III).³⁰ It can be seen that smaller particles with a higher ratio of surface atoms show a stronger absorption in this region, which results in a stronger brown coloration of the dispersions (see inset in Figure 3.5a). This suggests that the absorption arises from Ni(III) states at the surface of the nanoparticles that are probably present in the form of NiOOH or Ni(III) oxide moieties.³¹ The steep absorption in the UV region below 350 nm is attributed to the band gap absorption in NiO.³² The so-called Tauc plot in Figure S3.4b (supporting information) shows a linear relation in the energy range around 3.8 to 4.1 eV for $n = 2$ (see UV-Vis characterization in the experimental section), indicating a direct transition as often reported for the semiconducting NiO nanoparticles.^{33,34}

This is supported by the observation that the absorption coefficients of the NiO nanoparticle dispersions in this region are in the range of $10^4 - 10^5 \text{ cm}^{-1}$, also indicating a direct transition (Figure S3.4a in the supporting information). Extrapolation of the linear portion of the high energy part of the plots yields band gap values of 3.73, 3.78 and 3.79 eV for NP-3.3, NP-3.8 and NP-4.8, respectively (Figure S3.4b in the supporting information).

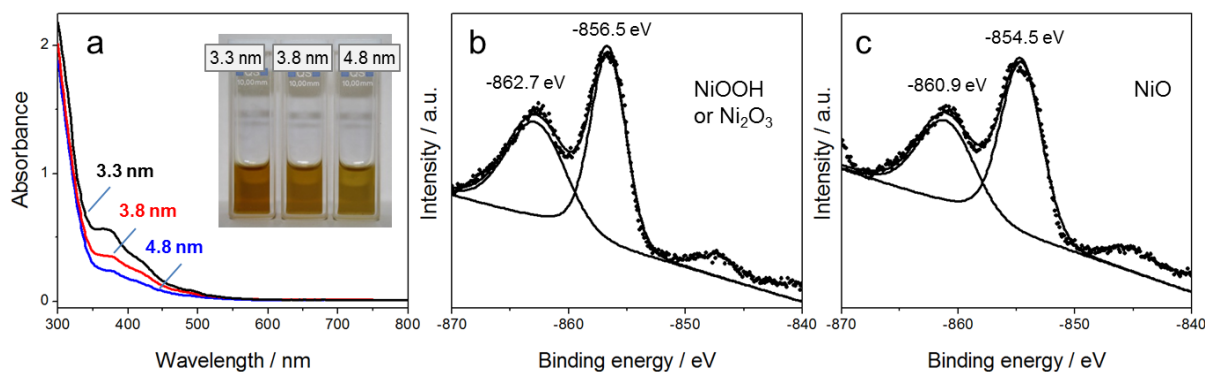


Figure 3.5 (a) UV-Vis absorption spectra of dispersions of NiO nanoparticles in ethanol with sizes of 3.3 nm (black, NP-3.3), 3.8 nm (red, NP-3.8) and 4.8 nm (blue, NP-4.8), and the photographs of the corresponding dispersions in an inset (5 mM concentration). X-ray photoelectron spectra (XPS) of as prepared (b) and argon polished (c) NiO nanoparticles (NP-3.3). The XPS spectra show the energy region between 840 and 870 eV corresponding to the Ni $2p_{3/2}$ and its shake up-signal. The points correspond to the experimental spectra, and the lines are the fitted curves using a Doniach Sunjic functional.

The attribution of the long wavelength absorption to nickel(III) states on the surface of the NiO particles is supported by magnetic measurements and by XPS analysis. The magnetic susceptibility measurements (Figure S3.5 in the supporting information) indicate an effective moment of $\mu_{eff} = 3.01 \mu_B$ in the temperature region between 150 K and 250 K which is in line with the Ni(II) states with respect to a g -factor of $g = 2.14$. Additionally, a fit above 300 K agrees well with the presence of Ni(III) states with $\mu_{eff} = 3.89 \mu_B$ and a paramagnetic Curie temperature of $\theta_p = -230$ K. XPS measurements on the as prepared particles (Figure 3.5b) reveal a binding energy of -856.5 and -862.7 eV for the Ni $2p_{3/2}$ and its shake up-signal, respectively. According to literature this can be interpreted as a nickel(III) state,³⁵⁻³⁷ which could be in the form of Ni_2O_3 , NiOOH or *tert*-butoxide groups attached to the surface of NiO. Quantification of the elements in XPS shows a ratio of Ni to O atoms of nearly 1:2, which could indicate that the Ni(III) states are present in the form of NiOOH on the surface of the nanoparticles (Table S3.1 in the supporting information). However, this is only tentative since

the surface may be contaminated. On the other hand, XPS measurements made after sputtering the surface with argon ions (Figure 3.5c) show a different binding energy for the Ni $2p_{3/2}$ and its shake up-signal (-854.5 and -860.9 eV), which is typical for NiO.³⁸ Quantification gives an atomic ratio of 1:1 confirming NiO. This is also in good agreement with the non-surface selective XRD measurements which only show a signal for NiO. In conclusion, the combination of the results of XRD, XPS, UV-Vis absorption and magnetic susceptibility measurements indicates that the as-synthesized nanoparticles have a core of NiO and some form of nickel(III) states on their surface.

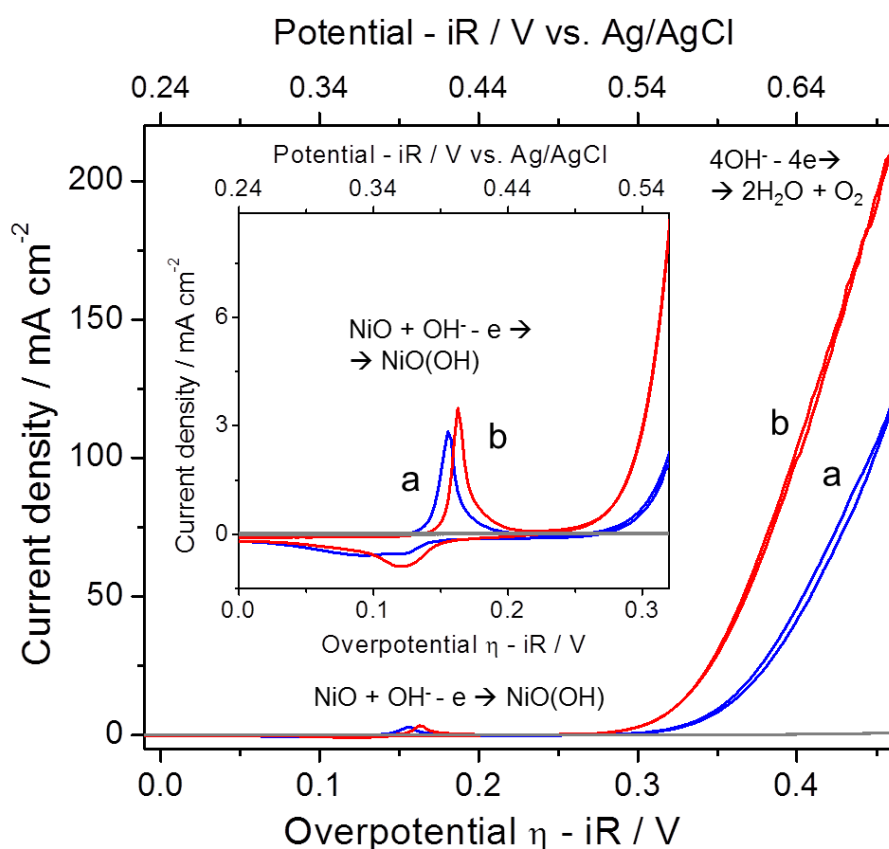


Figure 3.6 Cyclic voltammograms of NiO nanoparticles (NP-3.3) on Au-coated QCM electrodes in 0.5 M KOH. (a) Preconditioned by cycling 30 times from 0.1 to 0.7 V vs. sat. Ag/AgCl electrode with a scan rate $\nu = 20 \text{ mV s}^{-1}$ and (b) electrochemically aged by applying a constant current of 7.5 mA cm^{-2} for 2.5 h. The gray line corresponds to a voltammogram taken on the bare Au electrode aged at the same conditions as (b). The voltammograms were taken at a scan rate of 20 mV s^{-1} .

The presence of Ni(III) states on the surface of the nanoparticles under ambient conditions suggests that the surface Ni atoms are highly reactive (Ni(III) states are commonly associated with the electrocatalytic activity of nickel compounds).^{27,28} Therefore, we have tested our NiO nanoparticles as catalysts for the electrochemical oxidation of water. For that purpose, NiO nanoparticles NP-3.3 were deposited as thin films on Au-coated QCM crystals. The use of QCM crystals enables an accurate determination of the NiO mass loading, which was $20 \pm 0.8 \mu\text{g cm}^{-2}$ for the thinnest films.

Cyclic voltammograms (CVs) taken in 0.5 M KOH show the typical behavior for NiO in basic media. The CVs feature a pair of anodic and cathodic peaks centered around 0.370 V vs. Ag/AgCl corresponding to the oxidation of NiO



followed by a current due to O₂ evolution (Figure 3.6). It should be noted that only a very low current was measured on the bare Au electrode under the same conditions (see grey line in Figure 3.6). The current for the NiO modified electrodes increases during the first few cycles and reaches a stable value after 30 scans, after which it remains stable and does not change anymore with prolonged cycling. Electrodes preconditioned in this way show a narrow anodic and a broad cathodic peak in the reversed scan, corresponding to the NiO/NiOOH redox reaction of NiO. The charge obtained from the integration of the cathodic peak corresponds to about 2.7 mC cm^{-2} which corresponds to $10 \pm 2 \%$ of the deposited NiO independent of the mass loading on the electrode. The same fraction of electrochemically active Ni atoms was obtained for electrodes with about 2.5 times (6.0 mC cm^{-2}) and about 4.5 times (9.9 mC cm^{-2}) higher mass loadings. The measured charge closely agrees with the theoretical value corresponding to oxidation/reduction of the particle surface, which can be calculated assuming that only surface Ni atoms are electrochemically active. Using the specific surface area of the NP-3.3 NiO nanoparticles of $210 \text{ m}^2 \text{ g}^{-1}$ determined by Kr sorption (Figure S3.6 in the supporting information), the real surface area (roughness factor) of the electrodes with a mass loading of $20 \mu\text{g cm}^{-2}$ is equal to $42 \text{ cm}^2 \text{ cm}^{-2}$. This leads to a surface charge value of 2.76 mC cm^{-2} using the estimated surface density of Ni atoms of $4.08 \cdot 10^{14} \text{ cm}^{-2}$ for a 110 plane. This good agreement with the electrochemically obtained charge (2.7 mC cm^{-2}) indicates that indeed surface Ni atoms are preferentially electrochemically active and that the surface of the NiO nanoparticles is also electrochemically accessible for the thicker films.

Unlike the previously reported ultrathin NiO films that completely transform to layered Ni(OH)₂ after prolonged electrochemical treatment,³⁹ the NiO electrodes assembled from our nanoparticles obtained by the *tert*-butanol route retain their integrity. The amount of Ni atoms involved in the Ni(II)/Ni(III) reaction remains practically unchanged after prolonged cycling, as determined from the charge obtained by integration of the corresponding peaks. The integrated charge remains almost constant even after extended electrochemical aging of the electrodes, which was performed galvanostatically by applying a current of 7.5 mA cm⁻² for 2.5 h. However, the aging leads to a small shift of the NiO redox potential to more positive values (from 0.370 ± 0.001 V to 0.385 ± 0.002 V vs. Ag/AgCl, respectively). The positive shift in the redox potential is usually assigned to a phase transformation of the OH-terminated Ni atoms in basic media, from a disordered α-modification to a more ordered and more catalytically active β-modification.²⁷ The shift in the peak in our case is accompanied by a decrease in the overpotential of the OER process. The overpotential required for 1 mA cm⁻² OER current density changes from 305 mV for the conditioned electrode to 280 mV for the aged electrode, respectively. Preconditioned and aged electrodes show similar Tafel slopes for the OER process of 40 mV dec⁻¹ at an overpotential of 300 mV, which is consistent with the values reported for NiO.^{40,41} (Figure S3.7 in the supporting information).

The electrodes prepared from our NiO nanoparticles show high turnover frequencies (TOF), defined as the number of O₂ molecules formed per active metal site per second) at relatively low overpotentials. The TOF calculated per active Ni atom (determined from the real surface area of the electrodes) for the aged electrodes described above is 0.29 s⁻¹ at an overpotential of $\eta = 300$ mV. This value is 30 times higher than the TOF value of 0.009 s⁻¹ at the same overpotential reported for IrO_x thin film electrodes that are known as some of the most active OER catalysts. The TOF value for our ultrasmall NiO particles is also significantly higher than that of 0.21 s⁻¹ for Fe-doped ultrathin NiO layers which was the highest reported value so far.⁴¹ This makes our NiO nanoparticles very promising catalysts for electrochemical water splitting.

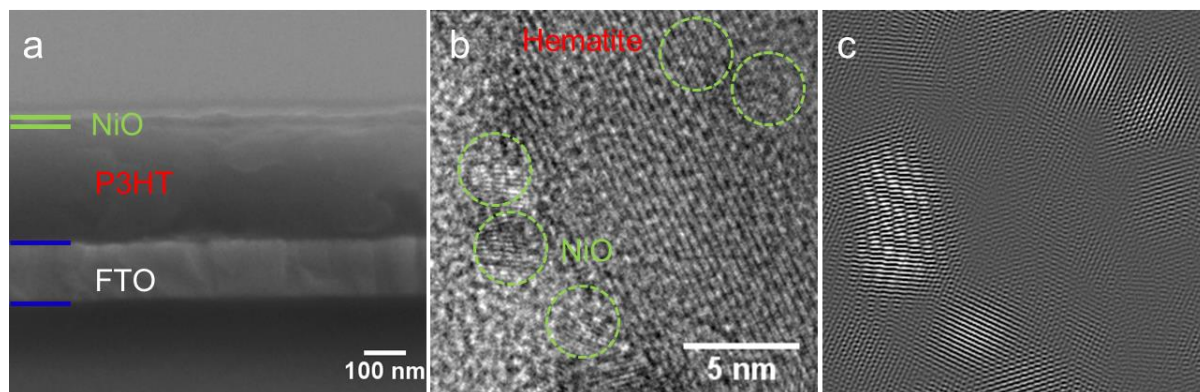


Figure 3.7 Deposition of NiO nanoparticles from ethanolic dispersions on different substrates. (a) As thin compact films on the top of a P3HT polymer layer (SEM image, cross-section) and (b) as single non-agglomerated nanoparticles on crystalline mesoporous Fe_2O_3 hematite. Top view HRTEM image and (c) its inverse FFT image, after masking the hematite lattice plane contribution.

The dispersibility of the crystalline NiO nanoparticles allows for a controlled deposition of crystalline NiO layers on various flat and porous substrates. Crystalline layers with tunable thickness can therefore be easily processed from the colloidal dispersions, and importantly the films do not require further temperature treatment for crystallization. This enables deposition of NiO layers on temperature-sensitive polymers or other organic materials.¹⁵ We demonstrate the possibility of the deposition of a compact 7 nm thick NiO layer on top of a P3HT polymer layer (Figure 3.7a), which would be particularly interesting for the fabrication of organic or hybrid solar cells.¹⁵ Furthermore, the high dispersibility and the very small size of the nickel oxide nanoparticles allow us to distribute them homogeneously not only on flat substrates but also on high surface area porous host materials for possible catalytic applications. This is demonstrated in Figure 3.7b, c showing the homogeneous distribution of the individual non-agglomerated NiO nanoparticles on a mesoporous hematite host, which is an interesting material for photoelectrochemical water splitting.

3.4 CONCLUSION

We describe for the first time the preparation of ultrasmall, crystalline and dispersible NiO nanoparticles, which are promising candidates as catalysts for electrochemical oxygen generation. Using a solvothermal reaction in *tert*-butanol, very small nickel oxide nanocrystals can be prepared with sizes tunable from 2.5 to 5 nm and a narrow particle size distribution. The crystals are perfectly dispersible in ethanol even after drying, giving stable transparent colloidal dispersions. The nanoparticles dried at room temperature contain about 50 % of organics, which can be completely removed at about 100 °C leaving an organics-free surface. Besides the decreasing particle dimensions and the increasing surface area, the nanoscaling in our synthesis leads to a changed stoichiometry of the surface compared to the bulk. Our data demonstrate that although the crystalline structure of the obtained nanocrystals corresponds to a phase-pure stoichiometric nickel(II) oxide, the decrease in the particle size evidently leads to the change in surface properties and an increased amount of electrocatalytically active sites.. The nanoparticles of 3.3 nm in size demonstrate very high turn-over frequencies of 0.293 s^{-1} at an overpotential of $\eta = 300 \text{ mV}$ for electrochemical oxygen generation, even outperforming expensive iridium oxide catalysts. Additionally, their unique features such as the high crystallinity and dispersibility allow for the deposition of crystalline NiO layers on temperature sensitive substrates such as polymers, without the necessity of a subsequent heat treatment for crystallization. This would enable the preparation of hybrid organic/inorganic devices such as polymer solar cells. We believe that the unique features of these NiO nanocrystals provide great potential for the preparation of numerous composite materials with applications in fields such as (photo)electrochemical water splitting.

3.5 EXPERIMENTAL SECTION

3.5.1 SYNTHESIS OF NIO NANOPARTICLES

Nickel(II) acetylacetonate was purchased from Alfa Aesar (95 % purity). Nickel(II) acetate tetrahydrate was purchased from Aldrich (98 % purity), *tert*-butanol was purchased from Sigma-Aldrich (puriss. p.a., ACS reagent, ≥ 99.7 %). All chemicals were used as received. *tert*-Butanol was dried over a 4 Å molecular sieve at 28 °C and filtered prior to use.

For the synthesis of nickel oxide nanoparticles with different sizes, 0.13 g (0.50 mmol) of nickel(II) acetylacetonate ($\text{Ni}(\text{acac})_2$) was added to 14 mL of *tert*-butanol (0.147 mol) at ambient conditions forming a turbid light green suspension. The reaction mixture was stirred for 10 min, then transferred into a Teflon autoclave liner and subsequently hermetically sealed. The autoclaves were kept at 200 °C in a laboratory oven for different reaction times. The as-prepared powders were dried in air at 60 °C in a laboratory oven. The reproducibility of the reaction is very sensitive to the mass transfer conditions in the autoclave reactors, which are strongly influenced by the geometry of the autoclave and the stirring conditions. The most reproducible results were achieved for 20 mL cylindrical autoclaves (5.3 cm \times 8 cm) that were rotated in the oven with a rate of ca. 250 rpm. For these conditions, about 2.5 nm (NP-2.5), 3.3 nm (NP-3.3), 3.8 nm (NP-3.8) and 4.8 nm (NP-4.8) phase-pure NiO nanoparticles were obtained after 16 h, 17 h, 24 h and 33 h reaction time, respectively. For bigger autoclaves, the reaction temperature has to be increased to 210 °C and the reaction time prolonged to at least 20 h to observe the formation of the nanoparticles.

Dispersions of the NiO nanoparticles were prepared in ethanol by the addition of concentrated acetic acid. In a typical procedure, 2.4 mg of the dried NiO powder was covered with 4 μL of acetic acid and afterwards dispersed in 1 mL of ethanol to obtain a colloidal dispersion with a NiO concentration of 0.03 mol L⁻¹.

The NiO nanoparticle dispersions (0.03 mol L⁻¹) were used for the fabrication of thin films by spin coating on fluorine-doped tin oxide coated glass (FTO) and on polymer layers of poly(3-hexylthiophene-2,5-diyl) (P3HT) deposited on FTO. 40 μL of the dispersion was cast onto the substrate with a size of 1.5 \times 1.5 cm and spun at 2000 rpm for 30 s. With this method thin films with a thickness of approximately 7 nm are obtained.

For the deposition of the NiO nanoparticles on mesoporous hematite layers, 5 μL of the NiO dispersions were drop cast onto the hematite substrate with dimensions of 1 cm^2 and dried at room temperature.

3.5.2 CHARACTERIZATION

Wide angle X-ray diffraction analysis was carried out in reflection mode using a Bruker D8 Discover diffractometer with Ni-filtered Cu K_α radiation ($\lambda = 1.5406 \text{ \AA}$) equipped with a LynxEye position sensitive detector. Powder XRD patterns of the samples were collected in a 2θ range from 5° to 67° with a step size of 0.05 and fixed counting time of 0.1 second per step. The size of the crystalline domains was calculated from the XRD patterns for the most intensive NiO signal at $2\theta = 43^\circ$ using the Scherrer equation.

Dynamic light scattering measurements were performed on a MALVERN Zetasizer-Nano instrument equipped with a 4 mW He-Ne laser (633 nm) and an avalanche photodiode detector.

TEM measurements were carried out using a FEI Titan 80-300 equipped with a field emission gun operated at 300 kV. For the sample preparation a drop of a strongly diluted dispersion of a sample in ethanol was placed on a holey carbon coated copper grid and evaporated.

SEM images were obtained with a JEOL JSM-6500F scanning electron microscope equipped with a field emission gun operated at 4 kV. The films were prepared on silicon substrates and glued onto a brass sample holder with silver lacquer.

Raman spectroscopy was carried out using a LabRAM HR UV-Vis (HORIBA JOBIN YVON) Raman Microscope (OLYMPUS BX41) with a SYMPHONY CCD detection system and a He-Ne laser ($\lambda = 633 \text{ nm}$). Spectra were recorded using a lens with a 100-fold magnification.

Thermogravimetric analysis of the samples was performed on a NETZSCH STA 440 C TG/DSC (heating rate of 10 K min^{-1} in a stream of synthetic air of about 25 mL min^{-1}).

X-ray photoelectron spectroscopy (XPS) analysis of the particles on a silicon substrate was performed using a VSW HA 100 electron analyzer and the K_α radiation provided by a non-

monochromatized magnesium anode system (Mg K_{α} = 1253.6 eV). Ar ion polishing was done at 1000 eV for 10 minutes. The recorded elemental peaks were fitted using a Doniach-Sunjic function⁴² and the elemental ratios were calculated by the equation

$$\frac{X_A}{X_B} = \frac{I_A/S_A}{I_B/S_B} \quad (3.2)$$

where $\frac{I_A}{I_B}$ is the ratio of fitted areas, and S is the sensitivity factor.

The UV-visible spectra of the samples were measured with a Perkin Elmer Lambda 1050 spectrophotometer equipped with an integrating sphere.

The band gap E_g of NiO was determined from the measured spectra using the relationship

$$h\nu - E_g \propto (\alpha h\nu)^n \quad (3.3)$$

Where $h\nu$ is the photon energy, α is the absorption coefficient, and the exponential factor n being either 2 for a direct allowed transition or $\frac{1}{2}$ for an indirect allowed transition. The absorption coefficient α was calculated from the absorbance using equations (3.4) – (3.9).

$$A = -\log_{10} \frac{I_t}{I_0} = \varepsilon c_{\text{solid}} l \quad (3.4)$$

where A is the absorbance, I_0 is the incident light, I_t is the transmitted light, ε is the molar absorption coefficient, c_{solid} is the concentration of nickel oxide in the dispersion (5 mM), and l is the optical path length (1 cm).

$$-\ln \frac{I_t}{I_0} = \alpha l = -2.303 \log_{10} \frac{I_t}{I_0} = \varepsilon c_{\text{solid}} l \quad (3.5)$$

$$\Rightarrow \alpha = 2.303 \varepsilon c_{\text{solid}} \quad (3.6)$$

The concentration c_{solid} of the solid NiO was calculated from the molar volume V_M that is given by the molar mass M_{NiO} (74.69 g mol⁻¹) and the density of NiO ρ_{NiO} (6.67 g cm⁻³):

$$c_{\text{solid}} = \frac{1}{V_M} = \frac{\rho}{M} = 89.3 \frac{\text{Mol}}{\text{dm}^3} = 89.3 M \quad (3.7)$$

ε was calculated from the concentration of nickel oxide in the dispersion $c_{\text{dispersion}}$ (5 mM):

$$\varepsilon = \frac{A}{c_{\text{dispersion}} l} = \frac{A}{5 \cdot 10^{-3}} \quad (3.8)$$

$$\Rightarrow \alpha(\lambda) = 2.303 \frac{A(\lambda)}{5 \cdot 10^{-3}} \cdot 89.3 \text{ cm}^{-1} \quad (3.9)$$

A Magnetic Property Measurement System (MPMS) from Quantum Design was used to determine the temperature dependent dc-susceptibility $\chi(T)$ and the magnetic field dependent magnetization $m(H)$. These measurements were performed in a temperature range between 2 and 400 K and in magnetic fields up to 10 kOe. A small amount of NiO powder (9.41 mg) was mounted between two KEL-F staves fitted in a straw. The susceptibility data are normalized to one mol of the respective formula unit (f.u.).

3.5.3 ELECTRODE PREPARATION

The electrodes were prepared by deposition of the dispersed nickel oxide nanoparticles either by spin coating or by drop casting on QCM crystals (KVG 10 MHz QCM devices with gold electrodes from Quartz Crystal Technology GmbH). In a typical drop casting procedure, 4 μL of nickel oxide dispersion was cast on the Au layer of a QCM crystal. A mask was used to cover the non-active surface of the QCM chip exposing an area of 0.196 cm^2 . The loaded QCM crystal was dried in air at ambient conditions for 5 min. For the spin coating method 8 μL of nickel oxide dispersion was deposited on a masked QCM crystal and spun at 1000 rpm for 10 s. The QCM electrodes prepared with both methods were subsequently heated to 240 $^{\circ}\text{C}$ in a laboratory oven with a heating ramp of 4 $^{\circ}\text{C min}^{-1}$ and a dwell time of 2 h.

3.5.4 ELECTROCHEMICAL MEASUREMENTS

Electrochemical measurements were performed in a three-electrode setup using an Autolab potentiostat/galvanostat PGSTAT302N with FRA32M module operating with Nova 1.9 software. All the measurements were performed in 0.5 M KOH electrolyte solution (Sigma-Aldrich, volumetric solution) at pH 13.43. Pt mesh (2 cm^2) was used as a counter electrode. Au/QCM crystals with NiO nanoparticles deposited on one side (preparation is described

above) were used as working electrodes. To provide an electric connection to the QCM electrode, a silver wire was connected to the respective part of the QCM crystals using silver lacquer. The silver lacquer and the wire were sealed afterwards in inert two-component epoxy resin (Gatan, Inc). All potentials were measured vs. Ag/AgCl/KCl sat. reference electrode, whose potential is +0.989 V vs. the reversible hydrogen electrode (RHE) at pH 13.43 (+0.197 V vs. NHE). The electrochemical data were corrected for uncompensated resistance R_s . The R_s was determined as minimum total impedance in the frequency regime between 10 and 50 kHz at open circuit conditions and at a potential of 0.2 V vs. Ag/AgCl electrode, where no Faradaic processes take place. The resistance was taken as an average of 3 measurements, 90 % of this value was compensated. R_s was typically around 6 – 7 Ohm for the NiO-coated Au/QCM electrodes. The overpotential η was calculated using the equation

$$\eta = E - E_{\text{OER}} - iR_s \quad (3.10)$$

Where E is the potential recorded vs. Ag/AgCl reference electrode, E_{OER} is the reversible potential of the OER vs. Ag/AgCl reference electrode (0.240 V at pH 13.43), and i is the current. Current densities are calculated using the geometric surface area of the Au/QCM electrode (0.196 cm²).

The pre-conditioning of the NiO electrodes was achieved using cyclic voltammetry (CVA). The electrodes were cycled between 0 V and 0.7 V vs. Ag/AgCl in 0.5 M KOH at a scan rate of 20 mV s⁻¹ until the current had reached stable values and did not change anymore with repetitive cycling (typically 30 cycles). The CVA measurements on these pre-conditioned electrodes were made at scan rates from 2 mV s⁻¹ to 20 mV s⁻¹ without stirring the electrolyte. The aging was performed galvanostatically by applying a current density of 7.5 mA cm⁻² for 2.5 h in a two-electrode mode in a stirred 0.5 M KOH solution. The electrolyte was replaced after the aging procedure by a fresh one for subsequent CVA measurements.

The turn-over frequency (TOF) at the overpotential of $\eta = 0.3$ V was calculated on the basis of surface Ni atoms according to:

$$\text{TOF} = \frac{i}{4 F n_{\text{surf}}} \quad (3.11)$$

Where i is the current, F is Faraday's constant, and n_{surf} is the surface concentration of Ni atoms (mol cm⁻²). The surface concentration of Ni atoms was calculated from the mass

3.6 REFERENCES

loading of the films m (g cm^{-2}), the BET surface area of the nanoparticles of $2.1 \cdot 10^6 \text{ cm}^2 \text{ g}^{-1}$ determined by Kr sorption and estimated surface density N_{NiO} of Ni atoms in NiO of $4.08 \cdot 10^{14} \text{ cm}^{-2}$ according to:

$$n_{\text{surf}} = m \text{ BET} \frac{N_{\text{NiO}}}{N_A} \quad (3.12)$$

Where N_A is the Avogadro constant.

Alternatively, the number of electrochemically accessible Ni atoms was determined from the charge corresponding to the NiO redox reaction according to the equation (3.1). As the charge obtained from the anodic peak of the NiO redox process may contain some contribution from the OER process we have used the cathodic peak to determine the amount of the catalytically active Ni atoms.

3.6 REFERENCES

1. Kuhlbeck, H.; Shaikhutdinov, S.; Freund, H.-J. *Chem. Rev.* **2013**, *113*, 3986.
2. Kim, T. W.; Hwang, S. J.; Jung, S. H.; Chang, J. S.; Park, H.; Choi, W.; Choy, J. H.; *Adv. Mater.* **2008**, *20*.
3. Poizot, P.; Laruelle, S.; Grugeon, S.; Dupont, L.; Tarascon, J. M. *Nature* **2000**, *407*, 496.
4. Liu, H.; Wang, G.; Liu, J.; Qiao, S.; Ahn, H. *J. Mater. Chem.* **2011**, *21*, 3046.
5. Lu, Q.; Lattanzi, M. W.; Chen, Y.; Kou, X.; Li, W.; Fan, X.; Unruh, K. M.; Chen, J. G.; Xiao, J. Q. *Angew. Chem.* **2011**, *123*, 6979.
6. Kim, S. I.; Lee, J. S.; Ahn, H. J.; Song, H. K.; Jang, J. H. *ACS Appl. Mater. Interfaces* **2013**, *5*, 1596.
7. Gillaspie, D. T.; Tenent, R. C.; Dillon, A. C. *J. Mater. Chem.* **2010**, *20*, 9585.
8. Hoa, N. D.; El-Safty, S. A. *Chem. Eur. J.* **2011**, *17*, 12896.

-
9. Zhao, B.; Ke, X.-K.; Bao, J.-H.; Wang, C.-L.; Dong, L.; Chen, Y.-W.; Chen, H.-L. *J. Phys. Chem. C* **2009**, *113*, 14440.
 10. Cao, X.; Xu, Y. J.; Wang, N. *Sens. Actuators B* **2011**, *153*, 434.
 11. Titirici, M.-M.; Antonietti, M.; Thomas, A. *Chem. Mater.* **2006**, *18*, 3808.
 12. Joshi, R. K.; Schneider, J. J. *Chem. Soc. Rev.* **2012**, *41*, 5285.
 13. Pang, H.; Lu, Q.; Li, Y.; Gao, F. *Chem. Commun.* **2009**, 7542.
 14. Yuan, Y.; Xia, X.; Wu, J.; Yang, J.; Chen, Y.; Guo, S. *Electrochem. Commun.* **2010**, *12*, 890.
 15. Manders, J. R.; Tsang, S.-W.; Hartel, M. J.; Lai, T.-H.; Chen, S.; Amb, C. M.; Reynolds, J. R.; So, F. *Adv. Funct. Mater.* **2013**, *23*, 2993.
 16. Niederberger, M.; Pinna, N. *Metal Oxide Nanoparticles in Organic Solvents: Synthesis, Formation, Assembly and Application*; Springer London, **2009**.
 17. H. Zhang, X. Yu, P. V. Braun, *Nature Nanotech.* **2011**, *6*, 277-281.
 18. Mishra, A. K.; Bandyopadhyay, S.; Das, D. *Mater. Res. Bull.* **2012**, *47*, 2288;
 19. Xia, B.; Lenggoro, I. W.; Okuyama, K. *Chem. Mater.* **2002**, *14*, 2623;
 20. Wang, D. S.; Xie, T.; Peng, Q.; Zhang, S. Y.; Chen, J.; Li, Y. D. *Chem. Eur. J.* **2008**, *14*, 2507.
 21. Pilban Jahromi, S.; Huang, N. M.; Muhamad, M. R.; Lim, H. N. *Ceram. Int.* **2013**, *39*, 3909.
 22. Hayat, K.; Gondal, M. A.; Khaled, M. M.; Ahmed, S. *J. Mol. Catal. A: Chem.* **2011**, *336*, 64.
 23. Sue, K.; Kawasaki, S.-i.; Suzuki, M.; Hakuta, Y.; Hayashi, H.; Arai, K.; Takebayashi, Y.; Yoda, S.; Furuya, T. *Chem. Eng. J.* **2011**, *166*, 947.
 24. Beach, E. R.; Shqau, K.; Brown, S. E.; Rozeveld, S. J.; Morris, P. A. *Mater. Chem. Phys.* **2009**, *115*, 371.
-

3.6 REFERENCES

25. Feckl, J. M.; Fominykh, K.; Döblinger, M.; Fattakhova-Rohlfing, D.; Bein, T. *Angew. Chem. Int. Ed.* **2012**, *51*, 7459.
 26. Szeifert, J. M.; Feckl, J. M.; Fattakhova-Rohlfing, D.; Liu, Y.; Kalousek, V.; Rathousky, J.; Bein, T. *J. Am. Chem. Soc.* **2010**, *132*, 12605.
 27. Liu, Y.; Szeifert, J. M.; Feckl, J. M.; Mandlmeier, B.; Rathousky, J.; Hayden, O.; Fattakhova-Rohlfing, D.; Bein, T. *ACS nano* **2010**, *4*, 5373.
 28. Desvaux, C.; Amiens, C.; Fejes, P.; Renaud, P.; Respaud, M.; Lecante, P.; Snoeck, E.; Chaudret, B. *Nat Mater* **2005**, *4*, 750.
 29. Mironova-Ulmane, N.; Kuzmin, A.; Steins, I.; Grabis, J.; Sildos, I.; Pärns, M. *J. Phys.: Conf. Ser.* **2007**, *93*, 012039.
 30. Gorschlüter, A.; Merz, H. *Phys. Rev. B* **1994**, *49*, 17293.
 31. Gonzalez-Elipe, A. R.; Holgado, J. P.; Alvarez, R.; Munuera, G. *J. Phys. Chem.* **1992**, *96*, 3080.
 32. Adler, D.; Feinleib, J. *Phys. Rev. B* **1970**, *2*, 3112.
 33. Li, X.; Zhang, X.; Li, Z.; Qian, Y. *Solid state commun.* **2006**, *137*, 581
 34. Davar, F.; Fereshteh, Z.; Salavati-Niasari, M. *J. Alloys Compd* **2009**, *476*, 797.
 35. Biesinger, M. C.; Payne, B. P.; Lau, L. W. M.; Gerson, A.; Smart, R. S. C. *Surf. Interface Anal.* **2009**, *41*, 324.
 36. Hoffer, B. W.; van Langeveld, A. D.; Janssens, J. P.; Bonne, R. L. C.; Lok, C. M.; Moulijn, J. A. *J. Catal.* **2000**, *192*, 432;
 37. McIntyre, N. S.; Cook, M. G.; *Anal. Chem.* **1975**, *47*, 2208.
 38. Selvam, P.; Viswanathan, B.; Srinivasan, V. *J. Electron. Spectrosc. Relat. Phenom.* **1989**, *49*, 203.
 39. Lyons, M. E.; Brandon, M. P. *Int. J. Electrochem. Sci.* **2008**, *3*, 1386.
 40. Yeo, B. S.; Bell, A. T. *J. Phys. Chem. C* **2012**, *116*, 8394.
-

41. Trotochaud, L.; Ranney, J. K.; Williams, K. N.; Boettcher, S. W. *J. Am. Chem. Soc.* **2012**, *134*, 17253.
42. Doniach, S.; Sunjic, M. *J. Phys. C: Solid State Phys.* **1970**, *3*, 285.

3.7 SUPPORTING INFORMATION

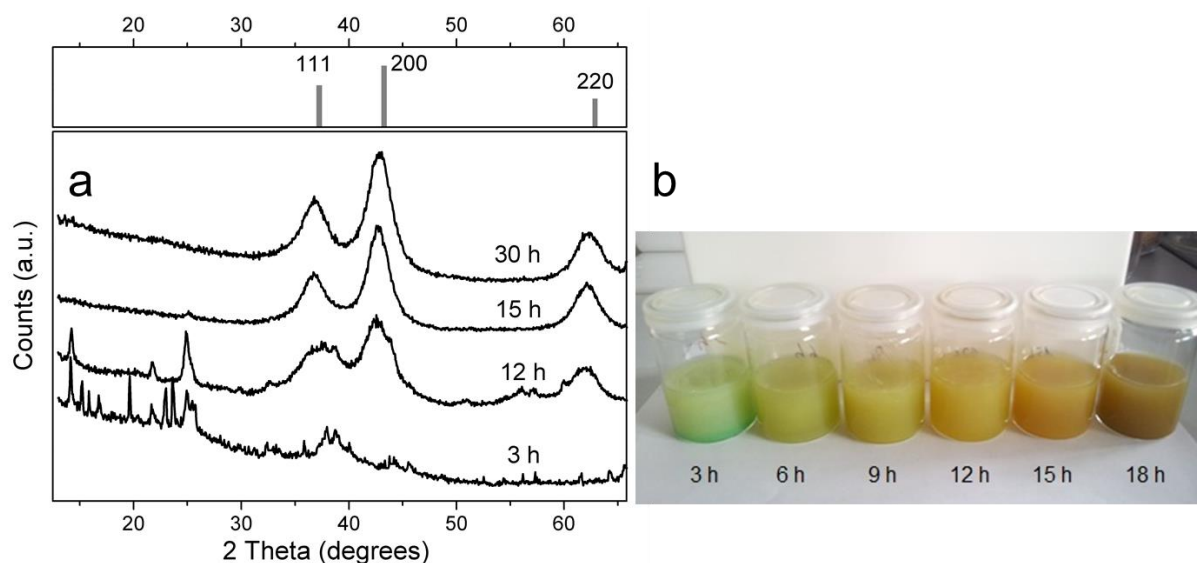


Figure S3.1 XRD patterns (a) and photograph (b) of the reaction products obtained after reaction of $(0.036 \text{ mol L}^{-1})$ $\text{Ni}(\text{acac})_2$ in *tert*-BuOH for different reaction times at $200 \text{ }^\circ\text{C}$. The top pattern in Figure S3.1a corresponds to the ICDD card number 01-071-1179 referring to NiO with rock salt structure.

The formation of nickel oxide at $200 \text{ }^\circ\text{C}$ starts only after 12 h of reaction. Reactions carried out for 12 h to 15 h show broadened NiO reflections with increasing intensity in the course of the reaction. This indicates the formation of small crystalline particles, but still some amounts of non-reacted $\text{Ni}(\text{acac})_2$ precursor remain. For reaction times longer than 16 h NiO reflections are exclusively observed in the XRD patterns. The reaction progress is also clearly noticeable in the appearance of the reaction mixture, which changes its color from light green for the precursor solution to brown after 18 h of reaction.

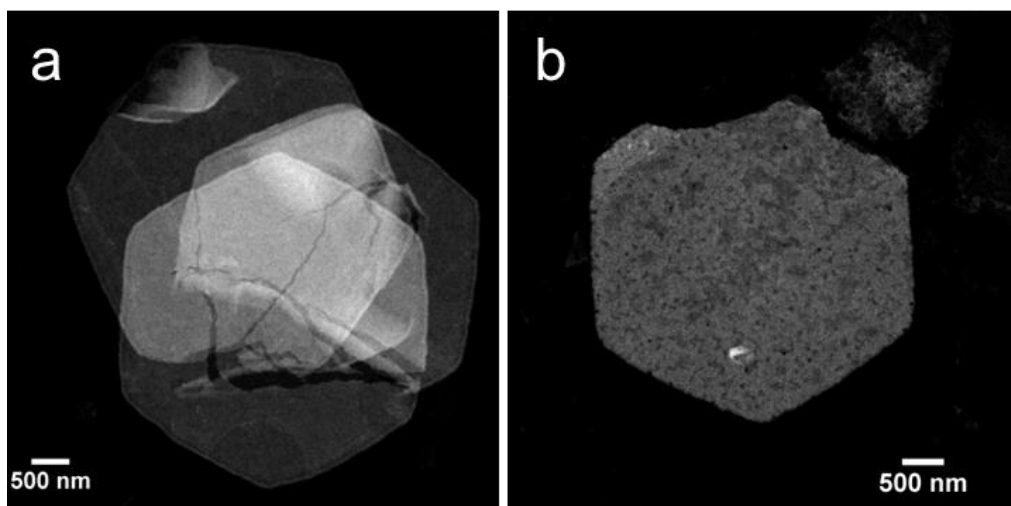


Figure S3.2 STEM image of the hexagonal supercrystals assembled from the NiO nanoparticles obtained from the reaction of Ni(acac)₂ at 200 °C after 17 h (NP-3.3).

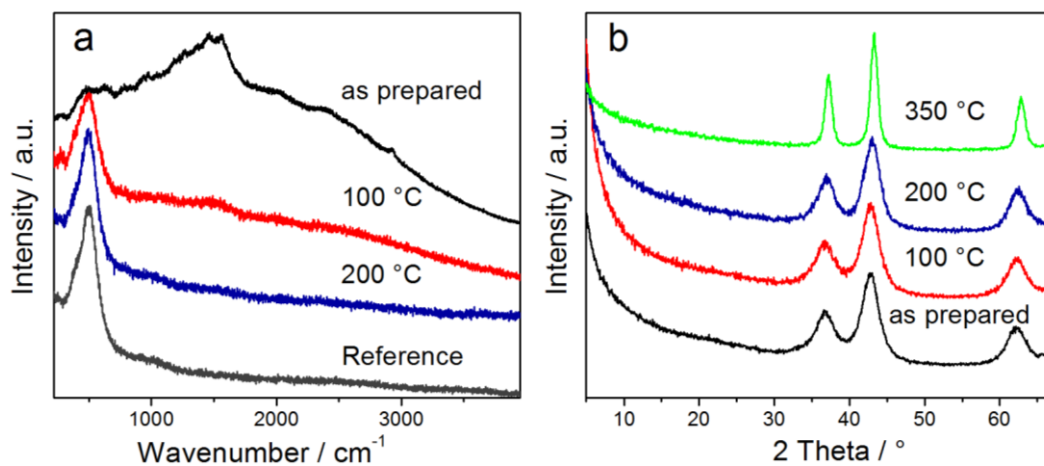


Figure S3.3 (a) Raman spectra of as-prepared NiO nanopowders (NP-3.3) and after heating at 100 °C and 200 °C. The bottom spectrum corresponds to the commercial NiO nanopowders (Sigma-Aldrich, 99.8 % trace metal basis, < 50 nm). (b) XRD powder patterns of the as prepared NiO nanoparticles (NP-3.3) and after heating to 100 °C–350 °C.

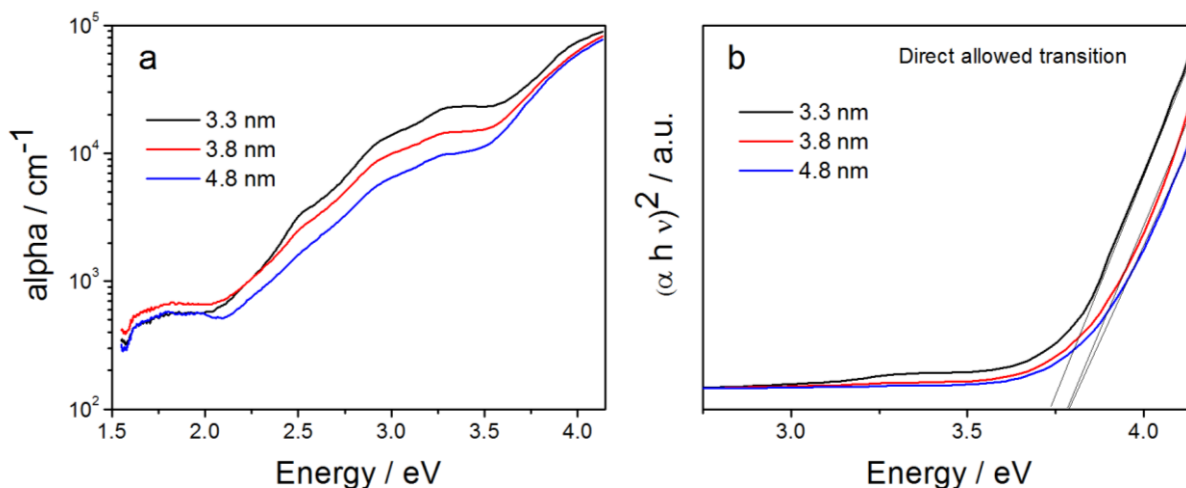


Figure S3.4 (a) Absorption coefficient α of the NiO nanoparticles with various sizes. (b) Tauc plot for the determination of the band gap of NiO.

Table S3.1 Atomic proportions from the quantification of XPS spectra.

Sample	C 1s / %	Ni 2p / %	O 1s / %
NiO untreated	21.3 ^a	24.8	48.8
NiO sputtered	7.5	39.6	48.3

^aThe high carbon content for the untreated nanoparticles is typical for samples prepared *ex situ* and which were exposed to ambient conditions, but could also be an indication for surface bound *tert*-butoxide groups originating from the chemical synthesis of the nanoparticles in *tert*-butanol.

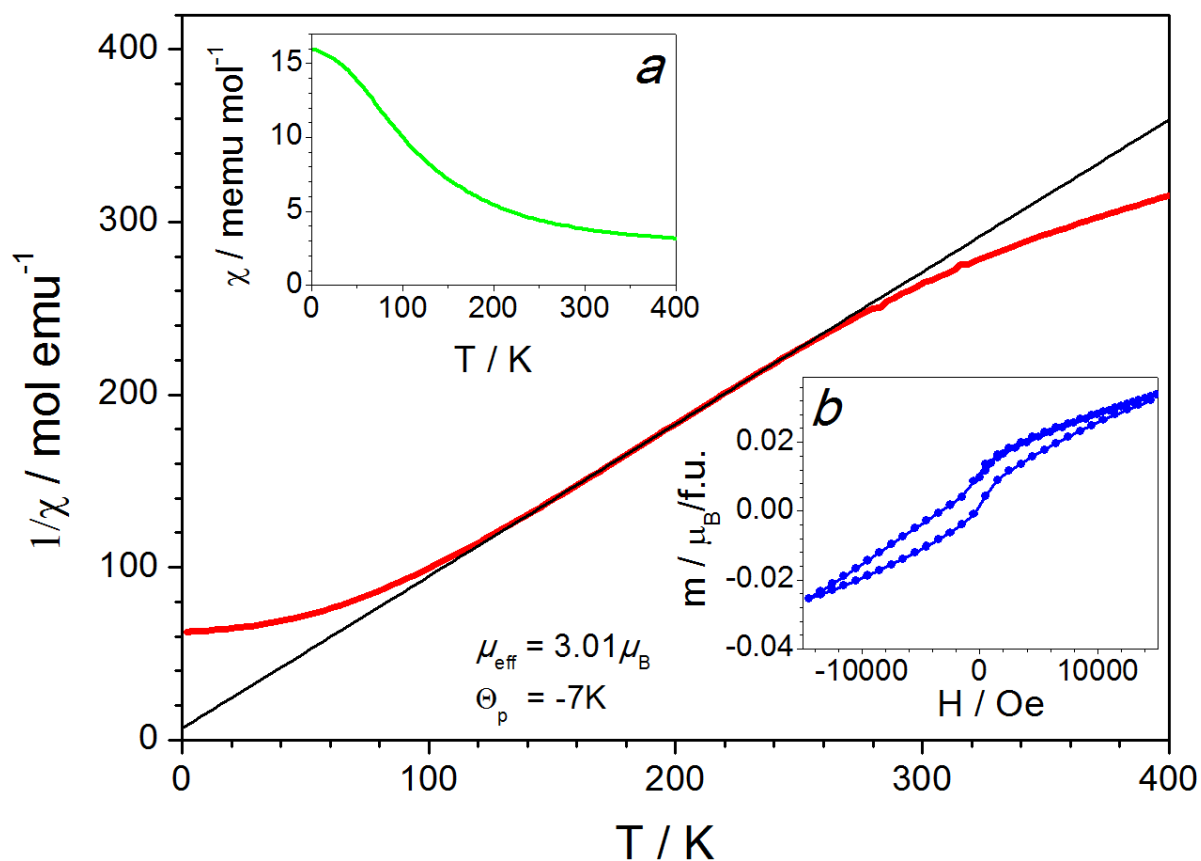


Figure S3.5 The temperature dependence of the inverse magnetic susceptibility $1/\chi$ of NiO (red curve). The solid black line is a linear fit to the data in the temperature range between 150 K and 250 K. From the slope of the fit an effective magnetic moment of $\mu_{\text{eff}} = \mu_B 3.01\mu_B$ is calculated which is in good agreement with a Ni(II) state. The flattening above 300 K may be due to the presence of some Ni(III) atoms. Insert (a) pictures χ vs. T . The linear offset of about 2 emu mol^{-1} may be due to a spontaneous magnetization of some Ni clusters which is support by the hysteresis loop in the insert (b).

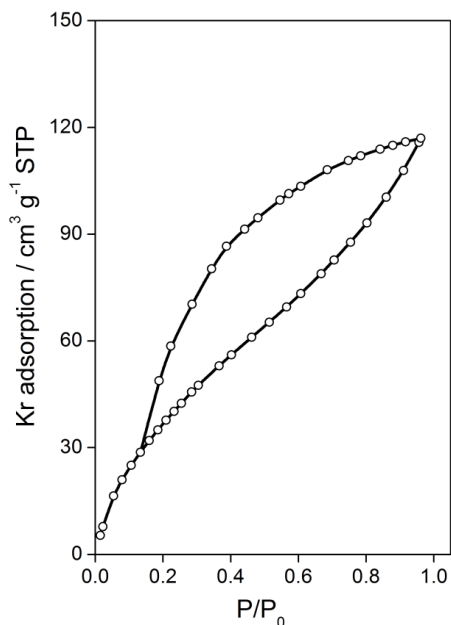


Figure S3.6 Kr sorption isotherm (measured at 77 K) on NiO nanoparticles (NP-3.3) which were tempered at 240 °C. The BET surface area corresponds to 210 m² g⁻¹. The isotherm demonstrates a hysteresis due to the textural porosity between the nanoparticles. The particle size was calculated from the BET surface area and NiO density of 6.67 g cm⁻³ using a spherical model corresponding to around 4 nm particle diameter.

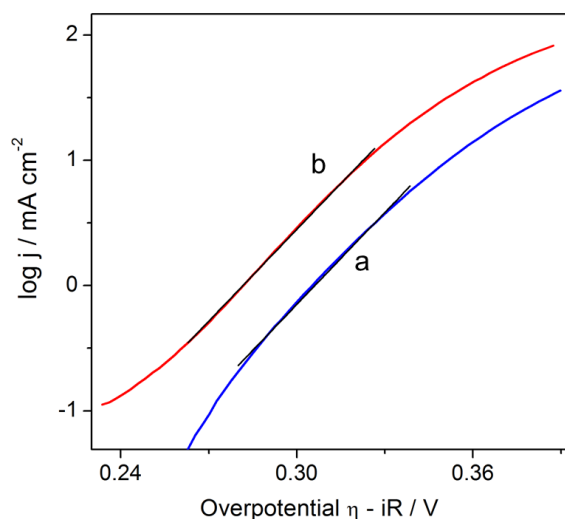


Figure S3.7 Tafel plots for NiO nanoparticles (NP-3.3) on Au-coated QCM electrodes in 0.5 M KOH: pre-conditioned by cycling 30 times from 0.1 to 0.7 V vs. sat. Ag/AgCl electrode with a scan rate $\nu = 20 \text{ mV s}^{-1}$ (blue line, a), and electrochemically aged by applying a constant current of 7.5 mA cm⁻² for 2.5 h (red line, b). Tafel plots were obtained from voltammograms taken at scan rate $\nu = 20 \text{ mV s}^{-1}$. The lines correspond to the Tafel slopes of the OER process measured at an overpotential of 300 mV.

4 IRON-DOPED NICKEL OXIDE NANOCRYSTALS AS HIGHLY EFFICIENT ELECTROCATALYSTS FOR ALKALINE WATER SPLITTING

This chapter is based on the following publication:

Ksenia Fominykh, Petko Chernev, Ivelina Zaharieva, Johannes Sicklinger, Goran Stefanic, Markus Döblinger, Alexander Müller, Aneil Pokharel, Sebastian Böcklein, Christina Scheu, Thomas Bein and Dina Fattakhova-Rohlfing *ACS Nano* **2015**, *9*, 5180.

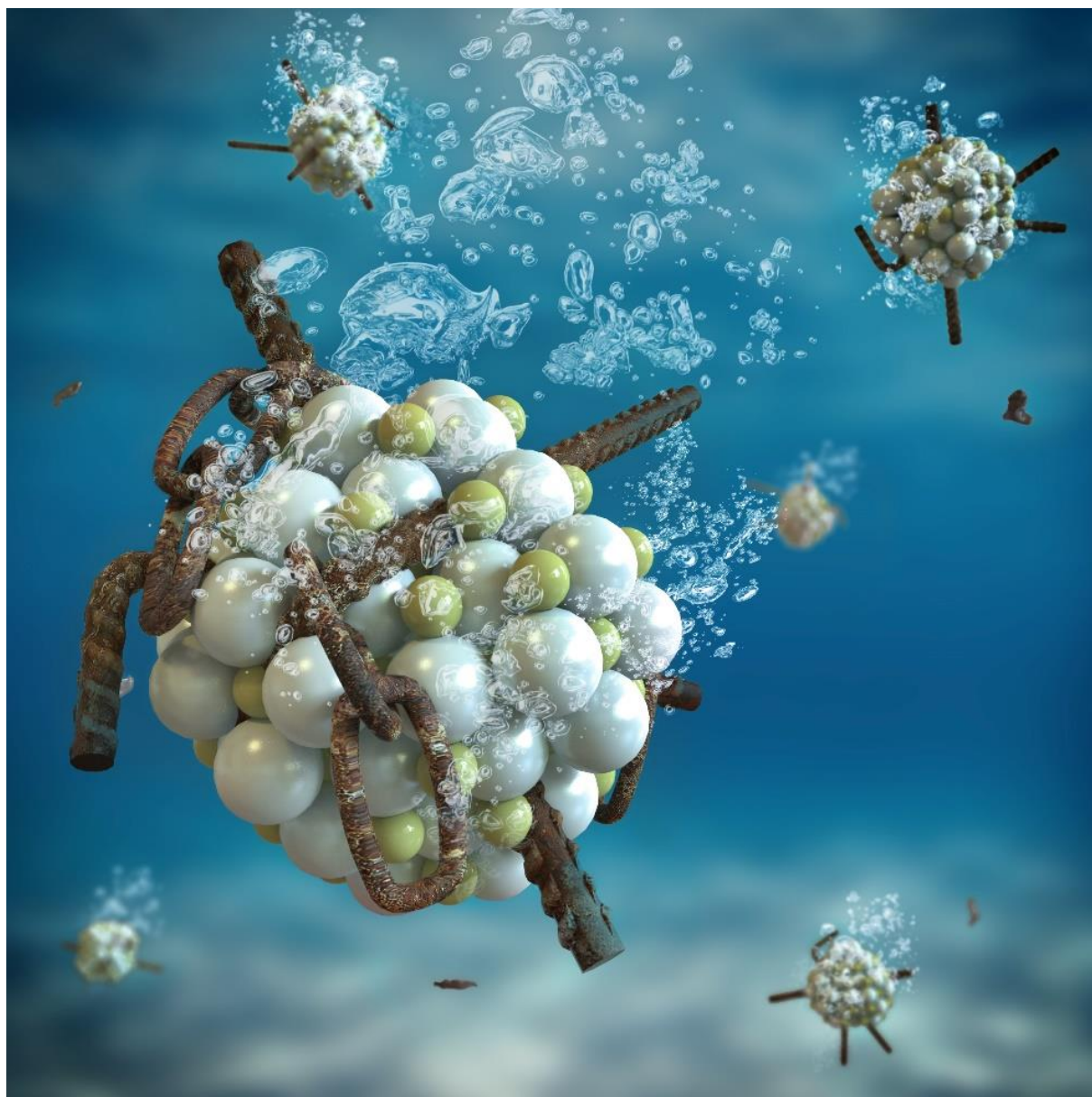


Figure 4.1 Image created by Christoph Hohmann (Nanosystems Initiative Munich, NIM) published as special article title image in the GIT Labor-Fachzeitschrift 12/2015 Wiley-VCH Verlag GmbH & Co. KGaA, GIT VERLAG, Weinheim, 26–28 (used with permission from the publisher).

4.1 ABSTRACT

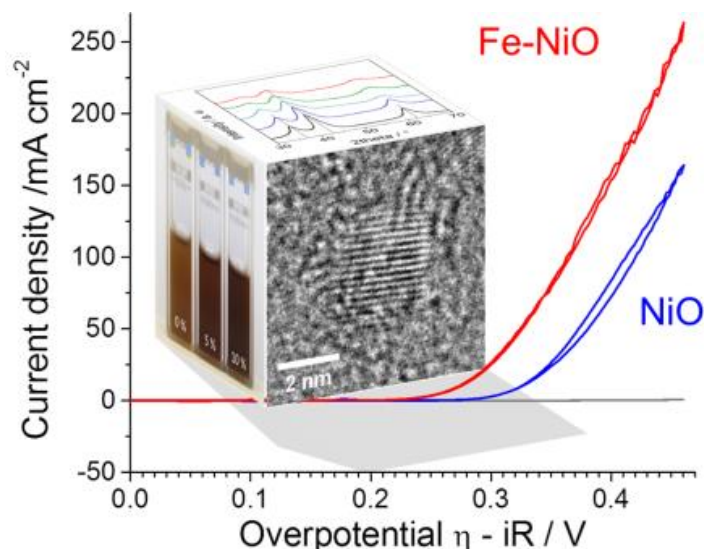


Figure 4.2 ToC image illustrating the crystalline structure, ultrasmall size and perfect dispersibility of the Fe-doped NiO nanoparticles combined with their extraordinary performance in electrochemical water splitting.

Efficient electrochemical water splitting to hydrogen and oxygen is considered a promising technology to overcome our dependency on fossil fuels. Searching for novel catalytic materials for electrochemical oxygen generation is essential for improving the total efficiency of water splitting processes. We report the synthesis, structural characterization and electrochemical performance in the oxygen evolution reaction of Fe-doped NiO nanocrystals. The facile solvothermal synthesis in *tert*-butanol leads to the formation of ultrasmall crystalline and highly dispersible $\text{Fe}_x\text{Ni}_{1-x}\text{O}$ nanoparticles with dopant concentrations of up to 20 %. The increase in Fe-content is accompanied by a decrease in particle size resulting in non-agglomerated nanocrystals of 1.5 – 3.8 nm in size. The Fe-content and composition of the nanoparticles are determined by X-ray photoelectron spectroscopy and energy-dispersive X-ray spectroscopy measurements while Mössbauer and extended X-ray absorption fine structure analyses reveal a substitutional incorporation of Fe(III) into the NiO rock salt structure. The excellent dispersibility of the nanoparticles in ethanol allows for the preparation of homogeneous ca. 8 nm thin films with a smooth surface on various substrates. The turnover frequencies (TOF) of these films could be precisely calculated using a quartz crystal microbalance. $\text{Fe}_{0.1}\text{Ni}_{0.9}\text{O}$ was found to have the highest electrocatalytic water oxidation activity in basic media with a TOF of 1.9 s^{-1} at the overpotential of 300 mV. The

current density of 10 mA cm^{-2} is reached at the overpotential of 297 mV with a Tafel slope of 37 mV dec^{-1} . The extremely high catalytic activity, facile preparation and low cost of the single crystalline $\text{Fe}_x\text{Ni}_{1-x}\text{O}$ nanoparticles make them very promising catalysts for the oxygen evolution reaction.

4.2 INTRODUCTION

The splitting of water into oxygen and hydrogen provides a promising solution to the generation and storage of hydrogen from renewable energy sources, such as solar and wind power.^{1,2} For high rate hydrogen production both half reactions of the water splitting process, *i.e.* water oxidation and reduction, have to proceed with optimum efficiency. The hydrogen evolution reaction follows a simple mechanism and can be catalyzed by many metals and metal oxides at low overpotentials.³ A major challenge however is the slow rate of the oxygen evolution reaction (OER), which proceeds *via* several steps with high activation energies requiring large overpotentials for the transfer of four electrons.^{4,5} To solve this problem, efficient water oxidation catalysts are needed, which has initiated an intensive search on different classes of materials acting as possible OER catalysts.⁶⁻¹⁵ The state of the art electrocatalysts for oxygen generation are expensive and rare iridium and ruthenium oxides,^{1,2,16-18} severely restricting their large scale applications. More attractive alternatives such as abundant and low cost first-row transition metal oxides have been intensively explored as OER catalysts, but their long term stability and catalytic performance were found to be inferior.¹⁸ Recent developments, however, demonstrate that the OER activity of these materials can be substantially enhanced and tuned in a broad range by substitutional doping with different ions resulting in mixed compounds such as $\text{Ni}_{1-x}\text{Fe}_x\text{O}$ with very high catalytic activities at low overpotentials comparable to that of IrO_2 .¹⁹⁻²¹

Fe-Ni-O mixed compounds have been known for decades and are considered among the best electrocatalysts for alkaline water electrolysis.²²⁻²⁶ Still, the numerous publications reported up to date demonstrate the very strong impact of crystalline structure and morphology on the electrocatalytic activity, which can differ by orders of magnitude for different Fe-Ni-O compounds.^{19,21,27,28} Most of the literature on this subject concerns layered structures such as Ni-Fe double hydroxides (Fe/Ni(OH)_2),^{27,29} oxyhydroxides (Fe/NiOOH)¹⁹ or amorphous

phases^{30,31} either formed directly or as a result of structural transformations of NiO_x.¹³ The activity of rock salt-type nickel oxide compounds was considered to be inferior due to their compact structure resulting in a low accessibility of catalytically active sites. We have recently demonstrated that the catalytic performance of rock salt-type nickel oxide increases dramatically due to a decrease in the particle size.³² In the present work we demonstrate that the electrocatalytic activity increases by almost an order of magnitude by introducing Fe atoms into the structure, which makes it by far the highest among all reported FeNi oxide materials and indeed, to our knowledge among all reported alkaline OER catalysts.^{13,19-21}

We present for the first time a solvothermal synthesis pathway for the preparation of ultrasmall, crystalline and dispersible Fe-doped NiO nanoparticles (NPs) with Fe-contents of up to 20 at% using *tert*-butanol (*t*BuOH) as solvent and reactant, as well as their application as highly efficient electrocatalyst for the oxygen evolution reaction. The particles show the highest turnover frequency (TOF) of 1.9 s⁻¹ at an overpotential of 300 mV for 10 % Fe(III)-doping, thus outperforming bulk iron nickel oxide and expensive rare earth iridium oxide catalysts. The combination of decreased particle size and high crystallinity is highly beneficial for the greatly enhanced electrocatalytic activity and the stability of the structure, which remains preserved after prolonged electrolysis in basic media. The material contains inexpensive abundant elements and meets the criteria of high catalytic activity at low overpotentials, stability in basic media and low cost, making this OER catalyst environmentally and economically attractive.

4.3 RESULTS AND DISCUSSION

For the synthesis of crystalline NiO nanoparticles doped with Fe(III) we used a solvothermal reaction in *tert*-butanol that leads to the direct formation of crystalline nanoparticles *via* a chemical reaction with the solvent. The suitability of this reaction pathway for the fabrication of ultrasmall colloidal nanocrystals was demonstrated by us in previous reports for several titanate systems and undoped NiO nanoparticles.³²⁻³⁵ Key to the successful fabrication of doped and mixed oxides without phase separation is matching the reactivity of Fe and Ni precursors. Nickel(II) acetylacetonate (Ni(acac)₂) and Fe(III) acetylacetonate (Fe(acac)₃) were found to be the most suitable precursor combination, enabling the fabrication of phase-pure

$\text{Fe}_x\text{Ni}_{1-x}\text{O}$. In the following the samples will be labeled as NP-X% with X being the Fe-content.

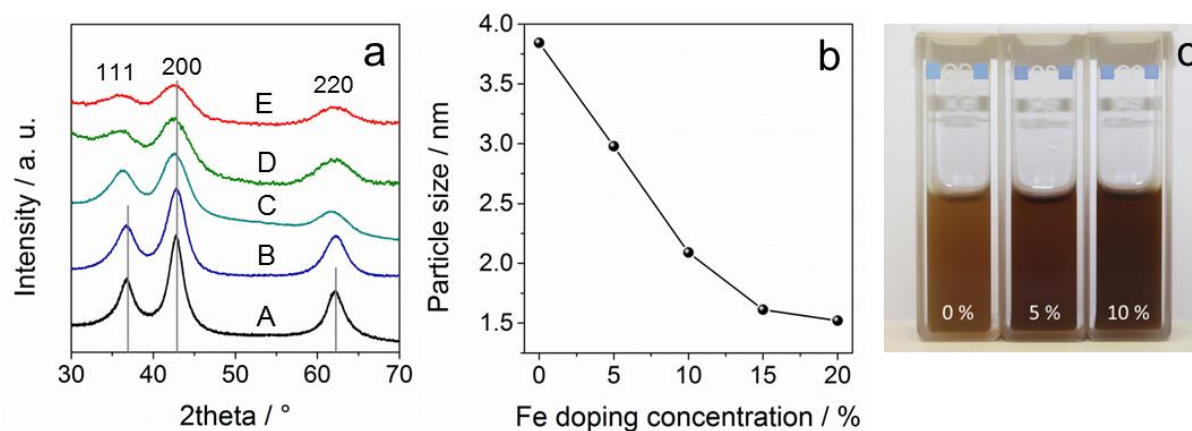


Figure 4.3 Crystallite size and dispersions of the $\text{Fe}_x\text{Ni}_{1-x}\text{O}$ nanoparticles with different Fe-doping concentration: (a) Powder XRD patterns of the dried $\text{Fe}_x\text{Ni}_{1-x}\text{O}$ nanoparticles NP-0% (A), NP-5% (B), NP-10% (C), NP-15% (D) and NP-20% (E) (NiO pattern: ICDD card number 01-071-1179). (b) Crystalline domain size of nanoparticles with increasing Fe-content calculated from the XRD patterns using the Scherrer equation for the most intensive (200) NiO signal at $2\theta = 43^\circ$; (c) Image of $\text{Fe}_x\text{Ni}_{1-x}\text{O}$ nanoparticle dispersions (concentration: 2 mg mL^{-1}) in ethanol; the numbers indicate the Fe-doping concentrations.

The samples with Fe-contents up to 20 at% show broadened reflections of phase-pure $\text{Fe}_x\text{Ni}_{1-x}\text{O}$ in the X-ray diffraction (XRD) patterns indicating the formation of small crystalline particles (Figure 4.3a). The formation of any additional Fe-phases could not be observed, which indicates complete incorporation of Fe-atoms into the NiO lattice. The reflections show a shift to lower 2θ angles with increasing doping concentrations implying that the lattice constants are shifted to higher values, which indicates substitutional incorporation of Fe-ions into the NiO rock salt structure. The size of the nanocrystals calculated from the line broadening in the XRD patterns decreases with higher Fe-doping concentration and corresponds to $3.8 \pm 0.1 \text{ nm}$ for NP-0%, $3.0 \pm 0.1 \text{ nm}$ for NP-5%, $2.0 \pm 0.1 \text{ nm}$ for NP-10%, $1.6 \pm 0.1 \text{ nm}$ for NP-15%, and $1.5 \pm 0.1 \text{ nm}$ for NP-20%, respectively. The particle size decreases almost linearly with increasing doping concentration as calculated for the most intensive (200) NiO reflection in the XRD patterns using the Scherrer equation (Figure 4.3b). The lattice parameters of the $\text{Fe}_x\text{Ni}_{1-x}\text{O}$ nanoparticles are in agreement with Vegard's law (Figure S4.1 in the supporting information). The particles are non-agglomerated and form

stable colloidal dispersions in ethanol with the addition of very small amounts of acetic acid. As an example, ethanolic dispersions of NP-0%, NP-5% and NP-10% with concentrations of 2 mg mL^{-1} are shown in Figure 4.3c.

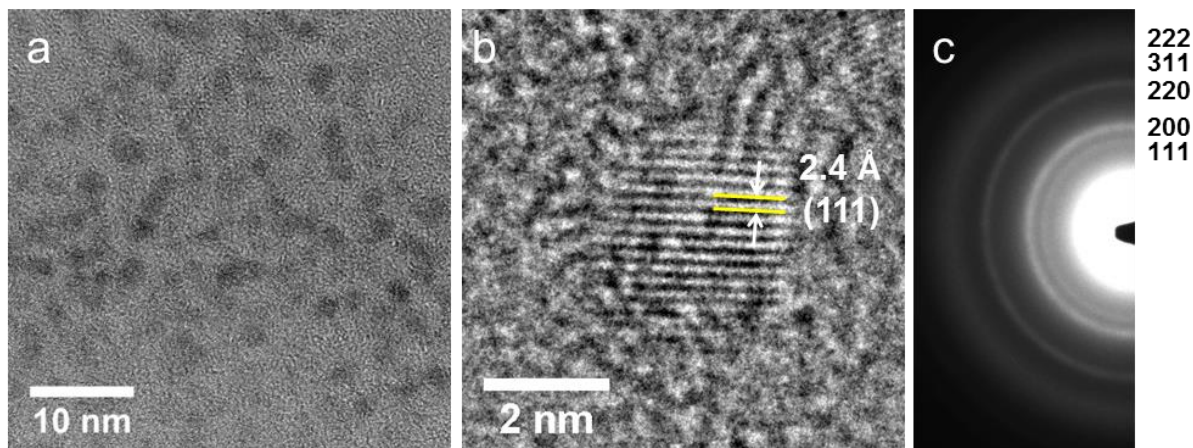


Figure 4.4 TEM images of the $\text{Fe}_{0.1}\text{Ni}_{0.9}\text{O}$ nanoparticles (NP-10%). (a) Overview of the nanoparticles dispersed on the TEM grid; (b) HRTEM image of a single $\text{Fe}_{0.1}\text{Ni}_{0.9}\text{O}$ nanoparticle. (c) Electron diffraction pattern taken of several tens of $\text{Fe}_{0.1}\text{Ni}_{0.9}\text{O}$ nanoparticles. The corresponding d-values are 2.44 \AA (111), 2.09 \AA (200), 1.47 \AA (220), 1.26 \AA (311) and 1.2 \AA (222).

Transmission electron microscopy (TEM) images of nanoparticles containing 10 % Fe (Figures 4.4a, b) and 20 % Fe (Figure S4.2 in the supporting information) show non-agglomerated crystals with a narrow particle size distribution (Figure S4.3 in the supporting information). The presence of lattice fringes and the absence of defects in HRTEM images (Figure 4.4b) reveal the single-crystalline structure of the individual particles. The electron diffraction pattern taken of an area of about 150 nm in diameter shows several rings due to averaging over several tens of particles (Figure 4.4c). The rings can be indexed using the NiO rock salt structure, confirming the XRD results. The average particle size determined from the TEM images is $2.0 \pm 0.4 \text{ nm}$ and $1.8 \pm 0.4 \text{ nm}$ for the particles containing 10 % and 20 % Fe, respectively. This is in good agreement with the sizes calculated from XRD patterns.

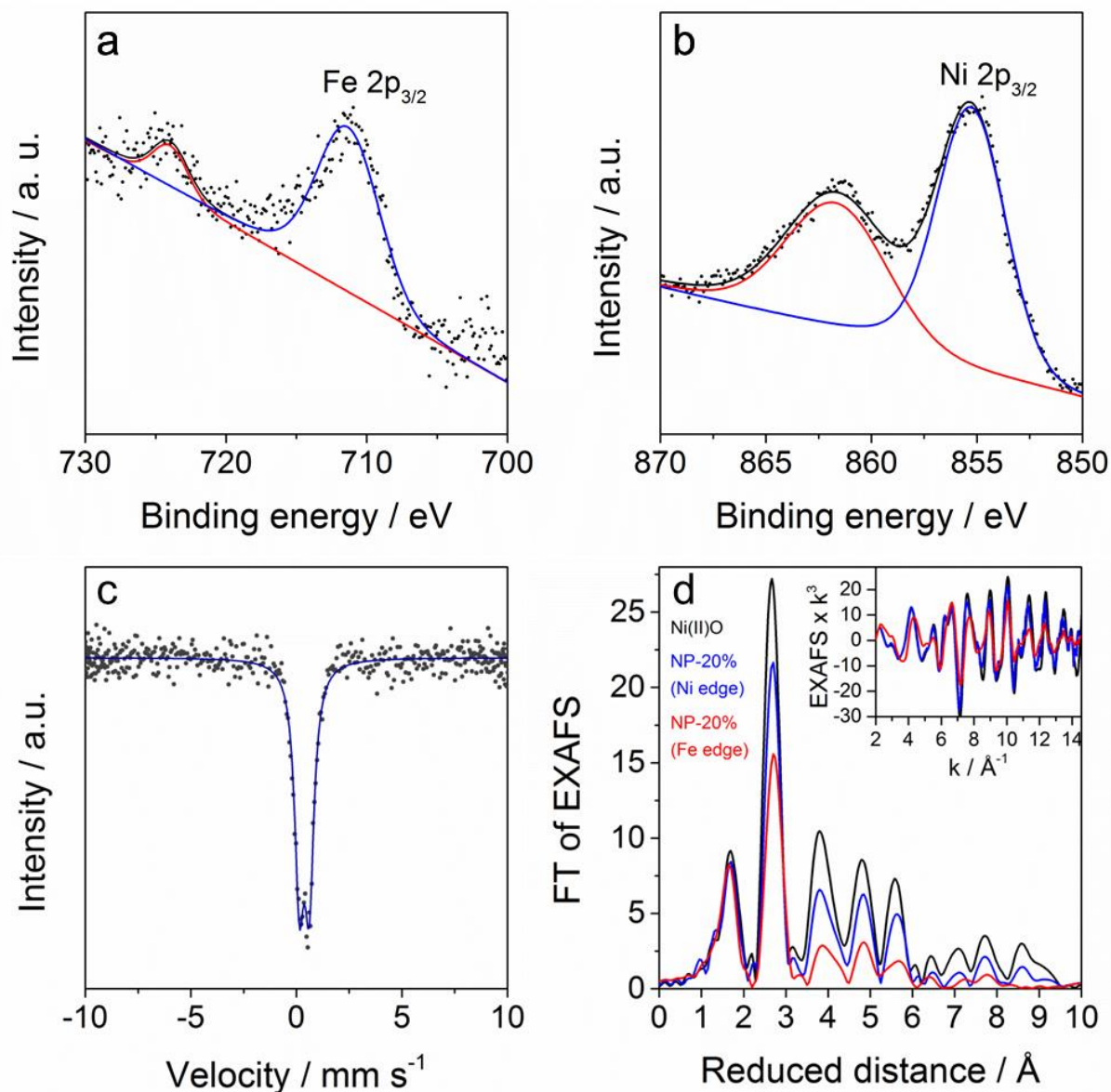


Figure 4.5 X-ray photoelectron spectra of 10 % Fe(III)-doped NiO nanoparticles. (a) Fe 2p peaks and (b) Ni 2p peaks. Spectra were taken using a Mg source. The points correspond to the experimental spectra, and the lines are the fitted curves and the Gaussian individual peak fits, respectively. The corresponding fitting parameters are listed in Table S4.2 (supporting information); (c) Mössbauer spectrum of the sample NP-10%; (d) Fourier-transformed EXAFS spectra collected from 20 % Fe(III)-doped NiO nanoparticles at the Ni (blue line) and Fe (red line) K-edges and crystalline NiO reference (black line). The original k³ weighted spectra are shown in the inset.

4.3 RESULTS AND DISCUSSION

X-ray photoelectron spectroscopy measurements of NP-10% show the Ni 2p doublet typical for NiO in the energy region between 850 and 870 eV (Figure 4.5b).³⁶⁻³⁸ The binding energies at 711 and 724 eV correspond to Fe 2p_{3/2} and Fe 2p_{1/2} peaks, respectively (Figure 4.5a). These signal positions are typical for Fe₂O₃ and indicate the presence of Fe-atoms in the oxidation state Fe(III).^{39, 40} At the same time the presence of a separate Fe₂O₃ phase can be excluded due to missing shakeup satellites at 719 and 732 eV⁴⁰ indicating the incorporation of Fe(III) into the NiO lattice. Quantification of the elements for NP-10% shows an atomic ratio of Ni:Fe = 12:1 corresponding to 8 % Fe, which is slightly lower than the Fe(III) content of 10 % in the reaction mixture and the value of 11 % determined in energy-dispersive X-ray spectroscopy (EDX) measurements, and may be attributed to surface defects.

For a more detailed investigation of the oxidation state of Fe-atoms within the nanoparticles, ⁵⁷Fe Mössbauer spectra were recorded for the samples NP-10% and NP-20%. The spectra are characterized by a paramagnetic quadrupole doublet with isomer shift values characteristic for Fe(III)-ions in the high spin state, 0.37 and 0.33 mm s⁻¹ for NP-10% and NP-20%, respectively (Figures 4.5c, S4.4 and Table S4.1 in the supporting information).⁴¹ The increase in the amount of the incorporated iron caused an increase of the electric field gradient (quadrupole splitting increase from 0.49 mm s⁻¹ to 0.66 mm s⁻¹), which can be attributed to a reduced symmetry of the chemical environment around the nucleus. The results reveal the presence of high-spin Fe(III)-ions in octahedral sites which is consistent with a successful incorporation of Fe(III) into the rock salt structure of NiO.⁴²

X-ray absorption spectroscopy was used to examine the oxidation state and the position of Fe and Ni-atoms within the Fe_xNi_{1-x}O lattice. For comparison, NP-0% and NP-20% were analyzed both in powder form and after deposition on a FTO electrode. In addition, commercially available NiO powder (Sigma-Aldrich) and Fe₂O₃ (Sigma-Aldrich) were measured as references. The oxidation state of the Ni ions is +II and of the Fe-ions +III as judged from the X-ray absorption near edge structure (XANES) spectra and by comparison of the absorption edge position with the measured references (Figure S4.5 in the supporting information). No difference in the edge shape or position was found between the nanoparticles in powder form and those deposited on the electrode. Information about the atomic structure can be obtained from the extended X-ray absorption fine structure (EXAFS) spectra. Comparing the Fourier transforms of the EXAFS spectra shown in Figure 4.5d, it can be seen that the local atomic structure around both Ni and Fe centers is identical to that of the

rock salt structure of the NiO reference. This structure is confirmed by the simulations as shown in Figures S4.6, S4.7 and Tables S4.3, S4.5 in the supporting information. The different amplitudes of the peaks indicate different degrees of local disorder, which is reflected in the simulations by the higher Debye-Waller factor (lower peak amplitudes) for the nanoparticles. Another possible reason for the decrease in the peak amplitudes of the higher coordination shells in the nanoparticles is the higher proportion of surface atoms, for which not all long-range shells exist. Particularly high disorder or, alternatively, a higher proportion of surface atoms, is found around the Fe centers. As evident from the EXAFS spectrum, the Fe centers in the NP-20% are located in a rock salt type structure, and thus either are incorporated into the NiO lattice or form their own Fe-only phase which is rather unlikely since HRTEM images only show single crystalline nanoparticles. Ni and Fe-ions behave virtually identically as X-ray backscatterers and it is not possible to distinguish them in the EXAFS analyses (Figure S4.7 and Table S4.4 in the supporting information.). However, the Fe K-edge position shows that iron is in the oxidation state +III, and the EXAFS simulations at the Fe K-edge result in Fe-O distances of 2.01 Å matching those expected for Fe(III) in octahedral coordination and not the one for Fe(II).⁴³ Since the rock salt structure is not compatible with the oxidation state of +III of the Fe-ions, we conclude that in the Fe-doped NiO nanoparticles individual Fe-ions are incorporated in the Ni oxide lattice replacing Ni-ions. A situation where Fe is predominantly on the surface of the NiO nanoparticle thus preventing further growth of the crystals cannot be excluded and could explain the smaller particle size with Fe doping. However in this case the Fe needs to be part of the same rock salt lattice as evident from the virtually identical EXAFS spectra measured at the Ni and at the Fe edges.

Different studies report a limited solubility of Fe in NiO (up to 6 at%) accompanied by the formation of Ni-Fe spinel or Fe₂O₃ phase at low calcination temperatures.^{44,45} Landon *et al.*³⁹ describe the formation of an additional NiFe₂O₄ phase with increasing Fe-content in the NiO lattice already at around 5 % Fe. In our material we do not observe any formation of additional phases up to at least 20 at% Fe according to the results of several methods such as XRD, Mössbauer spectroscopy and EXAFS, which supports the assumption that the Fe-atoms are incorporated into the NiO structure. Additionally, Raman spectra of NP-0% and NP-20% showing only the presence of the Fe_xNi_{1-x}O phase are shown in Figure S4.8 in the supporting information. The unusually high solubility of Fe in the rock salt NiO structure can originate

from the kinetic control of the Fe-NiO phase formation in a solvothermal process, as well as the effect of the nanoscale where the metastable and defect phases often show higher stability than in the bulk.

To test the catalytic activity of Fe-doped NiO nanoparticles in electrochemical water oxidation, the particle dispersions were deposited as thin films on gold electrodes of the piezoelectric quartz crystals for the exact determination of their loading using the Sauerbrey equation.⁴⁶ Spin coating of the particle dispersions results in the formation of uniform films with an average thickness of 8 nm (Figure 4.6a, inset).

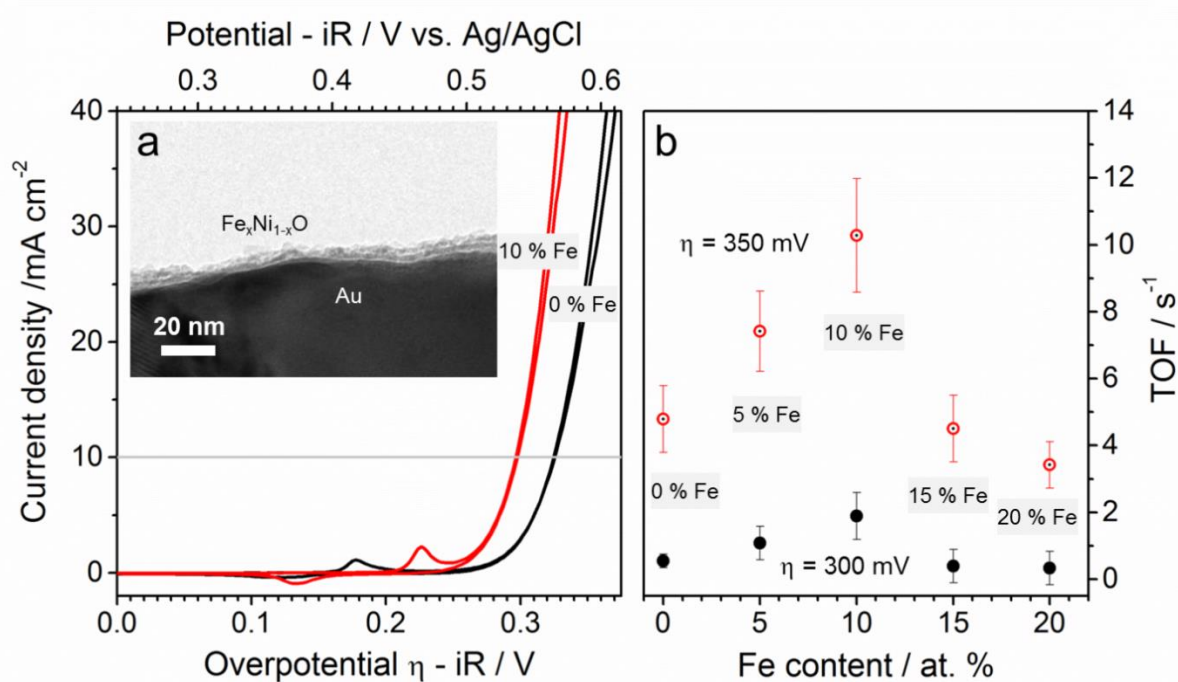
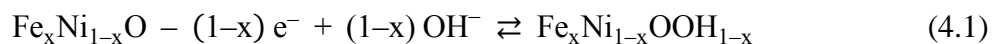


Figure 4.6 (a) Cyclic voltammograms of Au/QCM electrodes coated with thin films of NP-0% and NP-10%. The inset shows a cross-section HR-TEM image of the NP-10% film deposited by spin-coating on the Au/QCM substrate; (b) TOF values at an overpotential of $\eta = 300$ mV (filled circles) and $\eta = 350$ mV (open circles) for NP-0%, NP-5%, NP-10%, NP-15% and NP-20%.

The voltammograms of both undoped and Fe-doped NiO thin film electrodes show reversible oxidation peaks corresponding to the reaction



followed by the current corresponding to the OER reaction at more positive potentials. The introduction of Fe-atoms into the NiO lattice leads to a positive shift in the formal potential of the first process from 389 mV vs. Ag/AgCl for the undoped nanoparticles to 420 mV for the NP-10% particles, indicating that the electrochemical oxidation of Ni(OH)₂ to NiOOH is suppressed with increasing Fe-content, which was also observed in previous studies.^{21, 22, 24, 29} Electrochemical measurements show that the peak area and the formal potential do not change over several hundred cycles revealing a high stability of the Fe-doped material. A typical example of a stability measurement where the electrode potential was measured for 10 and 3 h at constant current densities of 10 and 200 mA cm⁻², respectively, is shown in Figure S4.9 in the supporting information.

According to the CV curves the highest current densities and therefore the highest catalytic activity were obtained for 10 % Fe(III)-doped NiO nanoparticles. The current densities rise with increasing doping concentration from NP-0% to NP-10% and drop significantly with further increase in Fe-content with NP-15% and NP-20% showing even lower catalytic activities than the undoped NiO sample.

In order to quantify the electrocatalytic activity of the Fe-doped NiO nanoparticles, we calculated turnover frequency values (corresponding to the moles of oxygen evolved per second per active site) at different overpotentials. This is one of the generally accepted figures of merit of electrocatalytic materials.¹⁹⁻²¹ A critical issue in TOF calculation is the assessment of the active surface area, which is often challenging for thin electroactive layers. For our films deposited from nanoparticle dispersions on the piezoelectric Au/quartz electrodes we could determine surface areas precisely from the specific surface area of 117 m² g⁻¹ determined by nitrogen sorption (Figure S4.10 in the supporting information) and the measured mass loading of 22.5 μg cm⁻². Using the theoretical surface density of Ni-atoms of 4.08 · 10¹⁴ cm⁻² in NP-10% and the fraction of Ni atoms on the surface (X-ray photoelectron spectroscopy, XPS) we obtained a surface charge of 1.50 mC cm⁻². This value closely agrees with the charge obtained by integration of the voltammetric peaks of the Fe_xNi_{1-x}O oxidation

process (1.43 mC cm^{-2}) corresponding to $5 \pm 2 \%$ of the total Ni content, indicating that only surface atoms are involved in the electrochemical reaction.

The TOF values calculated by this method for all Fe-doping concentrations at overpotentials of $\eta = 300 \text{ mV}$ and $\eta = 350 \text{ mV}$ are shown in Figure 4.6b. As already noticed for the current densities, the turnover frequencies increase with higher doping concentration up to 10 % showing TOF values of 0.55 s^{-1} at $\eta = 300 \text{ mV}$ for pure NiO (NP-0%), 1.1 s^{-1} for NP-5% and an extremely high value of 1.9 s^{-1} for NP-10%. With further increase in Fe-content the TOF strongly decrease showing values of only 0.39 s^{-1} and 0.33 s^{-1} at $\eta = 300 \text{ mV}$ for NP-15% and NP-20%, respectively. The TOF value obtained for the NP-10% nanoparticles not only favorably compares to other NiO-based compounds, but it is one of the highest reported so far for different known types of OER materials.^{7,8,13,19,32} The Tafel slope for the electrode with the best performance (NP-10%) is 37 mV dec^{-1} (Figure S4.11 in the supporting information) which is a typical value for anhydrous Fe/Ni oxides.²²

The high OER electrocatalytic activity of ultrasmall nickel oxide nanoparticles was already reported by us previously.³² The beneficial effect of the reduced crystal size of undoped NiO to only a few nanometers and the surface properties of the nanoparticles on the catalytic performance is shown by the very high TOF values (0.55 s^{-1}) compared to bulk material. When doping the nanocrystals with iron the catalytic activity of the NiO is even further increased with TOF values of up to 1.9 s^{-1} for NP-10% in the present study.

It should be noted that the TOF values reported for different materials strongly depend on the method of surface area determination. McCrory *et al.*²⁰ and Louie *et al.*²¹ presented a route for the calculation of the surface area using the measured capacitance of the material. Following this method, we have obtained a surface area of 0.35 cm^2 using the measured capacitance of $21 \text{ }\mu\text{F}$ (Figure S4.12 in the supporting information) and assuming a specific capacitance of $60 \text{ }\mu\text{F cm}^{-2}$ for flat oxide electrodes,⁴⁷ which is almost 10 times lower than the specific surface area determined by the direct method described above. The use of this surface area leads to a greatly overestimated TOF value of 17 s^{-1} for NP-10%, which is almost 10 times higher than the TOF obtained by the direct method. The large discrepancy between the TOF values determined with different methods suggests that the results obtained from the capacitance measurements should be interpreted with great care and only be used for the estimation of activity trends in the same type of materials, but not for the calculation of

absolute values. The error in the surface area determination should become even more significant for insulating or poorly conducting layers, such as $\text{Fe}_{1-x}\text{Ni}_x\text{O}$, where an increase in surface area does not necessarily translate into an increase in the double layer capacitance. A similar point was raised by Louie *et al.*,²¹ who obtained drastically different TOF values for the same materials using a different calculation method. Thus, they calculated extremely high TOF values of up to 87 s^{-1} (TOF_{max}) from capacitive measurements assuming that only surface Ni atoms are catalytically active, and very small values of $0.005 - 0.008 \text{ s}^{-1}$ (TOF_{min}) for the same material assuming that each atom in the layer is electrocatalytically active. The application of the latter method of TOF determination to our system (taking the amount of the Ni atoms from the mass loading) leads to a TOF_{min} value of 0.26 s^{-1} , which is 30 times higher than the TOF_{min} reported by Louie *et al.*. However, similar to the results of Louie *et al.*, this value is much lower than the TOF_{max} of 17 s^{-1} calculated for the same NP-10% film, which again shows that this method should be applied with great care.

McCrorry *et al.*²⁰ recently described a method to benchmark OER catalysts. For example, they calculated the current density for a given overpotential of 350 mV. The two materials with the best catalytic performance were IrO_x (42 mA cm^{-2}) and NiFeO_x (15 mA cm^{-2}). Following this method, we obtained a current density of $59 \pm 5 \text{ mA cm}^{-2}$ at an overpotential of 350 mV for the electrode with 10 % Fe-doped NiO. This value is higher than that of any other reported OER known to us including other NiFeO_x morphologies.^{7,8,13,19,30} This demonstrates the strong impact of morphology and nanoscaling on the electrocatalytic performance, which opens new perspectives for the further development of active electrocatalysts.

To conclude, higher Fe(III) doping concentrations increased the catalytic activity of Fe-doped NiO NPs. A similar observation is described in the literature for mixed iron nickel oxide phases. These mixed metal oxide catalysts attained the best OER activity for 10 % Fe(III) content.³⁹ The same applies to solution cast thin films with the formal composition $\text{Fe}_x\text{Ni}_{1-x}\text{O}$.¹⁹

In addition to the extremely high electrocatalytic activity, the excellent dispersibility of the $\text{Fe}_x\text{Ni}_{1-x}\text{O}$ nanoparticles offers additional advantages, such as a great flexibility towards the fabrication of different electrode architectures. Thus, thin homogeneous layers can be obtained by spin coating of particle dispersions. It is also expected that the nanoparticles can be homogeneously distributed on porous substrates with complex geometry by drop casting.

4.4 CONCLUSION

We describe a novel synthesis route for the preparation of ultrasmall, crystalline and dispersible NiO nanoparticles substitutionally doped with Fe(III). They reveal great potential as an extremely efficient inexpensive catalyst for the electrochemical oxygen evolution. Various undoped and Fe-doped NiO nanoparticles were successfully synthesized using a solvothermal reaction in *t*BuOH with the acetylacetonates of nickel(II) and iron(III) serving as precursors. In this way ultrasmall and highly dispersible nanocrystals of doped nickel oxide with Fe-doping concentrations of up to 20 % could be obtained. The particles form stable non-agglomerated colloidal dispersions in ethanol. The particle size is in the range of 1.5 – 3.8 nm and strongly depends on the doping concentration, leading to smaller particles with increasing iron content. The presence of iron as Fe(III) and nickel as Ni(II) on the surface and within the nanoparticles was confirmed by XPS, EXAFS and Mössbauer spectroscopy. The electrocatalytic activity of NiO is clearly enhanced with increasing Fe-doping concentration reaching an optimum at 10 % iron content. The highest turnover frequency of 1.9 s⁻¹ was obtained for Fe(III)-doped NiO nanoparticles even at a low overpotential of 300 mV, outperforming expensive catalysts such as iridium oxide. The unique features of these Fe-doped NiO nanocrystals provide great potential for their application as an efficient and competitive anode material in the field of electrochemical water splitting.

4.5 EXPERIMENTAL SECTION

4.5.1 SYNTHESIS OF IRON-DOPED NICKEL OXIDE NANOPARTICLES

Nickel(II) acetylacetonate was purchased from Alfa Aesar (95 % purity), iron(III) acetylacetonate was purchased from Sigma-Aldrich (97 % purity) and *tert*-butanol was purchased from Sigma-Aldrich (puriss. p.a., ACS reagent, ≥ 99.7 %). All chemicals were used as received except for *tert*-butanol which was dried over a 4 Å molecular sieve at 28 °C and filtered prior to use.

For the solvothermal synthesis of iron-doped nickel oxide nanoparticles 917.5 mg (3.571 mmol) of nickel(II) acetylacetonate (Ni(acac)₂) was mixed with

iron(III) acetylacetonate ($\text{Fe}(\text{acac})_3$) in the desired molar composition. The Fe-doping concentration c_{Fe} was calculated using the equation

$$c_{\text{Fe}} = \frac{n_{\text{Fe}}}{n_{\text{Ni}} + n_{\text{Fe}}} \quad (4.2)$$

with n_x being the molar amount of the respective precursor. For 5 %, 10 %, 15 % and 20 % Fe-doping 66.4 mg (0.188 mmol), 140.5 mg (0.397 mmol), 164.9 mg (0.466 mmol) and 210.6 mg (0.595 mmol) of the iron precursor was added, respectively. The solid mixture was mixed with 100 mL of *tert*-butanol under vigorous stirring in a glass autoclave liner forming an orange suspension, then placed into a Parr Series 4760 pressure vessel (300 mL) autoclave reactor and hermetically sealed. The reactions were carried out under continuous stirring at 205 °C for 20 h in case of 5 % and 10 % doping and for 30 h in case of 15 % and 20 % doping resulting in uniform brown dispersions of nanoparticles. The as-prepared particles were dried in air by evaporating the solvent at 80 °C on a hot plate. At these conditions phase pure iron-doped nickel oxide nanoparticles with 3.8 ± 0.1 nm (0 % Fe), 3.0 ± 0.1 nm (5 % Fe), 2.0 ± 0.1 nm (10 % Fe), 1.6 ± 0.1 nm (15 % Fe) and 1.5 ± 0.1 nm (20 % Fe) in size were obtained.

Dispersions of the Fe-doped and undoped NiO nanoparticles were prepared in ethanol by the addition of acetic acid. In a typical procedure, 1.1 mg of the dried powder was covered with 8 μL of acetic acid. After sonication for 5 min the particles were dispersed in 500 μL ethanol (absolute) and sonicated for another 5 min to obtain a colloidal dispersion with a metal oxide concentration of 0.03 mol L^{-1} .

4.5.2 CHARACTERIZATION

Wide angle X-ray diffraction analysis was carried out in transmission mode using a STOE STADI P diffractometer with $\text{Cu K}_{\alpha 1}$ radiation ($\lambda = 1,54060 \text{ \AA}$) and a Ge(111) single crystal monochromator equipped with a DECTRIS solid state strip detector Mythen 1K. Powder XRD patterns of the samples were collected with an omega-2theta scan in a 2θ range from 5° to 70° with a step size of 1° , a fixed counting time of 90 s/step and a resolution of 0.05° . The size of the crystalline domains was calculated from the XRD patterns for the most intensive (200) reflection using the Scherrer equation.

TEM measurements were carried out using a FEI Titan 80–300 instrument equipped with a field emission gun operated at 300 kV. For the sample preparation a drop of a strongly diluted dispersion of a sample in ethanol was deposited on a holey carbon coated copper grid and evaporated. Contaminations were removed by hydrogen-oxygen plasma cleaning for 15 s at 50 mW and large-area illumination in the TEM for 40 min. The cross-sections were prepared following a procedure described by Strecker *et al.*⁴⁸

X-ray photoelectron spectroscopy analysis of the particles was performed on a silicon substrate using a VSW HA 100 electron analyzer and the K_{α} radiation was provided by a non-monochromatized magnesium anode system ($Mg K_{\alpha} = 1253.6$ eV). Ar ion polishing was done at 1000 eV for 10 min. The recorded elemental peaks were fitted using a Doniach-Sunjic function⁴⁹ and the elemental ratios were calculated by the equation

$$\frac{X_A}{X_B} = \frac{I_A/S_A}{I_B/S_B} \quad (4.3)$$

where $\frac{I_A}{I_B}$ is the ratio of fitted areas, and S is the sensitivity factor.

⁵⁷Fe Mössbauer spectra were recorded at 20 °C in the transmission mode using a standard *WissEl* (Starnberg, Germany) instrumental configuration. A ⁵⁷Co/Rh Mössbauer source was used. The velocity scale and all data refer to the metallic α -Fe absorber at 20 °C. A quantitative analysis of the recorded spectra was made using the *MossWinn* program.

X-ray absorption spectra (XANES/EXAFS) were collected at the BESSY synchrotron radiation source operated by the Helmholtz-Zentrum Berlin. The measurements were acquired at the KMC-1 bending-magnet beamline at 20 K in a cryostat (Oxford-Danfysik) with a liquid-helium flow system. The powder samples were diluted by mixing with boron nitride (BN) powder (Sigma-Aldrich) to a ratio of 1:10 and measured in absorption mode using ionization chambers (Oxford-Danfysik). The films deposited on FTO were measured in fluorescence mode using a 13-element energy-resolving Ge detector (Canberra) and selecting the Ni or Fe K_{α} fluorescence emission. The data were collected up to 800 eV above the Ni and Fe absorption K-edges. After the ionization chamber used to measure the absorption of the sample, Ni or Fe metal foil was placed and measured in absorption mode as internal energy standard. The energy calibration was done by shifting the energy axis such that the first inflection point in the absorption edge of the Fe foil corresponds to 7112 eV and for the Ni

foil to 8333 eV. These values were used as E_0 in the conversion of the energy axis from eV to k scale when extracting the EXAFS spectrum. For the Fourier transformation a cosine window function was applied on 10 % from both sides of the EXAFS range between k 2.3 Å⁻¹ and 14.4 Å⁻¹. Further details related to data evaluation and error calculation are given in previous studies.⁵⁰

Nitrogen sorption measurements were carried out at 77 K with dried powders of Fe_xNi_{1-x}O nanoparticles using a QUANTACHROME Autosorb iQ instrument. The powders were degassed at 150 °C for at least 12 h before measurement.

Raman spectroscopy was carried out using a LabRAM HR UV-Vis (HORIBA JOBIN YVON) Raman Microscope (OLYMPUS BX41) with a SYMPHONY CCD detection system and a He-Ne laser ($\lambda = 633$ nm). Spectra were recorded using a lens with a 50-fold magnification.

4.5.3 ELECTRODE PREPARATION

The electrodes were prepared by deposition of the dispersed iron-doped nickel oxide nanoparticles by spin coating on Quartz crystal microbalance (QCM) crystals (KVG 10 MHz QCM devices with gold electrodes from Quartz Crystal Technology GmbH). For the spin coating method 8 μ L of nickel oxide dispersion was deposited on a masked QCM crystal exposing an area of 0.196 cm² and spun at 1000 rpm for 10 s. The QCM electrodes prepared in this way were subsequently heated to 240 °C in a laboratory oven with a heating ramp of 4 °C min⁻¹ and a dwell time of 2 h resulting in ~8 nm thick films.

The mass loading was calculated from the resonance frequencies of the QCM crystals before and after coating using the Sauerbrey equation

$$\Delta f = - C_f \Delta m \quad (4.4)$$

With Δf being the change in frequency, C_f the sensitivity factor of the QCM crystal and Δm the change in mass.⁴⁶

4.5.4 ELECTROCHEMICAL MEASUREMENTS

Electrochemical measurements were performed in a three-electrode setup using an Autolab PGSTAT302N potentiostat/galvanostat with a FRA32 M module operating with Nova 1.10.2 software. All measurements were performed in 0.5 M KOH electrolyte solution (Sigma-Aldrich, volumetric solution) at pH 13.43. Pt mesh (2 cm²) was used as a counter electrode. Au/QCM crystals coated with Fe_xNi_{1-x}O nanoparticles were used as working electrodes. To provide an electrical connection to the QCM electrode, a silver wire was connected to the respective part of the QCM crystal using silver lacquer. The silver lacquer and the wire were sealed afterward in inert two-component epoxy resin (Gatan, Inc). All potentials were measured vs. Ag/AgCl/KCl (sat.) reference electrode with a potential of +0.989 V vs. the reversible hydrogen electrode at pH 13.43 (+0.197 V vs. NHE). The electrochemical data were corrected for uncompensated resistance R_s . R_s was determined as minimum total impedance in the frequency regime between 10 and 50 kHz at open circuit conditions and at a potential of 0.2 V vs. Ag/AgCl, where no faradaic processes take place. 95 % of the measured resistance was compensated. R_s was typically around 6 – 8 Ohm for all Fe_xNi_{1-x}O-coated Au/QCM electrodes. The overpotential η was calculated using the equation

$$\eta = E - E_{\text{OER}} - iR_s \quad (4.5)$$

Where E is the potential recorded vs. the Ag/AgCl reference electrode, E_{OER} is the reversible potential of the OER vs. the Ag/AgCl reference electrode (0.240 V at pH 13.43), and i is the current. Current densities are calculated using the geometric surface area of the Au/QCM electrode (0.196 cm²).

The preconditioning of the NiO electrodes was performed using cyclic voltammetry (CVA). The electrodes were cycled between 0 V and 0.7 V vs. Ag/AgCl in 0.5 M KOH at a scan rate of 20 mV s⁻¹ until the current had reached stable values and did not change anymore with repetitive cycling at scan rates of 20 mV s⁻¹ (typically 35 cycles).

The turnover frequency (TOF) at the overpotential of $\eta = 0.3$ V was calculated on the basis of active Ni-atoms according to:

$$\text{TOF} = \frac{i}{4 Q_{\text{exp}}} \quad (4.6)$$

where i is the current and Q_{exp} is the charge corresponding to the Fe-NiO redox reaction according to the equation (4.1) assuming that only one electron is transferred per Ni atom. As the charge obtained from the anodic peak of the NiO redox process may contain some contribution from the OER process we have used the cathodic peak to determine the amount of the catalytically active Ni atoms.

The ratio of catalytically active sites to the theoretical total number of active sites was calculated using the relation of the experimental charge values Q_{exp} to the theoretical charge values Q_{th} $\left(\frac{Q_{\text{exp}}}{Q_{\text{th}}}\right)$. Q_{exp} was obtained by integration of the cathodic peak which corresponds to the reduction of NiOOH to NiO. Q_{th} was calculated using the total amount of $\text{Fe}_x\text{Ni}_{1-x}\text{O}$ in the films. For NP-0% to NP-20% the ratio $\frac{Q_{\text{exp}}}{Q_{\text{th}}}$ is between 3 % and 9 % indicating that only surface atoms are catalytically active.

The surface area was determined from N_2 -sorption isotherms (BET surface area) and calculated *via* measurements of the electrochemical capacitance of the interface between the film and the electrolyte. In this method the electrodes were cycled potentiostatically in a potential range where no oxidation or reduction processes take place, typically between 0.17 and 0.23 V vs. Ag/AgCl/KCl (sat.) at scan rates ranging from 1 to 20 mV s^{-1} . The measured capacitance was obtained by plotting the capacitance current at 0.2 V against the scan rate (Figure S4.12 in the supporting information).

The stability of the Fe-doped NiO electrodes was tested using the 10 % doped sample. The electrode potential was measured at a constant current density of 10 mA cm^{-2} for 10 h and at 200 mA cm^{-2} for 3 h vs. Hg/HgO/1 M KOH in 0.5 M KOH.

4.6 REFERENCES

1. Cook, T. R.; Dogutan, D. K.; Reece, S. Y.; Surendranath, Y.; Teets, T. S.; Nocera, D. G. *Chem. Rev.* **2010**, *110*, 6474.
2. Walter, M. G.; Warren, E. L.; McKone, J. R.; Boettcher, S. W.; Mi, Q.; Santori, E. A.; Lewis, N. S. *Chem. Rev.* **2010**, *110*, 6446.

4.6 REFERENCES

3. Nørskov, J. K.; Bligaard, T.; Logadottir, A.; Kitchin, J. R.; Chen, J. G.; Pandelov, S.; Stimming, U. *J. Electrochem. Soc.* **2005**, *152*, J23.
4. Dau, H.; Limberg, C.; Reier, T.; Risch, M.; Roggan, S.; Strasser, P. *ChemCatChem* **2010**, *2*, 724.
5. Bockris, J. O. M. *J. Chem. Phys.* **1956**, *24*, 817.
6. Zhao, Z.; Wu, H.; He, H.; Xu, X.; Jin, Y. *Adv. Funct. Mater.* **2014**, *24*, 4698.
7. Yeo, B. S.; Bell, A. T. *J. Phys. Chem. C* **2012**, *116*, 8394.
8. Liu, X.; Wang, F. *Coord. Chem. Rev.* **2012**, *256*, 1115.
9. Dincă, M.; Surendranath, Y.; Nocera, D. G. *Proc. Natl. Acad. Sci. U. S. A.* **2010**, *107*, 10337.
10. Suntivich, J.; May, K. J.; Gasteiger, H. A.; Goodenough, J. B.; Shao-Horn, Y. A. *Science* **2011**, *334*, 1383.
11. Kim, T. W.; Choi, K. S. *Science* **2014**, *343*, 990.
12. Reier, T.; Oezaslan, M.; Strasser, P. *ACS Catal.* **2012**, *2*, 1765.
13. Trotochaud, L.; Boettcher, S. W. *Scr. Mater.* **2014**, *74*, 25.
14. Chen, Z.; Meyer, T. J. *Angew. Chem., Int. Ed.* **2013**, *52*, 700.
15. Grimaud, A.; Carlton, C. E.; Risch, M.; Hong, W. T.; May, K. J.; Shao-Horn, Y. J. *J. Phys. Chem. C* **2013**, *117*, 25926.
16. Trasatti, S. *J. Electroanal. Chem. Interfacial Electrochem.* **1980**, *111*, 125.
17. Matsumoto, Y.; Sato, E. *Mater. Chem. Phys.* **1986**, *14*, 397.
18. Man, I. C.; Su, H.-Y.; Calle-Vallejo, F.; Hansen, H. A.; Martínez, J. I.; Inoglu, N. G.; Kitchin, J.; Jaramillo, T. F.; Nørskov, J. K.; Rossmeisl, J. *ChemCatChem* **2011**, *3*, 1159.

19. Trotochaud, L.; Ranney, J. K.; Williams, K. N.; Boettcher, S. W. *J. Am. Chem. Soc.* **2012**, *134*, 17253.
 20. McCrory, C. C. L.; Jung, S.; Peters, J. C.; Jaramillo, T. F. *J. Am. Chem. Soc.* **2013**, *135*, 16977.
 21. Louie, M. W.; Bell, A. T. *J. Am. Chem. Soc.* **2013**, *135*, 12329.
 22. Corrigan, D. A. *J. Electrochem. Soc.* **1987**, *134*, 377.
 23. Corrigan, D. A. *J. Electrochem. Soc.* **1989**, *136*, 723.
 24. Hu, C.-C.; Wu, Y.-R.. *Mater. Chem. Phys.* **2003**, *82*, 588.
 25. Miller, E. L.; Rochelaeu, R. E. *J. Electrochem. Soc.* **1997**, *144*, 3072.
 26. Chen, Y.-W. D.; Noufi R. N. *J. Electrochem. Soc.* **1984**, *131*, 731.
 27. Gong, M.; Li, Y.; Wang, H.; Liang, Y.; Wu, J. Z.; Zhou, J.; Wang, J.; Regier, T.; Wei, F.; Dai, H. *J. Am. Chem. Soc.* **2013**, *135*, 8452.
 28. Trotochaud, L.; Young, S. L.; Ranney, J. K.; Boettcher, S. W. *J. Am. Chem. Soc.* **2014**, *136*, 6744.
 29. Li, X.; Walsh, F. C.; Pletcher, D. *Phys. Chem. Chem. Phys.* **2011**, *13*, 1162.
 30. Smith, R. D.; Prevot, M. S.; Fagan, R. D.; Trudel, S.; Berlinguette, C. P. *J. Am. Chem. Soc.* **2013**, *135*, 11580.
 31. Smith, R. D.; Prevot, M. S.; Fagan, R. D.; Zhang, Z.; Sedach, P. A.; Siu, M. K.; Trudel, S.; Berlinguette, C. P. *Science* **2013**, *340*, 60.
 32. Fominykh, K.; Feckl, J. M.; Sicklinger, J.; Döblinger, M.; Böcklein, S.; Ziegler, J.; Peter, L.; Rathousky, J.; Scheidt, E.-W.; Bein, T.; Fattakhova-Rohlfing, D.. *Adv. Funct. Mater.* **2014**, *24*, 3123.
 33. Szeifert, J. M.; Feckl, J. M.; Fattakhova-Rohlfing, D.; Liu, Y.; Kalousek, V.; Rathousky, J.; Bein, T. *J. Am. Chem. Soc.* **2010**, *132*, 12605.
-

4.6 REFERENCES

34. Liu, Y.; Szeifert, J. M.; Feckl, J. M.; Mandlmeier, B.; Rathousky, J.; Hayden, O.; Fattakhova-Rohlfing, D.; Bein, T. *ACS Nano* **2010**, *4*, 5373.
 35. Feckl, J. M.; Fominykh, K.; Doblinger, M.; Fattakhova-Rohlfing, D.; Bein, T. *Angew. Chem., Int. Ed.* **2012**, *51*, 7459.
 36. Biesinger, M. C.; Payne, B. P.; Grosvenor, A. P.; Lau, L. W. M.; Gerson, A. R.; Smart, R. S. C. *Appl. Surf. Sci.* **2011**, *257*, 2717.
 37. Hoffer, B.; Dickvanlangeveld, A.; Janssens, J.; Bonne, R.; Lok, C.; Moulijn, J. J. *Catal.* **2000**, *192*, 432.
 38. McIntyre, N. S.; Cook, M. G. *Anal. Chem.* **1975**, *47*, 2208.
 39. Landon, J.; Demeter, E.; İnoğlu, N.; Keturakis, C.; Wachs, I. E.; Vasić, R.; Frenkel, A. I.; Kitchin, J. R. *ACS Catal.* **2012**, *2*, 1793.
 40. Yamashita, T.; Hayes, P. Analysis of XPS Spectra of Fe²⁺ And Fe³⁺ Ions in Oxide Materials. *Appl. Surf. Sci.* **2008**, *254*, 2441.
 41. Douvalis, A. P.; Jankovic, L.; Bakas, T. *J. Phys.: Condens. Matter* **2007**, *19*, 436203.
 42. Horner, O.; Mouesca, J.-M.; Oddou, J.-L.; Jeandey, C.; Niviere, V.; Mattioli, T. A.; Mathe, C.; Fontecave, M.; Maldivi, P.; Bonville, P. *Biochemistry* **2004**, *43*, 8815.
 43. Kanowitz, S. M.; Palenik, G. J. *Inorg. Chem.* **1998**, *37*, 2086.
 44. Raghavan, V. *J. Phase Equilib. Diffus.* **2010**, *31*, 369.
 45. Wulf, G. L.; Carter, T. J.; Wallwork, G. R. *Corros. Sci.* **1969**, *9*, 689.
 46. Sauerbrey, G. *Z. Phys A: Hadrons Nucl.* **1959**, *155*, 206.
 47. Trasatti, S.; Petrii, O. A. *Pure Appl. Chem.* **1991**, *63*, 711.
 48. Strecker, A.; Salzberger, U.; Mayer, J. *Prakt. Metallogr.* **1993**, *30*, 482.
 49. Doniach, S.; Sunjic, M. *J. Phys. C: Solid State Phys.* **1970**, *3*, 285.
 50. Wiechen, M.; Zaharieva, I.; Dau, H.; Kurz, P. *Chem. Sci.* **2012**, *3*, 2330.
-

4.7 SUPPORTING INFORMATION

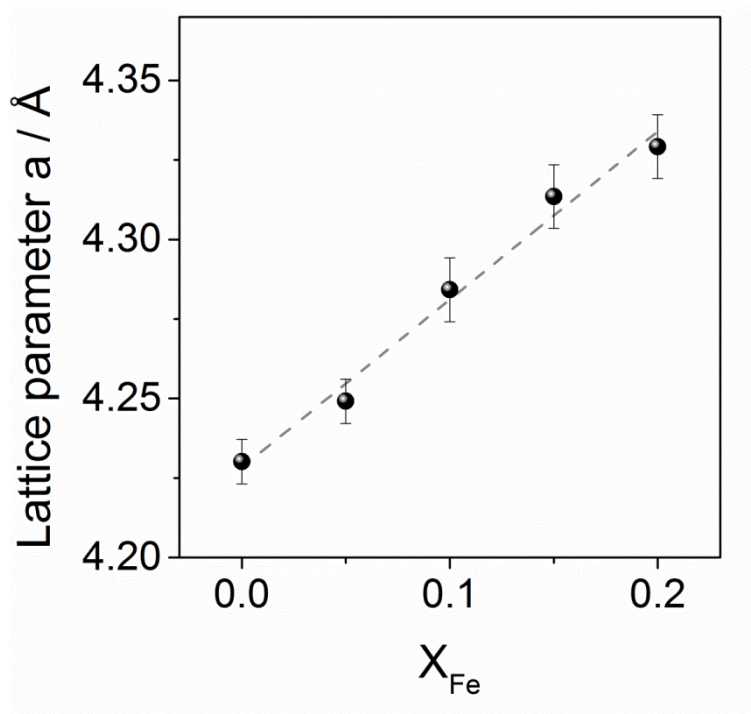


Figure S4.1 Demonstration of the lattice parameters of the $\text{Fe}_x\text{Ni}_{1-x}\text{O}$ nanoparticles following Vegard's law.

The lattice parameters of the $\text{Fe}_x\text{Ni}_{1-x}\text{O}$ particles with different Fe content follow Vegard's law (Figure S4.1). The undoped NiO nanoparticles obtained by our approach show a slightly larger lattice parameter of 4.22 Å than the bulk NiO (4.17 Å). This effect was already described in the literature for nanosized nickel oxide.¹

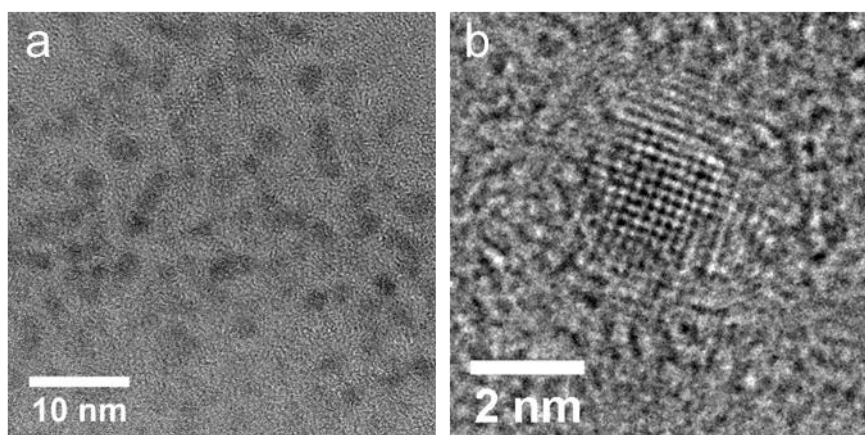


Figure S4.2 TEM images of the $\text{Fe}_{0.2}\text{Ni}_{0.8}\text{O}$ nanoparticles NP-20%. (a) Overview of the nanoparticles dispersed on the TEM grid. (b) HRTEM image of a single $\text{Fe}_{0.2}\text{Ni}_{0.8}\text{O}$ nanoparticle.

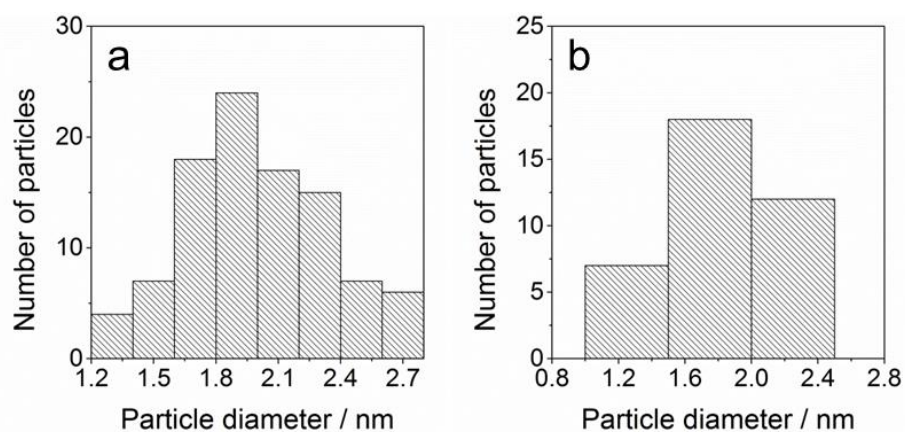


Figure S4.3 Particle size distribution determined from TEM images: (a) 2.0 ± 0.4 nm for NP-10%; (b) 1.8 ± 0.4 nm for NP-20%

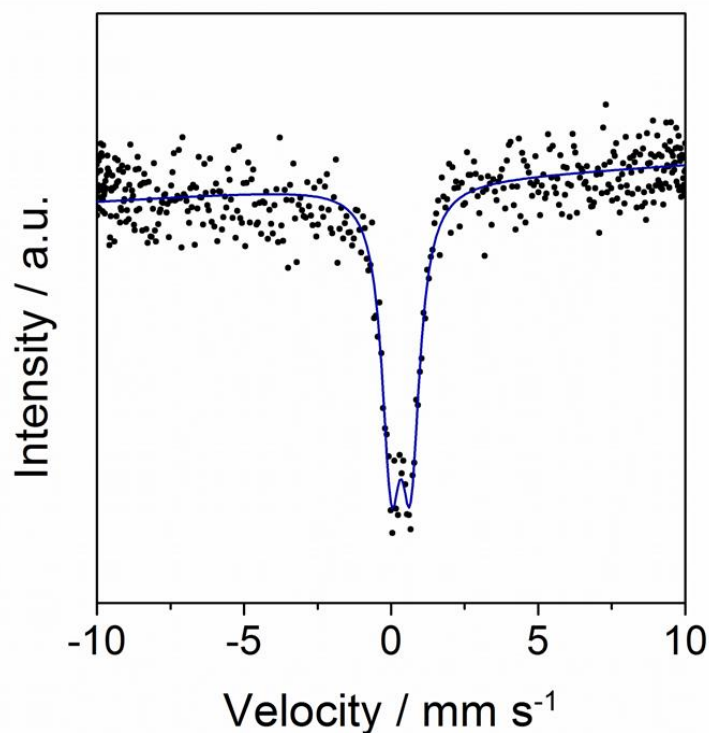


Figure S4.4 Mössbauer spectrum of as prepared NiO nanoparticles containing 20 % Fe.

Table S4.1 ^{57}Fe Mössbauer parameters of samples NP-10% and NP-20% (identification is performed according to Douvalis *et al.*²⁾)

Sample	Spectral line	$\delta / \text{mm s}^{-1}$	$\Delta / \text{mm s}^{-1}$	Identification
NP-10%	Q	0.37	0.49	Fe(III)
NP-20%	Q	0.33	0.66	Fe(III)

Δ = Isomer shift given relative to $\alpha\text{-Fe}$.

Δ = quadrupole splitting

Errors: $\delta = \pm 0.01 \text{ mm s}^{-1}$, $\Delta = \pm 0.01 \text{ mm s}^{-1}$

4.7 SUPPORTING INFORMATION

Table S4.2 XPS fitting parameters for the Fe 2p and Ni 2p peaks.

	Peak Nr	Lorentz FWHM / eV	Asymmetry	Gauss FWHM / eV	Height	Position / eV	Area	Area rel	Area sum
Fe 2p	0	0.3	0.05	4.979	3632.38	-711.21	2163.35	0.867	2494
	1	0.3	0.05	2.752	585.47	-723.89	330.65	0.133	2494
Ni 2p	0	0.3	0.05	3.586	33584.7	-855.18	19468.8	0.585	33293.6
	1	0.3	0.05	5.411	24429.5	-861.52	13824.8	0.415	33293.6

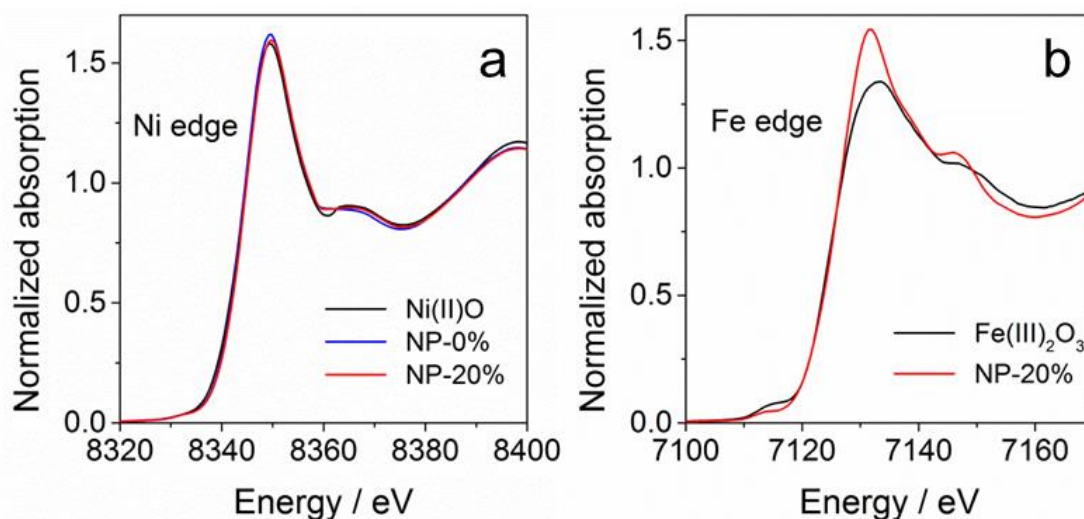


Figure S4.5 XANES spectra of the $\text{Fe}_x\text{Ni}_{1-x}\text{O}$ nanoparticles measured (a) at the Ni and (b) the Fe K-edges. Two reference crystalline oxides (Ni(II)O and $\text{Fe(III)}_2\text{O}_3$) are also shown. Based on the comparison of the edge positions, the oxidation state of Ni is +II and of Fe is +III.

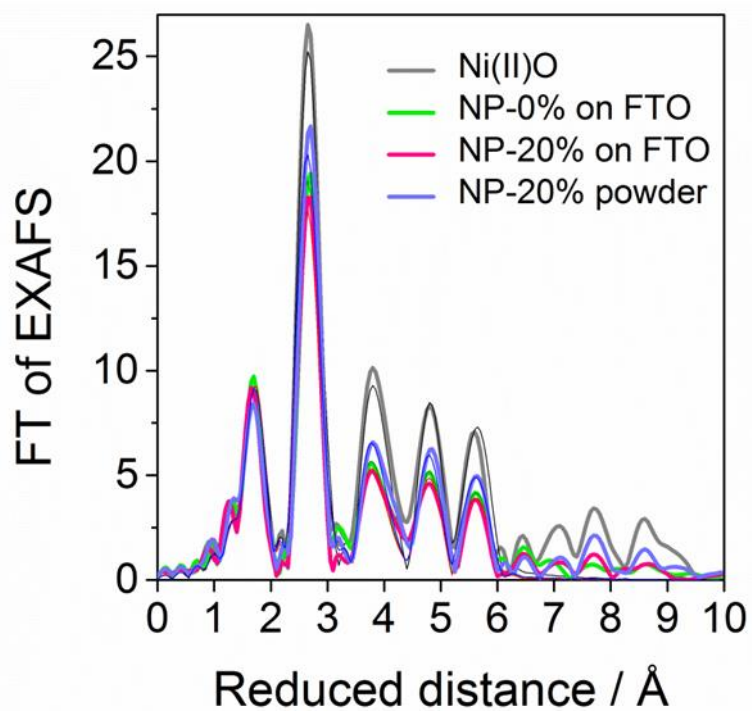


Figure S4.6 Fourier transformed EXAFS spectra measured at the Ni K-edge of the Ni(II)O reference, undoped and 20 % Fe(III)-doped NiO nanoparticles deposited on FTO, and 20 % Fe(III)-doped NiO nanoparticles in powder form. Experimental data are shown with thick lines and the simulations with thin lines.

4.7 SUPPORTING INFORMATION

Table S4.3 Simulation parameters for the curves presented in Figure S4.6. (Ni K-edge). The parameters marked with asterisks (*) were fixed during the simulation. All coordination numbers (N) and atom-atom distances (R) were fixed to the values predicted from the rock salt Ni(II)O crystal structure.³ The Debye-Waller factors (σ) for the Ni-O shells were fixed to typical values found for oxygen octahedrally coordinated to transition metal complexes. Errors representing 68 % confidence interval are shown in parenthesis. Amplitude-reduction factor of 0.8 was used. The slight increase of the Debye-Waller factor for the NP-20% after deposition on FTO as compared to the same material in powder form most likely reflects the smaller particle size of the material deposited on the FTO electrode.

	Shell	N	$R / \text{\AA}$	$\sigma / \text{\AA}$			
				Ni(II)O	NP-0% on FTO	NP-20% on FTO	NP-20% powder
1	Ni-O	6*	2.09*				
2	Ni-O	8*	3.63*	0.059*	0.059*	0.059*	0.059*
3	Ni-Ni	12*	2.96*	0.066 (0.002)	0.077 (0.002)	0.080 (0.002)	0.074 (0.002)
4	Ni-Ni	6*	4.19*				
5	Ni-Ni	24*	5.13*				
6	Ni-Ni	12*	5.92*	0.078 (0.003)	0.096 (0.004)	0.098 (0.004)	0.090 (0.004)
7	Multiple-scattering from shells 1 and 4	6*					
8	Multiple-scattering from shells 3 and 6	12*					

Table S4.4 Comparison of three Ni EXAFS simulations of the powder NP-20% sample: a) varying the Debye-Waller factors only (i.e. accounting only for disorder effects); b) varying the coordination numbers only (i.e. accounting for particle size effects only); c) varying coordination numbers and Debye-Waller factors. The parameters marked with asterisks (*) were fixed during the simulation. All atom-atom distances (R) and coordination numbers (N , when fixed) were fixed to the values predicted from the rock salt Ni(II)O crystal structure.³ The Debye-Waller factors (σ), when fixed, were taken from the fit for Ni(II)O (Table S4.3). Coordination numbers for the multiple-scattering shells were set equal to the coordination numbers of the longer of the corresponding single-scattering shells. Errors representing 68 % confidence interval are shown in parenthesis. Amplitude-reduction factor of 0.8 was used. Note that the most reasonable fit (lowest reduced chi-squared value) is achieved when considering disorder effects only; letting both N and σ free (fit c)) results in intermediate values for N and σ , which would suggest that the observed lowering of the amplitude of the long-range EXAFS peaks could be explained by both particle-size effects and increased disorder; however, we caution against over-interpretation of the data because of the large parameter errors in fit c) and because of the very large number of scattering atoms that affect the EXAFS and the prominent multiple-scattering effects that cannot be simulated sufficiently well.

Shell	$R / \text{\AA}$	a) Fit with constant N		b) Fit with constant σ		c) Free fit		
		N	$\sigma / \text{\AA}$	N	$\sigma / \text{\AA}$	N	$\sigma / \text{\AA}$	
1	Ni-O	2.09*	6*	0.09 (0.01)	4.6 (0.8)	0.059*	7 (2)	0.09 (0.01)
2	Ni-O	3.63*	8*		0 (3)		1 (5)	
3	Ni-Ni	2.96*	12*	0.074 (0.002)	9.6 (0.6)	0.066*	11 (2)	0.071 (0.006)
4	Ni-Ni	4.19*	6*		4.2 (0.7)		5 (2)	
5	Ni-Ni	5.13*	24*		17 (3)		19 (6)	
6	Ni-Ni	5.92*	12*	0.091 (0.004)	7 (2)	0.078*	8 (3)	0.08 (0.01)
7	Multiple-scattering from shells 1 and 4		6*		4.2		5	
8	Multiple-scattering from shells 3 and 6		12*		7		8	
Reduced χ^2				1.49		1.61		1.64

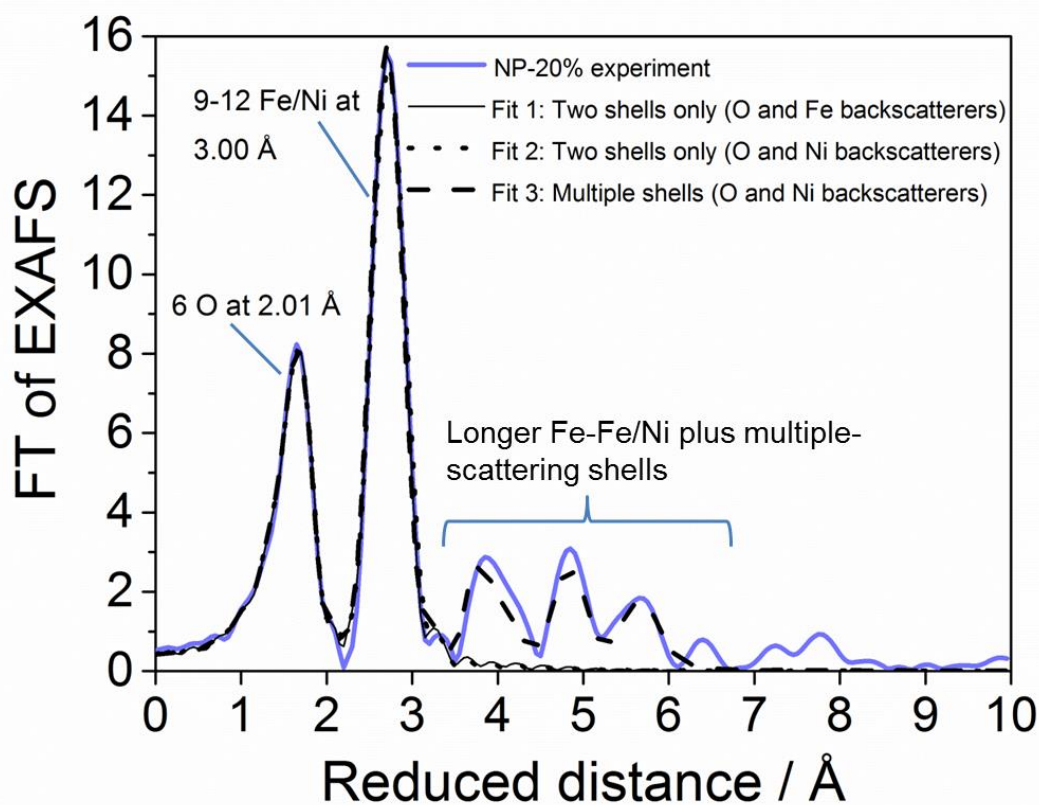


Figure S4.7 Fourier transformed EXAFS spectra of 20 % Fe(III)-doped NiO nanoparticles measured at the Fe K-edge (experiment and simulations). In addition to the multiple shell simulation (Fit 3, dashed line) where only O and Ni backscatterers are considered, simulation of only the first two peaks with O and Fe backscatterers (Fit 1, solid line) and O and Ni backscatterers (Fit 2, dashed line) are shown. Simulation parameters are given in Table S4.5.

Table S4.5 Simulation parameters for the curves presented in Figure S4.7 (Fe K-edge). The parameters marked with asterisks (*) were fixed during the simulation. Coordination numbers (N) and atom-atom distances (R) were fixed to the values predicted from the rock salt Ni(II)O crystal structure. Errors representing 68 % confidence interval are shown in parenthesis. Amplitude-reduction factor of 0.9 was used.

Shell	Fit using Fe-Fe			Fit using Fe-Ni			Fit assuming Fe inside the NiO lattice			
	N	$R/\text{\AA}$	$\sigma/\text{\AA}$	N	$R/\text{\AA}$	$\sigma/\text{\AA}$	N	$R/\text{\AA}$	$\sigma/\text{\AA}$	
1	Fe-O	6*	2.02 (0.02)	0.082 (0.010)	6*	2.01 (0.02)	0.082 (0.010)	6*	2.01 (0.01)	0.082 (0.010)
2	Fe-O	–	–	–	–	–	–	8*	3.63*	
3	Fe-Ni	–	–	–	12 (2)	3.00 (0.01)	0.088 (0.007)	12*	3.00 (0.01)	0.087 (0.003)
4	Fe-Fe	10 (2)	3.01 (0.01)	0.080 (0.007)	–	–	–	–	–	–
5	Fe-Ni	–	–	–	–	–	–	6*	4.19*	
6	Fe-Ni	–	–	–	–	–	–	24*	5.13*	
7	Fe-Ni	–	–	–	–	–	–	12*	5.92*	0.12 (0.01)
8	Multiple-scattering from shells 1 and 5	–	–	–	–	–	–	6*	–	
9	Multiple-scattering from shells 3 and 7	–	–	–	–	–	–	12*	–	

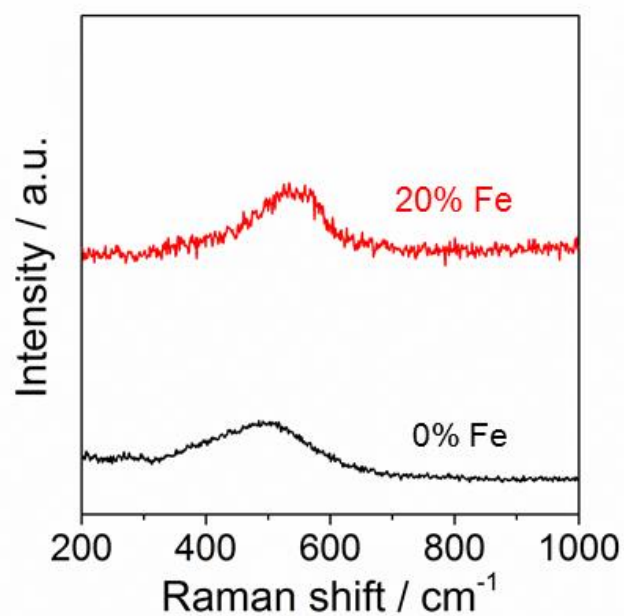


Figure S4.8 Raman spectra of the NP-0% and NP-20% powders. The broad band at around 500 cm⁻¹ corresponds to NiO and is slightly shifted to higher wavenumbers with increasing Fe content.

STABILITY TESTS

Figure S4.9 shows the results of stability measurements on the NP-10% electrodes. The change in the overpotential was measured for 10 h galvanostatically at a constant current density of 10 mA cm^{-2} . We attribute the increase in the overpotential after 10 h from 0.27 to 0.30 V to accumulation of bubbles on the electrode surface (Figure S4.9a, blue line). The small decrease in the overpotential after around 6 h is due to a spontaneous detachment of several accumulated bubbles from the electrode. This effect becomes visible in a comparison with a measurement at the same conditions where the working electrode was periodically lifted from the electrolyte for 1 s and placed back in order to remove the bubbles (Figure S4.9a, grey line). In this case the overpotential remains constant at around 0.27 V, in contrast to the stability curve measured without bubble removal which shows an increasing overpotential. The removal of the working electrode from the electrolyte leads to large potential jumps followed by a drop in the overpotential (after placing the electrode back into the electrolyte) which subsequently saturates at around 0.27 V. Figure S4.9c shows CV curves measured before and after the stability test showing no visible changes in the electrochemical performance. The $\text{Fe}_x\text{Ni}_{1-x}\text{O}$ electrode oxidation and reduction peaks shift to higher potentials after galvanostatic conditioning corresponding to the structural transformation of the surface Ni atoms, presumably because of conversion of $\alpha\text{-Ni(OH)}_2$ to $\beta\text{-Ni(OH)}_2$ on the surface as was reported in the literature.^{4, 5} At the same time the charge (which corresponds to the theoretical charge calculated from the surface density of Ni-atoms and the fraction of Ni atoms on the surface) and therefore the amount of the OER active sites do not increase. This supports the assumption that the structural transformations affect only atoms located on the surface while the structural integrity of the bulk of the nanoparticles remains preserved. This is also confirmed by the Raman spectroscopy measurements, which demonstrate the structural stability of the $\text{Fe}_x\text{Ni}_{1-x}\text{O}$ phase after the prolonged electrolysis (Figure S4.9d). Additionally, the stability of NP-10% was measured using the same setup at a constant current density of 200 mA cm^{-2} for 3 h. In this case the bubbles produced on the electrode detach quickly and do not accumulate on the surface which would result in an increasing overpotential. Figure S4.9b demonstrates that the electrode overpotential remains stable at comparatively low overpotentials during the galvanostatic conditioning even at higher current densities.

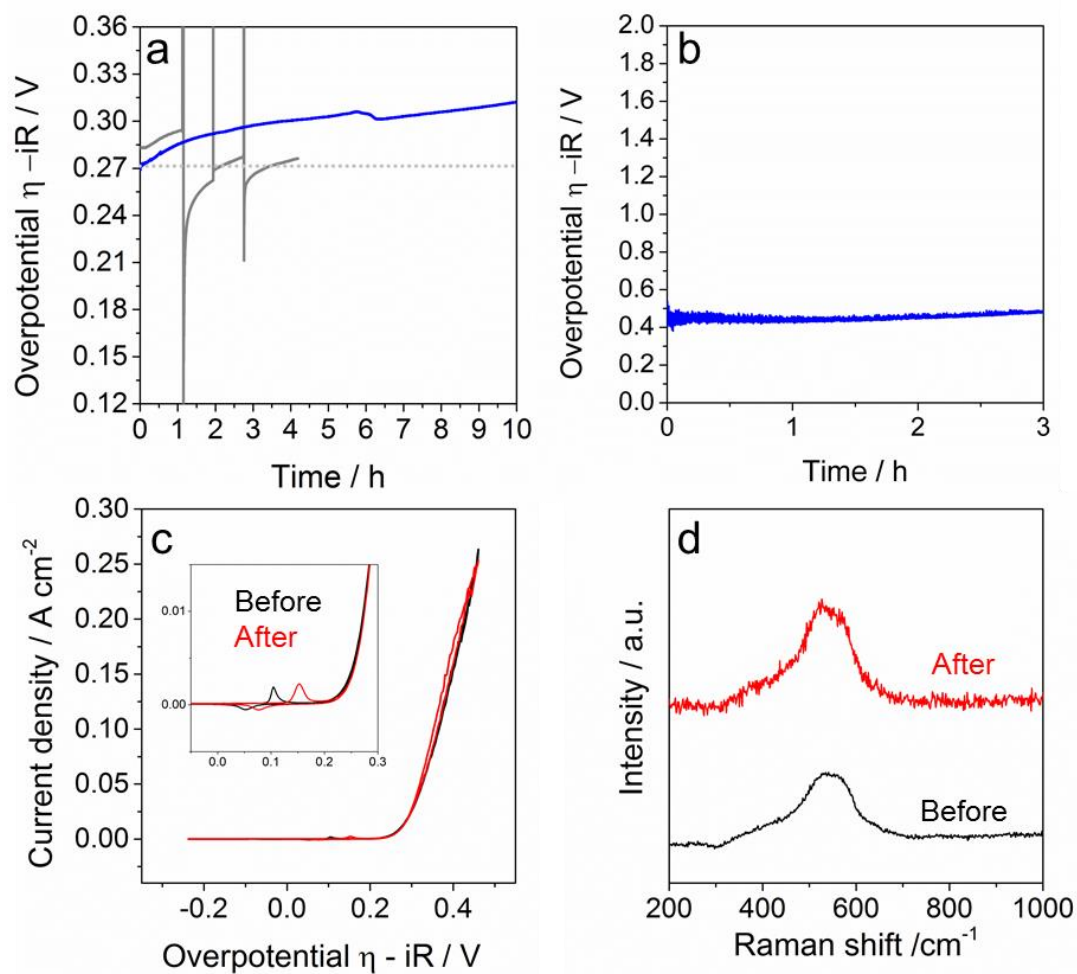


Figure S4.9 Stability of the Fe_{0.1}Ni_{0.9}O coated Au electrodes measured in 0.5 M KOH vs. Hg/HgO/1M KOH: (a) electrode potential measured for 10 h at a constant current density of 10 mA cm⁻² without removal of accumulated bubbles (blue line) and for 4.2 h with removal of accumulated bubbles (grey line), (b) electrode potential measured at a constant current density of 200 mA cm⁻² for 3 h without removal of accumulated bubbles (c) Cyclic voltammograms measured before (black) and after (red) the stability test with a scan rate of 20 mV s⁻¹, (d) Raman spectra measured on NP-10% coated Au/QCM crystals before (black) and after (red) CV measurements.

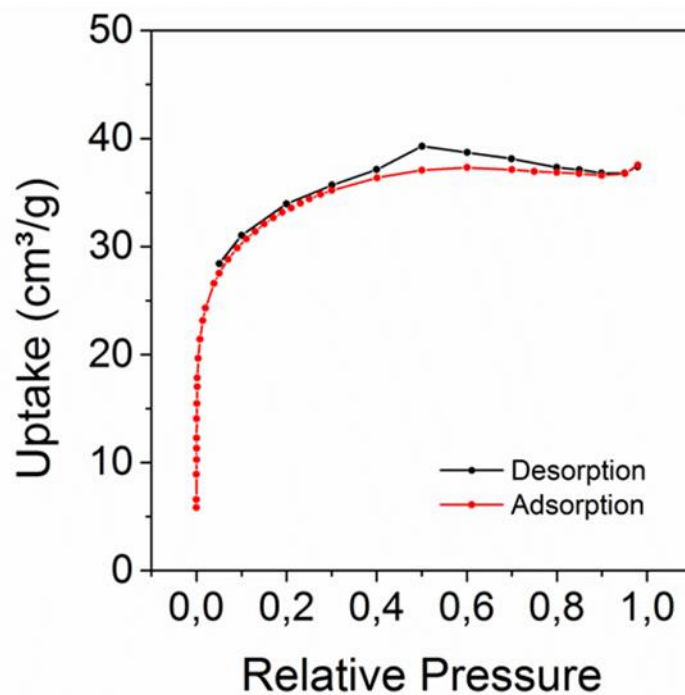


Figure S4.10 Nitrogen sorption isotherm of the nanoparticles NP-10% heated to 240 °C to remove organic residues.

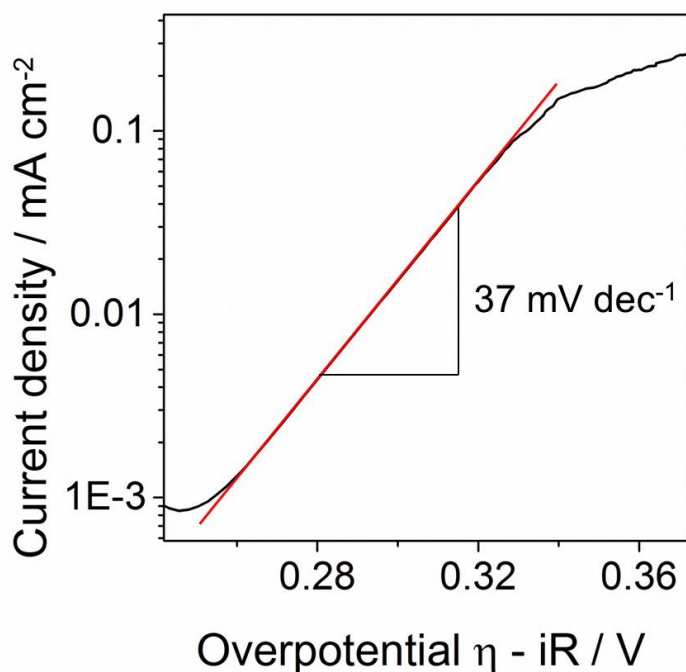


Figure S4.11 Tafel slope corresponding to the cyclic voltammogram taken at a scan rate of 20 mV s⁻¹ for NP-10% on Au/QCM electrode in 0.5 M KOH vs. Ag/AgCl.

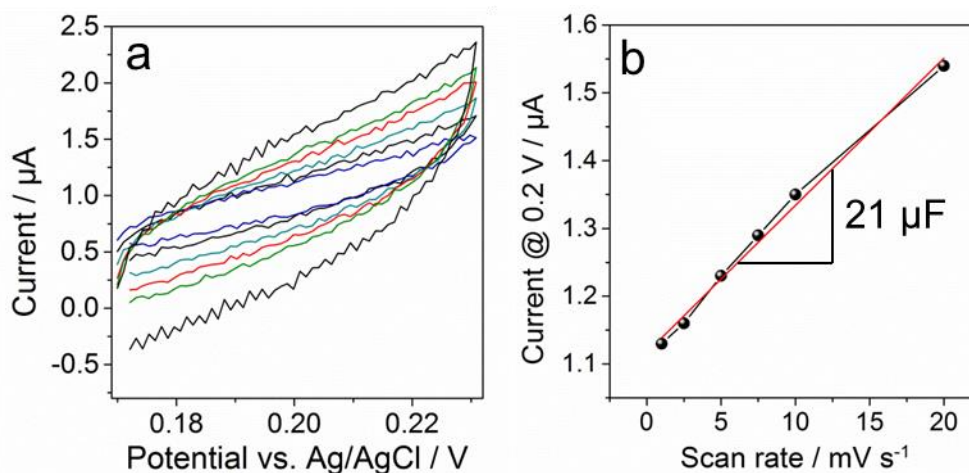


Figure S4.12 Electrochemical capacitance measured in 0.5 M KOH vs. Ag/AgCl using the electrode prepared with NP-10%. (a) Typical voltammograms obtained during the measurements; (b) capacitive current at 0.2 V vs. Ag/AgCl, the determined slope is $21 \mu\text{F}$.

4.7.1 REFERENCES

1. Jahromi, S.P.; Pandikumar, A.; Goh, B. T.; Lim, Y. S.; Basirun, W. J.; Lim, H. N.; Huang, N. M. *RSC Adv.* **2015**, *5*, 14010.
2. Douvalis, A. P.; Jankovic, L.; Bakas, T. *J. Phys.: Condens. Matter* **2007**, *19*, 436203.
3. Cairns, R. W.; Ott, E. *J. Am. Chem. Soc.* **1933**, *55*, 527.
4. Trotochaud, L.; Ranney, J. K.; Williams, K. N.; Boettcher, S. W. *J. Am. Chem. Soc.* **2012**, *134*, 17253.
5. Wehrens-Dijksma, M.; Notten, P. H. L. *Electrochim. Acta* **2006**, *51*, 3609.

5 ROCK SALT Ni/Co OXIDES WITH UNUSUAL NANOSCALE- STABILIZED COMPOSITION AS WATER SPLITTING ELECTROCATALYSTS

Ksenia Fominykh, Gülen Ceren Tok, Patrick Zeller, Hamidreza Hajiyani, Thomas Miller, Markus Döblinger, Rossitza Pentcheva, Thomas Bein and Dina Fattakhova-Rohlfing.

5.1 ABSTRACT

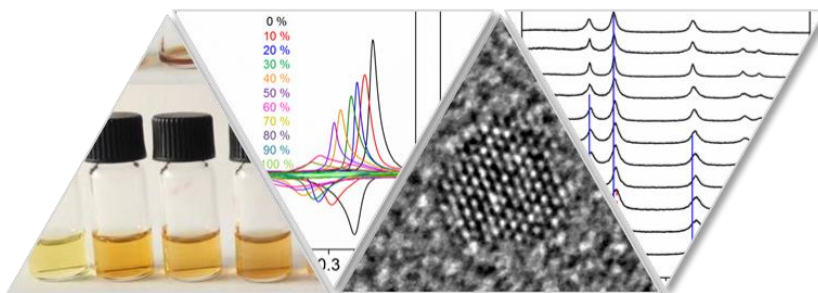


Figure 5.1 ToC image demonstrating the excellent dispersibility, crystallinity and ultrasmall size of the $\text{Ni}_x\text{Co}_{1-x}\text{O}$ nanoparticles combined with the extraordinary high miscibility of Ni and Co atoms in the whole composition range.

The influence of nanoscale on the formation of metastable phases is an important aspect of nanostructuring, which can lead to the discovery of unusual material compositions. We report the synthesis, structural characterization and electrochemical performance in the hydrogen evolution reaction (HER) and oxygen evolution reaction (OER) of Ni/Co mixed oxide nanocrystals and investigate the influence of nanoscaling on their composition and solubility range. Using a solvothermal synthesis in *tert*-butanol we obtained ultrasmall crystalline and highly dispersible $\text{Ni}_x\text{Co}_{1-x}\text{O}$ nanoparticles with rock salt type structure. The mixed oxides feature non-equilibrium phases with unusual miscibility in the whole composition range, which was attributed to a stabilizing effect of the nanoscale combined with kinetic control of particle formation. Substitutional incorporation of Co and Ni atoms into the rock salt lattice has a remarkable effect on the formal potentials of NiO oxidation that shift continuously to lower values with increasing Co content. This can be related to a monotonic reduction of the work function of (001) and (111)-oriented surfaces with increase in Co content, as obtained from DFT+*U* calculations. Furthermore, the electrocatalytic performance of the $\text{Ni}_x\text{Co}_{1-x}\text{O}$ nanoparticles in water splitting changes significantly. OER activity continuously increases with increasing Ni contents, while HER activity shows an opposite trend, increasing for higher Co contents. The high electrocatalytic activity and tunable performance of the non-equilibrium $\text{Ni}_x\text{Co}_{1-x}\text{O}$ nanoparticles in HER and OER demonstrate great potential in the design of electrocatalysts for overall water splitting.

5.2 INTRODUCTION

Development of high performance electrochemical energy conversion and storage technologies represents one of the most urgent goals of contemporary energy research. Nanostructuring is considered among the key strategies to maximize the performance of materials in various electrochemical applications comprising electrocatalysis, batteries and supercapacitors.¹⁻³ The advantages of nanostructuring are diminishing dimensions of the bulk, resulting in shortened charge transport pathways, as well as a greatly increased surface area beneficial for the interfacial charge transfer processes. Due to the great impact of size and morphology on the electrochemical performance, the efforts in development of nanostructured materials have been so far predominantly focused on control over their dimensions. Other aspects such as formation of non-equilibrium phases have attracted much less attention. However, observations of different groups point to the possibility of obtaining novel compositions that exist only on the nanoscale.⁴⁻⁶ Kanatzidis *et al.* have described a series of new rock salt phases in the Pb/Sb-Se family. Even more, these phases were found to be stable only as nanosized crystals.⁷ Buriak *et al.* have observed complete solubility of iron in rock salt NiO nanocrystals with formation of non-equilibrium Fe/Ni-O mixed compounds by reducing the domain sizes to a few nanometers.⁴ In contrast, only 6 at% solubility was reported for the corresponding bulk phase synthesized *via* a high temperature solid state reaction.⁸ Our group demonstrated unusually high solubility of metal ions in different ternary metal oxide nanoparticles with phase compositions that are not found in bulk materials.⁹⁻¹² In addition to size effects, the impact of chemical fabrication routes on the composition of nanomaterials is also of particular interest. Chemical reactions are often kinetically rather than thermodynamically controlled, enabling the formation of metastable and non-stoichiometric phases and tuning of defect chemistry in nanosized materials.¹³

The discovery of novel nanoscale-specific compositions has the potential to emerge as a new direction in materials research. Besides the academic interest, the composition control on the nanoscale can become an additional tool to tune the performance of materials in different energy-related fields.^{4,14} Electrocatalysis is one of the applications which is extremely sensitive to any changes in stoichiometry and phase composition of catalysts, and thus could benefit from the discovery of novel material libraries.^{3,9,15-23}

In the present study the influence of nanoscaling on the solubility range of nickel cobalt oxides is investigated. Ni/Co-O compounds have attracted great interest in many energy-related fields and find applications as anodes in lithium ion batteries, as supercapacitors or electrocatalysts for water splitting.^{18,23-32} $\text{Ni}_x\text{Co}_{1-x}\text{O}$ is known to be among the most active non-precious electrocatalysts for the overall water splitting in alkaline media comprising both oxygen evolution reaction (OER) and hydrogen evolution reaction (HER).^{3,18,23}

Various Ni/Co oxides with different structures and morphologies ranging from crystalline nanoparticles to amorphous films have been fabricated for water splitting and other energy conversion applications.^{16,21,24,27,29,33} NiO and CoO both show rock salt structure with only a minor lattice mismatch of 1.6 % due to almost identical crystal ionic radii of Co and Ni.^{28,33} This suggests that substitutional doping of the NiO lattice would be possible to relatively high Co contents without generating much lattice strain.³³ In spite of the structural similarity, the synthesis of rock salt type $\text{Ni}_x\text{Co}_{1-x}\text{O}$ solid solutions in the whole composition range has not yet been reported. The solubility of Co in the NiO lattice is often limited to a maximum concentration. At Co contents beyond 10 – 25 at%, the oxides tend to form either physical mixtures containing additional phases or another stable oxide, the Co_3O_4 spinel ($\text{Ni}_x\text{Co}_{3-x}\text{O}_4$ if doped with Ni).^{23,25,27-30,33-37} Several articles report the synthesis of rock salt type NiCoO_2 with 50 at% Co content, but not other possible compositions.^{24,38} Only one example of a completely miscible phase was described by Xiao *et al.* who reported the formation of crystalline rock salt $\text{Ni}_x\text{Co}_{1-x}\text{O}$ nanorods as a composite material on graphene oxide, whose influence could be in fact one of the reasons for the formation of unusual solid solution compositions.³⁹ The authors also pointed out that a synthesis of single phase NaCl type $\text{Ni}_x\text{Co}_{1-x}\text{O}$ using classical methods is nearly impossible. Various synthesis pathways for Ni/Co oxides were reported also by other groups using electrodeposition, thermal decomposition, sol-gel and solvothermal techniques.^{23-25,28,30,33} The composition of the obtained materials differed strongly depending on the synthesis strategy, but in general thermodynamically controlled synthesis methods were found to result in more stable phases or phase mixtures above a critical concentration.

We introduce for the first time a pathway for the fabrication of crystalline non-agglomerated $\text{Ni}_x\text{Co}_{1-x}\text{O}$ nanoparticles of 2 – 4 nm in size with rock salt type structure and Ni/Co miscibility in the whole composition range. The nanoparticles are formed in a non-aqueous reaction in *tert*-butanol established by our group.^{9-11,40-42} The moderate reactivity of the

solvent, typical for non-aqueous reaction routes, leads to a slow reaction with the metal precursors resulting in a controlled formation of ultras-small oxide nanocrystals.¹³ The kinetic control enables the formation of thermodynamically less stable phases with increased solubility of the elements in mixed oxides.^{9,10,40-42} The water splitting performance of the Ni_xCo_{1-x}O nanoparticles was tested in basic media revealing an overall trend of higher OER electrocatalytic activity for high Ni contents and higher HER activity for high Co contents. The best OER performance was shown by pure NiO with a current density of 10 mA cm⁻² at the overpotential of 350 mV. The HER activity of CoO reached 2.14 mA cm⁻² at 100 mV overpotential. The measured electrocatalytic activities for all Ni/Co compositions were found to be similar to the best values reported in the literature.^{16-18,21,23,43}

5.3 RESULTS AND DISCUSSION

Crystalline Ni_xCo_{1-x}O nanoparticles in the present study were obtained *via* a solvothermal reaction in *tert*-butanol (*t*BuOH).^{9-11,40-42} The formation of metal oxides using this reaction pathway is mostly kinetically controlled. Similar reactivity of the different precursors with *t*BuOH is therefore an important condition to obtain phase-pure materials. The combination of nickel(II) acetylacetonate (Ni(acac)₂) and Co(II) acetylacetonate (Co(acac)₂) in different ratios was found to be most suitable for the formation of phase-pure Ni_xCo_{1-x}O mixed oxides.

In the following the particles containing different Co amounts will be denoted as NP-X with X being the total molar fraction of Co in the sample in at% (e.g. NP-10 for the composition Ni_{0.9}Co_{0.1}O).

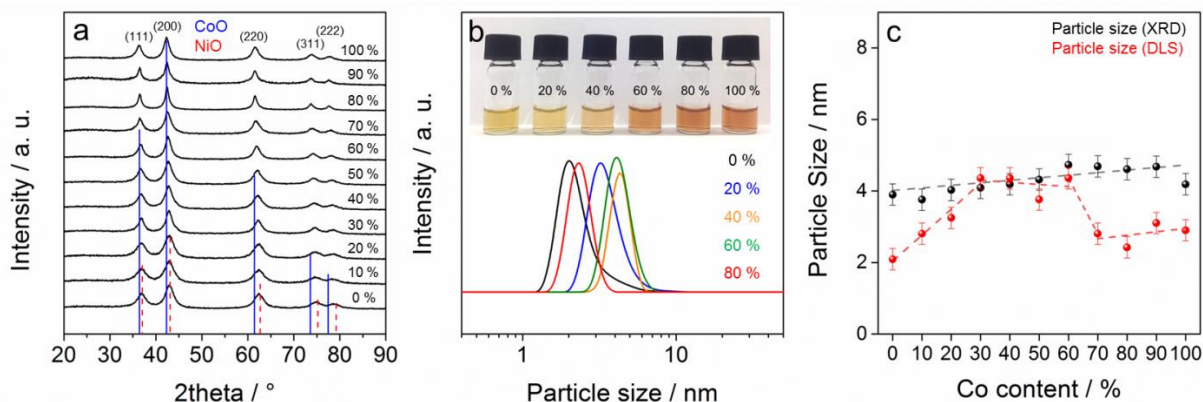


Figure 5.2 Crystallite size and dispersibility of the $\text{Ni}_x\text{Co}_{1-x}\text{O}$ nanoparticles. (a) Powder XRD patterns of the dried nanocrystals NP-0 – NP-100 (sample codes indicating 0 – 100 at% Co content), CoO pattern ICDD card number 00-043-1004 (solid line), NiO pattern ICDD card number 00-047-1049 (dashed line). (b) DLS analysis of ethanolic $\text{Ni}_x\text{Co}_{1-x}\text{O}$ nanoparticle dispersions with different Co content. Inset: Image of $\text{Ni}_x\text{Co}_{1-x}\text{O}$ nanoparticle dispersions (concentration: 2 mg mL^{-1}) in EtOH. The numbers indicate the Co content in at%. (c) Crystalline domain size of nanoparticles with increasing Co content calculated from the XRD patterns for the most intensive (200) signal using the Scherrer equation (black) and obtained from DLS measurements (red).

X-ray diffraction (XRD) patterns of as-prepared nanoparticles show cubic rock salt structure without the presence of any additional amorphous or crystalline phases throughout the whole range from 0 – 100 at% Co content (Figure 5.2a). Both binary oxides NiO and CoO crystallize in the rock salt structure and show almost identical XRD patterns. The lattice parameter of CoO is slightly larger with 4.261 \AA compared to that of NiO (4.195 \AA) showing a small shift to lower 2θ angles. Accordingly, the reflections of the mixed oxides $\text{Ni}_x\text{Co}_{1-x}\text{O}$ are expected to appear between the corresponding signals of the single oxides. The XRD patterns in Figure 5.2a clearly show a shift to lower angles with increasing Co content indicating substitutional incorporation of Co into the NiO structure (or vice versa for higher Co amounts) and following Vegard's law (Figure S5.1 in the supporting information). Also the peak shapes suggest substitutional incorporation of the elements. The presence of two separate NiO and CoO phases usually results in clearly visible shoulders in the reflections.^{35,37} Additionally, the broad signals indicate very small crystallite sizes which were calculated for the different Co contents using the Scherrer equation from the most intensive (200) peak at approximately $42^\circ 2\theta$. The particles are perfectly dispersible in ethanol (EtOH) upon addition of small amounts of acetic acid (HOAc) (the dispersion process is illustrated in Figure S5.2 in

the supporting information). The size of dispersed nanoparticles measured by dynamic light scattering (DLS, red dots) together with that estimated from the XRD patterns (black dots) is shown in Figure 5.2c. Both methods reveal nanocrystals of around 4 nm in the range between 30 at% and 60 at% Co content. DLS-based particle sizes below and above that range are even smaller with around 2 nm, while XRD-calculated sizes remain relatively constant. It should be noted however that DLS is very sensitive to the number of particles which may be increased for smaller size at very high and very low Co concentrations. Examples of DLS curves for NP-0 – NP-80 revealing the ultrasmall dimensions and a narrow size distribution are presented in Figure 5.2b.

The Co precursor was found to be slightly more reactive at the same reaction conditions than the nickel compound leading to larger particles of up to 19 nm for powders with high cobalt concentrations. We attribute this effect to the better solubility of $\text{Co}(\text{acac})_2$ in *t*BuOH compared to $\text{Ni}(\text{acac})_2$, which only dissolves at 200 °C. The corresponding XRD patterns with calculated particle sizes are summarized in Figure S5.3 in the supporting information. To obtain smaller nanoparticles the reaction conditions had to be optimized, especially for particles with higher Co contents NP-70 – NP-100. By reducing the temperature from 200 °C down to 180 °C and the reaction time from 20 h to 12 h, it was possible to obtain about 4 nm small particles for all Ni/Co ratios. It is remarkable that the $\text{Co}(\text{acac})_2$ obviously has an influence on the solubility of $\text{Ni}(\text{acac})_2$. Even at 180 °C the signals of the unreacted Ni precursor are missing in the XRD, which means that all of the Ni precursor was dissolved and could react together with $\text{Co}(\text{acac})_2$ to form nanocrystals.

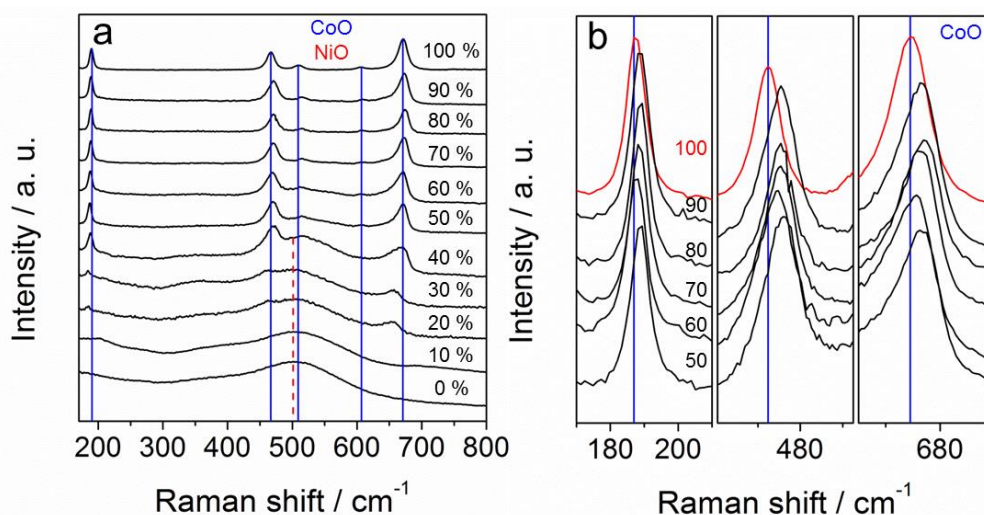


Figure 5.3 Raman spectra of the as-prepared $\text{Ni}_x\text{Co}_{1-x}\text{O}$ nanopowders. (a) Overview of the recorded spectra of NP-0 – NP-100. The lines indicate the location of NiO (dashed) and CoO (solid) bands. (b) Position of bands corresponding to CoO in the nanoparticles NP-50 – NP-100. The numbers indicate the Co content in at%.

Raman spectra of the $\text{Ni}_x\text{Co}_{1-x}\text{O}$ nanoparticles with different Ni/Co ratios are shown in Figure 5.3a. The broad band in the range between 450 cm^{-1} and 600 cm^{-1} with its maximum at around 500 cm^{-1} corresponds to the first order one-phonon mode of NiO.^{9,42,44,45} In the spectra of Co-containing nanoparticles additional peaks appear at 183 cm^{-1} , 462 cm^{-1} and 653 cm^{-1} , attributed to CoO T_{2g} , E_g and A_{1g} phonon modes, respectively.^{46,47} The spectra are dominated by NiO modes for low Co concentrations below 20 at% and CoO modes for higher Co contents beyond 50 at%, suggesting the formation of single phase mixed Ni/Co oxides. Between NP-20 and NP-40 both NiO and CoO phonon modes are present. The Raman spectra in this range do not provide unambiguous evidence for the formation of solid solutions because similar spectra could be expected also for a physical mixture of individual oxides. Nevertheless, the clearly visible shift of the CoO peaks in the spectra of the mixed $\text{Ni}_x\text{Co}_{1-x}\text{O}$ nanoparticles compared to pure CoO is a strong indication for the formation of mixed phases caused by expected changes in the structure (Figure 5.3b). For instance, the A_{1g} band shifts from 673 cm^{-1} to 668 cm^{-1} and the T_{2g} band shifts from 471 cm^{-1} to 465 cm^{-1} from NP-50 to NP-100, respectively.

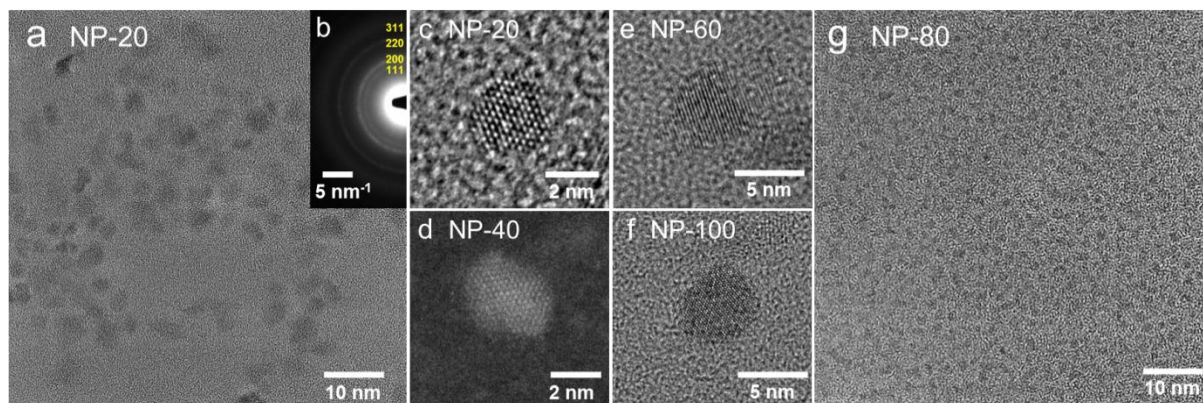


Figure 5.4 TEM images of the $\text{Ni}_x\text{Co}_{1-x}\text{O}$ nanoparticles. Overview of (a) NP-20 and (g) NP-80 crystals dispersed on the TEM grid. (b) ED pattern of several tens of NP-20 crystals. HRTEM images of single nanocrystals (c) NP-20 (e) NP-60 and (f) NP-100. (d) STEM image of a single NP-40 nanocrystal.

Transmission electron microscopy (TEM) images illustrate the crystalline structure and ultrasmall size of the $\text{Ni}_x\text{Co}_{1-x}\text{O}$ nanoparticles. Examples of high resolution transmission electron microscopy (HRTEM) and scanning transmission electron microscopy (STEM) images are shown in Figures 5.4 and S5.4 in the supporting information. The micrographs show well-dispersed crystals with a narrow particle size distribution and a predominantly spherical shape. Clearly visible lattice fringes and missing defects in HRTEM images illustrate the single crystalline character of the nanoparticles (Figures 5.4c – f). The electron diffraction (ED) pattern in Figure 5.4b was recorded for NP-20 at an area of around 150 nm in diameter and shows several rings that originate from averaging over several tens of particles, and can be indexed using the NiO rock salt structure. The corresponding d-values are 2.44 Å (111), 2.11 Å (200), 1.48 Å (220) and 1.27 Å (311) which is in close agreement with literature values and XRD results.⁴⁸

The average particle size determined from the TEM images (over several tens of particles) is in the range between 1.8 nm and 4.5 nm for all Ni/Co ratios. This correlates well with the sizes calculated from XRD patterns and measured by DLS. It should be noted that an increased number of ultrasmall 1 – 2 nm particles was observed in TEM for some samples, especially those with high Co contents (Figure 5.4g). This is in good agreement with the DLS measurements. However, bigger particles of up to 4.5 nm in diameter such as in Figure 5.4f constitute a major part of the samples.

Quantification of the elements in the samples was performed using inductively coupled plasma-atomic absorption spectroscopy (ICP-AAS), energy-dispersive X-ray spectroscopy (EDX) and X-ray photoelectron spectroscopy (XPS). The obtained amounts of Co are listed in Table S5.1 in the supporting information. ICP-AAS measurements reveal that the Co concentration within the particles mainly corresponds to the Co amount applied in the reaction mixture for all tested Ni/Co ratios showing only minor deviations. EDX-based Co amounts recorded for NP-20, NP-40, NP-60 and NP-80 averaged over several tens of nanoparticles confirm the ICP values. This indicates that both precursors in the initial mixture have reacted completely and are incorporated into the oxide structure.

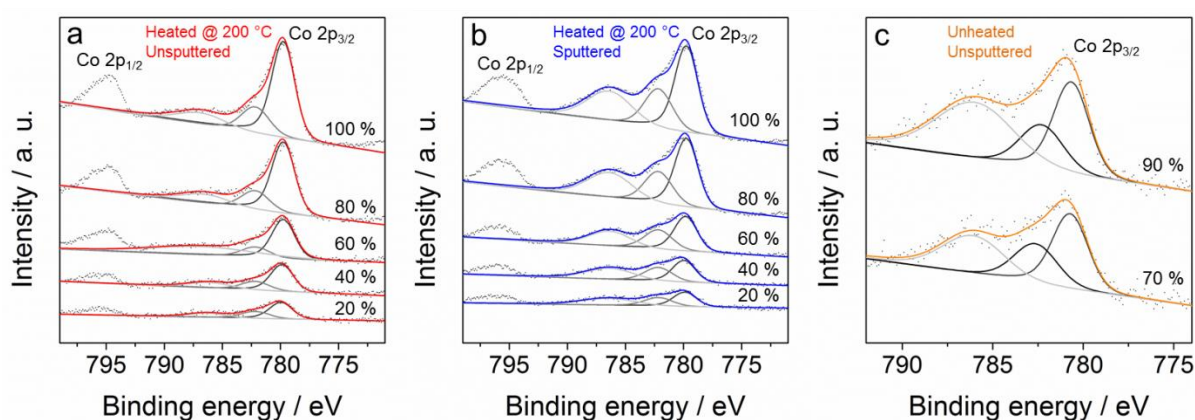


Figure 5.5 XPS spectra of the $\text{Ni}_x\text{Co}_{1-x}\text{O}$ nanoparticles, Co 2p peaks of nanoparticle layers (a) heated at 200 °C and (b) sputtered with Ar^+ ions. The spectra were taken using a Mg K_α source. The points correspond to the experimental data, and the lines are the fitted curves and the individual peak fits, respectively. The corresponding fitting parameters are listed in Table S5.2 in the supporting information. (c) Co 2p_{3/2} peaks of nanoparticle layers dried under high vacuum. The numbers indicate the Co content in at%.

XPS spectra show correlating Co contents for NP-20 and NP-80. The spectra in Figure 5.5 show typical Co 2p_{3/2} peaks for NP-20 – NP-100 with the main and satellite peaks at around 780 eV and 786 eV, respectively. For the particles with the intermediate Ni/Co ratios (NP-40 and NP-60) the Co content is around 10 at% lower than applied in the synthesis, pointing to the possible formation of surface defects or a depletion of Co content on the surface. Analysis of the oxidation states reveals that according to the peak shape characteristics the proportion of Co(III) is increasing with increasing Co content in the films (Figure 5.5a and Table S5.1 in the supporting information).⁴⁹ Presumably, the particles were partially oxidized on the surface

after heating in air at 200 °C to remove organic residues. Sputtering of the same samples with Ar^+ ions leads to peak shapes characteristic for Co(II) (Figure 5.5b and Table S5.1 in the supporting information) indicating that the cobalt remains in the oxidation state +II in the core of the films. Non-sputtered samples NP-70 and NP-90 dried under high vacuum (hv) at room temperature (RT) (Figure 5.5c) contain exclusively Co(II) confirming oxidation of Co due to heating in air and excluding reduction caused by the argon beam during sputtering.^{49,50} The Ni $2p_{3/2}$ doublet with the main peak binding energy of 853.8 ± 0.1 eV exactly matches the literature value for Ni(II) in NiO in all sputtered and hv-dried samples (Figure S5.5 and Table S5.1 in the supporting information).^{49,51-53} In conclusion, the combined ICP-AAS, EDX and XPS results indicate that the Ni/Co ratios initially applied in the syntheses remain preserved in the particles. The oxidation state +II was found for both Co and Ni in all as-prepared particle powders, indicating that no separate phase such as Co_3O_4 or CoOOH is formed. However, the surface Co atoms may be partially oxidized after heating in air.

To determine the influence of intermixing on the surface properties and work function, DFT calculations were performed on the bulk and surface of $\text{Ni}_x\text{Co}_{1-x}\text{O}$ ($x = 0.0, 0.5, 1.0$). In the bulk, the most stable $\text{Ni}_{0.5}\text{Co}_{0.5}\text{O}$ cation ordering was found to be the alternating Ni and Co layers along the [111] direction (see computational details). The cation ordering with alternating Ni and Co layers along the [001] direction was found to be around 28 meV f.u.⁻¹ less stable. In particular, the DFT lattice constant of $\text{Ni}_{0.5}\text{Co}_{0.5}\text{O}$ is the average of the end members, following Vegard's law. Adopting the most stable $\text{Ni}_{0.5}\text{Co}_{0.5}\text{O}$ bulk cation configuration, the (001) and (111) surfaces were built as illustrated in Figure S5.6 in the supporting information. The (001) surface contains a mixture of Ni, Co and O atoms, while the (111) surfaces are terminated by a Ni or a Co layer, respectively. Table 5.1 shows calculated lattice parameters and magnetic moments μ_B of the bulk NiO, CoO and the mixed $\text{Ni}_{0.5}\text{Co}_{0.5}\text{O}$ phase. The lattice constants are in very good agreement with the experimental data showing only minor deviations. The magnetic moments remain largely unchanged in the Ni/Co mixed phase as compared to the end members (see spin density of the (001) and (111) oriented surfaces in Figure S5.7 in the supporting information). Stronger reduction of the surface magnetic moments is observed at the (111)-oriented surfaces. Since the magnetic moment is directly related to the configuration of electrons in the d band and therefore to the oxidation state, it additionally indicates that the Ni and Co oxidation states of +II remain

preserved in $\text{Ni}_x\text{Co}_{1-x}\text{O}$ as already observed in XPS spectra of our Ar-sputtered samples (Table S5.1 in the supporting information).

Table 5.1 DFT+ U computed values of the lattice constants (experimental values are given in brackets) and magnetic moments of the cations in the bulk compounds.

	Lattice constants / Å	Magnetic moments μ_B	
		Ni(II)	Co(II)
NiO	4.191 (4.195)	1.58	–
$\text{Ni}_{0.5}\text{Co}_{0.5}\text{O}$	4.233 (4.23)	1.60	2.63
CoO	4.279 (4.261)	–	2.64

The electrocatalytic activity of the $\text{Ni}_x\text{Co}_{1-x}\text{O}$ nanoparticles for water splitting was tested in basic media. Due to the high dispersibility of the nanoparticles they can be deposited from solution on various substrates with the formation of homogeneous electrocatalytic layers (see SEM images of different layer morphologies in Figure S5.8 in the supporting information). For quantitative characterization and accurate determination of the mass loading, the electroactive layers were prepared on gold-coated QCM quartz crystals as described by us previously.^{9,42} The typical electrode mass loading was $20 \pm 2 \mu\text{g cm}^{-2}$. Cyclic voltammograms of the $\text{Ni}_x\text{Co}_{1-x}\text{O}$ electrodes with different Co contents show water oxidation currents at potentials beyond 0.5 V vs. Ag/AgCl corresponding to the oxygen evolution reaction (OER) and water reduction currents at potentials below -1.1 V vs. Ag/AgCl due to the hydrogen evolution reaction (HER) (Figure S5.9 in the supporting information). The couples of redox peaks between 0.250 V and 0.400 V vs. Ag/AgCl (Figure 5.6a) correspond to the reversible oxidative hydroxylation of NiO according to^{54,55}



Since Co oxide does not show prominent redox peaks in this range, it is not expected to significantly contribute to the redox process.^{16,56-59} Accordingly, the specific charge of this process (calculated as oxidation peak area per total mass loading) is proportional to the amount of electrochemically accessible Ni atoms. With increasing Co content the specific charge decreases continuously from 231 C g^{-1} for NP-0 to 68 C g^{-1} for NP-70 (Figure 5.6b). Beyond 70 at% Co content the peaks become practically indistinguishable. The relative ratio of peak areas for Co-containing nanoparticles compared to that of pure NiO closely matches

the proposed molar concentration of Ni in the particles, in good agreement with the elemental ratios obtained by other methods. More importantly, the peak potentials of this process shift continuously to lower values with increasing Co content (Figures 5.6a, b). Since the potential is an intensive property depending only on the energy of the system but not on the amount, the observation of the potential shift is a strong indication for the incorporation of Co into the NiO structure (or vice versa) and complete intermixing of the elements within the particles forming new phases. In case of physical mixtures the specific charges corresponding to individual oxides are expected to change according to their relative amounts, but the formal redox potential should remain constant if the phase composition does not change. This also applies to the particles NP-20 – NP-40, whose phase purity could not be unambiguously confirmed by Raman measurements, suggesting the formation of a single $\text{Ni}_x\text{Co}_{1-x}\text{O}$ phase also in this range. The experimentally observed continuous shift in redox potentials of mixed oxides (estimated as a work function) is also supported by DFT calculations. The theoretically calculated work function of the pure oxides and the substitutionally mixed $\text{Ni}_{0.5}\text{Co}_{0.5}\text{O}$ phase show nearly linear dependence on the Co concentration for the (111) surface (Figure 5.6c), in excellent agreement with the experimental data. For the (001) surface DFT calculations predict a monotonic but non-linear behavior. This can be attributed to the difference in surface termination and the respective cation-cation interactions. The (111) surfaces of $\text{Ni}_{0.5}\text{Co}_{0.5}\text{O}$ contain exclusively Ni or Co terminations (Figure S5.6 in the supporting information), while the (001) surface contains mixed Ni/Co layers resulting in homoionic and heteroionic interactions, respectively.

Besides the remarkable effect on the formal NiO oxidation potential, the substitutional incorporation of Co atoms into the rock salt NiO lattice (or vice versa) also significantly affects the electrocatalytic performance of $\text{Ni}_x\text{Co}_{1-x}\text{O}$ nanoparticles in water splitting, both in the OER and the HER process (Figures 5.7a, b).

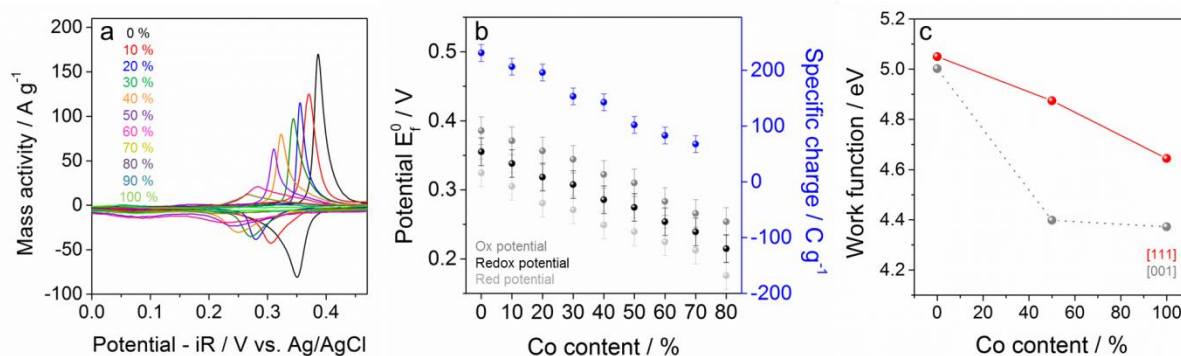


Figure 5.6 Redox potentials of $\text{Ni}_x\text{Co}_{1-x}\text{O}$ (NP-0 – NP-100). (a) Redox peaks in the potential range 0 – 47 mV obtained from cyclic voltammograms of nanoparticle electrodes in 0.5 M KOH vs. Ag/AgCl. The currents were normalized to the electrode mass loading (mass activity). The numbers indicate the Co content in at%. (b) Anodic peak (dark grey), cathodic peak (light grey) and formal (black) potentials of NP-0 – NP-80. Specific charge corresponding to the peak areas of the electrode oxidation peaks of NP-0 – NP-70 (blue). (c) DFT+ U computed variation of the work function of (111) (red) and (001) (grey) oriented surfaces of $\text{Ni}_x\text{Co}_{1-x}\text{O}$ as a function of the Co content.

The water oxidation behavior of $\text{Ni}_x\text{Co}_{1-x}\text{O}$ nanoparticles demonstrates a distinct trend of increasing OER activity with increasing Ni content. Figure 5.7c illustrates the current densities at the overpotentials $\eta = 300$ mV and 350 mV (red and light red dots).

The best OER performance is shown by pure nano-NiO with the current density $j = 1.2 \text{ mA cm}^{-2}$ at $\eta = 300$ mV and $j = 10 \text{ mA cm}^{-2}$ at $\eta = 350$ mV. The electrocatalytic activity reduces significantly and continuously with decreasing Ni content reaching 0.25 mA cm^{-2} at $\eta = 300$ mV and 1.1 mA cm^{-2} at $\eta = 350$ mV for pure CoO. Corresponding overpotentials are shown in Figure 5.7d (red and light red dots), demonstrating an increase from 299 mV to 348 mV at 1 mA cm^{-2} and from 350 mV to 426 mV at 10 mA cm^{-2} for NiO and CoO, respectively. The electrocatalytic performance of Ni/Co mixed oxides in OER was investigated by several groups. The majority of the publications, however, deal with compounds different from rock salt $\text{Ni}_x\text{Co}_{1-x}\text{O}$ and include carbon nanocomposites, spinel type $\text{Ni}_x\text{Co}_{3-x}\text{O}_4$ and amorphous materials.^{15-18,20,21,23,30,56-60}

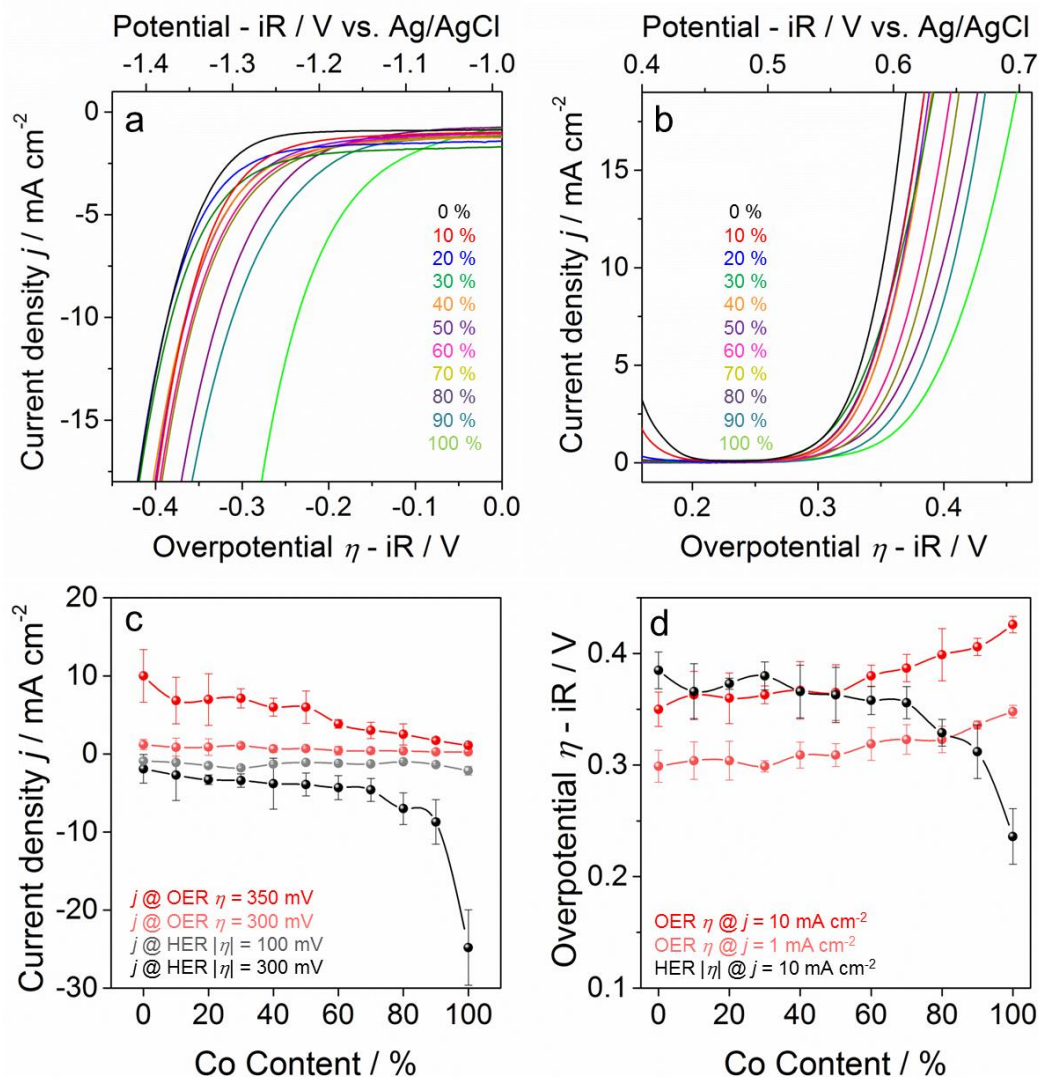


Figure 5.7 Cyclic voltammograms of electrode layers composed of $\text{Ni}_x\text{Co}_{1-x}\text{O}$ nanoparticles (NP-0 – NP-100) in 0.5 M KOH vs. Ag/AgCl. (a) Detailed overview of CV curves in the HER range. (b) Detailed overview of CV curves in the OER range. (c) Current densities at OER overpotentials of 300 mV (light red) and 350 mV (red) and HER overpotentials of 100 mV (grey) and 300 mV (black). (d) OER overpotentials at current densities of 1 mA cm^{-2} (light red) and 10 mA cm^{-2} (red) and HER overpotentials at 10 mA cm^{-2} (black).

The literature on the electrochemical activity of Ni/Co oxides with rock salt structure is scarce, although their promising electrocatalytic activity in the OER was suggested in the theoretical work of Bajdic *et al.*⁴³ They showed that substitutional doping of the CoO surface with 25 at% Ni decreases the OER overpotential from 480 mV to 360 mV, respectively. This was attributed to the dopant-induced increase in adsorption free energy of intermediate $^*\text{OOH}$ species, the formation of which was calculated to be the potential limiting step.

Trotochaud *et al.* reported fabrication of mixed Ni/Co oxides *via* electrodeposition, however in this way only 25 at% Co could be accommodated into the NiO rock salt structure without phase changes.²³ Beyond this concentration the $\text{Ni}_x\text{Co}_{3-x}\text{O}_4$ spinel phase was formed. The authors compared overpotentials η at 1 mA cm^{-2} which decreased continuously with growing Ni content from 381 mV for CoO_x to 300 mV for NiO_x . The current densities at $\eta = 300 \text{ mV}$ increased from CoO_x with 0.02 mA cm^{-2} to NiO_x with 1.01 mA cm^{-2} . McCrory *et al.* published a benchmarking overview for HER and OER electrocatalysts, which also included several Ni/Co mixed oxides, although their possible structure and phase composition were not reported.¹⁸ The OER overpotential at their CoO_x electrodes was 420 mV and was reduced to 380 mV upon doping with 50 at% Ni at $j = 10 \text{ mA cm}^{-2}$. Accordingly, the current density at 350 mV overpotential increased from 0.6 mA cm^{-2} to 2 mA cm^{-2} , respectively. Interestingly, the overpotential rose again to 470 mV for pure NiO_x . The different electrocatalytic behavior of undoped NiO_x in both studies may be attributed to different nanomorphologies, which have an influence on the properties of the resulting materials. To conclude, the observed OER activity of our mixed phase nanoparticles roughly correlates with literature values showing even higher performance in some cases.^{16-18,21,23,43}

Besides the remarkable influence on the OER activity, the substitution of Ni and Co atoms in the rock salt $\text{Ni}_x\text{Co}_{1-x}\text{O}$ structure also has a strong impact on the HER performance. The HER activity of the $\text{Ni}_x\text{Co}_{1-x}\text{O}$ nanocrystals illustrated in Figures 5.7c, d (grey and black dots) increases continuously with growing Co content. The overpotential at 10 mA cm^{-2} decreases from 385 mV for NP-0 to 236 mV for NP-100, and the current density at 100 mV HER overpotential increases accordingly reaching 2.14 mA cm^{-2} for pure CoO. It should be noted that the electrocatalytic performance of Ni/Co mixed oxides in the HER is much less investigated compared to the OER.²⁰ Corrigan *et al.* observed a slight decrease in the overpotential necessary to produce 16 mA cm^{-2} from 369 mV for undoped NiO_x to 364 mV for 11 at% Co content.⁶¹ McCrory *et al.* reported decreasing overpotentials at 10 mA cm^{-2} from 290 mV for NiO_x over 240 mV for 25 at% Co amount to 220 mV for CoO_x demonstrating enhanced HER activity with growing Co concentration, contrary to OER where Ni plays the decisive role.¹⁸ The parameters describing the electrocatalytic activity of the nanosized $\text{Ni}_x\text{Co}_{1-x}\text{O}$ particles in OER and HER are found to be in the same range as reported in the literature, partially showing even higher performance. For instance, the OER overpotentials at 1 mA cm^{-2} are up to $\sim 30 \text{ mV}$ lower than the values reported by Trotochaud

5.4 CONCLUSION

et al., especially for the mixed oxides and pure CoO_x . The overpotentials at 10 mA cm^{-2} are 15 – 120 mV lower than described by McCrory *et al.* for pure NiO_x and the mixed phases (10 % and 50 % Co content). The same group reported up to 0.6 mA cm^{-2} lower HER current densities at $\eta = 100 \text{ mV}$ for NiO_x and the Ni/Co oxide containing 25 % Co.

In general, the mixed metal $\text{Ni}_x\text{Co}_{1-x}\text{O}$ nanoparticles are not only consistent in their structure but they also demonstrate high electrocatalytic activity in both HER and OER, showing great potential for the design of electrocatalysts for overall water splitting.

5.4 CONCLUSION

We describe a solvothermal synthesis route for ultrasmall, crystalline and dispersible 2 – 4 nm $\text{Ni}_x\text{Co}_{1-x}\text{O}$ nanoparticles with rock salt type structure and in the whole range from 0 % to 100 % Co content. The exceptionally high solubility of Co and Ni in $\text{Ni}_x\text{Co}_{1-x}\text{O}$ may be attributed to the extremely small size of the nanoparticles showing the great influence of nanoscaling on the formation of new phases. Larger particles usually do not show this behavior, being able to incorporate only a few percent of the dopant without losing structural integrity.^{14,17,23,26,27,38}

The structure of the nanoparticles was analyzed by XRD, Raman, XPS and TEM measurements that indicate substitutional incorporation of the metal ions in the lattice. This finding is also supported by the shift of the electrode redox potential visible in cyclic voltammograms recorded in alkaline media. The DFT+*U* calculations indicate a monotonic dependence on Ni concentration of the work function for $\text{Ni}_x\text{Co}_{1-x}\text{O}$ surfaces with different crystallographic orientation, while an overall surface oxidation state of +II is maintained for the studied terminations. The electrocatalytic activity of the $\text{Ni}_x\text{Co}_{1-x}\text{O}$ nanoparticles in water splitting is similar to the best values reported in the literature. The particles show an overall trend of increasing OER electrocatalytic performance for increasing Ni concentration and higher HER activity with growing Co content. Summarizing, the ultrasmall $\text{Ni}_x\text{Co}_{1-x}\text{O}$ nanoparticles demonstrate unique structural properties with tunable electrocatalytic performance. Consisting of cheap and abundant elements the particles show great potential for applications as efficient overall water splitting electrocatalysts.

5.5 EXPERIMENTAL SECTION

5.5.1 SYNTHESIS OF $\text{Ni}_x\text{Co}_{1-x}\text{O}$ NANOPARTICLES

Nickel(II) acetylacetonate (95 % purity) , and cobalt(II) acetylacetonate (97 % purity) were purchased from Alfa Aesar and used as received. *tert*-Butanol was purchased from Sigma-Aldrich (puriss. p.a., ACS reagent, $\geq 99.7\%$), dried over a 4 Å molecular sieve at 28 °C and filtered prior to use.

For the solvothermal synthesis of $\text{Ni}_x\text{Co}_{1-x}\text{O}$ nanoparticles $\text{Ni}(\text{acac})_2$ was mixed with $\text{Co}(\text{acac})_2$ in the desired molar composition. The total amount of the metal precursors was kept at a constant value of 0.5 mmol. The Co doping concentration c_{Co} was calculated using the equation

$$c_{\text{Co}} = \frac{n_{\text{Co}}}{0.5 \text{ mmol}} \quad (5.2)$$

with n_{Co} being the molar amount of the Co precursor. As an example, for the synthesis of $\text{Ni}_{0.8}\text{Co}_{0.2}\text{O}$ nanocrystals 102.8 mg (0.4 mmol) of $\text{Ni}(\text{acac})_2$ was mixed with 25.7 mg (0.1 mmol) of $\text{Co}(\text{acac})_2$. The solid mixture was added to 14 mL *tert*-butanol under vigorous stirring in a glass autoclave liner forming a brownish suspension, then placed into a 22 mL custom made steel autoclave reactor and hermetically sealed. The reactions were carried out in the temperature range of 180 °C to 200 °C for 9 h – 20 h resulting in uniform brown dispersions of nanoparticles. The reaction conditions for all Ni/Co ratios are listed in Table 5.2.

Table 5.2 Synthesis conditions of the $\text{Ni}_x\text{Co}_{1-x}\text{O}$ nanoparticles.

Co content / %	Reaction temperature / °C	Reaction time / h
0 – 60	200	20
70	190	14
80	190	14
90	190	14
100	180	12

The as-prepared particles were dried in air by evaporating the solvent at 80 °C on a hot plate resulting in $\text{Ni}_x\text{Co}_{1-x}\text{O}$ nanopowders with particle sizes of around 4 nm.

Dispersions of the $\text{Ni}_x\text{Co}_{1-x}\text{O}$ nanoparticles were prepared in ethanol with the addition of acetic acid. In a typical dispersion procedure 1.1 mg of the dried powder was covered with 8 μL of acetic acid. After sonication for 5 min the particles were dispersed in 500 μL ethanol (absolute) and sonicated for another 5 min to obtain colloidal dispersions with a metal oxide concentration of 2 mg mL^{-1} .

5.5.2 CHARACTERIZATION

Wide angle X-ray diffraction analysis was performed in transmission mode using a STOE STADI P diffractometer with $\text{Cu K}_{\alpha 1}$ radiation ($\lambda = 1.54060 \text{ \AA}$) and a Ge(111) single crystal monochromator equipped with a DECTRIS solid state strip detector Mythen 1K. Powder XRD patterns of the samples were collected with an omega-2theta scan in the 2θ range from 5° to 70° with a step size of 1° and fixed counting time of 90 seconds per step and a resolution of 0.05° . Optimum quality measurements were performed on a STOE STADI P diffractometer with $\text{Mo K}_{\alpha 1}$ radiation ($\lambda = 0.709300 \text{ \AA}$) and a Ge(111) single crystal monochromator equipped with a DECTRIS solid state strip detector Mythen 1K. The size of the crystalline domains was calculated from the XRD patterns for the most intensive (200) reflection using the Scherrer equation.

TEM measurements were carried out using a Titan Themis 300 instrument equipped with a field emission gun operated at 300 kV. For the sample preparation a drop of a strongly diluted dispersion of a sample in ethanol was deposited on a holey carbon coated copper grid and evaporated. Contaminations were removed by plasma cleaning for 15 s at 50 mW and large-area illumination in the TEM for 40 min.

Dynamic light scattering measurements were performed on a MALVERN Zetasizer-Nano instrument equipped with a 4 mW He-Ne laser (633 nm) and an avalanche photodiode detector.

X-ray photoelectron spectroscopy (XPS) analysis of the particles was performed on a silicon substrate using a VSW HA 100 electron analyzer and the K_{α} radiation provided by a non-monochromatized Mg anode system ($\text{Mg K}_{\alpha} = 1253.6 \text{ eV}$). Ar-ion polishing was done at 1 keV for 5 min. The recorded elemental peaks were fitted using a Doniach-Sunjic function⁶³

with linear background subtraction and the elemental ratios were calculated using the equation

$$\frac{X_A}{X_B} = \frac{I_A/S_A}{I_B/S_B} \quad (5.3)$$

where $\frac{I_A}{I_B}$ is the ratio of fitted areas, and S is the sensitivity factor.

Raman spectroscopy was carried out using a LabRAM HR UV-Vis (HORIBA JOBIN YVON) Raman Microscope (OLYMPUS BX41) with a SYMPHONY CCD detection system and a He-Ne laser ($\lambda = 633$ nm). Spectra were recorded using a lens with a 50-fold magnification.

Quartz Crystal microbalance (QCM) measurements were performed on an in-house-designed QCM-setup, using KVG 10 MHz QCM devices with gold electrodes from Quartz Crystal Technology GmbH. The mass loading was calculated from the resonance frequencies of the QCM crystals before and after coating using the Sauerbrey equation

$$\Delta f = -C_f \Delta m \quad (5.4)$$

with Δf being the change in frequency, C_f the sensitivity factor of the QCM crystal and Δm the change in mass.⁶²

SEM images were obtained with a JEOL JSM-6500F scanning electron microscope equipped with a field emission gun operated at 5 kV. The films were prepared on Au substrates and glued onto a brass sample holder with silver lacquer.

Inductively coupled plasma-atomic absorption spectroscopy was carried out with a VARIAN VISTA RL CCD Simultaneous ICP-AAS.

5.5.3 ELECTRODE PREPARATION

The electrodes were prepared by spin coating of ethanolic $\text{Ni}_x\text{Co}_{1-x}\text{O}$ nanoparticle dispersions on gold coated QCM quartz crystals (KVG 10 MHz QCM devices with gold electrodes from Quartz Crystal Technology GmbH) forming thin films. For the spin coating method 8 μL of $\text{Ni}_x\text{Co}_{1-x}\text{O}$ dispersion with the concentration of 2 mg mL^{-1} was deposited on a masked QCM crystal exposing an area of 0.196 cm^2 and spun at 1000 rpm for 10 s. The QCM electrodes prepared in this way were subsequently heated to 240 $^\circ\text{C}$ in a laboratory oven with a heating ramp of 4 $^\circ\text{C min}^{-1}$ and a dwell time of 2 h.

5.5.4 ELECTROCHEMICAL MEASUREMENTS

Electrochemical measurements were performed in a three-electrode setup using an Autolab potentiostat/galvanostat PGSTAT302N with FRA32M module operating with Nova 1.10.4 software. All measurements were performed in 0.5 M KOH electrolyte solution (Sigma-Aldrich, volumetric solution) at pH 13.43. Pt mesh (2 cm^2) was used as a counter electrode. Au/QCM crystals coated with $\text{Ni}_x\text{Co}_{1-x}\text{O}$ nanoparticles were used as working electrodes. All potentials were measured vs. Ag/AgCl/KCl (sat.) reference electrode with a potential of +0.989 V vs. the reversible hydrogen electrode (RHE) at pH 13.43 (+0.197 V vs. NHE). The electrochemical data were corrected for uncompensated resistance R_s . R_s was determined as minimum total impedance in the frequency regime between 10 and 50 kHz at open circuit conditions and at a potential of 0.17 V vs. Ag/AgCl where no faradaic processes take place. 95 % of the measured resistance was compensated. R_s was typically around 10 – 12 Ohm for all $\text{Ni}_x\text{Co}_{1-x}\text{O}$ -coated Au/QCM electrodes. The OER overpotential η_{OER} was calculated using the equation

$$\eta_{\text{OER}} = E - E_{\text{OER}} - iR_s \quad (5.5)$$

where E is the potential recorded vs. Ag/AgCl reference electrode, E_{OER} is the reversible potential of the OER vs. Ag/AgCl reference electrode (0.240 V at pH 13.43), and i is the current.

The HER overpotential $|\eta_{\text{HER}}|$ was calculated using the equation

$$|\eta_{\text{HER}}| = -E - E_{\text{HER}} - iR_s \quad (5.6)$$

where E is the potential recorded vs. Ag/AgCl reference electrode, E_{HER} is the reversible potential of the OER vs. Ag/AgCl reference electrode (0.989 V at pH 13.43), and i is the current.

Current densities were calculated using the geometric surface area of the Au/QCM electrode (0.196 cm²). Mass activities are calculated using the respective mass loading on the Au/QCM electrode, usually 18 – 22 $\mu\text{g cm}^{-2}$.

The preconditioning of the Ni_xCo_{1-x}O electrodes was performed using cyclic voltammetry. The electrodes were cycled between -1.5 V and 0.7 V vs. Ag/AgCl in 0.5 M KOH at a scan rate of 20 mV s⁻¹ until the current had reached stable values and did not change anymore with repetitive cycling at scan rates of 20 mV s⁻¹ (typically 35 cycles, ca. 2 h).

1.1.1 COMPUTATIONAL DETAILS

Density functional theory (DFT) calculations were performed on CoO, NiO and Ni_{0.5}Co_{0.5}O surfaces with (001) and (111) orientation using the projector-augmented wave (PAW) pseudopotentials as implemented in VASP code.^{64,65} The generalized-gradient approximation (GGA) for the exchange-correlation functional was used with the effective Hubbard- U parameters. Different values between $U = 0$ and 8 eV have been used in the literature to model different structural, magnetic and electronic properties of transition metal oxides.⁶⁶⁻⁶⁹ We adopted the value of $U = 3.7$ for both Ni and Co in Ni_xCo_{1-x}O ($x = 0.0, 0.5$ and 1.0) to capture the structural and magnetic properties of the end members. The energy cutoff of 450 eV and a uniform $6 \times 6 \times 3$ k -points mesh was utilized to sample the Brillouin zone. Previous investigations demonstrate an AF-II antiferromagnetic ordering in Ni_xCo_{1-x}O where the adjacent ferromagnetic (111) planes are coupled antiferromagnetically along the [111]-direction.^{70,71} The total energies of different cation orderings were calculated for Ni_{0.5}Co_{0.5}O and the most stable configuration that was found to be the rock salt type ordering of cations was adopted to the system. The (001) surfaces were modeled by slabs containing 5 layers whereas the (111) slabs contained 5 cation and three oxygen layers. The atomic coordinates

were fully relaxed using the conjugate gradient method until the force on each atom was converged to less than 0.02 eV \AA^{-1} . The investigation of further surface terminations, reconstructions and the processes during OER and HER go beyond the scope of this study and will be addressed in a future study.

5.6 REFERENCES

1. Dubal, D. P.; Gomez-Romero, P.; Sankapal, B. R.; Holze, R. *Nano Energy* **2015**, *11*, 377.
2. Roy, P.; Srivastava, K. S. *J. Mater. Chem. A* **2015**, *3*, 2454.
3. Trotochaud, L.; Boettcher, S. W. *Scr. Mater.* **2014**, *74*, 25.
4. Bau, J. A.; Li, P.; Marenco, A. J.; Trudel, S.; Olsen, B. C.; Lubner, E. J.; Buriak, J. M. *Chem. Mater.* **2014**, *26*, 4796.
5. Bondi, J. F.; Misra, R.; Ke, X.; Sines, I. T.; Schiffer, P.; Schaak, R. E. *Chem. Mater.* **2010**, *22*, 3988.
6. Vasques, Y.; Luo, Z.; Schaak R. E. *J. Am. Chem. Soc.* **2008**, *130*, 11866.
7. Soriano, R. B.; Wu, J.; Kanatzidis, M. G. *J. Am. Chem. Soc.* **2015**, *137*, 9937.
8. Landon, J.; Demeter, E.; İnoğlu, N.; Keturakis, C.; Wachs, I. E.; Vasić, R.; Frenkel, A. I.; Kitchin, J. R. *ACS Catal.* **2012**, *2*, 1793.
9. Fominykh, K.; Cernev. P.; Zaharieva, I.; Sicklinger, J.; Stefanic, G.; Doeblinger, M.; Müller A.; Pokharel, A.; Böcklein, S.; Scheu, C.; Bein, T.; Fattakhova-Rohlfing D. *ACS Nano* **2015**, *9*, 5180.
10. Liu, Y.; Peters, K.; Mandlmeier, B.; Müller, A.; Fominykh, K.; Rathousky, J.; Scheu, C.; Fattakhova-Rohlfing, D. *Electrochim. Acta* **2014**, *140*, 108.
11. Liu, Y.; Szeifert, J. M.; Feckl, J. M.; Mandlmeier, B.; Rathousky, J.; Hayden, O.; Fattakhova-Rohlfing, D.; Bein, T. *ACS Nano* **2010**, *4*, 5373.

12. Peters, K.; Zeller, P.; Stefanic, G.; Skoromets, V.; Němec, H.; Kužel, P.; Fattakhova-Rohlfing, D. *Chem. Mater.* **2015**, *27*, 1090.
 13. Niederberger, M. *Acc. Chem. Res.* **2007**, *40*, 793.
 14. Hirsch, O.; Zeng, G.; Luo, L.; Staniuk, M.; Abdala, P. M.; van Beek, W.; Rechberger, F.; Süess, M. J.; Niederberger, M.; Koziej, D. *Chem. Mater.* **2014**, *26*, 4505.
 15. Bates, M. K.; Jia, Q.; Doan, H.; Liang, W.; Mukerjee, S. *ACS Catal.* **2016**, *6*, 155.
 16. Deng, X.; Tüysüz, H. *ACS Catal.* **2014**, *4*, 3701.
 17. Grewe, T.; Deng, X.; Weidenthaler, C.; Schüth, F.; Tüysüz, H. *Chem. Mater.* **2013**, *25*, 4926.
 18. McCrory, C. C.; Jung, S.; Ferrer, I. M.; Chatman, S. M.; Peters, J. C.; Jaramillo, T. F. *J. Am. Chem. Soc.* **2015**, *137*, 4347–4357.
 19. McCrory, C. C.; Jung, S.; Peters, J. C.; Jaramillo, T. F. *J. Am. Chem. Soc.* **2013**, *135*, 16977.
 20. Peng, Z.; Jia, D.; Al-Enizi, A. M.; Elzatahry, A. A.; Zheng, G. *Adv. Energy Mater.* **2015**, *5*, 1402031.
 21. Smith, R. D.; Prevot, M. S.; Fagan, R. D.; Trudel, S.; Berlinguette, C. P. *J. Am. Chem. Soc.* **2013**, *135*, 11580.
 22. Smith, R. D.; Prevot, M. S.; Fagan, R. D.; Zhang, Z.; Sedach, P. A.; Siu, M. K.; Trudel, S.; Berlinguette, C. P. *Science* **2013**, *340*, 60.
 23. Trotochaud, L.; Ranney, J. K.; Williams, K. N.; Boettcher, S. W. *J. Am. Chem. Soc.* **2012**, *134*, 17253.
 24. Du, W.; Gao, Y.; Tian, Q.; Li, D.; Zhang, Z.; Guo, J.; Qian, X. *J. Nanopart. Res.* **2015**, *17*, 368.
 25. Gennero de Chialvo, M. R.; Chialvo, A. C. *Electrochim. Acta* **1993**, *38*, 2247.
 26. Ho, J. C. K.; Piron, D. L. *J. Appl. Electrochem.* **1996**, *26*, 515.
-

5.6 REFERENCES

27. Mai, Y. J.; Tu, J. P.; Xia, X. H.; Gu, C. D.; Wang, X. L. *J. Power Sources* **2011**, *196*, 6388.
 28. Roginskaya, Y. E.; Morozova, O. E.; Lubnin, E. N.; Ulitina, Y. E.; Lopukhova, G. V.; Trasatti, S. *Langmuir* **1997**, *13*, 4621.
 29. Thi, T. V.; Rai, A. K.; Gim, J.; Kim, J. *J. Power Sources* **2015**, *292*, 23.
 30. Wu, G.; Li, N.; Zhou, D.-R.; Mitsuo, K.; Xu, B.-Q. *J. Solid State Chem.* **2004**, *177*, 3682.
 31. Zhang, J.; Liu, F.; Cheng, J. P.; Zhang, X. B. *ACS Appl. Mater. Interfaces* **2015**, *7*, 17630.
 32. Zhao, Y.; Zhang, X.; He, J.; Zhang, L.; Xia, M.; Gao, F. *Electrochim. Acta* **2015**, *174*, 51.
 33. Natu, G.; Hasin, P.; Huang, Z.; Ji, Z.; He, M.; Wu, Y. *ACS Appl. Mater. Interfaces* **2012**, *4*, 5922.
 34. De Faria, L. A.; Trasatti, S. *J. Electroanal. Chem.* **2003**, 355.
 35. Wang, H.; Wang, P.; Yin, Z. *Int. J. Electrochem. Sci.* **2013**, *8*, 7734.
 36. Sharma, R.; Acharya, A. D.; Moghe, S.; Shrivastava, S. B.; Gangrade, M.; Shripathi, T.; Ganesan, V. *Mater. Sci. Semicond. Process.* **2014**, *23*, 42.
 37. Roffi, T. M.; Uchida, K.; Nozaki, S. *J. Cryst. Growth* **2015**, *414*, 123.
 38. Yang, F.; Xie, Q.; Zhang, H.; Yu, S.; Zhang, X.; Shen, Y. *Sens. Actuators, B* **2015**, *210*, 232.
 39. Xiao, J.; Yang, S. *J. Mater. Chem.* **2012**, *22*, 12253–12262.
 40. Feckl, J. M.; Dunn, H. K.; Zehetmaier, P. M.; Müller, A.; Pendlebury, S. R.; Zeller, P.; Fominykh, K.; Kondofersky, I.; Döblinger, M.; Durrant, J. R.; Scheu, C.; Peter, L.; Fattakhova-Rohlfing, D.; Bein, T. *Adv. Mater. Interfaces* **2015**, *2*, 1500358.
 41. Feckl, J. M.; Fominykh, K.; Döblinger, M.; Fattakhova-Rohlfing, D.; Bein, T. *Angew. Chem., Int. Ed.* **2012**, *51*, 7459.
-

42. Fominykh, K.; Feckl, J. M.; Sicklinger, J.; Döblinger, M.; Böcklein, S.; Ziegler, J.; Peter, L.; Rathousky, J.; Scheidt, E.-W.; Bein, T.; Fattakhova-Rohlfing, D. *Adv. Funct. Mater.* **2014**, *24*, 3123.
 43. Bajdich, M.; Garcia-Mota, M.; Vojvodic, A.; Norskov, J. K.; Bell, A. T. *J. Am. Chem. Soc.* **2013**, *135*, 13521.
 44. De Los Santos Valladares, L.; Ionescu, A.; Holmes, S.; Barnes, C. H. W.; Bustamante Domínguez, A.; Avalos Quispe, O.; González, J. C.; Milana, S.; Barbone, M.; Ferrari, A. C.; Ramos, H.; Majima, Y. *J. Vac. Sci. Technol., B: Microelectron. Nanometer Struct.-Process., Meas., Phenom.* **2014**, *32*, 051808.
 45. Mironova-Ulmane, N.; Kuzmin, A.; Steins, I.; Grabis, J.; Sildos, I.; Pärs, M. *J. Phys.: Conf. Ser.* **2007**, *93*, 012039.
 46. Choi, H. C.; Jung, Y. M.; Noda, I.; Kim, S. B. *J. Phys. Chem. B* **2003**, *107*, 5806.
 47. Zhang, G.; Huang, H.; Li, W.; Yu, F.; Wu, H.; Zhou, L. *Electrochim. Acta* **2012**, *81*, 117.
 48. Ponnusamy, P. M.; Agilan, S.; Muthukumarasamy, N.; Raja, M.; Velauthapillai, D. *J. Mater. Sci: Mater. Electron.* **2015**, *27*, 399.
 49. Biesinger, M. C.; Payne, B. P.; Grosvenor, A. P.; Lau, L. W. M.; Gerson, A. R.; Smart, R. S. C. *Appl. Surf. Sci.* **2011**, *257*, 2717.
 50. Gallant, D.; Pezolet, M.; Simard, S. *J. Phys. Chem. B* **2006**, *110*, 6871.
 51. Biesinger, M. C.; Payne, B. P.; Lau, L. W. M.; Gerson, A.; Smart, R. S. C. *Surf. Interface Anal.* **2009**, *41*, 324.
 52. Hoffer, B.; Dickvanlangeveld, A.; Janssens, J.; Bonne, R.; Lok, C.; Moulijn, J. J. *Catal.* **2000**, *192*, 432.
 53. McIntyre, N. S.; Cook, M. G. *Anal. Chem.* **1975**, *47*, 2208.
 54. Lyons, M. E. G.; Brandon, M. P. *Int. J. Electrochem. Sci.* **2008**, *3*, 1386.
 55. Yeo, B. S.; Bell, A. T. *J. Phys. Chem. C* **2012**, *116*, 8394.
-

5.6 REFERENCES

56. Blakemore, J. D.; Gray, H. B.; Winkler, J. R.; Müller, A. M. *ACS Catal.* **2013**, *3*, 2497.
57. Chou, N. H.; Ross, P. N.; Bell, A. T.; Tilley, T. D. *ChemSusChem* **2011**, *4*, 1566.
58. Wang, H.; Lee, H. W.; Deng, Y.; Lu, Z.; Hsu, P. C.; Liu, Y.; Lin, D.; Cui, Y. *Nat. Commun.* **2015**, *6*, 7261.
59. Yeo, B. S.; Bell, A. T. *J. Am. Chem. Soc.* **2011**, *133*, 5587.
60. Yin, J.; Zhou, P.; An, L.; Huang, L.; Shao, C.; Wang, J.; Liu, H.; Xi, P. *Nanoscale* **2016**, *8*, 1390.
61. Corrigan, D. A.; Bendert, R. M. *J. Electrochem. Soc.* **1989**, *136*, 723.
62. Sauerbrey, G. Z. *Phys. A: Hadrons Nucl.* **1959**, *155*, 206.
63. Doniach, S.; Sunjic, M. *J. Phys. C: Solid State Phys.* **1970**, *3*, 285.
64. Kresse, G.; Hafner, J. *Phys. Rev. B* **1993**, *47*, 558.
65. Kresse, G.; Joubert, D. *Phys. Rev. B* **1999**, *59*, 1758.
66. Boussendel, A.; Baadji, N.; Haroun, A.; Dreyssé, H.; Alouani, M. *Phys. Rev. B* **2010**, *81*, 184432.
67. Dudarev, S. L.; Botton, G. A.; Savrasov, S. Y.; Humphreys, C. J.; Sutton, A. P. *Phys. Rev. B* **1998**, *57*, 1505.
68. Franchini, C.; Bayer, V.; Podloucky, R.; Paier, J.; Kresse, G. *Phys. Rev. B* **2005**, *72*, 045132.
69. Cococcioni, M.; de Gironcoli, S. *Phys. Rev. B* **2005**, *71*, 035105.
70. Schön, A.; Rödl, C.; Bechstedt, F. *Phys. Rev. B* **2012**, *86*, 115134.
71. Wdowik, U. D.; Parlinski, K. *Phys. Rev. B* **2007**, *75*, 104306.

5.7 SUPPORTING INFORMATION

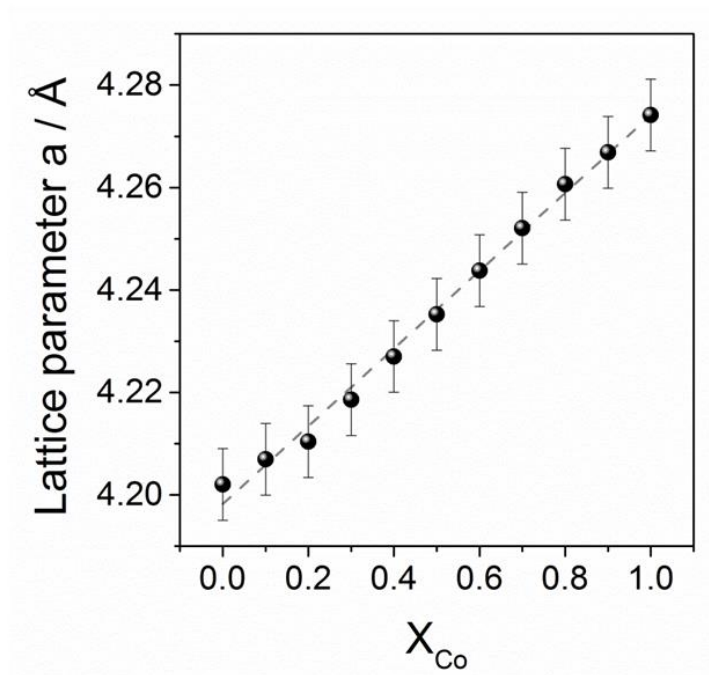


Figure S5.1 Demonstration of the lattice parameters of the $\text{Ni}_x\text{Co}_{1-x}\text{O}$ nanoparticles following Vegard's law.

The lattice parameters of the $\text{Ni}_x\text{Co}_{1-x}\text{O}$ particles with different Co content follow Vegard's law (Figure S5.1). The undoped NiO and CoO nanoparticles prepared by our synthesis route show slightly larger lattice parameters of 4.20 Å and 4.28 Å than the corresponding bulk materials, respectively. The literature values are 4.17 Å for NiO and 4.26 Å for CoO. This effect was already described in the literature for nanosized NiO and CoO and in our previous study.¹⁻³

5.7 SUPPORTING INFORMATION

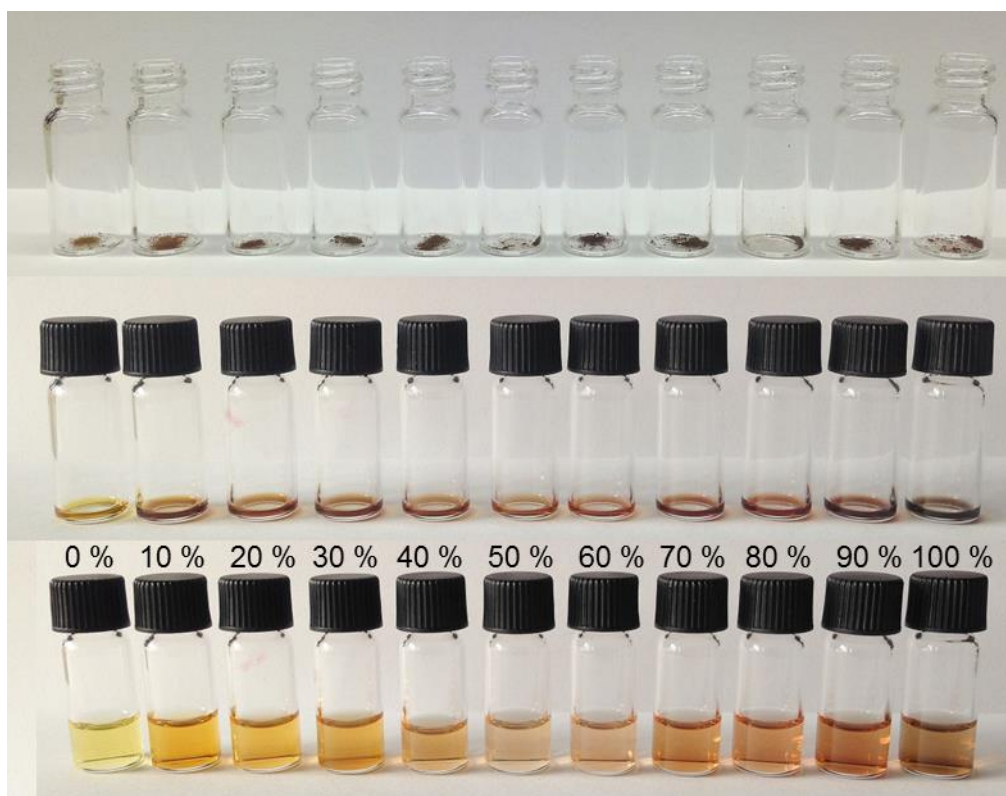


Figure S5.2 Preparation of $\text{Ni}_x\text{Co}_{1-x}\text{O}$ dispersions (concentration: 2 mg mL^{-1}). Top row: dried powders directly after synthesis. Middle row: dispersions after addition of HOAc. Bottom row: Dispersions after filling up with EtOH. The numbers indicate the Co content of each sample in at%.

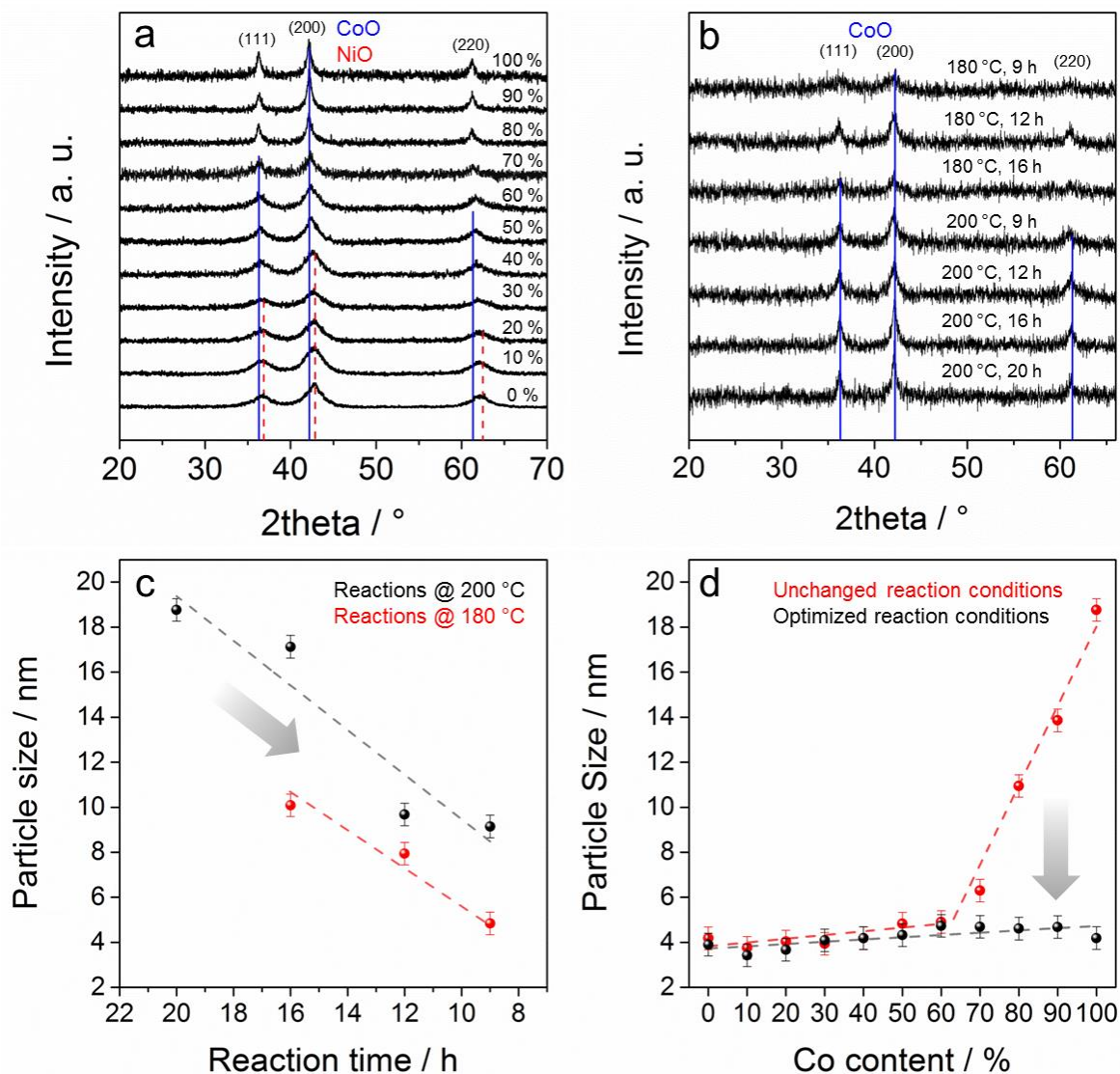


Figure S5.3 Influence of reaction conditions on crystallite size of $\text{Ni}_x\text{Co}_{1-x}\text{O}$ nanoparticles. (a) Powder XRD patterns of the dried nanocrystals NP-0 – NP-100 prepared at the same reaction conditions, CoO pattern ICDD card number 00-043-1004 (solid line), NiO pattern ICDD card number 00-047-1049 (dashed line). The numbers indicate the Co content in at%. (b) Powder XRD patterns of NP-100 prepared at the different reaction conditions. (c) Particle size of NP-100 calculated from the XRD patterns recorded after reactions at 200 °C (black) and 180 °C (red). (d) XRD particle sizes of NP-0 – NP-100 prepared at unchanged (red) and optimized reaction conditions (black).

The solvothermal synthesis in *t*BuOH at 200 °C for 20 h was designed for the rather unreactive precursor $\text{Ni}(\text{acac})_2$ that only dissolves in *t*BuOH after reaching 200 °C. For precursors like $\text{Co}(\text{acac})_2$ that dissolve at lower temperatures more easily, this high

temperature leads to much larger particles. The higher the ratio of $\text{Co}(\text{acac})_2$ in the reaction mixture, the more pronounced is this effect. Figure S5.3a shows XRD patterns of NP-0 – NP-100 prepared at 200 °C for 20 h. The reflections become narrower with increasing Co content revealing a drastic increase in particle size starting from NP-70 (Figure S5.3d, red dots). To obtain smaller particle sizes, the parameters temperature and time were optimized for each Ni/Co ratio to slow down the reaction. As an example, XRD patterns and corresponding particle sizes at different reaction conditions are demonstrated for NP-100 in Figures S5.3b, c. By decreasing the reaction time, the particle size was reduced from 19 nm to 9 nm. Further decrease to around 4 nm was achieved by reducing the temperature from 200 °C to 180 °C. The particle sizes after optimization of reaction conditions are shown in Figure S5.3d, black dots.

We note that the XRD patterns shown in Figures S5.3a, b were obtained using an XRD diffractometer with a Cu-source (Cu $K_{\alpha 1}$ radiation $\lambda = 1.54060 \text{ \AA}$). Due to strong fluorescence caused by interactions of Co containing compounds with the Cu radiation, the signal-to-noise ratio becomes less with increasing Co content. The XRD patterns with better quality shown in Figure 5.2 in the main text are recorded using a Mo-source diffractometer, which does not lead to Co fluorescence.

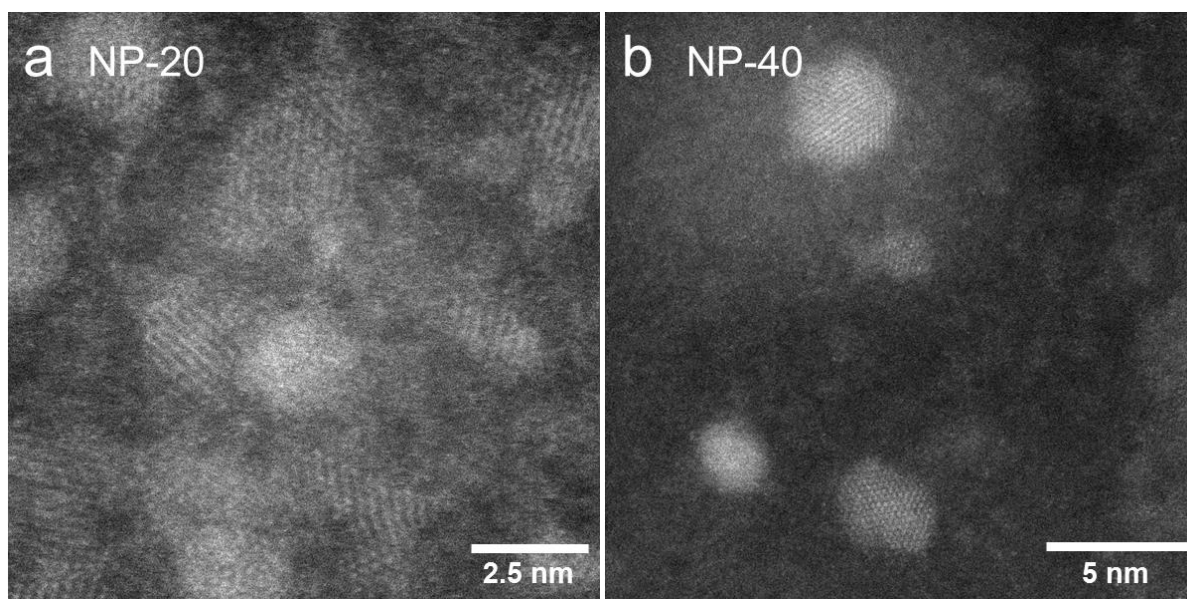


Figure S5.4 Scanning transmission electron microscopy (STEM) images of several (a) NP-20 and (b) NP-40 nanocrystals.

Table S5.1 Co content in reaction mixtures compared to Co content within the $\text{Ni}_x\text{Co}_{1-x}\text{O}$ nanoparticles determined by different methods.

Co content reaction / %	Co content (ICP) / %	Co content (EDX) / %	Co content (XPS) / %				Ni content (XPS) / %			
			Before sputtering		After sputtering		Before sputtering		After sputtering	
			Co(II)	Co(III)	Co(II)	Co(III)	Ni(II)	Ni(III)	Ni(II)	Ni(III)
10	10.1	–	–	–	–	–	–	–	–	–
20	19.1	19.8	15.1	2.0	18.5	0	82.91	0	81.47	0
30	29.3	–	–	–	–	–	–	–	–	–
40	42.6	39.9	16.1	12.1	30.7	0	71.81	0	69.32	0
50	46.4	–	–	–	–	–	–	–	–	–
60	60.5	59.8	13.7	35.8	51.0	0	50.5	0	49.0	0
70	70.3	–	58.1	0	–	–	–	–	–	–
80	81.6	79.3	23.0	61.3	86.4	0	15.6	0	13.6	0
90	90.4	–	72.7	0	–	–	–	–	–	–
100	100.0	100.0	14.0	86.0	100.0	0	0	0	0	0

5.7 SUPPORTING INFORMATION

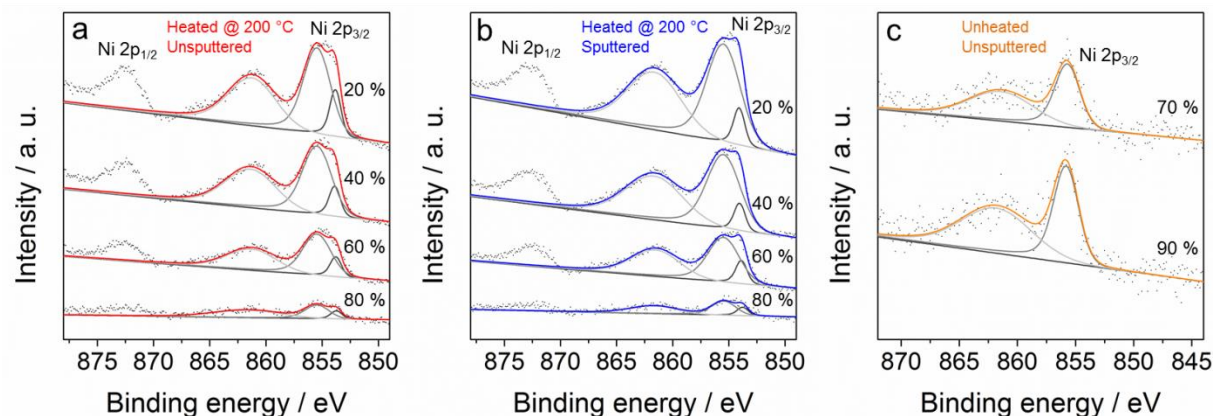


Figure S5.5 XPS spectra of the $\text{Ni}_x\text{Co}_{1-x}\text{O}$ nanoparticles, Ni 2p peaks of nanoparticle layers (a) heated at 200 °C and (b) heated at 200 °C and sputtered with Ar^+ ions. The spectra were taken using a Mg K_α source. The points correspond to the experimental data, and the lines are the fitted curves and the individual peak fits, respectively. The corresponding fitting parameters are listed in Table S5.2. (c) Ni 2p_{3/2} peaks of nanoparticle layers dried under high vacuum. The numbers indicate the Co content in at%.

Table S5.2 XPS fitting parameters for the Co 2p_{3/2} and Ni 2p_{3/2} peaks of non-sputtered samples.

Peak	Peak Nr	Lorentz FWHM / eV	Asymmetry	Gauss FWHM / eV	Position / eV
Ni 2p _{3/2}	1	0.3	0.05	1.0	~853.8
	2	0.3	0.05	2.3 – 3.2	~855.4
	3	0.3	0.05	~6	~861.5
Co 2p _{3/2}	1	0.3	0.05	2.1	~779.8
	2	0.3	0.05	2.6	~782.1
	3	0.3	0.05	~4.5	~786.1

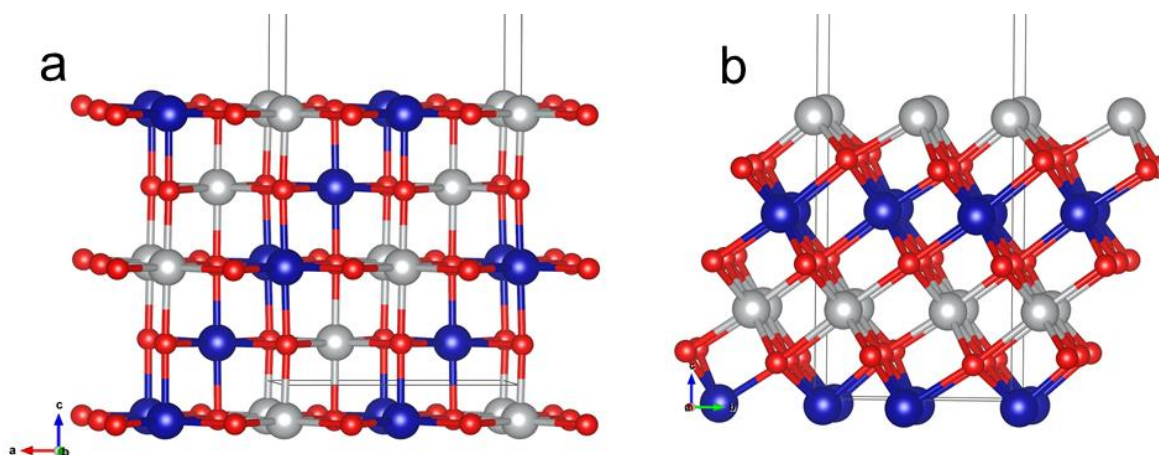


Figure S5.6 Slab models of (a) (001) and (b) (111)-oriented $\text{Ni}_{0.5}\text{Co}_{0.5}\text{O}$ surfaces. Blue and silver spheres correspond to Co and Ni cations with antiparallel alignment of magnetic moments, respectively. Red spheres correspond to O atoms.

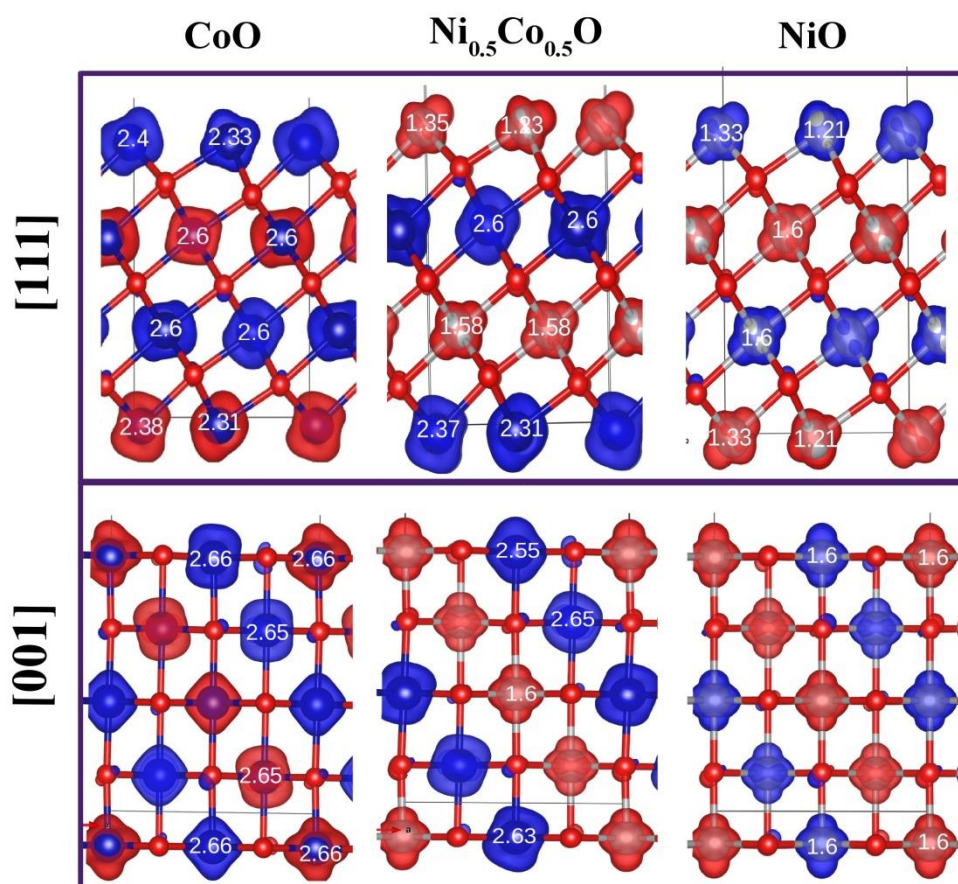


Figure S5.7 DFT+ U computed spin density of the (001) and (111) oriented surfaces in CoO, NiO and $\text{Ni}_{0.5}\text{Co}_{0.5}\text{O}$. The colors are related to the up spin (red) and the down spin (blue). The numbers indicate the corresponding magnetic moments μ_B .

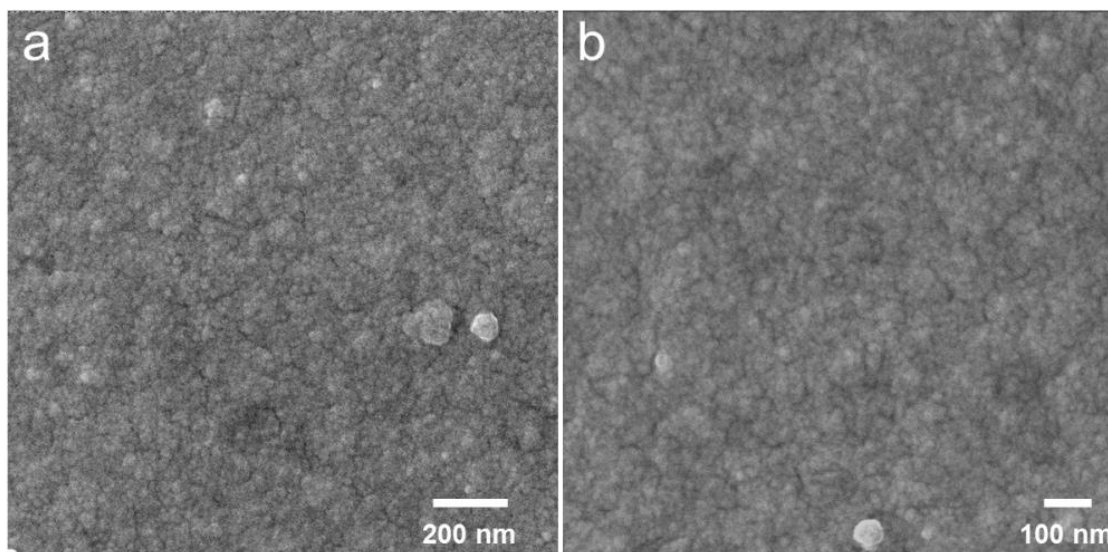


Figure S5.8 (a, b) SEM images of an NP-40 film on Au coated QCM crystals with different magnifications. The film was prepared from ethanolic dispersion *via* spin coating.

Scanning electron microscopy (SEM) images of the NP-40 film applied as electrode for electrochemical measurements are presented in Figures S5.8a, b in different magnifications. The films show a smooth surface morphology with some textural porosity typical for nanoparticle films reported in our previous studies.^{2,4}

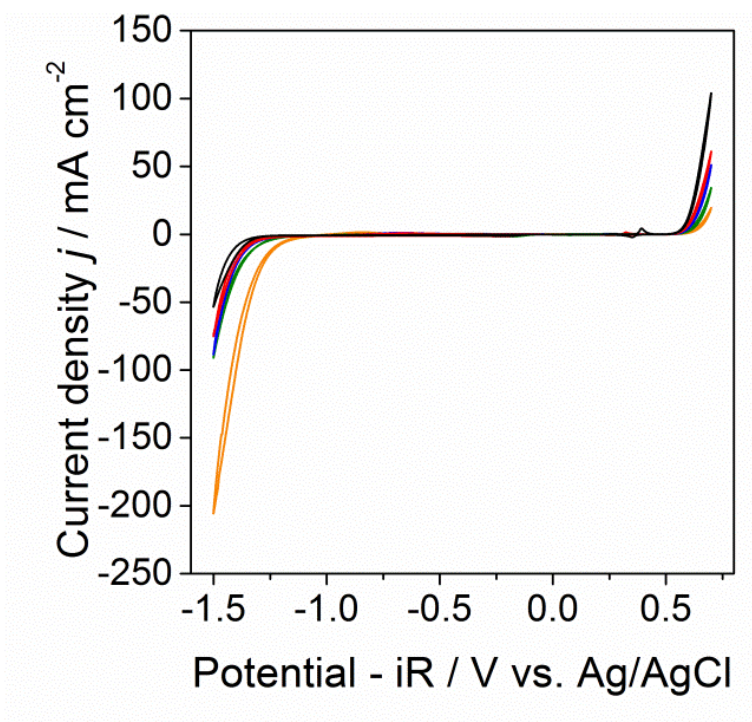


Figure S5.9 (a) Cyclic voltammograms of Au/QCM electrodes coated with thin films of $\text{Ni}_x\text{Co}_{1-x}\text{O}$ nanoparticles NP-0, NP-40, NP-60, NP-80 and NP-100. The numbers indicate the Co content in at%.

Typical cyclic voltammograms of selected nanoparticle samples are shown in Figure S5.9, demonstrating the electrocatalytic activity in OER and HER. It should be noted that practically no current was measured on the bare Au electrode under the same conditions, exhibiting no pronounced OER or HER activity.

1.1.2 REFERENCES

1. Jahromi, S.P.; Pandikumar, A.; Goh, B. T.; Lim, Y. S.; Basirun, W. J.; Lim, H. N.; Huang, N. M. *RSC Adv.* **2015**, *5*, 14010.
2. Fominykh, K.; Cernev. P.; Zaharieva, I.; Sicklinger, J.; Stefanic, G.; Doeblinger, M.; Müller A.; Pokharel, A.; Böcklein, S.; Scheu, C.; Bein, T.; Fattakhova-Rohlfing D. *ACS Nano* **2015**, *9*, 5180.
3. Ghosh M., Sampathkumaran E. V.; Rao C. N. R. *Chem. Mater.* **2005**, *17*, 2348.
4. Fominykh, K.; Feckl, J. M.; Sicklinger, J.; Döblinger, M.; Böcklein, S.; Ziegler, J.; Peter, L.; Rathousky, J.; Scheidt, E.-W.; Bein, T.; Fattakhova-Rohlfing, D. *Adv. Funct. Mater.* **2014**, *24*, 3123.

6 ULTRASMALL Co_3O_4 NANOCRYSTALS STRONGLY ENHANCE SOLAR WATER SPLITTING ON MESOPOROUS HEMATITE

This chapter is based on the following publication:

J. M. Feckl, H. K. Dunn, P. M. Zehetmaier, A. Müller, S. R. Pendlebury, P. Zeller, K. Fominykh, I. Kondofersky, M. Döblinger, J. R. Durrant, C. Scheu, L. Peter, D. Fattakhova-Rohlfing and T. Bein *Adv. Mater. Interfaces* **2015**, 2, 1500358.

The joint project is a collaboration of different groups involving synthesis of Co_3O_4 nanoparticles (J. M. Feckl and P. M. Zehetmaier), their electrochemical characterization (K. Fominykh), photoelectrochemical and transition absorption spectroscopy characterization (H. K. Dunn, S. R. Pendlebury, I. Kondofersky and J. R. Durrant), XPS (P. Zeller) and TEM analysis (A. Müller, M. Döblinger and C. Scheu). The following experiments were performed by K. Fominykh: fabrication of Co_3O_4 electrode layers, electrochemical characterization of their water oxidation performance and characterization of the dark electrocatalytic activity of Co_3O_4 nanoparticles.

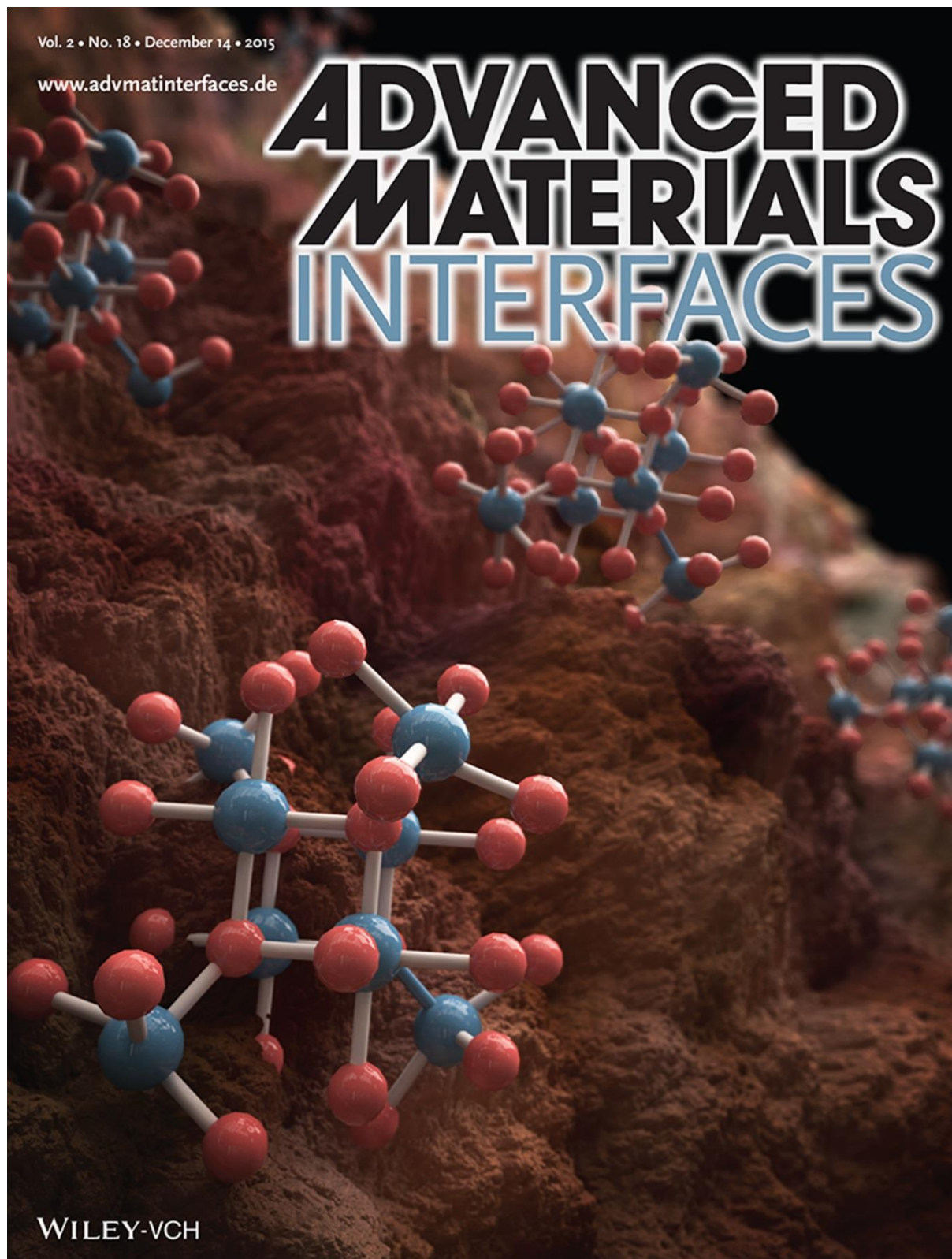


Figure 6.1 Image created by Christoph Hohmann (Nanosystems Initiative Munich, NIM) published as front cover in Adv. Mater. Interfaces 18/2015 (used with permission from the publisher).

6.1 ABSTRACT

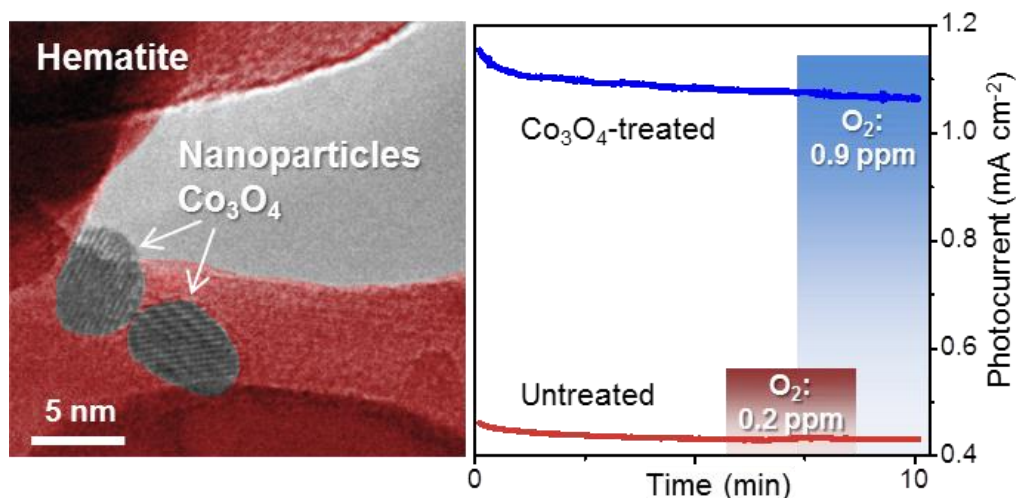


Figure 6.2 ToC image: Ultrasmall dispersible Co_3O_4 nanocrystals with an average size of 3 – 7 nm are prepared by a solvothermal reaction in *tert*-butanol. The small size and high dispersibility of the nanoparticles enable their homogeneous deposition on nanostructured Sn-doped hematite serving as a photoanode in light-driven water splitting. This surface treatment leads to a striking photocurrent increase.

The synthesis of crystalline, non-agglomerated, and perfectly dispersible Co_3O_4 nanoparticles with an average size of 3 – 7 nm using a solvothermal reaction in *tert*-butanol is reported. The very small size and high dispersibility of the Co_3O_4 nanoparticles allow for their homogeneous deposition on mesoporous hematite layers serving as the photoactive absorber in the light-driven water splitting reaction. This surface treatment leads to a striking photocurrent increase. While the enhancement of hematite photoanode performance by cobalt oxides is known, the preformation and subsequent application of well-defined cobalt oxide nanoparticles are novel and allow for the treatment of arbitrarily complex hematite morphologies. Photoelectrochemical and transient absorption spectroscopy studies show that this enhanced performance is due to the suppression of surface electron–hole recombination on time scales of milliseconds to seconds.

6.2 INTRODUCTION

The spinel Co_3O_4 is interesting for applications such as gas sensing,¹ electrochemical lithium ion storage,²⁻⁶ and as a catalyst for lithium air batteries,⁷ for the combustion of CH_4 ,⁸ for the oxidation of CO ,⁹ for the oxygen reduction reaction in fuel cells,^{10,11} or for electrochemical water oxidation.¹² Co_3O_4 has the highest turnover frequency for dark electrochemical water oxidation among the various cobalt oxides, and the catalytic activity is enhanced with decreasing crystallite size.¹² Interest in Co_3O_4 for photoelectrochemical water splitting was sparked by the work of Kanan and Nocera,¹³ and several other groups demonstrated the high efficiency of various cobalt compounds,¹⁴⁻²⁰ including Co_3O_4 ,²¹⁻²³ as oxygen evolving catalysts. The effect is pronounced in combination with Fe_2O_3 hematite photoanodes. Hematite offers several features attractive for solar water splitting,²⁴⁻²⁷ but also suffers from serious limitations including the sluggish kinetics of the oxygen evolution reaction (OER)²⁸⁻³⁰ and the high rate of electron–hole recombination at the surface.^{20,26,31-33} The photoelectrochemical water splitting efficiency of hematite photoanodes was found to improve significantly upon surface treatment with different cobalt compounds.^{14-17,19,20,34} The role of these surface treatments is not yet fully understood,³⁴ although some of them were found to suppress surface recombination but not to catalyze the hole transfer.^{19,35,36} The reported synthetic methods rely either on electrochemical deposition,¹⁴⁻¹⁷ *in situ* growth,^{19,23,37} or atomic layer deposition.^{20,34} However, the former methods are sensitive to the growth conditions or surface properties of the photoabsorber material and not always applicable to complex electrode geometries, while the latter is not easily and economically scalable.¹⁴⁻¹⁷ Consequently, the development of a facile procedure for the low-temperature deposition of Co_3O_4 with well-defined properties on any type of photoabsorber substrate, independent of surface properties or morphology, is very desirable. Dispersible nanoparticles are particularly interesting for this purpose, as their deposition from solution can easily be controlled.

Compared to an *in situ* growth process, the formation of nanocrystals in a separate process allows for a much better control of properties such as size, shape, and chemical composition. Although several Co_3O_4 morphologies such as nanotubes,^{6,38} needles,⁴ rods,¹¹ wires,⁵ hollow spheres,⁸ nanoboxes,³⁹ and nanoparticles^{12,37,40-45} are synthetically available, it appears that none of these have so far been applied to photoabsorbers for water splitting. Here we report the solvothermal synthesis of dispersible, non-agglomerated, and crystalline Co_3O_4

nanoparticles with sizes in the range of 3 – 7 nm. The nanoparticles can be dispersed in ethanol and homogeneously distributed on the surface of mesoporous hematite photoanodes by a simple drop-casting process. This treatment leads to a more than fivefold increase in photocurrent under AM 1.5 illumination compared to the untreated hematite electrodes. The performance enhancement is more pronounced for thicker films, suggesting that the reason for the increased photocurrents is enhanced electron collection in the mesoporous nanoparticle-containing hematite electrodes rather than acceleration of hole transfer at the hematite–solution interface. Efficient extraction of photogenerated electrons from a mesoporous photoanode requires retardation of their recombination with the photogenerated holes (and with intermediates in the water oxidation reaction), resulting in significantly more long-lived surface-accumulated holes, which are required for water oxidation on hematite. This observation was supported by transient absorption spectroscopy (TAS), which showed an increased lifetime of long-lived (ms to s time scale) photogenerated holes at or near the hematite surface.

6.3 RESULTS AND DISCUSSION

For the synthesis of dispersible crystalline Co_3O_4 nanoparticles we developed a solvothermal procedure in *tert*-butanol. This solvent has already been shown to be suitable for the preparation of dispersible, crystalline, and ultrasmall metal-oxide nanoparticles such as different titania compounds, NiO, and tin oxide.⁴⁶⁻⁵¹ For the preparation of Co_3O_4 nanoparticles, $\text{Co}(\text{OAc})_2$ was dispersed in a solution of Pluronic P123 in *tert*-butanol. After the addition of concentrated nitric acid to the reaction solution, the mixture was autoclaved at 120 °C for 17 h. Only a combination of $\text{Co}(\text{OAc})_2$, nitric acid, and Pluronic P123 led to the formation of small non-agglomerated particles. The use of $\text{Co}(\text{NO}_3)_2$ as an alternative precursor causes the fast growth of larger nanocrystals whose size cannot be decreased by changing reaction conditions or by adding stabilizing ligands. On the other hand, using $\text{Co}(\text{OAc})_2$ as a precursor leads to the formation of mostly amorphous material. We believe that the combination of $\text{Co}(\text{OAc})_2$ with nitric acid leads to the *in situ* formation of reactive $\text{Co}(\text{NO}_3)_2$ that can form Co_3O_4 . It seems reasonable to assume that the particles are capped by acetate ligands, limiting the particle growth. The presence of Pluronic P123 additionally stabilizes and limits the particle growth.

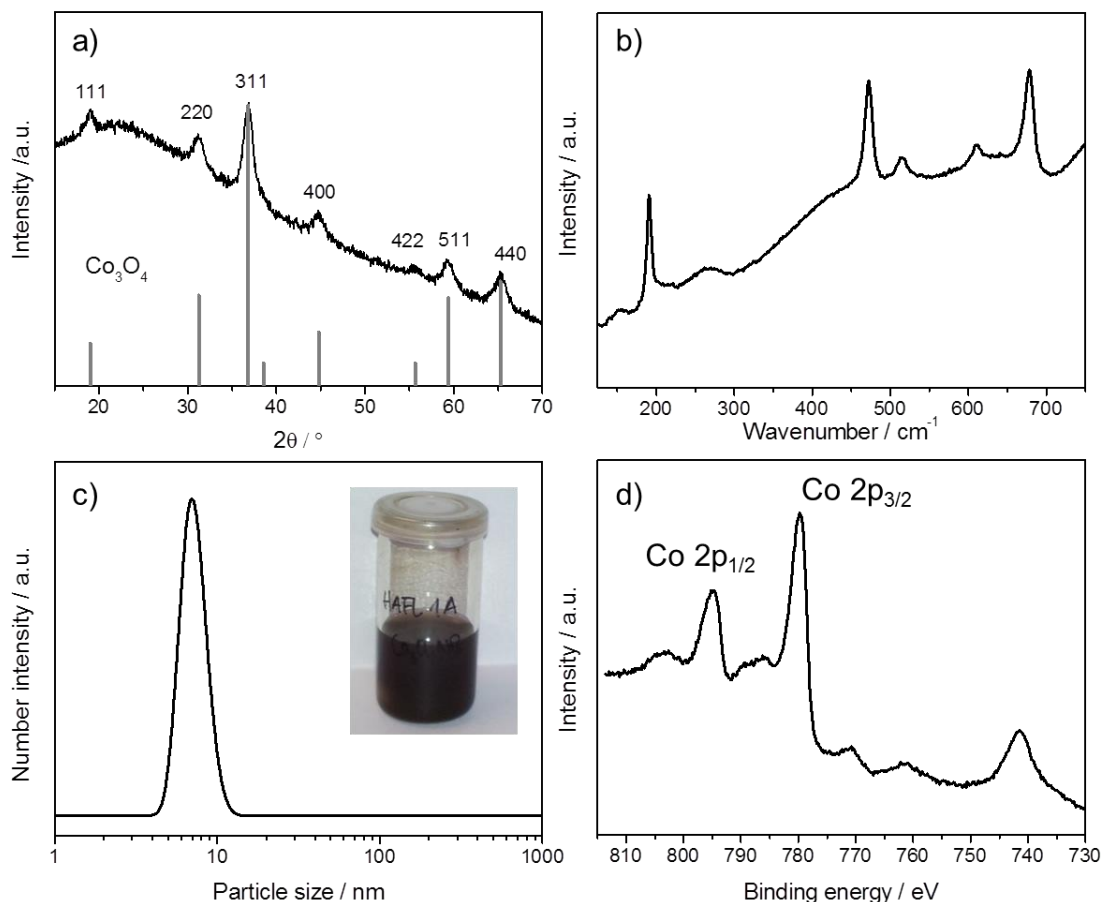


Figure 6.3 Morphology and composition of as-synthesized Co_3O_4 nanoparticles prepared *via* the *tert*-butanol route: (a) XRD pattern of nanoparticles with the corresponding ICDD card 00-043-1003 of Co_3O_4 and (b) Raman spectrum of the Co_3O_4 nanoparticles. The peaks at 190.7 (F_{2g}), 472.7 (E_g), 513.1 (F_{2g}), 610.0 (F_{2g}), and 678.6 (A_{1g}) cm^{-1} correspond to the Raman modes characteristic of Co_3O_4 .⁵² (c) DLS measurement of a diluted Co_3O_4 nanoparticle dispersion; the inset shows a photograph of a dispersion with a concentration of 22.8 mg Co_3O_4 nanoparticles after drying, dispersed in 4 mL ethanol; and (d) XPS spectrum of Co_3O_4 nanoparticles showing the Auger transitions of oxygen at 742 and 761 eV and the Co 2p signals, which are split by spin–orbit coupling into Co 2p_{3/2} (779.9 eV) and 2p_{1/2} (795.0 eV).

After cooling to room temperature, the nanoparticles could be collected simply by centrifugation or by drying the processed solution. X-ray diffraction (XRD) of the obtained solid proves the formation of about 7 nm small Co_3O_4 nanoparticles (size calculated according to the Scherrer equation from the broadening of the 311 reflection; Figure 6.3a). The high background in the XRD pattern is attributed to the fluorescence common for cobalt-containing materials when using Cu $K\alpha$ radiation. Additionally, the Raman spectrum of the

nanoparticles shows modes characteristic of Co_3O_4 (Figure 6.3b).⁵² The solid is easily redispersible in ethanol by adding a drop of concentrated acetic acid. This was proven by dynamic light scattering (DLS) measurements in Figure 6.3c, which show a narrow peak at around 7 nm. X-ray photoelectron spectroscopy (XPS) measurements were performed to determine the oxidation states of the cobalt oxide nanoparticles. Figure 6.3d shows the Auger transitions of oxygen at 742 and 761 eV and the Co 2p signals that are split by spin-orbit coupling into Co 2p_{3/2} and 2p_{1/2}. The binding energy of the Co 2p_{3/2} peak (779.9 eV) and the absence of a satellite at about 786 eV (which would indicate CoO) identify the samples as Co_3O_4 .⁵³ The XPS spectra before and after electrochemical testing look very similar, suggesting no significant changes in the material during the electrochemical reactions (Figure S6.1 in the supporting Information).

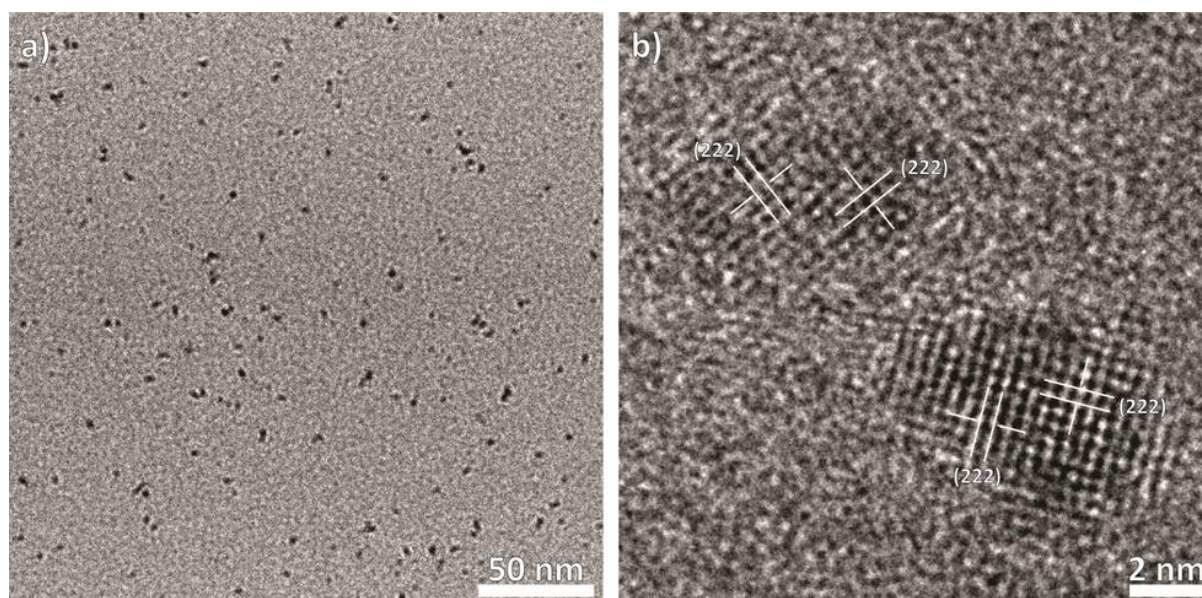


Figure 6.4 (a) TEM image of finely dispersed Co_3O_4 nanoparticles. (b) HRTEM image of two individual Co_3O_4 nanoparticles.

In good agreement with the data obtained by XRD and DLS, high-resolution transmission electron microscope (HRTEM) images show monocrystalline nanoparticles with d -spacings typical of Co_3O_4 (Figure 6.4). The particles sized 3 – 7 nm are non-agglomerated and evenly distributed on the surface of the TEM grid, indicating high dispersibility in ethanol (Figure 6.4a).

The ultrasmall and dispersible Co_3O_4 nanoparticles were applied as a surface treatment to mesoporous, Sn-doped hematite layers prepared by a wet chemical deposition described by Dunn *et al.*⁵⁴ The hematite electrodes prepared in this way feature a disordered mesoporous structure composed of elongated crystalline nanoparticles with an average size of around 40×80 nm. The thickness of the electrodes can be varied from about 50 to 400 nm by repetitive coating.⁵⁴ Even though the photocurrents are lower than those of state-of-the-art hematite photoelectrodes,⁵⁵ the morphology and photocurrents of the hematite films used in this study are similar to those prepared by other solution-based synthetic routes and therefore provide an excellent model system.⁵⁶ The Co_3O_4 nanoparticles were deposited onto the mesoporous hematite electrodes by drop-casting from an ethanolic dispersion. The degree of coating of the hematite photoanodes by Co_3O_4 could easily be controlled by diluting the particle dispersions to the desired concentration. After the deposition step, the samples were heated to 180 °C. This step was necessary to provide good adhesion of the nanoparticles to the mesoporous layer. TEM analysis showed that the Co_3O_4 nanoparticles (which could be identified by lattice spacings, energy-dispersive X-ray spectroscopy (EDX) measurements, and size) were for the most part homogeneously distributed throughout the whole volume of the mesoporous hematite layer. For a rather low nanoparticle loading depicted in Figure S6.2 (supporting Information), individual, non-agglomerated nanoparticles are evenly distributed on the hematite crystals, which can be attributed to their excellent dispersibility.

The Co_3O_4 -treated hematite films fabricated as described above were tested as photoanodes for the photoelectrochemical OER. The current-voltage curves obtained under AM 1.5 illumination are displayed in Figure 6.5 for a 350 nm thick mesoporous hematite film with and without the Co_3O_4 nanoparticle surface treatment. The photocurrent of the hematite electrodes with deposited Co_3O_4 nanoparticles is significantly higher than that of the untreated hematite films. The increase in photocurrent depends on the illumination direction, a phenomenon that will be discussed later. The increase in photocurrent is accompanied by an increase in the amount of detected oxygen (Figure S6.3 in the supporting information and the experimental section), indicating that the observed effect stems from the water oxidation process and not from any other reactions such as photocorrosion or the oxidation of organics.

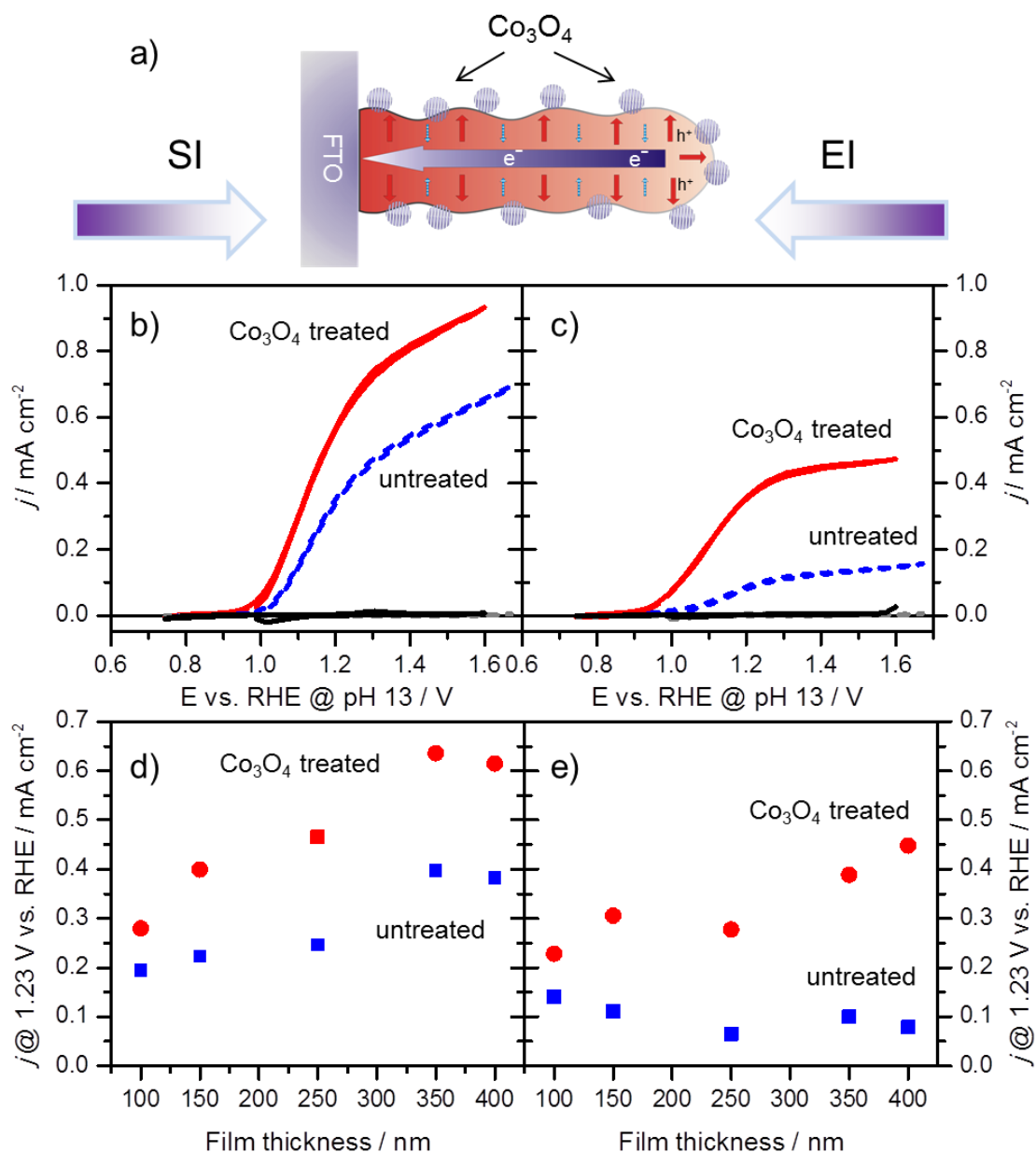


Figure 6.5 (a) Simplified illustration of the processes taking place in a porous hematite electrode during illumination. Red arrows indicate diffusion of the photogenerated holes to the hematite surface, the blue arrow indicates diffusion of photogenerated electrons to the substrate (current collector), and striped blue arrows represent their recombination with positive species, such as holes; illumination direction is indicated as SI (substrate illumination) and EI (electrolyte illumination). Current density–voltage curves for 350 nm nanostructured hematite films with (full red lines) and without (dashed blue lines) Co_3O_4 nanoparticle treatment under simulated AM 1.5 illumination through (b) the substrate and (c) the electrolyte. Dark j - V curves are also shown for the Co_3O_4 treated film (full black line) and untreated film (dashed gray line). Photocurrent at 1.23 V versus RHE of films of varying thicknesses with (red circles) and without the Co_3O_4 treatment (blue squares), when illumination is provided through the (d) substrate and (e) electrolyte.

We detect a cathodic shift in the photocurrent onset potential, although the observed effect is small compared to other reported cobalt treatments.^{32,57-59} Such a shift can indicate either catalysis of charge transfer or a lowering of surface recombination; the analysis of possible effects will be given below.

When deposited directly onto FTO, the Co_3O_4 nanoparticles do not produce any photocurrent, indicating that the observed improvements originate from the synergy between the hematite and the nanoparticles (Figure S6.4 in the supporting Information.). We note that the Co_3O_4 nanoparticles lower the onset potential of water oxidation in the dark, acting as catalysts for electrochemical water oxidation. To quantify the dark electrocatalytic activity, we prepared thin films by depositing particle dispersions on the Au electrodes of piezoelectric quartz crystal microbalance (QCM) chips. Using Au/QCM crystals as substrates allows for an accurate determination of the mass loading⁶⁰ and the direct calculation of turnover frequencies (TOF) from voltammetric data (Figure S6.5 in the supporting Information). The TOF values can either be calculated based on the mass loading of Co_3O_4 , assuming that all Co atoms are catalytically active (TOF_{min}), or by using the BET surface area based on the assumption that the catalytically active sites are located only on the surface of the electrode (TOF_{max}). We applied both methods to compute the TOF values for our Co_3O_4 nanoparticles. For example, the TOF_{min} values at overpotentials of $\eta = 300$ mV and $\eta = 400$ mV are 0.003 and 0.01 s^{-1} , respectively. The TOF_{max} at the same overpotentials were calculated as 0.021 and 0.63 s^{-1} , which is an order of magnitude higher than the corresponding TOF_{min} . The obtained results indicate that Co_3O_4 nanoparticles act as a reasonably good dark catalyst for the OER, although the TOF values do not surpass those of other cobalt oxide structures reported in the literature.^{21,58,59,61,62} It should also be noted that good dark catalysts do not necessarily act as catalysts when deposited on photoelectrodes.^{58,63} The explanation for this possibly lies in the different mechanisms of the light and dark OER, as the former involves minority carriers, whereas the latter involves majority carriers.

To elucidate how the Co_3O_4 nanoparticles improve the performance of hematite photoanodes, we compared their effect on the photocurrent for substrate (SI) and electrolyte (EI) side illumination. A scheme illustrating the various pathways of photogenerated charges in a mesoporous electrode is shown in Figure 6.5a. In porous hematite layers made up of particles of the same size, photogenerated holes (red arrows in Figure 6.5a) travel the same short distance to reach the oxide–solution interface, independent of the illumination direction.

Photogenerated electrons, in contrast, must travel through the porous layer to the FTO substrate, and for strongly absorbed light (i.e., at wavelengths where the penetration depth of the light is much less than the film thickness), the average distance travelled therefore depends on the illumination direction. Under EI, electron–hole pairs are generated far away from the substrate and electrons have a long collection pathway through the thickness of the film (blue arrow in Figure 6.5a). This leaves them vulnerable to recombination with surface species such as trapped holes (this loss pathway is depicted by blue striped arrows). Under SI, we expect more efficient electron collection, since the charges are generated very close to the FTO substrate. The comparison of the photocurrent under EI and SI thus gives insight into electron–hole recombination in porous electrodes;^{55,64} the description of this method for AM 1.5 illumination will be published separately.

For the untreated hematite electrode, the photocurrent measured when illuminating by an AM 1.5 solar simulator through the electrolyte is approximately a quarter of that obtained when illuminating through the substrate (Figures 6.5b, c). According to the arguments outlined above, this indicates that a considerable portion of photogenerated electrons is not collected when generated far from the FTO substrate. However, when applying Co_3O_4 nanoparticles to 100–400 nm thick mesoporous hematite layers, the photocurrent when illuminating through the substrate strongly increases by a factor of 1.6 compared to the untreated hematite electrode, reaching 0.64 mA cm^{-2} at 1.23 V versus the reversible hydrogen electrode (RHE) for the 350 nm thick electrode (Figures 6.5b, d). Much higher increases of up to a factor of nearly five are observed for EI (Figures 6.5c, e). Given that the losses to recombination under EI are expected to scale with the film thickness, one can expect a more dramatic effect of the Co_3O_4 nanoparticles on thicker films. Figure 6.5 illustrates the photocurrent at 1.23 V versus RHE of films of varying thickness under SI (Figure 6.5d) and EI (Figure 6.5e), with and without the Co_3O_4 nanoparticle treatment. Due to electron–hole recombination losses, the deviation between EI and SI increases as a function of thickness. However, the effect is reduced for Co_3O_4 -treated photoanodes, indicating a significant reduction of this loss pathway.

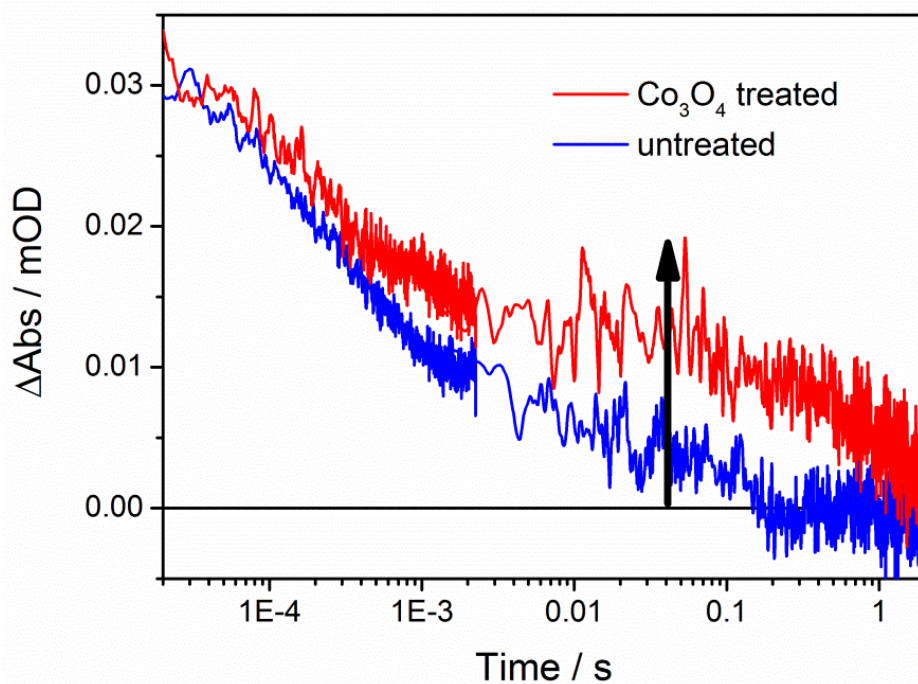


Figure 6.6 Photogenerated hole dynamics in untreated (blue) and Co_3O_4 treated (red) thin (50 nm) hematite photoanodes at open circuit in 1 M NaOH, excited at 455 nm and probed at 650 nm. The arrow indicates the increase in lifetime of photogenerated holes after treatment with Co_3O_4 .

The transient absorption dynamics of photogenerated holes at or near the hematite surface (probed at 650 nm, in accordance with previous studies³⁰ in untreated and Co_3O_4 -treated hematite at open circuit are shown in Figure 6.6 (the same data shown on a linear time axis are presented in Figure S6.7 in the supporting information). It is apparent that the Co_3O_4 treatment significantly increases the lifetime of the photogenerated hole signal on millisecond to second time scales. These results are consistent with the effect of other Co-based treatments (such as Co–Pi and cobalt nitrate) on the lifetime of surface-accumulated holes in hematite as studied by transient absorption spectroscopy and intensity modulated photocurrent spectroscopy.^{35,36} The increase in lifetime of photogenerated holes (of ≈ 500 ms) on these long time scales indicates that electron–hole recombination at the semiconductor surface has been retarded by the Co_3O_4 treatment.³³ These results are consistent with the photocurrent increase by Co_3O_4 treatment. Interestingly, treatment with cobalt nitrate, which has been reported to increase photocurrents of different hematite photoelectrodes^{32,57} by retarding recombination,³⁶ had little influence on the performance (Figure S6.6 in the supporting information).

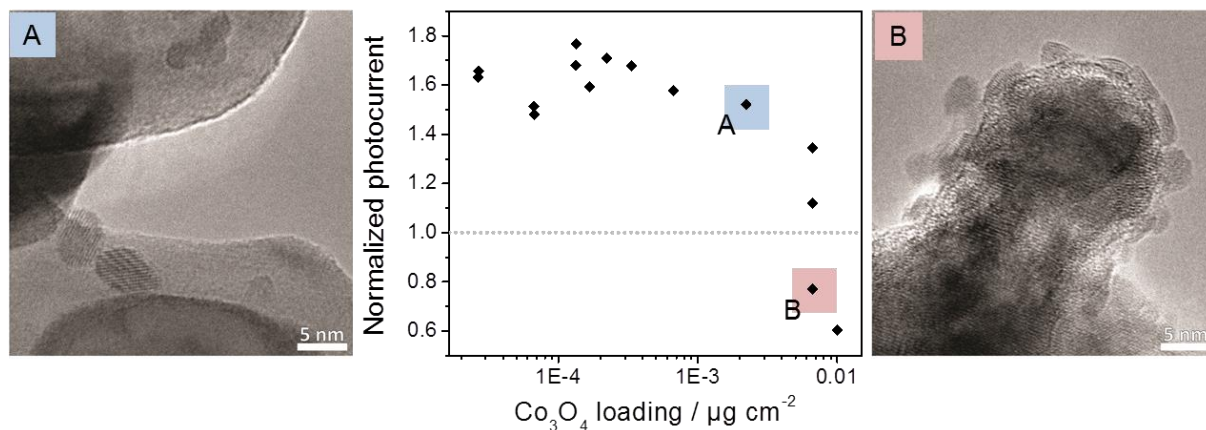


Figure 6.7 Normalized photocurrent at 1.164 V vs. RHE (pH 13) under 455 nm illumination with about $10^{17} \text{ cm}^{-2} \text{ s}^{-1}$ intensity, of Co_3O_4 -treated 150 nm Sn-doped hematite films as a function of Co_3O_4 nanoparticle loading on the active area of the electrodes. The normalized current is displayed as a ratio of photocurrent of Co_3O_4 nanoparticle-treated electrodes to that of an untreated electrode of the same thickness. On the left and right side the corresponding TEM images are shown to illustrate the different surface coverage.

The observed improvement in photocurrent depends on the mass loading of the Co_3O_4 nanoparticles in the mesoporous hematite electrodes, as shown in Figure 6.7. The best performance is observed for samples with a low loading of Co_3O_4 nanoparticles. TEM investigation of the best-performing samples demonstrates that the porous hematite layers contain homogeneously distributed non-agglomerated Co_3O_4 nanoparticles, with only a few Co_3O_4 nanoparticles observed on the hematite crystals (Figures 6.6a and S6.2 in the supporting information). In contrast, hematite photoanodes treated with concentrated nanoparticle dispersions show suppressed photocurrents compared to the non-treated photoanodes. Examination of such samples by TEM reveals a dense coverage with Co_3O_4 nanoparticles, leaving very little exposed Fe_2O_3 . We tentatively attribute the suppressed photocurrent in such densely decorated hematite films to the reduced exposed surface area and an increased parasitic light absorption by the black Co_3O_4 .⁶⁵

The obtained results demonstrate that the postsynthetic Co_3O_4 nanoparticle treatment significantly improves the electron collection in mesoporous hematite photoanodes. Photoelectrochemical and transient absorption spectroscopy studies suggest that this enhanced performance is due to the suppression of surface electron–hole recombination and not due to the catalysis of charge transfer. However, the way by which Co_3O_4 nanoparticles retard

electron–hole recombination at the semiconductor surface is not fully understood and additional studies are needed to elucidate the mechanism of this effect.

6.4 CONCLUSION

Ultrasmall Co_3O_4 nanoparticles were synthesized *via* a newly developed *tert*-butanol solvothermal synthesis protocol. The high dispersibility and very small size of these particles were proven by XRD, DLS, and TEM measurements and allow for the efficient distribution of these monocrystalline nanoparticles on mesoporous hematite films by a drop-casting process. This treatment leads to striking improvements in photoelectrochemical water oxidation rates, increasing the obtained photocurrent by a factor of nearly five. The improvement is attributed to a significant reduction in electron–hole recombination processes on millisecond to second time scales at the surface of the mesoporous network, and strongly depends on the degree of surface coverage by the Co_3O_4 nanoparticles. This demonstrates the importance of a homogeneous distribution of the applied nanoparticles on the highly porous host materials, which can easily be achieved with the stable colloidal dispersions presented in this study.

6.5 EXPERIMENTAL SECTION

6.5.1 SYNTHESIS OF COBALT OXIDE NANOPARTICLES

Co_3O_4 nanoparticles were synthesized in *tert*-butanol. All chemicals were purchased from Sigma-Aldrich and used as received. *tert*-Butanol was dried over a 4 Å molecular sieve at 28 °C and filtered prior to use (Sartorius minisart cellulose acetate membrane, 220 nm). In a typical reaction 50 mg (0.2 mmol) of $\text{Co}(\text{OAc})_2$ tetrahydrate was dispersed in a solution of 58 mg Pluronic P123 in 14 mL *tert*-butanol and treated for 45 min in an ultrasonic bath at room temperature. To accelerate the synthesis, 48 mg of concentrated nitric acid was added to the reaction solution. The reaction mixture was transferred into a Teflon lined steel autoclave (20 mL volume) and kept at 120 °C for 17 h. The nanoparticles can be collected by simply drying the processed solution or by centrifugation. The content of Co_3O_4 of the resulting centrifuged solid after drying at 180 °C (equivalent to the heat treatment after the deposition

of the nanoparticles on the nanostructured hematite electrodes) was determined to be 70 wt% by thermogravimetric analysis. The pellet was treated with one drop of concentrated acetic acid (35 mg acetic acid per 22.8 mg solid) and then redispersed in ethanol (1 mL ethanol for 1 mg solid). This dispersion was filtered with a 220 nm syringe filter (Sartorius minisart cellulose acetate membrane) and the concentration of Co_3O_4 nanoparticles in the resulting dispersion was determined by inductively coupled plasma atomic emission spectroscopy (ICP-AES) to be 0.667 mg mL^{-1} , which agrees well with the inorganic amount of 70 wt% determined by TGA. This dispersion was then diluted with ethanol (1:50) for DLS measurements, the preparation of TEM samples and the photo-electrochemical water splitting experiments.

6.5.2 ELECTRODE PREPARATION

The electrodes for dark electrochemical measurements were prepared by spin-coating of the cobalt oxide nanoparticle dispersions on Au/QCM crystals (KVG 10 MHz QCM devices with gold electrodes from Quartz Crystal Technology GmbH). In a typical procedure, 10 μL of a cobalt oxide dispersion were deposited on a masked QCM crystal covering an area of 0.196 cm^2 and spun at 1000 rpm for 10 s. The electrodes were subsequently heated in a laboratory oven to $200 \text{ }^\circ\text{C}$ with a heating ramp of $4 \text{ }^\circ\text{C min}^{-1}$ and a dwell time of 2 h.

The mass loading was calculated from the change in the resonance frequency of the QCM crystals before and after coating using the Sauerbrey equation

$$\Delta f = -C_f \Delta m \quad (6.1)$$

Where Δf is the change in frequency, C_f is the sensitivity factor of the QCM crystal and Δm is the change in mass.⁶⁰

6.5.3 PHOTOELECTRODE PREPARATION

The precursor solution for the 20 % Sn-precursor based hematite was prepared according to a procedure described in detail elsewhere.⁵⁴ In brief, 0.111 g (0.313 mmol) Sn(OAc)₄ was first dispersed under vigorous stirring at room temperature for 5 h and 15 min sonication in a mixture of Pluronic P123 (0.25 g) and 10 mL *tert*-butanol. Afterwards, 0.505 g (1.25 mmol) Fe(NO₃)₃·9H₂O was dissolved in the dispersion under sonication for 15 minutes, and then 2.5 mL water (Millipore) was added forming a dark red solution. The solution was stirred at room temperature overnight, resulting in a light brown dispersion of iron oxide. After cleaning the FTO glass (TEC 15 Pilkington TEC Glass™, 2.5 × 1.5 cm) by sequential sonication for 15 min each in detergent (1 mL Extran in 50 mL Millipore water), water (Millipore) and ethanol, the substrates were dried and masked with Scotch Tape on the conducting side to retain a non-covered area of 1.5 × 1.5 cm². The back of the substrates was completely masked to avoid contamination during the spin-coating procedure that would lead to a deterioration of the optical transparency of the substrates. Before spin-coating, the fresh solutions were filtered through a 220 nm syringe filter (Sartorius minisart cellulose acetate membrane) to remove agglomerates, ensuring the preparation of homogeneously smooth films. The masked substrates were covered with 100 μL of solution and spun at 1000 rpm for 30 seconds. To increase the film thickness, the films were dried for 5 minutes at 60 °C and spin-coated again. To remove the template and crystallize the material, the samples were calcined in air in a laboratory oven (3 hour ramp to 600 °C, 30 min dwell time). This results in films of about 50 nm thickness, which can be increased linearly by repeating the complete procedure. SEM cross-section images of these films are shown in Figure S6.8 in the supporting Information.

A Co₃O₄ nanoparticle surface treatment was applied to the Sn-containing mesoporous hematite thin films by drop casting. After depositing 10 μL of the Co₃O₄ nanoparticle dispersion in ethanol as described above onto a projected electrode area of 2.25 cm², the films were heated to 180 °C for 30 min. This step was necessary to provide a good adhesion of the nanoparticles to the mesoporous layer. All data reported herein are representative of several samples of each type (hematite film thickness and nanoparticle loading).

6.5.4 CHARACTERIZATION

X-ray diffraction analysis of the powders on microscopy slides was carried out in reflection mode (Bragg-Brentano) using a Bruker D8 Discover diffractometer with Ni-filtered Cu K α radiation and a position-sensitive detector (LynxEye). Raman spectra were recorded with a Jobin Yvon Horiba HR800 UV Raman microscope using a HeNe laser emitting at 632.8 nm.

Scanning electron microscopy (SEM) was performed on a JEOL JSM-6500F scanning electron microscope equipped with a field emission gun.

TEM analysis was carried out on a FEI Titan 80-300 (S)TEM with a Fischione Instruments (Model 3000) high angle annular dark field (HAADF) detector and an EDAX Energy-dispersive X-Ray Spectroscopy (EDX) detector. All measurements were conducted at an acceleration voltage of 300 kV. Pure Co₃O₄ nanoparticles were drop-coated on a copper grid with a holey carbon film, whereas of the treated hematite film material was removed and deposited on such a copper grid.

X-ray photoelectron spectroscopy (XPS) analysis was performed using a VSW HA 100 hemispherical analyzer and a VSW TA10 X-ray source providing non-monochromatized Mg K α radiation (Mg K α = 1253.6 eV).

Dynamic light scattering (DLS) of the cobalt oxide nanoparticles was performed using a Malvern Zetasizer-Nano equipped with a 4 mW He-Ne laser (633 nm) and an avalanche photodiode detector. The scattering data were weighted based on particle number.

Thermogravimetric analysis was performed on a Netzsch STA 440 C TG/DSC.

Inductively coupled plasma atomic emission spectroscopy was carried out with a VARIAN VISTA RL CCD Simultaneous ICP-AES.

6.5.5 ELECTROCHEMICAL MEASUREMENTS

Cyclic voltammetry measurements were performed at a scan rate of 20 mV s^{-1} between 0 V and 0.8 V in a three-electrode setup using an Autolab potentiostat/galvanostat PGSTAT302N with FRA32M module operating with Nova 1.10.2 software. A 0.5 M KOH solution (Sigma-Aldrich, volumetric solution, pH 13.43) was used as electrolyte in all measurements. Pt mesh (1 cm^2) was used as a counter electrode. Au/quartz crystals coated with Co_3O_4 nanoparticles were used as working electrodes. All potentials were measured vs. Ag/AgCl/KCl (sat.) reference electrode with a potential of +0.989 V vs. the reversible hydrogen electrode (RHE) at pH 13.43 (+0.197 V vs. NHE). The overpotential η was calculated using the equation

$$\eta = E - E_{\text{OER}} - iR_s \quad (6.2)$$

where E is the potential recorded vs. Ag/AgCl reference electrode, E_{OER} is the reversible potential of the OER vs. Ag/AgCl reference electrode (0.240 V at pH 13.43), i is the current, and R_s is the uncompensated resistance. R_s was determined by measuring the minimum total impedance in the frequency mode between 10 and 50 kHz at open circuit conditions at a potential of 0.2 V vs. Ag/AgCl, and was typically around 11 – 14 Ohm. All data were corrected for 95 % of the measured resistance. Current densities were calculated using the unmasked surface area of 0.196 cm^2 of the Au/quartz electrode.

The turnover frequency (TOF) was calculated according to:

$$\text{TOF} = \frac{i}{4 F n} \quad (6.3)$$

where i is the current, F is the Faraday constant and n is the amount of Co on the electrode determined either from the total amount of Co atoms using the mass loading (TOF_{min}) or from the number of surface Co atoms calculated using the BET surface area and the density of surface cobalt atoms in cobalt oxide of $6.1 \cdot 10^{18.66}$.

6.5.6 PHOTOELECTROCHEMICAL MEASUREMENTS

Hematite photoelectrodes were masked with a Teflon-coated glass fiber adhesive tape leaving a circular area of 1 cm in diameter exposed to a 0.1 M NaOH aqueous electrolyte. All electrochemical measurements were carried out with glass or quartz cells using a μ -Autolab III potentiostat equipped with a FRA2 impedance analyzer connected to a saturated Ag/AgCl reference electrode (Sigma Aldrich, 0.197 V vs. the standard hydrogen electrode) and a Pt mesh counter electrode. Potentials versus the reversible hydrogen electrode V_{RHE} were calculated from those measured at pH 13 versus the Ag/AgCl electrode $V_{\text{Ag/AgCl}}$ according to:

$$V_{\text{RHE}} = V_{\text{Ag/AgCl}} + 0.197 + 0.059 \text{ pH} \quad (6.4)$$

The light intensity was measured inside the cells using a 4 mm² photodiode, which had been calibrated against a certified Fraunhofer ISE silicon reference cell equipped with a KG5 filter.

The current-voltage characteristics of the films were obtained by scanning from negative to positive potentials in the dark or under illumination, with a 20 mV s⁻¹ sweep rate. Illumination, which was either provided by a high power light emitting diode (LED, Thorlabs, 455 nm), or an AM1.5G solar simulator (Solar Light Model 16S) at 100 mW cm⁻², was incident either through the substrate (SI) or the electrolyte (EI). A detailed description of the method for quantification of the electron diffusion length will be described in a following publication.

The dissolved O₂ was determined with a HANNA dissolved oxygen bench meter (HI 2400 DO Meter) using the same setup described above in an aqueous 1 M NaOH electrolyte. The electrolyte solution was purged with N₂ before each measurement until the dissolved oxygen in solution reached 0 ppm. During electrochemical measurements N₂ was purged above the solution. The films were illuminated through the electrolyte (EI) side using a blue diode (455 nm at 10¹⁷ s⁻¹ cm⁻²).

Current-voltage (*I-V*) curves were obtained by scanning from negative to positive potentials in the dark or under illumination at a 20 mV s⁻¹ sweep rate. Further chronoamperometric measurements were carried out at 1.56 V vs. RHE over 10 minutes while determining the concentration change of dissolved oxygen over time.

6.5.7 TRANSIENT ABSORPTION SPECTROSCOPY (TAS)

The dynamics of photogenerated holes in untreated and Co_3O_4 -treated hematite photoanodes were measured using microsecond to second timescale transient absorption spectroscopy (TAS). Band-gap excitation of hematite was achieved using a 455 nm pulsed laser (0.35 Hz, $210 \mu\text{J cm}^{-2}$ /pulse, $< 20 \text{ ns}$ pulse width), generated from the third harmonic (355 nm) of a Nd:YAG laser (Quantel Ultra, Lambda Photometrics) *via* an optical paramagnetic oscillator (Opolette, Opotek Inc.). This “pump” pulse was transmitted to the sample by a liquid light guide. A 100 W tungsten lamp (IL 1, Bantham) equipped with a monochromator (OBB-2001, Photon Technology International) was employed as the probe beam; holes in hematite were probed at 650 nm, in accordance with previous studies.³⁰ The sample was illuminated from the EI side (electrolyte-electrode). The transmitted probe light was filtered by several long-pass filters and a band-pass filter in order to remove scattered light from the laser before being focused on a silicon photodiode detector (S3751, Hamamatsu). Microsecond-millisecond timescale data were amplified and filtered (Costronics) and collected by an oscilloscope (TDS 2012c, Tektronics); millisecond-second timescale data were collected with a DAQ card (NI USB-6211, National Instruments). All data were acquired using home-built Labview software. Each trace shown is the average of 300 – 500 individual measurements. Signals due to laser scatter were subtracted from μs -ms timescale data.

6.6 REFERENCES

1. Su, D. W.; Liu, H.; Ahn, H. J. Wang, G. X. *J. Nanosci. Nanotechnol.* **2013**, *13*, 3354.
2. Liu, D.; Wang, X.; Wang, X.; Tian, W.; Bando, Y.; Golberg, D. *Sci. Rep.* **2013**, *3*, 2543.
3. Lou, X. W.; Deng, D.; Lee, J. Y.; Feng, J.; Archer, L. A. **2008**, *20*, 258.
4. Lou, X. W.; Deng, D.; Lee, J. Y.; Archer, L. A. *J. Mater. Chem.* **2008**, *18*, 4397.
5. Li, Y.; Tan, B.; Wu, Y. *Nano Lett.* **2008**, *8*, 265.
6. Du, N.; Zhang, H.; Chen, B.; Wu, J.; Ma, X.; Liu, Z.; Zhang, Y.; Yang, D.; Huang, X.; Tu, J. *Adv. Mater.* **2007**, *19*, 4505.

6.6 REFERENCES

7. Sun, C.; Li, F.; Ma, C.; Wang, Y.; Ren, Y.; Yang, W.; Ma, Z.; Li, J.; Chen, Y.-J.; Kim, Y.; Chen, L. *J. Mater. Chem. A* **2014**, *2*, 7188.
 8. Wang, C.-A.; Li, S.; An, L. *Chem. Commun.* **2013**, *49*, 7427.
 9. Xie, X.; Li, Y.; Liu, Z.-Q.; Haruta, M.; Shen, W. *Nature* **2009**, *458*, 746.
 10. Xiao, J.; Kuang, Q.; Yang, S.; Xiao, F.; Wang, S.; Guo, L. *Sci. Rep.* **2013**, *3*, 2300.
 11. Xu, J.; Gao, P.; Zhao, T. *Energy Environ. Sci.* **2012**, *5*, 5333.
 12. Chou, N. H.; Ross, P. N.; Bell, A. T.; Tilley, T. D. *ChemSusChem* **2011**, *4*, 1566.
 13. Kanan, M. W.; Nocera, D. G. *Science* **2008**, *321*, 1072.
 14. Barroso, M.; Cowan, A. J.; Pendlebury, S. R.; Grätzel, M.; Klug, D. R.; Durrant, J. R.. *J. Am. Chem. Soc.* **2011**, *133*, 14868.
 15. Klahr, B.; Gimenez, S.; Fabregat-Santiago, F.; Bisquert, J.; Hamann, T. W. *J. Am. Chem. Soc.* **2012**, *134*, 16693.
 16. Zhong, D. K.; Gamelin, D. R. *J. Am. Chem. Soc.* **2010**, *132*, 4202.
 17. Zhong, D. K.; Sun, J.; Inumaru, H.; Gamelin, D. R.; *J. Am. Chem. Soc.* **2009**, *131*, 6086.
 18. Artero, V.; Chavarot-Kerlidou, M.; Fontecave, M. *Angew. Chem., Int. Ed.* **2011**, *50*, 7238.
 19. Cummings, C. Y.; Marken, F.; Peter, L. M.; Tahir, A. A.; Wijayantha, K. U. *Chem. Commun.* **2012**, *48*, 2027.
 20. Riha, S. C.; Klahr, B. M.; Tyo, E. C.; Seifert, S.; Vajda, S.; Pellin, M. J.; Hamann, T. W.; Martinson, A. B. F. *ACS Nano* **2013**, *7*, 2396.
 21. Blakemore, J. D.; Gray, H. B.; Winkler, J. R.; Müller, A. M. *ACS Catal.* **2013**, *3*, 2497.
 22. Jiao, F.; Frei, H. *Angew. Chem., Int. Ed.* **2009**, *48*, 1841.
-

-
23. Xi, L.; Tran, P. D.; Chiam, S. Y.; Bassi, P. S.; Mak, W. F.; Mulmudi, H. K.; Batabyal, S. K.; Barber, J.; Loo, J. S. C.; Wong, L. H. *J. Phys. Chem. C* **2012**, *116*, 13884.
 24. Hamann, T. W. *Dalton Trans.* **2012**, *41*, 7830.
 25. Lin, Y.; Yuan, G.; Sheehan, S.; Zhou, S.; Wang, D.; *Energy Environ. Sci.* **2011**, *4*, 4862.
 26. Sivula, K.; Le Formal, F.; Grätzel, M. *ChemSusChem* **2011**, *4*, 432.
 27. Katz, M. J.; Riha, S. C.; Jeong, N. C.; Martinson, A. B. F.; Farha, O. K.; Hupp, J. T. *Coord. Chem. Rev.* **2012**, *256*, 2521.
 28. Bolton, J. R.; Strickler, S. J.; Connolly, J. S. *Nature* **1985**, *316*, 495.
 29. Brilllet, J.; Yum, J.-H.; Cornuz, M.; Hisatomi, T.; Solaraska, R.; Augustynski, J.; Graetzel, M.; Sivula, K. *Nat. Photonics* **2012**, *6*, 824.
 30. Pendlebury, S. R.; Cowan, A. J.; Barroso, M.; Sivula, K.; Ye, J.; Gratzel, M.; Klug, D. R.; Tang, J.; Durrant, J. R. *Energy Environ. Sci.* **2012**, *5*, 6304.
 31. Cesar, I.; Kay, A.; Martinez, J. A. G.; Grätzel, M. *J. Am. Chem. Soc.* **2006**, *128*, 4582.
 32. Kay, A.; Cesar, I.; Grätzel, M. *J. Am. Chem. Soc.* **2006**, *128*, 15714.
 33. Le Formal, F.; Pendlebury, S. R.; Cornuz, M.; Tilley, S. D.; Grätzel, M.; Durrant, J. R. *J. Am. Chem. Soc.* **2014**, *136*, 2564.
 34. Gamelin, D. R. *Nat. Chem.* **2012**, *4*, 965.
 35. Barroso, M.; Mesa, C. A.; Pendlebury, S. R.; Cowan, A. J.; Hisatomi, T.; Sivula, K.; Grätzel, M.; Klug, D. R.; Durrant, J. R. *Proc. Natl. Acad. Sci. USA* **2012**, *109*, 15640.
 36. Peter, L. M.; Wijayantha, K. G. U.; Tahir, A. A. *Faraday Discuss.* **2012**, *155*, 309.
 37. Liang, Y.; Li, Y.; Wang, H.; Zhou, J.; Wang, J.; Regier, T.; Dai, H. *Nat. Mater.* **2011**, *10*, 780.
 38. Zhuo, L.; Ge, J.; Cao, L.; Tang, B. *Cryst. Growth Des.* **2008**, *9*, 1.
 39. He, T.; Chen, D.; Jiao, X.; Wang, Y. *Adv. Mater.* **2006**, *18*, 1078.
-

6.6 REFERENCES

40. Yuming, D.; Kun, H.; Lin, Y.; Aimin, Z. *Nanotechnology* **2007**, *18*, 435602.
 41. Staniuk, M.; Hirsch, O.; Kränzlin, N.; Böhlen, R.; van Beek, W.; Abdala, P. M.; Koziej, D.; *Chem. Mater.* **2014**, *26*, 2086.
 42. Farhadi, S.; Safabakhsh, J.; Zaringhadam, P. *J. Nanostruct. Chem.* **2013**, *3*, 69.
 43. He, T.; Chen, D.; Jiao, X. *Chem. Mater.* **2004**, *16*, 737.
 44. Jana, N. R.; Chen, Y.; Peng, X. *Chem. Mater.* **2004**, *16*, 3931.
 45. Shi, N.; Cheng, W.; Zhou, H.; Fan, T. X.; Niederberger, M. *Chem. Commun.* **2015**, *51*, 1338.
 46. Feckl, J. M.; Fominykh, K.; Döblinger, M.; Fattakhova-Rohlfing, D.; Bein, T. *Angew. Chem. Int. Ed.* **2012**, *51*, 7459.
 47. Fominykh, K.; Feckl, J. M.; Sicklinger, J.; Döblinger, M.; Böcklein, S.; Ziegler, J.; Peter, L.; Rathousky, J.; Scheidt, E. W.; Bein, T.; Fattakhova-Rohlfing, D. *Adv. Funct. Mater.* **2014**, *24*, 3123.
 48. Liu, Y.; Szeifert, J. M.; Feckl, J. M.; Mandlmeier, B.; Rathousky, J.; Hayden, O.; Fattakhova-Rohlfing, D.; Bein, T. *ACS Nano* **2010**, *4*, 5373.
 49. Szeifert, J. M.; Feckl, J. M.; Fattakhova-Rohlfing, D.; Liu, Y.; Kalousek, V.; Rathousky, J.; Bein, T. *J. Am. Chem. Soc.* **2010**, *132*, 12605.
 50. Fominykh, K.; Chernev, P.; Zaharieva, I.; Sicklinger, J.; Stefanic, G.; Döblinger, M.; Müller, A.; Pokharel, A.; Böcklein, S.; Scheu, C.; Bein, T.; Fattakhova-Rohlfing, D. *ACS Nano* **2015**, *9*, 5180.
 51. Peters, K.; Zeller, P.; Stefanic, G.; Skoromets, V.; Neřmec, H.; Kuzel, P.; Fattakhova-Rohlfing, D.; *Chem. Mater.* **2015**, *27*, 1090.
 52. Hadjiev, V. G.; Iliev, M. N.; Vergilov, I. V. *J. Phys. C* **1988**, *21*, L199.
 53. Biesinger, M. C.; Payne, B. P.; Grosvenor, A. P.; Lau, L. W. M.; Gerson, A. R.; Smart, R. S. C. *Appl. Surf. Sci.* **2011**, *257*, 2717.
-

54. Dunn, H. K.; Feckl, J. M.; Müller, A.; Fattakhova-Rohlfing, D.; Morehead, S. G.; Roos, J.; Peter, L. M.; Scheu, C.; Bein, T. *Phys. Chem. Chem. Phys.* **2014**, *16*, 24610.
55. Cesar, I.; Sivula, K.; Kay, A.; Zboril, R.; Grätzel, M. *J. Phys. Chem. C* **2008**, *113*, 772.
56. Sivula, K.; Zboril, R.; Le Formal, F.; Robert, R.; Weidenkaff, A.; Tucek, J.; Frydrych, J.; Grätzel, M.; *J. Am. Chem. Soc.* **2010**, *132*, 7436.
57. McDonald, K. J.; Choi, K.-S. *Chem. Mater.* **2011**, *23*, 4863.
58. Lin, F.; Boettcher, S. W. *Nat. Mater.* **2014**, *13*, 81.
59. Mills, T. J.; Lin, F.; Boettcher, S. W. *Phys. Rev. Lett.* **2014**, *112*, 148304.
60. Sauerbrey, G. *Z. Phys.* **1959**, *155*, 206.
61. Esswein, A. J.; McMurdo, M. J.; Ross, P. N.; Bell, A. T.; Tilley, T. D. *J. Phys. Chem. C* **2009**, *113*, 15068.
62. Trotochaud, L.; Ranney, J. K.; Williams, K. N.; Boettcher, S. W. *J. Am. Chem. Soc.* **2012**, *134*, 17253.
63. Yang, X.; Du, C.; Liu, R.; Xie, J.; Wang, D. *J. Catal.* **2013**, *304*, 86.
64. Soedergren, S.; Hagfeldt, A.; Olsson, J.; Lindquist, S.-E. *J. Phys. Chem.* **1994**, *98*, 5552.
65. Trotochaud, L.; Mills, T. J.; Boettcher, S. W. *J. Phys. Chem. Lett.* **2013**, *4*, 931.
66. Esswein, A. J.; McMurdo, M. J.; Ross, P. N.; Bell, A. T.; Tilley, T. D. *J. Phys. Chem. C* **2009**, *113*, 15068.

6.7 SUPPORTING INFORMATION

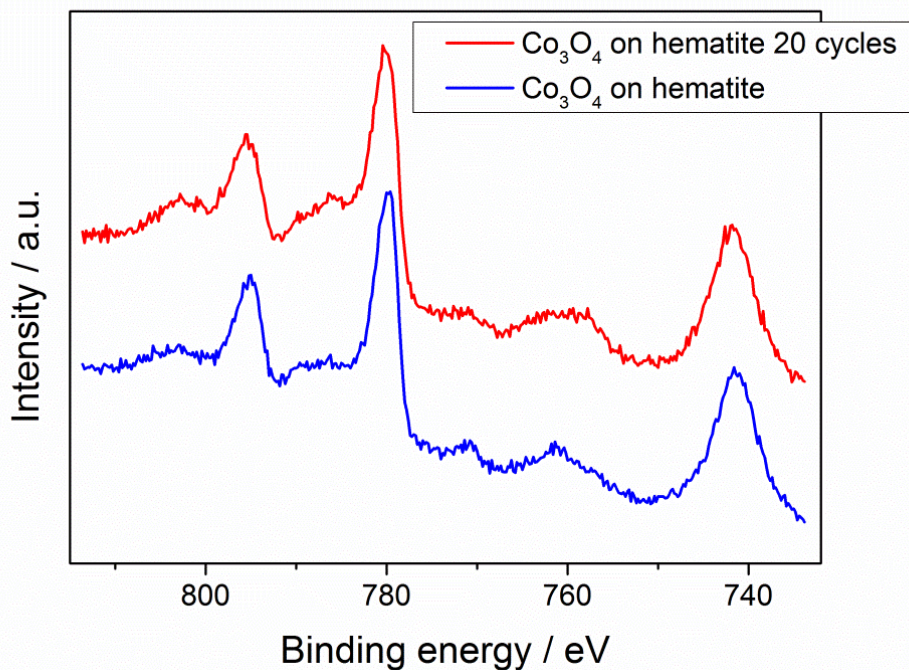


Figure S6.1 XPS spectra of cobalt oxide nanoparticles deposited on top of Sn-doped hematite electrodes before and after 20 cyclic voltammetry scans under 455 nm illumination, incident photon flux $10^{17} \text{ cm}^{-2} \text{ s}^{-1}$. The XPS spectra exhibit the Auger transitions of oxygen at 742 and 761 eV and the Co 2p signals that are split by spin-orbit coupling into Co 2p_{3/2} (779.9 eV) and 2p_{1/2} (795.0 eV).

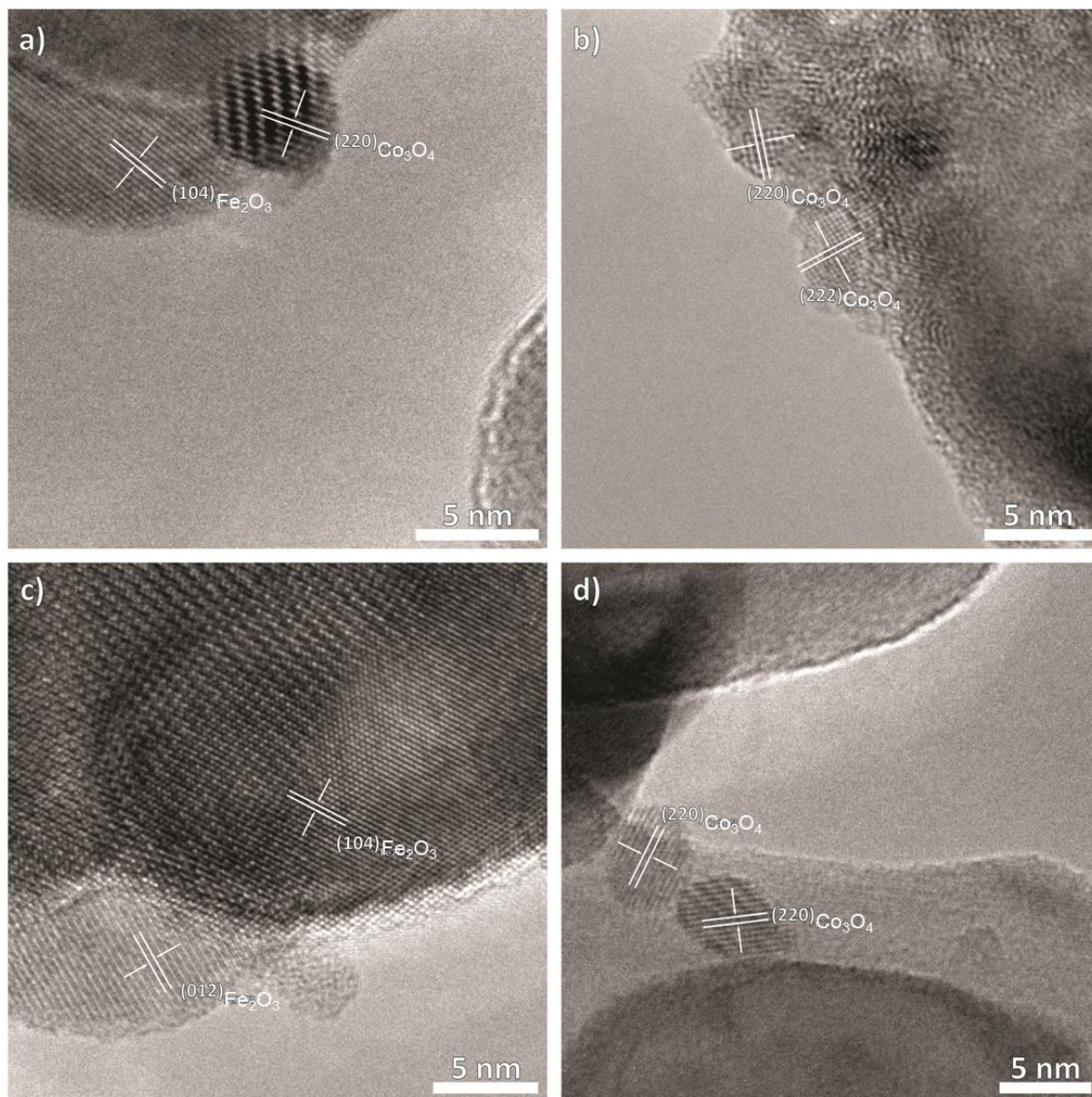


Figure S6.2 HR-TEM images of the cobalt oxide nanoparticle-treated mesoporous hematite layers removed from the substrate. Rare occurrences of agglomerates (c) that could be observed in addition to individual nanoparticles (b) are most likely a result of nanoparticles being caught in pores during the drop-casting process.

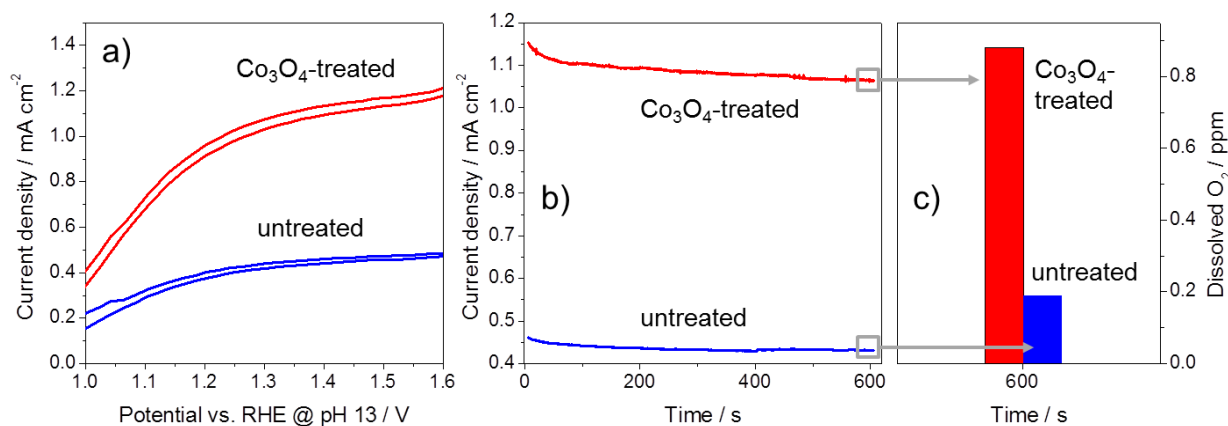


Figure S6.3 (a) Cyclic voltammograms of tin-doped hematite films on FTO with (red line) and without (blue line) Co₃O₄ treatment. (b) Potentiostatic measurements on untreated (blue) and Co₃O₄-treated (red) tin-doped hematite samples at 1.56 V vs. RHE over 10 minutes. (c) Amount of dissolved oxygen in electrolyte after 10 minute measurement at 1.56 V vs. RHE and under illumination (455 nm LED, with about 10^{17} cm⁻² s⁻¹ intensity).

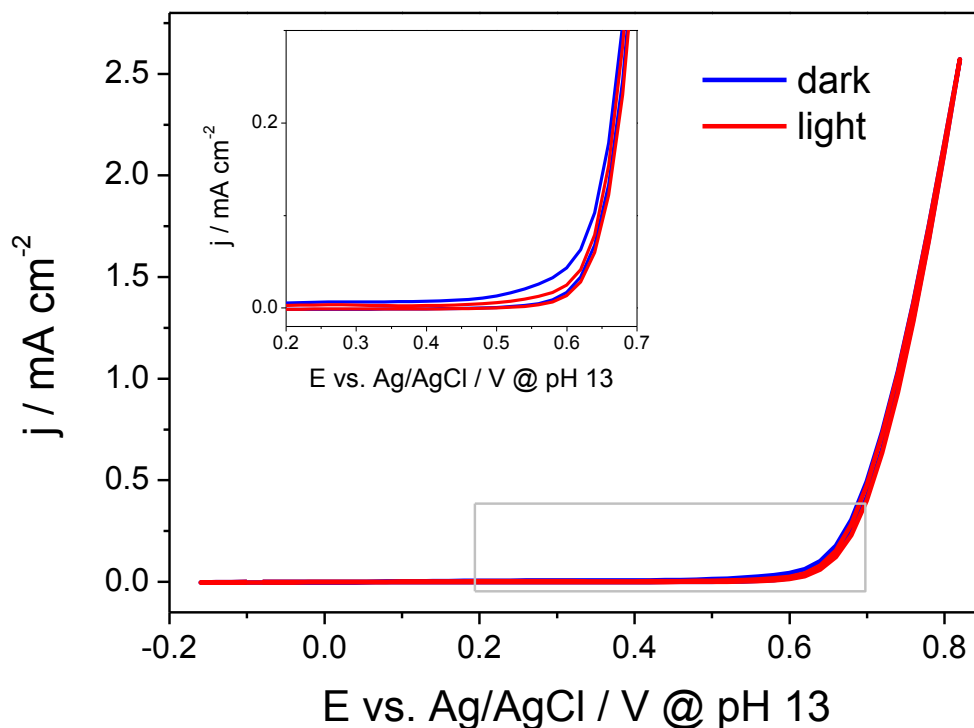


Figure S6.4 Cyclic voltammograms of a Co₃O₄ treated (red) FTO electrode in the dark (blue) and under illumination (455 nm LED, with about 10^{17} cm⁻² s⁻¹ intensity) (red). An inset shows a zoomed area marked in grey.

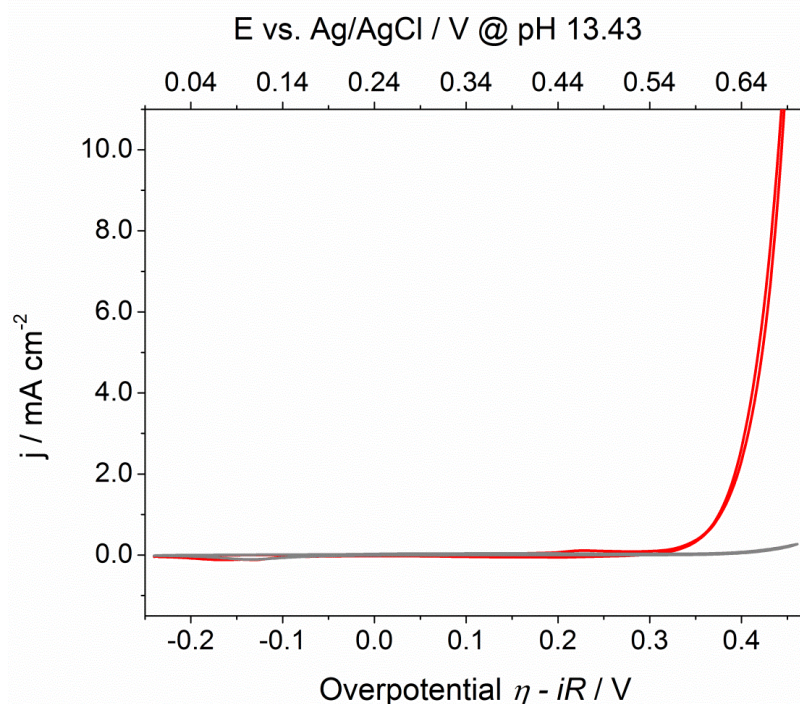


Figure S6.5 Dark CV curves of a Co_3O_4 electrode prepared on a Au/QCM crystal (red line) and a bare Au/QCM crystal (grey line). The electrodes were cycled vs. Ag/AgCl in 0.5 M KOH with the scan rate of 20 mV s^{-1} . The reduction peak at the potential of ca. 0.1 V vs. Ag/AgCl corresponds to the Au electrode and is visible in both CV curves.

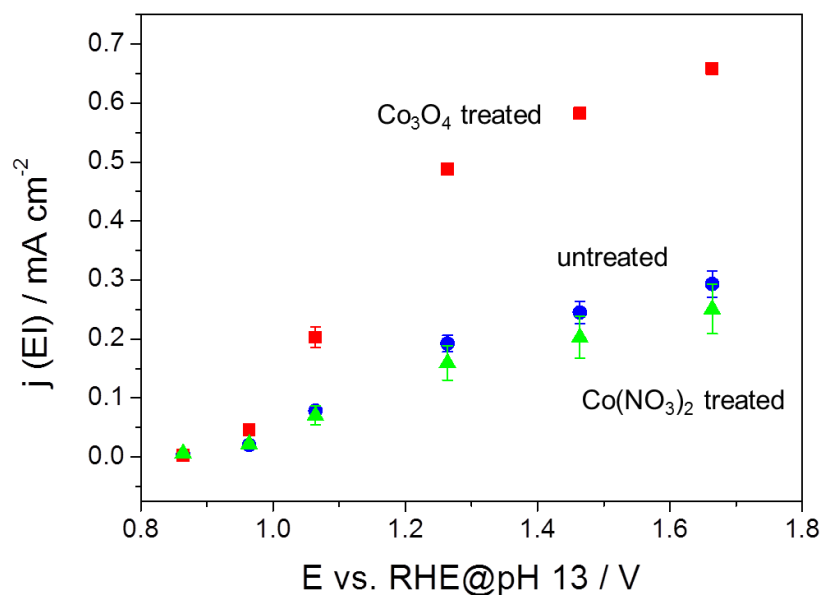


Figure S6.6 Steady state photocurrent under 455 nm illumination with about $10^{17} \text{ cm}^{-2} \text{ s}^{-1}$ intensity from the electrolyte side of 150 nm Sn-doped hematite films (blue), as well as identical films treated with Co_3O_4 (red) and $\text{Co}(\text{NO}_3)_2$ (green).

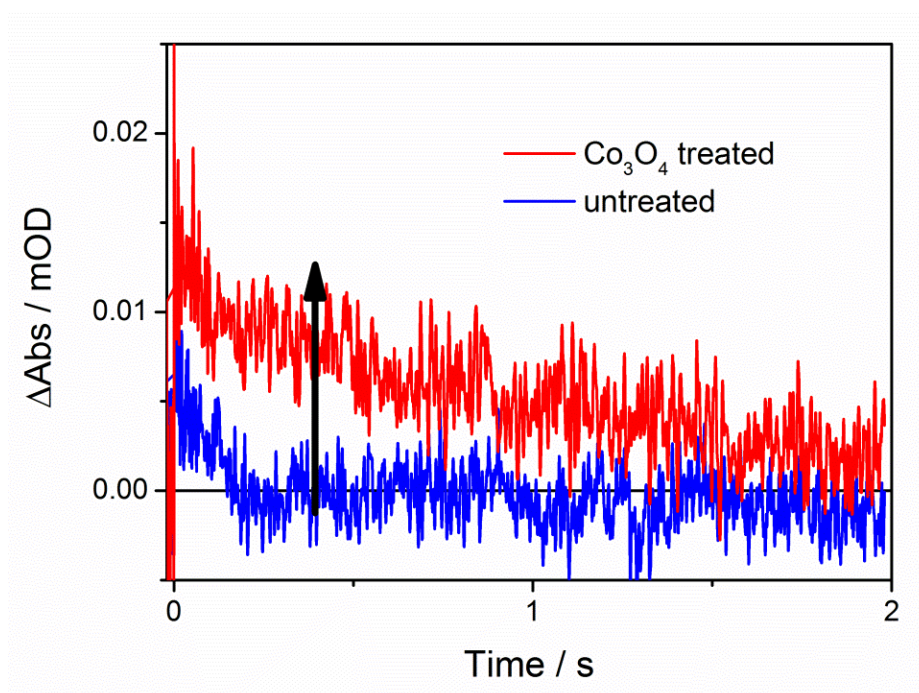


Figure S6.7 Dynamics of surface-accumulated photogenerated holes in untreated (blue) and Co₃O₄ treated (red) thin (50 nm) hematite photoanodes at open circuit in 1 M NaOH, excited at 455 nm and probed at 650 nm, shown on a linear time-axis. The arrow indicates the increase in lifetime of photogenerated holes after treatment with Co₃O₄.

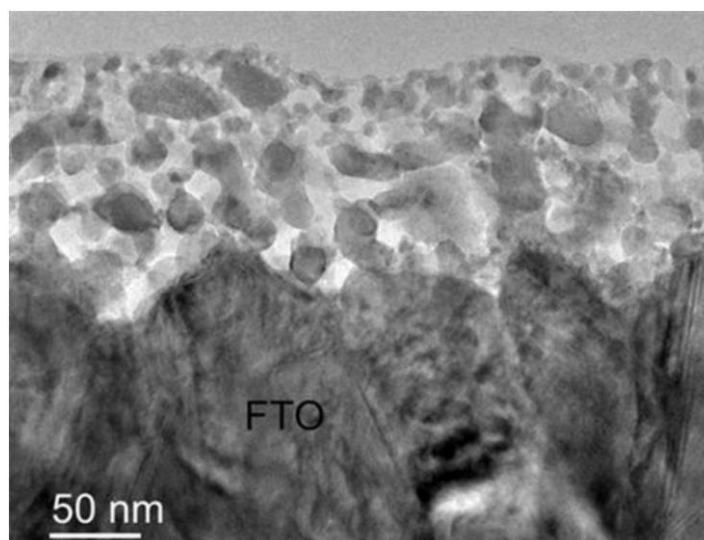


Figure S6.8 TEM cross-section image of mesoporous Sn-containing hematite film on FTO substrate.

**7 SINGLE PHASE DOPED
IRON OXYHYDROXIDE
NANOCRYSTALS
INCORPORATING
EXTRAORDINARY HIGH
AMOUNTS OF
DIFFERENT ELEMENTS**

Ksenia Fominykh, Daniel Böhm, Alena Folger, Markus Döblinger, Christina Scheu, Thomas Bein and Dina Fattakhova-Rohlfing.

7.1 ABSTRACT

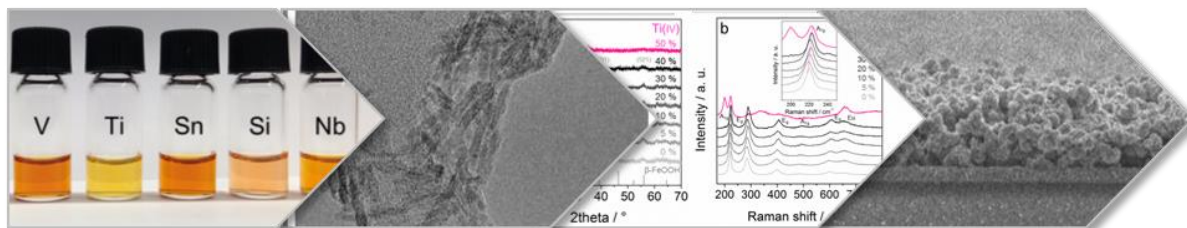


Figure 7.1 ToC image demonstrating the dispersibility, crystallinity, phase composition and elongated shape of the β -FeOOH nanoparticles doped with various elements. The nanocrystals assemble *in situ* to mesoporous hierarchical films with tunable thickness.

Dispersible non-agglomerated akaganeite (β -FeOOH) nanocrystals doped with various elements in different oxidation states (Co(II), Ni(II), V(III), Ti(IV), Sn(IV), Si(IV), Nb(V)) were prepared using a microwave assisted solvothermal synthesis in *tert*-butanol. Divalent ions could reach doping concentrations of 15 at%, whereas atoms with higher oxidation states are incorporated in concentrations of up to 40 at%. The high doping concentration is attributed to the kinetic control of the phase formation during the solvothermal reaction. Depending on the doping element, different crystal shapes were observed in transmission electron microscopy (TEM) ranging from spherical 4 nm particles to nanorods with 4 nm in width and up to 100 nm in length. The particles are perfectly dispersible in water giving stable colloidal dispersions that can be deposited on different substrates to produce 35 – 250 nm thin films. Additionally, 2.9 μ m thick films consisting of interconnected mesoporous spheres can be prepared *in situ* during the reactions. The nanostructures assembled from akaganeite nanocrystals can be topotactically transformed to hematite (α -Fe₂O₃) by heating between 480 °C and 600 °C without losing the morphology, which can be used for the fabrication of doped hematite nanostructures. The tunable properties of the doped akaganeite nanoparticles make them excellent candidates for a wide range of applications as well as versatile building blocks for the fabrication of doped hematite nanomorphologies.

7.2 INTRODUCTION

Nanostructured iron oxides and oxyhydroxides are intensively investigated materials for different areas of technology because of their semiconducting properties in combination with abundance, stability and low toxicity.¹⁻⁸ Akaganeite (β -FeOOH) is one of the iron oxyhydroxide polymorphs that is widely used in electrocatalysis, lithium-ion batteries and ion-exchange applications.^{7,9-11} Its crystal structure has monoclinic symmetry and forms a tunnel matrix of double chains of edge-sharing Fe(III)O₃(OH)₃ octahedra. The channels are usually occupied by chloride ions or other halogenides that were found to be essential for the stabilization of the tunnel structure and therefore for the formation of β -FeOOH.^{10,12-14} Due to the intrinsically elongated tunnel-type structure, akaganeite particles preferentially adopt a rodlike shape.^{1,15,16} The thermal stability of akaganeite is rather low and hence it easily undergoes phase transition to the more stable hematite (α -Fe₂O₃).^{1,15,17-19} An interesting feature of this transformation is its topotactic character, meaning that the morphology of the parent akaganeite structure is retained in the resulting hematite.^{1,17,20} This fact was exploited by several groups to fabricate anisotropically shaped nanostructured hematite photoanodes exhibiting very good performances for photoelectrochemical (PEC) water oxidation.^{1,6,8,15,18,21-23}

The most common method to produce akaganeite structures is the hydrolysis of aqueous FeCl₃ solutions at low pH upon heating to 70 – 100 °C.^{4,12,24-26} This process is generally very fast resulting in rather large particles of up to 500 nm in size.^{12,25} To overcome this issue other wet chemical routes such as coprecipitation, microemulsion, surfactant mediation and solvothermal syntheses were applied to effectively reduce the crystal dimensions.^{4,7,14,15,26,27} In this way also particles with morphologies different from the preferred rodlike shape were obtained, including stars and spheres.^{4,26,28} The microemulsion technique was shown to be the most suitable for fabricating very small nanoparticles of only a few nanometers in size.²⁶ Although significant progress has been achieved in controlling the dimensions and shape of the akaganeite nanomorphologies, the dispersibility of the reported nanoparticles still remains a serious issue as the particles obtained by different methods are typically strongly agglomerated.²⁶⁻²⁸

Besides nanoscaling, the development of synthesis strategies giving access to doped akaganeite nanostructures was pursued by several groups.^{15,24,25,28} Doping with different

elements is an efficient tool to tune the morphology and corresponding physico-chemical properties of akaganeite and the resulting hematite. Doping of akaganeite with Co(II), Ti(IV), Si(IV) was reported using hydrolysis of aqueous precursor solutions at room temperature, but the maximum doping level was rather low reaching only around 4 at%^{24,25,28}

In the present study we report the fabrication of very small crystalline and dispersible non-agglomerated akaganeite nanoparticles with a tunable particle shape using a novel solvothermal microwave reaction in *tert*-butanol. The developed method enables incorporation of Co(II), Ni(II), V(III), Ti(IV), Sn(IV), Si(IV) and Nb(V) into the β -FeOOH crystal lattice with very high concentrations reaching 40 at%. The maximum doping level and the nanomorphology of the nanocrystals ranging from spheres to high-aspect ratio nanorods are strongly influenced by the nature of the incorporated ions. Furthermore, the particles are suitable for the preparation of porous hierarchical hematite films, which are of interest for applications in photoelectrochemical devices.

7.3 RESULTS AND DISCUSSION

Nanocrystals of akaganeite (β -FeOOH) were synthesized *via* a microwave assisted solvothermal reaction in *tert*-butanol (*t*BuOH). The formation of the β -FeOOH phase strongly depends on the choice of the Fe precursor (Figure S7.1a in the supporting information). Since halogen ions are necessary to stabilize the tunnel structure of the akaganeite phase, it was formed only when iron chloride ($\text{FeCl}_3 \cdot 6\text{H}_2\text{O}$) was used as a precursor.²⁵ The corresponding XRD analysis in Figure S7.1a in the supporting information shows a single phase β -FeOOH pattern. The average size of the crystalline domains calculated from the broadening of the (310) peak corresponds to around 8 nm. To further decrease the particle dimensions, the reaction parameters were optimized. Figure S7.1b in the supporting information shows XRD patterns of selected powders obtained at different reaction conditions. By reducing the temperature from 120 °C to 80 °C and the microwave radiation power from 1200 W to 120 W it was possible to reduce the crystal size to around 4.6 nm according to XRD analysis. The same conditions were kept for all further reactions to investigate the influence of various dopant elements, namely Co(II), Ni(II), V(III), Ti(IV), Sn(IV), Si(IV) and Nb(V), on the composition, size and morphology of the particles. Further in the text we use the term dopant

for these additives, whilst noting that the levels of their incorporation are many orders of magnitude higher than those encountered in classical semiconductor physics.

The possibility of incorporating dopant ions into the β -FeOOH lattice and the maximum doping level depend on different factors, among which the nature of the dopants, their ionic radii and the charge are expected to play a major role. Generally, the ions with the same or slightly smaller size than Fe(III) in the akaganeite structure are not expected to cause much lattice strain and should be incorporated more readily than larger ions. The ionic radii of the different elements investigated in this work are listed in Table 7.1. Furthermore, the charge of incorporated ions can influence the maximum doping level. An excess of positive charge induced by ions with an oxidation state higher than +III can be easily balanced by incorporated Cl^- or OH^- ions in the akaganeite structure, as was discussed by different groups.^{21,28} In contrast, lower valence ions would reduce the total charge that should be compensated by the uptake of counter cations, which is however less preferential.²⁹ Besides the structural factors, synthesis parameters such as reaction conditions and reactivity of the precursors affect the maximum doping level and the phase purity. To ensure a similar reactivity with FeCl_3 , the dopant ions were introduced as nitrate or chloride salts in the reaction mixtures with the exception of Ti(IV) because of the very high reactivity of TiCl_4 .

The structural composition of the doped akaganeite materials was investigated by X-ray diffraction (XRD) and Raman spectroscopy, although the β -FeOOH phase was found to be very sensitive to the Raman laser beam ($\lambda = 633 \text{ nm}$, 10 mW). Apparently, a phase transition from akaganeite to the thermodynamically more stable hematite is caused by the laser during the measurement (see the time resolved Raman study in Figure S7.2 in the supporting information) as was also reported by other groups.^{30,31} Despite this fact, Raman spectroscopy can be used for an indirect analysis of phase composition of doped compounds due to its sensitivity to crystalline impurities. Detection of a phase-pure hematite spectrum can therefore be interpreted as an indication of phase purity of the parent akaganeite sample. The structure and morphology of β -FeOOH doped with different ions is described in greater detail in the following. The doped samples are assigned as AX, where A is the dopant element and X is the doping concentration in at% (for example Sn10 for β -FeOOH doped with 10 at% Sn).

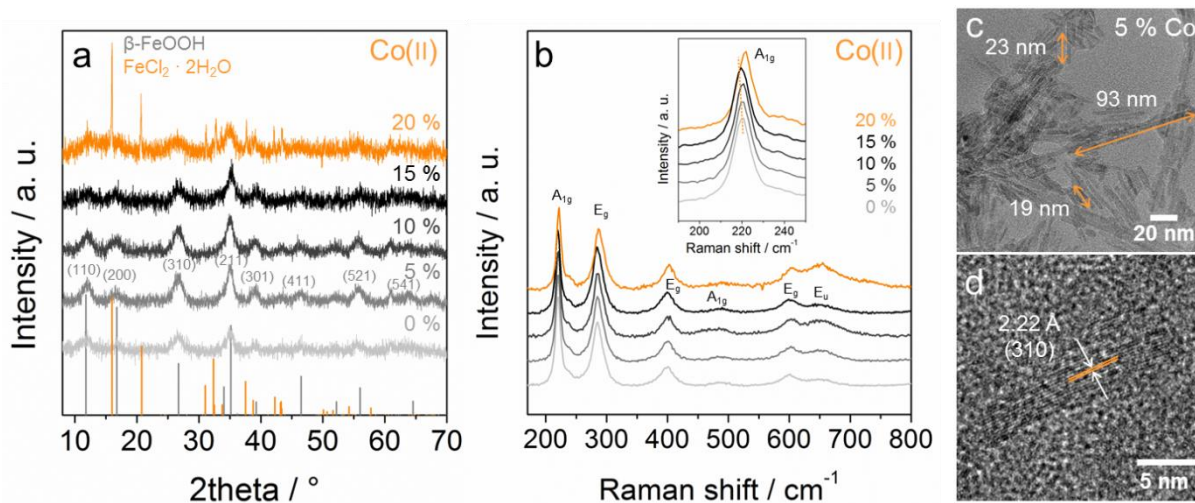
β -FeOOH containing divalent Co(II) and Ni(II) ions

Figure 7.2 Structural and morphological analysis of Co(II) doped β -FeOOH nanocrystals. (a) XRD patterns, β -FeOOH pattern ICDD card number 01-075-1594 (grey line), $\text{FeCl}_2 \cdot 2\text{H}_2\text{O}$ pattern ICDD card number 01-072-0268 (orange lines) and (b) Raman spectra of the Co0 – Co20 powders. The bands at 221 cm^{-1} (A_{1g}), 237 cm^{-1} (E_g), 284 cm^{-1} (E_g), 398 cm^{-1} (E_g), 489 cm^{-1} (A_{1g}), 601 cm^{-1} (E_g) and 649 cm^{-1} (E_u) correspond to hematite.^{30,31} The band at 654 cm^{-1} is assigned to the water libration mode in $\text{FeCl}_2 \cdot 2\text{H}_2\text{O}$.³² The numbers indicate the Co amounts in at%. TEM images of (c) several Co5 nanoparticles and (d) a single Co5 nanocrystal.

Addition of $\text{Co}(\text{NO}_3)_2$ to the reaction mixture leads to a formation of Co(II)-doped β -FeOOH nanoparticles incorporating up to 15 at% cobalt ions. XRD patterns of Co5 – Co15 powders (Figure 7.2a) show a phase pure akaganeite structure, while in the corresponding Raman spectra only the hematite bands are visible.^{30,31} Furthermore, the hematite peaks in the Raman spectra of Co5 – Co15 particles are slightly shifted compared to that of undoped akaganeite (for instance the A_{1g} mode at 221 cm^{-1} shifts to 219 cm^{-1} (see inset in Figure 7.2b) indicating successful incorporation of Co(II) ions into the β -FeOOH lattice. Further increase in Co doping however leads to the formation of an additional $\text{FeCl}_2 \cdot 2\text{H}_2\text{O}$ phase visible in the XRD patterns as well as in the Raman spectra.

High-resolution transmission electron microscopy (HRTEM) images of the cobalt doped particles Co5 are shown in Figures 7.2c, d and S7.5c in the supporting information. The crystals exhibit an anisotropic rod-like shape with around 4 nm in width and 20 nm in length

giving an average aspect ratio of 5/1. The smaller particles comprise the major part of the sample, however a few 90 – 100 nm long rods with the same width are observed as well. The corresponding electron diffraction (ED) pattern can be indexed according to the β -FeOOH phase (Figure S7.5a in the supporting information). The TEM image of a typical particle in Figure 7.2d shows its elongated shape with a crystal growth perpendicular to the (310) direction.

Similar results are obtained when $\text{Ni}(\text{NO}_3)_2$ is added instead of $\text{Co}(\text{NO}_3)_2$ to the reaction mixture, although the incorporation level and the phase purity of the Ni(II)-doped akaganeite are lower than those of the Co(II)-doped material. XRD patterns (Figure S7.4a in the supporting information) show the presence of only one phase structurally similar to β -FeOOH for up to 20 at% Ni. Beyond this concentration, $\text{NiCl}_2 \cdot 2\text{H}_2\text{O}$ is formed as an additional phase and the yield of β -FeOOH is decreased, respectively. Raman spectra (Figure S7.4b in the supporting information) reveal that a nickel ferrite (NiFe_2O_4)³³ impurity is formed already at low Ni contents of 5 and 10 at%. However, hematite is still the dominating phase indicating that mainly akaganeite is formed in the reaction. The band shift to lower wavenumbers from Ni0 to Ni10 indicates successful incorporation of Ni(II) into the β -FeOOH lattice (inset in Figure S7.4b). In the spectrum of Ni20, the intensity of the hematite signals is significantly reduced and nickel ferrite is the dominating phase. Beyond 20 at% the hematite bands vanish completely and only nickel ferrite is visible.

From the above results we conclude that, the divalent ions Co(II) and Ni(II) can be incorporated into the β -FeOOH structure with a maximum concentration of 15 at% for both elements (Figures 7.2a, b and S7.4a, b in the supporting information). Ni(II)-doped samples contain some nickel ferrite impurities. This may be associated with the lower oxidation state and the larger ionic radii of dopant ions compared to Fe(III) in akaganeite (mismatch of 14 % and 7 % for Co(II) and Ni(II), respectively).

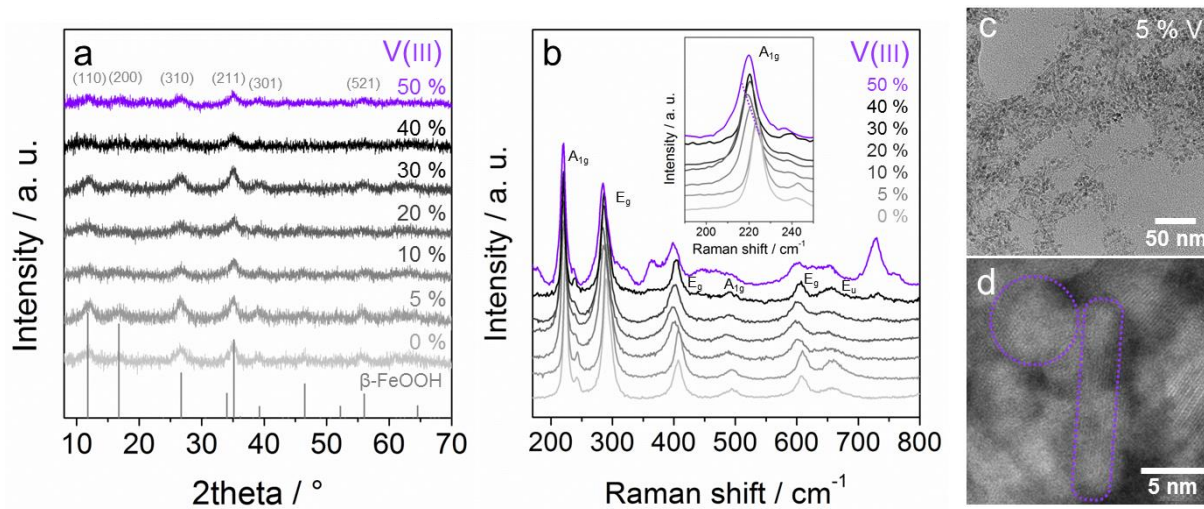
β -FeOOH containing trivalent V(III) ions

Figure 7.3 Structural and morphological analysis of V(III) doped β -FeOOH nanocrystals. (a) XRD patterns and (b) Raman spectra of the V0 – V50 powders. β -FeOOH pattern ICDD card number 01-075-1594 (grey lines). The numbers indicate the V amounts in at%. (c) TEM images of a large number of V5 nanoparticles. (d) STEM image of a few V5 nanocrystals.

Trivalent vanadium was examined as another possible dopant for β -FeOOH. V(III) not only has the same oxidation state but also an ionic radius that closely matches that of Fe(III). Therefore, it may be expected to substitute iron up to high concentrations. Indeed, XRD patterns of V(III) doped samples show phase-pure akaganeite structure for V concentrations of up to 50 at% (Figure 7.3a). The Raman spectra reveal phase-pure hematite structure for V5 – V20 with a shift to lower wavenumbers indicating successful incorporation (Figure 7.3b). However, for higher V levels of 30 at% the Raman spectra indicate the formation of an additional iron vanadate (FeVO_4) phase, although at low amounts.^{34,35} The bands corresponding to FeVO_4 increase for the higher vanadium concentration and become very distinct for the V50 samples.^{34,35} Therefore, the maximum doping concentration of V(III) without phase separation is 20 at% according to the Raman analysis, although β -FeOOH is still formed to a large extent even for high V content in the range of 30 – 50 at% and a shift in the Raman signals is observed for up to 30 at%.

Incorporation of V(III) into β -FeOOH has a strong impact on the particle morphology. TEM and scanning transmission electron microscopy (STEM) images of V5 in Figures 7.3c, d

reveal that the nanorod-like shape typical for the undoped β -FeOOH is practically not present and mostly spherical particles are formed. A few crystals exhibit elongated shape but they are much smaller than the Co(II)-doped crystals, with around 10 nm in length and an average aspect ratio of 2.3/1. The average size of the crystalline domains estimated from the line broadening in XRD patterns is around 4.8 nm, in good agreement with the TEM data.

β -FeOOH containing tetravalent Ti(IV), Sn(IV) and Si(IV) ions

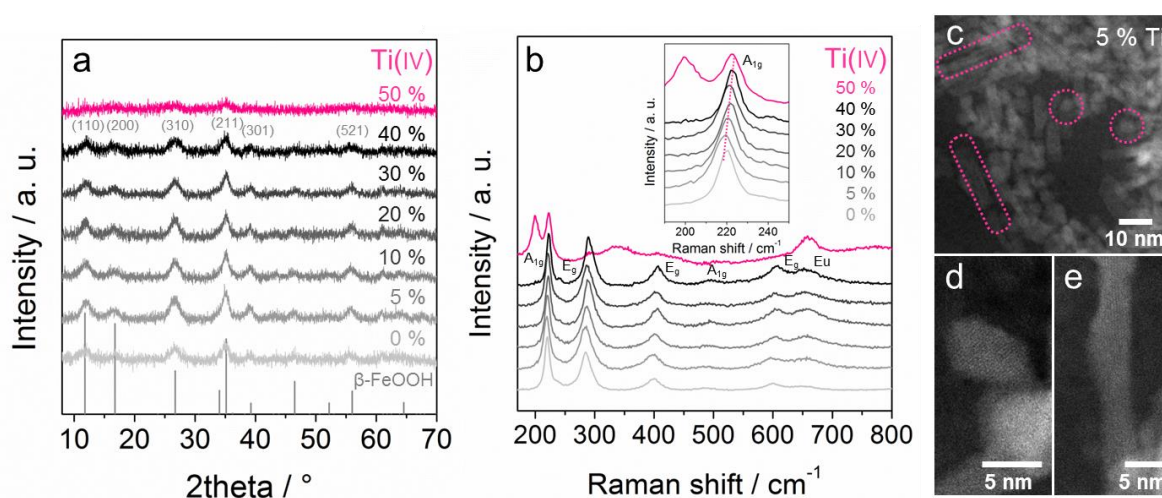


Figure 7.4 Structural and morphological analysis of Ti(IV) doped β -FeOOH nanocrystals. (a) XRD patterns and (b) Raman spectra of the Ti0 – Ti50 powders. β -FeOOH pattern ICDD card number 01-075-1594 (grey lines). The numbers indicate the Ti amounts in at%. STEM image of (c) a large number of Ti5 nanoparticles, (d) a single near spherical Ti5 nanoparticle and (d) a single Ti5 nanorod.

Incorporation of tetravalent Ti, Sn and Si ions into β -FeOOH is particularly interesting with regard to the properties of the resulting hematite, for which doping with these elements was shown to greatly improve its photoanode performance in solar water splitting.^{22,36-41} For the nanocrystals synthesized in the presence of Ti(IV), XRD patterns exclusively show reflections of akaganeite for Ti5 – Ti50 (Figure 7.4a). However, the broadening of the reflections is significantly higher for Ti50, indicating decrease in the particle size for this Ti content. The Raman spectra in Figure 7.4b show hematite structure for Ti5 – Ti40 with a continuous shift of the hematite bands to higher wavenumbers for increasing Ti content. For a Ti content

exceeding 40 at%, the hematite bands vanish almost completely and FeTiO_3 bands arise at 200 cm^{-1} , 223 cm^{-1} , 337 cm^{-1} and 658 cm^{-1} .⁴² 40 at% can be therefore considered as the solubility limit for Ti(IV) in the β - FeOOH structure, which is much higher than that of the Co(II), Ni(II) and V(III) ions described above. We tentatively attribute this finding to the Ti(IV) ionic radius of 74.5 pm, which is slightly smaller than that of Fe(III).

Similar to the V(III)-containing β - FeOOH described above, incorporation of Ti(IV) has a strong impact on particle morphology even at low concentrations. The STEM images of Ti5 particles in Figures 7.4c – e show a mixture of nanorods and spherical particles. The fraction of nanocrystals with elongated shape with an aspect ratio of 5.1/1 is higher than for the V doped sample. Figures 7.4d, e show single particles with different shapes and widths of around 5 nm.

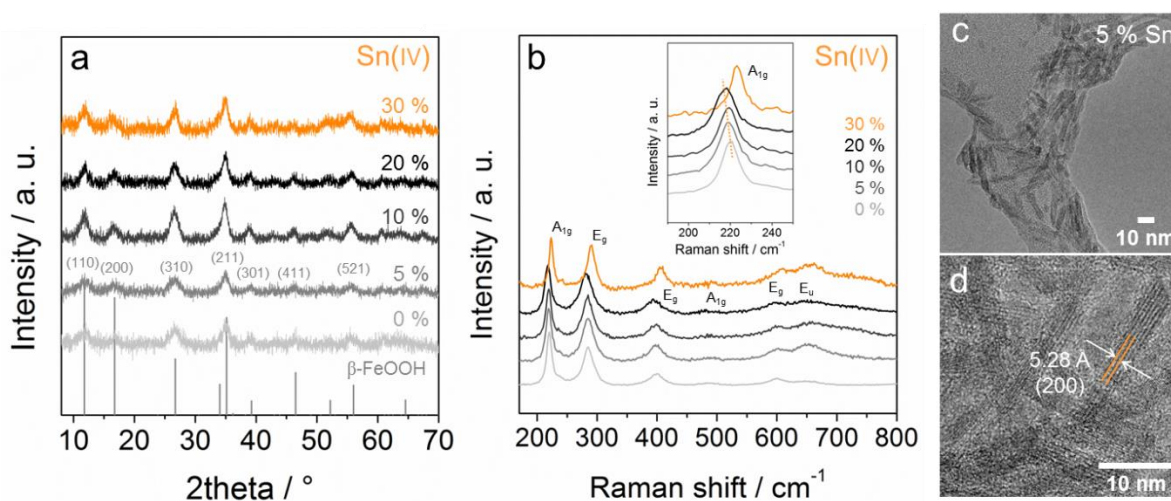


Figure 7.5 Structural and morphological analysis of Sn(IV) doped β - FeOOH nanocrystals. (a) XRD patterns and (b) Raman spectra of the Sn0 – Sn30 powders. β - FeOOH pattern ICDD card number 01-075-1594 (grey lines). The numbers indicate the Sn amounts in at%. (c) TEM overview image of a large number of Sn5 nanoparticles. (d) TEM image of a few Sn5 nanocrystals.

Sn(IV) and Si(IV) exhibit similar behavior as dopant elements in the akaganeite structure. For Sn0 – Sn30 as well as for Si0 – Si25 only the akaganeite phase is present in the XRD patterns (Figures 7.5a and S7.4c in the supporting information), and only the hematite phase is

detected in the Raman spectra without phase separation (Figures 7.5b and S7.4d in the supporting information).

The maximum doping concentration of Sn(IV) exceeds that of Ni(II), despite the same ionic radius of 83 pm. TEM images of Sn5 particles (Figures 7.5c, d and S7.5) reveal their uniform elongated shape with an average aspect ratio of 6.7/1. With increasing Sn content the particle shape becomes less anisotropic. For Sn20 particles the average aspect ratio is significantly reduced to 2.5/1 (Figures S7.3e, f in the supporting information). The ED pattern in Figure S7.5b in the supporting information corresponds to the akaganeite phase, confirming the XRD results. The lattice analysis of several crystals reveals that the preferred growth direction is parallel to the (200) planes (HRTEM image in Figure 7.5d).

β -FeOOH nanoparticles containing pentavalent Nb(v) ions

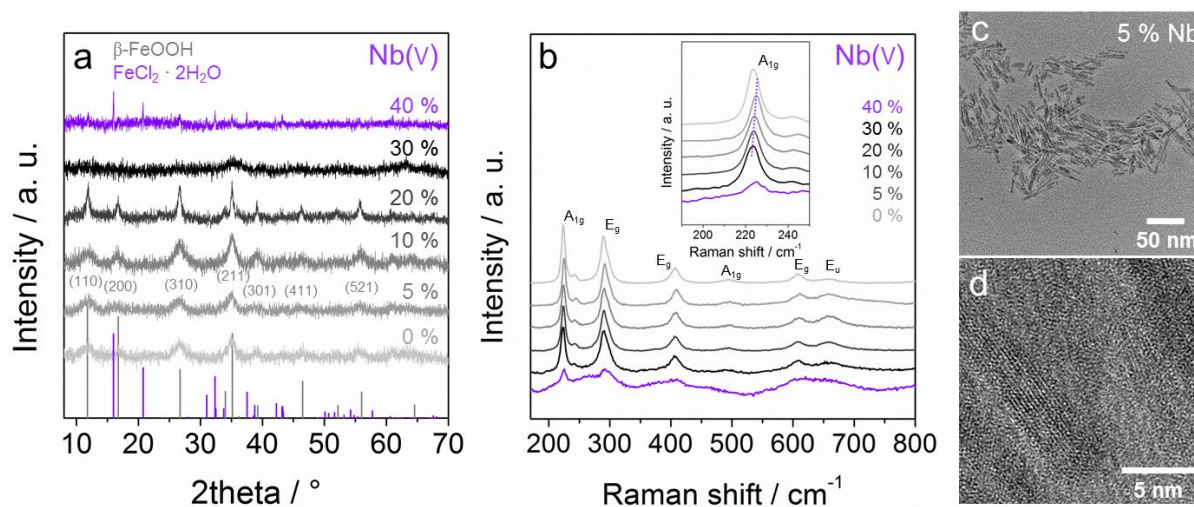


Figure 7.6 Structural and morphological analysis of Nb(v) doped β -FeOOH nanocrystals. (a) XRD patterns and (b) Raman spectra of the Nb0 – Nb40 powders. β -FeOOH pattern ICDD card number 01-075-1594 (grey lines). $\text{FeCl}_2 \cdot 2\text{H}_2\text{O}$ pattern ICDD card number C00-072-0268 (violet lines). The numbers indicate the Nb amounts in at%. (c) TEM overview image of a large number of Nb5 nanoparticles. (d) TEM image of a single Nb5 nanocrystal.

According to XRD and Raman measurements, phase-pure akaganeite nanocrystals containing Nb(v) are obtained for up to 30 at% Nb ions (Figures 7.6a, b). The high Nb uptake may be

attributed to its ionic radius of 78 pm matching that of Fe(III). Furthermore, Raman spectra exhibit a consistent shift of hematite bands to higher wavenumbers with increasing Nb content, pointing to successful incorporation of Nb(v) into the β -FeOOH structure. The XRD-based particle size continuously increases from 4.6 to 16 nm in the range of Nb0 to Nb20, respectively, which was not observed for other dopants where the particle size remained rather constant. Interestingly, the mean particle size decreases to around 3 nm for Nb30 at the same reaction conditions. The TEM images of Nb5 in Figures 7.6c, d demonstrate uniform anisotropic crystal morphology with shorter lengths than Sn5 (in the range of 13 nm) and an aspect ratio of 4.3/1. For the Nb40 sample the presence of $\text{FeCl}_2 \cdot 2\text{H}_2\text{O}$ and a significantly reduced intensity of the hematite bands are detected in the XRD patterns and in the Raman spectra, respectively.

Table 7.1 Precursors and ionic parameters of Fe(III) and the dopant elements. Maximum doping concentrations and particle morphology.

Dopant	Ionic radius / pm	Precursor	Max. doping concentration (XRD) / %	Max. doping concentration (Raman) / %	Nanoparticle shape	Aspect ratio
Fe(III)	78.5	$\text{FeCl}_3 \cdot 6\text{H}_2\text{O}$	–	–	–	–
Co(II)	88.5	$\text{Co}(\text{NO}_3)_2 \cdot 6\text{H}_2\text{O}$	15	15	Rods	5/1
Ni(II)	83	$\text{Ni}(\text{NO}_3)_2 \cdot 6\text{H}_2\text{O}$	20	15	–	–
V(III)	78	VCl_3	50	20	Spheres	2.3/1
Ti(IV)	74.5	$\text{Ti}(\text{O}i\text{Bu})_4$	50	40	Spheres + rods	5.1/1 (rods)
Sn(IV)	83	$\text{SnCl}_4 \cdot 5\text{H}_2\text{O}$	30	30	Rods	6.7/1
Si(IV)	54	SiCl_4	25	25	–	–
Nb(V)	78	NbCl_5	30	30	Rods	4.3/1

Table 7.1 summarizes the main results of the structural analysis along with the particle morphology obtained from TEM. The results demonstrate the suitability of the microwave-assisted synthesis in *t*BuOH enabling the fabrication of dispersible phase-pure crystalline akaganeite nanoparticles that can incorporate various transition metal ions in very high concentrations. The highest doping concentrations of up to 40 at% were obtained for V(III), Ti(IV) and Nb(v) ions. The lowest uptake limit of 15 at% was observed for the divalent Co(II) and Ni(II) ions. The dopant/Fe atomic ratios within the particles were verified by energy dispersive X-ray spectroscopy (EDX). Examples of V, Ti and Sn doped single particles analyzed by EDX are demonstrated in Figure S7.3 in the supporting information. Noticeably, doping contents reported in literature for akaganeite (around 4 at%) are much lower than these values.^{15,24,25,28,43} We can therefore hypothesize that an ultrasmall crystallite size can play an

important role in the formation of unusual structural compositions in mixed oxides and an increased solubility of the dopants.^{24,36,43} Several groups have previously described the formation of thermodynamically less stable phases that only exist on the nanoscale.⁴⁴⁻⁴⁶ The different dopants have a strong impact on the size and morphology of the β -FeOOH nanocrystals. In most cases an elongated nanorod-like shape exhibiting different aspect ratios was observed. This type of particle morphology was often reported for akaganeite and other iron oxyhydroxides.^{4,15,25,27,16} The particle lengths described in the literature are, however, mostly in the range of 100 – 500 nm which is far larger than the dimensions observed in the present study.

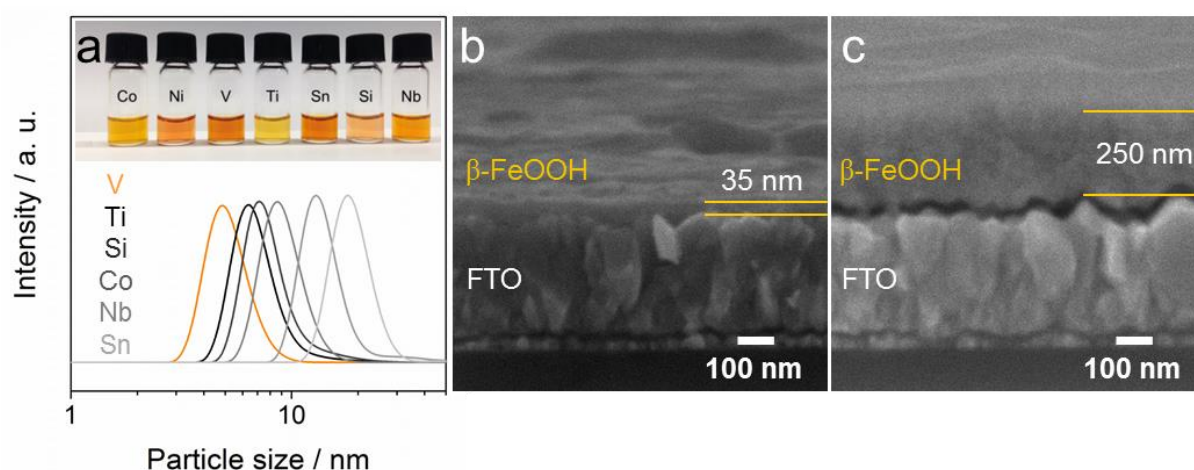


Figure 7.7 Dispersibility of doped β -FeOOH crystals and preparation of thin films. (a) DLS curves of dispersions containing different dopants (the color code of the dopants is consistent with the curves). Inset: photograph of doped β -FeOOH nanoparticle dispersions in water (concentration 2 mg mL^{-1}). The dispersions are denoted with the respective dopant element. SEM side view images of β -FeOOH thin films prepared using (b) a 2 mg mL^{-1} and (c) a 10 mg mL^{-1} nanoparticle dispersion.

A remarkable feature of the nanosized akaganeite particles described above is their excellent dispersibility without agglomeration. Even dried powders can be redispersed in water and water/ethanol ($\text{H}_2\text{O}/\text{EtOH}$) mixtures after the addition of very small amounts of acetic acid (HOAc) in the μL range. An image of particle dispersions with different dopants is shown in the inset in Figure 7.7a. The perfect dispersibility of the crystals is demonstrated by dynamic light scattering (DLS) measurements. Selected examples are shown in Figure 7.7a revealing effective particle sizes in the range between 5 nm and 18 nm. It should be noticed that

unambiguous size determination with DLS is only possible for spherical particles. For β -FeOOH crystals with elongated shape, DLS gives the size of a sphere calculated from the measured translational diffusion coefficient. Thus different diameters of up to 22 nm were often recorded for the same samples. Nevertheless, DLS provides a good approximation of the particle size and shows the high quality of the akaganeite dispersions.

Colloidal nanoparticle dispersions can be coated on different substrates to give homogeneous thin films. Figures 7.7b, c show side view scanning electron microscopy (SEM) images of nanoparticle films prepared *via* spin coating on FTO substrates. The film thickness can be varied between 35 nm and 250 nm by applying different particle concentrations between 2 mg mL^{-1} and 10 mg mL^{-1} , respectively. The thickness is homogeneous over a large area as shown in Figures S7.6a, b in the supporting information.

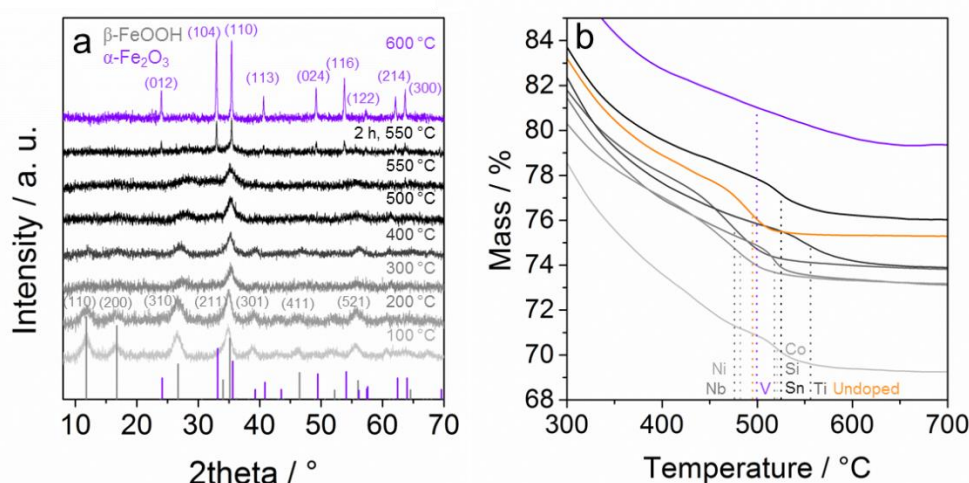


Figure 7.8 (a) XRD heating study of undoped β -FeOOH particles with a step size of 100°C below 500°C and 50°C above 500°C , respectively. (b) TGA curves of undoped and doped β -FeOOH samples in the range of $25 - 900^\circ\text{C}$. The doping concentration for all doped samples is 10 at%.

Upon thermal treatment in air the nanocrystals undergo a phase change from the monoclinic akaganeite to the hexagonal hematite structure. Phase transition temperatures reported in the literature are mostly in the range of 300°C .^{17,18,21} Post *et al.* described a mechanism for the phase transition where akaganeite continuously releases water and chloride ions which leads to reduced cell parameters and degradation of the crystalline structure that becomes completely amorphous at around 300°C . Crystalline hematite with large domain size is

formed afterwards upon further increase in temperature.²¹ Interestingly, the β -FeOOH nanocrystals described in the present study do not form any detectable amorphous phases with increasing temperature. Figure 7.8a illustrates an XRD heating study of the undoped crystals where XRD patterns were recorded with a step size of 100 °C and a dwell time of 30 min for each step. The patterns reveal an increasing particle size from 4.6 nm at 100 °C to 5 nm at 200 °C, the akaganeite structure however remains unchanged. At higher temperatures between 300 °C and 500 °C the (211) reflection becomes very pronounced while the (110), (200) and (521) reflections gradually lose intensity. Furthermore, (310) and (211) shift to higher and (521) to lower angles, respectively, with increasing temperature indicating the formation of intermediate phases. For instance, the (211) reflection shifts from 34.0° to 35.4° which is the hematite (110) peak position. In contrast to literature findings with larger crystal sizes the phase transition to α -Fe₂O₃ was observed in the high temperature range between 500 °C and 600 °C which was therefore investigated in greater detail with a step size of 50 °C. At 550 °C the hematite (110) peak appears with low intensity. After 2 h heating at the same temperature the hematite pattern becomes more pronounced, however the broad signal at $2\theta = 35^\circ$ indicates the presence of an intermediate mixed phase. At 600 °C the transition to hematite is complete showing only hematite signals with a large crystalline domain size of 50 nm.

Mass losses and phase transformations of differently doped particles were investigated using thermogravimetric analysis (TGA) and differential scanning calorimetry (DSC) curves (Figures 7.8b and S7.7 in the supporting information). Phase transition to hematite takes place at around 500 °C for the undoped particles; however this temperature is significantly influenced by introducing dopant elements. For instance nanocrystals containing 10 at% of Nb(V) undergo the phase transition already at around 470 °C and Ti(IV) doping leads to a much higher transition temperature of around 550 °C. The V(III) containing sample shows a mass loss in a very broad temperature range between 400 °C and 600 °C. This should be taken into account when preparing hematite structures from akaganeite building blocks. Generally, the heating study clearly demonstrates an increased thermal stability of the doped β -FeOOH nanocrystals compared to the akaganeite structures described in the literature. Nevertheless, the thermally induced phase transformation provides a facile way to fabricate doped hematite films starting from the akaganeite nanocrystals. Thus the β -FeOOH films shown in

Figures 7.7b, c can be used for the fabrication of crystalline α -Fe₂O₃ thin films by heating in air.

Additionally, akaganeite thick films can be grown *in situ* on FTO substrates directly during the microwave reactions. The SEM images in Figures 7.9a, c, e shows a β -FeOOH film in different magnifications. The film exhibits disordered macroporous morphology with a film thickness of 4.2 μ m consisting of interconnected akaganeite spheres (SEM cross-section in Figure 7.9a). The average size of the spheres is relatively large (750 nm). However, the XRD-based domain size is still in the range of a few nanometers indicating that the small akaganeite nanocrystals act as building blocks for the macro-spheres.

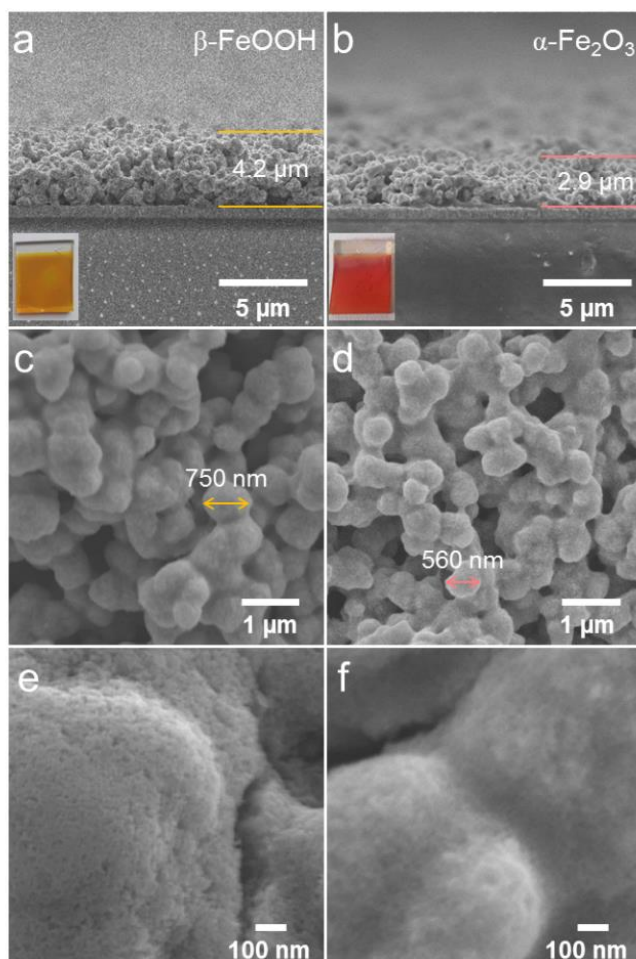


Figure 7.9 SEM images of a β -FeOOH film grown *in situ* during the microwave reaction. (a, c, e) Different magnifications of the as-prepared β -FeOOH film. (b, d, f) Different magnifications of the film after annealing at 600 °C and phase transition to α -Fe₂O₃.

7.4 CONCLUSION

The high resolution image reveals that the spheres are mesoporous with pore sizes of around 10 nm (Figure 7.9e). The different dopants have no significant influence on the morphology and thickness of the films showing similar porous structures for all samples. An interesting feature of this process is a possibility to fabricate thick stable films. By increasing the reaction time to 2.5 h even 30 μm thick films could be obtained (Figure S7.8 in the supporting information). Calcination of akaganeite films at 600 $^{\circ}\text{C}$ results in the formation of hematite layers. The insets in Figures 7.9a, b show photographs of the non-heated and heated films with the typical dark yellow akaganeite and bright red hematite color, respectively. The corresponding SEM images in Figures 7.9b, d, f demonstrate that the initial film morphology and the mesoporous structure of the spheres remain preserved during the heating process. However, the spheres shrink to around 560 nm leading to a reduction of total film thickness by 22 % (to 2.9 μm). In general, all the films prepared from dispersions or *in situ* during the synthesis are very homogeneous showing a complete coverage over a large area as demonstrated in the SEM overview images in Figures S7.6 and S7.9 in the supporting information. The unique porous morphology retained even after heating to 600 $^{\circ}\text{C}$ and phase transformation to $\alpha\text{-Fe}_2\text{O}_3$ make the $\beta\text{-FeOOH}$ nanoparticles excellent starting materials for the fabrication of hematite films.

7.4 CONCLUSION

The microwave-assisted synthesis in *t*BuOH enables the fabrication of dispersible phase-pure crystalline $\beta\text{-FeOOH}$ akaganeite nanoparticles that can incorporate various metal ions. This reaction method allows for a kinetic control of the particle formation resulting in ultrasmall particle sizes and increased solubility of dopants in oxide phases. Additionally the uptake level was influenced by the oxidation state of the dopants showing the lowest contents of 15 at% for divalent Co(II) and Ni(II) and maximum concentration of 40 at% for the tetravalent Ti(IV) without losing the structural integrity of akaganeite. We note that literature values for larger crystallite sizes are in the range of 1–4 at% for several doped $\beta\text{-FeOOH}$ structures.^{15,24,25,28,43} The nanomorphology of the akaganeite nanocrystals was influenced by the dopant as well and ranged from nearly spherical with 5 at% V to nanorod-like with an aspect ratio of 5/1 for 5 at% Sn. The particles can be used for film fabrication, whereby different film thicknesses are possible ranging from several nanometers for the films prepared

from particle dispersions to several micrometers for the films grown *in situ* during the solvothermal reaction. Investigation of thermal behavior of the akaganeite nanoparticles revealed a phase transition to hematite at different temperatures between 480 °C and 600 °C depending on the incorporated doping element. The tunable properties *via* incorporation of different metal ions makes the akaganeite nanoparticles attractive candidates for a variety of applications as well as the preparation of doped hematite nanostructures.

7.5 EXPERIMENTAL SECTION

7.5.1 SYNTHESIS OF DOPED IRON OXYHYDROXIDE NANOPARTICLES

Iron(III) chloride hexahydrate ($\text{FeCl}_3 \cdot 6\text{H}_2\text{O}$) (Sigma-Aldrich, ACS reagent, 97 % purity), cobalt(II) nitrate hexahydrate ($\text{Co}(\text{NO}_3)_2 \cdot 6\text{H}_2\text{O}$) (Sigma-Aldrich, ≥ 98 % purity), nickel(II) nitrate hexahydrate ($\text{Ni}(\text{NO}_3)_2 \cdot 6\text{H}_2\text{O}$) (Sigma-Aldrich, purum, ≥ 97 % purity), vanadium(III) chloride (VCl_3) (Aldrich, 97 % purity), titanium(IV) butoxide ($\text{Ti}(\text{O}i\text{Bu})_4$) (Sigma-Aldrich, reagent grade, 97 % purity), tin(IV) chloride pentahydrate ($\text{SnCl}_4 \cdot 5\text{H}_2\text{O}$) (Sigma-Aldrich, 98 % purity), silicon(IV) chloride (SiCl_4) (Aldrich, 99 % purity), niobium(v) chloride (NbCl_5) (Alfa Aesar, 99 % purity) were used as received. *tert*-Butanol was purchased from Sigma-Aldrich (puriss. p.a., ACS reagent, ≥ 99.7 %), dried over a 4 Å molecular sieve at 28 °C and filtered prior to use. For the solvothermal microwave assisted synthesis of metal (M)-doped β -FeOOH nanoparticles (M = Co, Ni, V, Ti, Sn, Si, Nb), $\text{FeCl}_3 \cdot 6\text{H}_2\text{O}$ was mixed with the dopant precursor in the desired molar composition while the total amount of the metal precursors was kept at a constant value of 0.6 mmol. The dopant concentration c_M was calculated using the equation

$$c_M = \frac{n_M}{0.6 \text{ mmol}} \quad (7.1)$$

with n_M being the molar amount of the metal dopant precursor. As an example, for the synthesis of $\text{Sn}_{0.2}\text{Fe}_{0.8}\text{OOH}$ nanocrystals 129.7 mg (0.48 mmol) of $\text{FeCl}_3 \cdot 6\text{H}_2\text{O}$ was mixed with 42.1 mg (0.12 mmol) of $\text{SnCl}_4 \cdot 5\text{H}_2\text{O}$. The solid mixtures were added to 14 mL *tert*-butanol in a microwave Teflon vessel forming a yellow to rusty-red suspension depending on the dopant, then placed into a ceramic microwave reactor and hermetically sealed. The reactions were carried out under vigorous stirring at 80 °C for 1 h resulting in

uniform brown, red or yellow dispersions of nanoparticles. The as-prepared particles were dried in air by evaporating the solvent at 80 °C on a hot plate resulting in M/ β -FeOOH nanopowders exhibiting various particle shapes and sizes.

Dispersions of the M/ β -FeOOH nanoparticles were prepared in water or water/ethanol mixtures with the addition of acetic acid. In a typical dispersion procedure, 1 mg of the dried powder was covered with 500 μ L water (Millipore) and 20 μ L of acetic acid was added to the turbid mixture. After 10 min colloidal dispersions with a metal oxide concentration of 2 mg mL⁻¹ were obtained.

7.5.2 CHARACTERIZATION

Wide angle X-ray diffraction analysis was carried out in transmission mode using a STOE STADI P diffractometer with Cu K $_{\alpha 1}$ radiation ($\lambda = 1.54060 \text{ \AA}$) and a Ge(111) single crystal monochromator equipped with a DECTRIS solid state strip detector Mythen 1K. Powder XRD patterns of the samples were collected with an omega-2theta scan in the 2θ range from 5° to 70° with a step size of 1° and fixed counting time of 90 seconds per step and a resolution of 0.05°. The size of the crystalline domains was calculated from the XRD patterns for the most intensive (310) reflection using the Scherrer equation.

Raman spectroscopy was carried out using a LabRAM HR UV-Vis (HORIBA JOBIN YVON) Raman Microscope (OLYMPUS BX41) with a SYMPHONY CCD detection system and a He-Ne laser ($\lambda = 633 \text{ nm}$). Spectra were recorded using a lens with a 50-fold magnification.

TEM measurements were carried out using a FEI Titan 80–300 instrument equipped with a field emission gun operated at 300 kV. For the sample preparation a drop of a strongly diluted dispersion of a sample in ethanol was deposited on a holey carbon coated copper grid and evaporated. Contaminations were removed by plasma cleaning for 15 s at 50 mW and large-area illumination in the TEM for 40 min.

Dynamic light scattering measurements were performed on a MALVERN Zetasizer-Nano instrument equipped with a 4 mW He-Ne laser (633 nm) and an avalanche photodiode detector.

SEM images were obtained with a JEOL JSM-6500F scanning electron microscope equipped with a field emission gun operated at 5 kV. The films were prepared on Au substrates and glued onto a brass sample holder with silver lacquer.

Thermogravimetric analysis of the samples was performed on a NETZSCH STA 440 C TG/DSC (heating rate of 10 K min⁻¹ in a stream of synthetic air of about 25 mL min⁻¹).

7.5.3 FILM PREPARATION

For film preparation fluorine doped tin oxide coated glass (FTO, TEC 15 Pilkington TEC Glass™, 2.5 × 1.5 cm) was used as conductive substrate. Prior to use the FTO was washed by sequential sonication for 15 min each in detergent (1 mL Extran in 50 mL Millipore water), water (Millipore) and ethanol (absolute) and dried in a N₂ stream. The electrodes were prepared *in situ* by placing the FTO substrates in a specially designed sample holder that allows for magnetic stirring during the microwave reaction while keeping the substrates covered in solution. The M/β-FeOOH films grown in this way were approximately 3 μm thick, exhibiting a porous structure. After the synthesis the non-conductive side of the FTO was cleaned with 1 M hydrochloric acid (HCl), as well as 1 cm of the conductive side leaving a coated area of ca. 1.5 × 1.5 cm. To produce metal doped hematite films the electrodes were subsequently heated to 600 °C in a laboratory oven with a heating ramp of 3.33 °C min⁻¹ and a dwell time of 30 min.

7.6 REFERENCES

1. Kim, J. Y.; Magesh, G.; Youn, D. H.; Jang, J. W.; Kubota, J.; Domen, K.; Lee, J. S. *Sci. Rep.* **2013**, *3*, 2681.
2. Mohapatra, M.; Anand, S. *Int. J. Engin. Sci. Technol.* **2010**, *2*, 127.
3. Song, H.-J.; Liu, L.; Jia, X.-H.; Min, C. *J. Nanoparticle Res.* **2012**, *14*.
4. Wang, X.; Chen, X.; Gao, L.; Zheng, H.; Ji, M.; Tang, C.; Shen, T.; Zhang, Z. *J. Mater. Chem.* **2004**, *14*, 905.

7.6 REFERENCES

5. Yu, L.; Wang, L. P.; Xi, S.; Yang, P.; Du, Y.; Srinivasan, M.; Xu, Z. *J. Chem. Mater.* **2015**, *27*, 5340.
6. Yu, Q.; Meng, X.; Wang, T.; Li, P.; Ye, J. *Adv. Funct. Mater.* **2015**, *25*, 2686.
7. Zhang, X.; Du, Y. *RSC Adv.* **2016**, *6*, 17504.
8. Zong, X.; Thaweesak, S.; Xu, H.; Xing, Z.; Zou, J.; Lu, G. M.; Wang, L. *Phys. Chem. Chem. Phys.* **2013**, *15*, 12314.
9. Chemelewski, W. D.; Lee, H. C.; Lin, J. F.; Bard, A. J.; Mullins, C. B. *J. Am. Chem. Soc.* **2014**, *136*, 2843.
10. Chitrakar, R.; Tezuka, S.; Sonoda, A.; Sakane, K.; Hirotsu, T. *Ind. Eng. Chem. Res.* **2009**, *48*, 2107.
11. Zou, M.; Wen, W.; Li, J.; Lin, Y.; Lai, H.; Huang, Z. *J. Energy Chem.* **2014**, *23*, 513.
12. Carroll, D.; Richmond, W. R. *Am. Mineral.* **2008**, *93*, 1641.
13. Luna, C.; Ilyn, M.; Vega, V.; Prida, V. M.; González, J.; Mendoza-Reséndez, R. *J. Phys. Chem. C* **2014**, *118*, 21128.
14. Parameshwari, R.; Priyadarshini, P.; Chandrasekaran, G. *Am. J. Mater. Sci.* **2011**; *1*, 18.
15. Song, Y.; Bac, B. H.; Lee, Y.-B.; Kim, M. H.; Kang, I. M. *CrystEngComm* **2011**, *13*, 287.
16. Wei, C.; Wang, X.; Nan, Z.; Tan, Z. *J. Chem. Eng. Data* **2010**, *55*, 366.
17. Sayed, F. N.; Polshettiwar, V. *Sci. Rep.* **2015**, *5*, 9733.
18. Klimas, V.; Mažeika, K.; Pakštas, V.; Spudulis, E.; Jagminas, A. *J. Fluorine Chem.* **2015**, *173*, 55.
19. Piao, Y.; Kim, J.; Na, H. B.; Kim, D.; Baek, J. S.; Ko, M. K.; Lee, J. H.; Shokouhimehr, M.; Hyeon, T. *Nat. Mater.* **2008**, *7*, 242.
20. Xavier, A. M.; Ferreira, F. F.; Souza, F. L. *RSC Adv.* **2014**, *4*, 17753.

21. Post, J. E.; Heaney, P. J.; von Dreele, R. B.; Hanson, J. C. *Am. Mineral.* **2003**, *88*, 782.
 22. Liao, P.; Keith, J. A.; Carter, E. A. *J. Am. Chem. Soc.* **2012**, *134*, 13296.
 23. Žic, M.; Ristić, M.; Musić, S. *Mater. Chem. Phys.* **2010**, *120*, 160.
 24. Holm, N. G. *Geologiska Föreningen i Stockholm Förhandlingar* **2010**, *107*, 297.
 25. Ishikawa, T.; Motoki, T.; Katoh, R.; Yasukawa, A.; Kandori, K.; Nakayama, T.; Yuse, F. *J. Colloid Interface Sci.* **2002**, *250*, 74.
 26. Xiaojuan, L.; Yuxiang, Y.; Xiangnong, L.; Hui, Z.; Haiping, Y.; Zheyu, Z.; Yaru, C. *Russ. J. Inorg. Chem.* **2014**, *53*, 367.
 27. Richmond, W. R.; Cowley, J. M.; Parkinson, G. M.; Saunders, M. *CrystEngComm* **2006**, *8*, 36.
 28. Cornell, M. R. *Z. Pflanzenernähr. Bodenk.* **1992**, *155*, 449.
 29. Kozin, P. A.; Boily, J.-F. *J. Phys. Chem. C* **2013**, *117*, 6409.
 30. de Faria, D. L. A.; Silva, S. V.; de Oliveira, M. T. *J. Raman Spectr.* **1997**, *28*, 873.
 31. Jubb, A. M.; Allen, H. C. *ACS Appl. Mater. Interfaces* **2010**, *2*, 2804.
 32. Graf, L. *Solid State Commun.* **1978**, *27*, 1361.
 33. Dixit, G.; Singh, J. P.; Srivastava, R.C.; Agrawal, H. M. Chaudhary, R. J. *Adv. Mater. Lett.* **2012**, *3*, 21.
 34. Zhang, A.-M.; Liu, K.; Ji, J.-T.; He, C.-Z.; Tian, Y.; Jin, F.; Zhang, Q.-M. *Chin. Phys. B* **2015**, *24*, 126301.
 35. Dixit, A.; Lawes, G. *J. Phys.: Condens. Matter* **2009**, *21*, 456003.
 36. Annamalai, A.; Shinde, P. S.; Jeon, T. H.; Lee, H. H.; Kim, H. G.; Choi, W.; Jang, J. *S. Sol. Energy Mater. Sol. Cells* **2016**, *144*, 247.
 37. Lee, M. H.; Park, J. H.; Han, H. S.; Song, H. J.; Cho, I. S.; Noh, J. H.; Hong, K. S. *Int. J. Hydrogen Energy* **2014**, *39*, 17501.
-

7.6 REFERENCES

38. Tamirat, A. G.; Su, W.-N.; Dubale, A. A.; Chen, H.-M.; Hwang, B.-J. *J. Mater. Chem. A* **2015**, *3*, 5949.
39. Wang, L.; Lee, C.-Y.; Schmuki, P. *Electrochem. Commun.* **2013**, *30*, 21.
40. Mirbagheri, N.; Wang, D.; Peng, C.; Wang, J.; Huang, Q.; Fan, C.; Ferapontova, E. E. *ACS Catal.* **2014**, *4*, 2006.
41. Hou, Y.; Zuo, F.; Dagg, A.; Feng, P. *Angew. Chem.* **2013**, *52*, 1248.
42. Raghavender, A. T.; Hoa Hong, N.; Joon Lee, K.; Jung, M.-H.; Skoko, Z.; Vasilevskiy, M.; Cerqueira, M. F.; Samantilleke, A. P. *J. Magn. Magn. Mater.* **2013**, *331*, 129.
43. Tufo, A. E.; García, K. E.; Barrero, C. A.; Sileo, E. E. *Hyperfine Interact.* **2013**, *224*, 239.
44. Fominykh, K.; Cernev. P.; Zaharieva, I.; Sicklinger, J.; Stefanic, G.; Doeblinger, M.; Müller A.; Pokharel, A.; Böcklein, S.; Scheu, C.; Bein, T.; Fattakhova-Rohlfing D. *ACS Nano* **2015**, *9*, 5180.
45. Bau, J. A.; Lubner, E. J.; Buriak, J. M. *ACS Appl. Mater. Interfaces* **2015**, *7*, 19755.
46. Soriano, R. B.; Wu, J.; Kanatzidis, M. G. *J. Am. Chem. Soc.* **2015**, *137*, 9937.

7.7 SUPPORTING INFORMATION

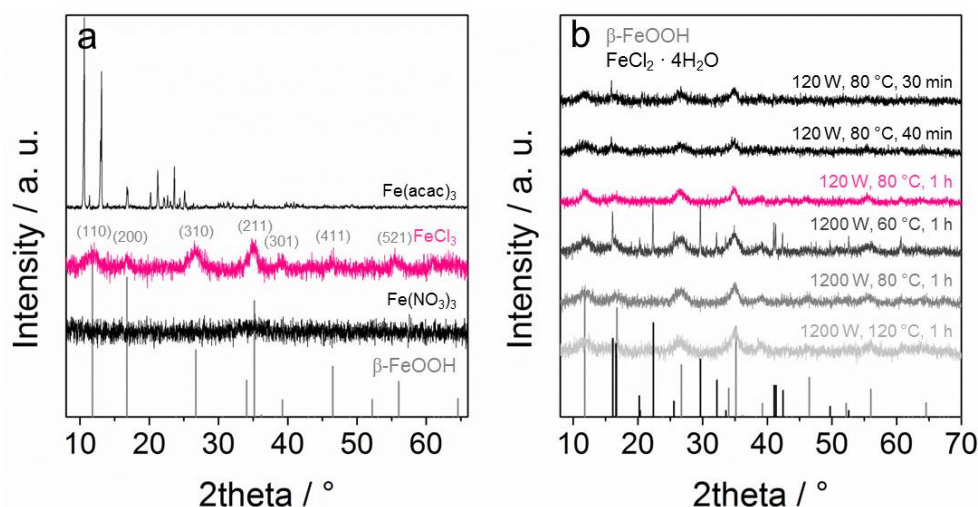


Figure S7.1 Influence of different iron precursors on the formation of akaganeite and variation of reaction conditions. (a) XRD patterns of powders obtained at the same reaction conditions using Fe(NO₃)₃, Fe(acac)₃ (black) and FeCl₃ (pink) as precursors. (b) XRD patterns of samples obtained using FeCl₃·6H₂O at different reaction conditions. The numbers indicate the microwave power in W, temperature in °C and reaction time in hours or minutes. β-FeOOH pattern ICDD card number C01-075-1594 (grey lines). FeCl₂·4H₂O pattern ICDD card number C00-016-0123. (black lines)

The Fe compounds Fe(NO₃)₃, Fe(acac)₃ and FeCl₃ were investigated as precursors for the akaganeite synthesis. The XRD patterns in Figure S7.1a show the formation of β-FeOOH only in case of FeCl₃. Iron nitrate results in an amorphous phase and Fe(acac)₃ did not react at the relatively low temperature of 120 °C, probably because the solubility of iron acetylacetonate in *tert*-butanol is rather low. The sharp reflexes in the XRD pattern correspond to the precursor signals. Figure S7.1b shows XRD patterns of selected powders obtained at different reaction conditions. The initial synthesis was performed at 1200 W microwave power, 120 °C for 1 h and resulted in phase-pure 8 nm β-FeOOH particles (calculated from the (310) peak using the Scherrer equation). To obtain smaller crystals the reaction temperature was reduced to 80 °C and resulted in particle sizes of around 4.6 nm. The further decreased temperature of 60 °C was too low to obtain phase-pure akaganeite, since a second phase corresponding to FeCl₂·2H₂O is visible in the XRD pattern (Figure S7.1b, grey scale). Further reactions were carried out at 80 °C with reduced

microwave radiation power. The smallest particle dimensions of around 5 nm were obtained at 120 W for 1 h (Figure S7.1b, pink). Further decrease in the reaction time to 40 min and 30 min again resulted in a mixture of β -FeOOH and $\text{FeCl}_2 \cdot 2\text{H}_2\text{O}$. The reaction conditions 120 W, 80 °C and 1 h were therefore applied in all following reactions.

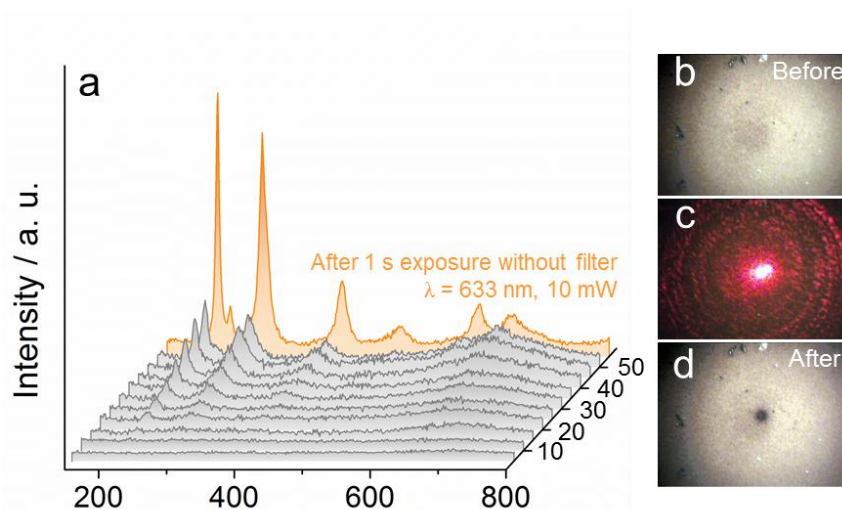


Figure S7.2 Time-resolved Raman investigation of the undoped β -FeOOH powder. (a) Raman spectra recorded every 5 min with a filter reduced intensity of the laser beam (grey). The orange spectrum was taken after exposure of the sample to the laser with full intensity for 1 s. Micrographs of the sample with a 10-fold magnification (b) before, (c) during and (d) after the Raman measurement, showing a dark spot caused by the laser beam.

Figure S7.2 shows an *in situ* time resolved Raman study of the undoped β -FeOOH. The spectra were taken with a time step of 5 min using an intensity-reducing laser filter with an optical density of 0.6 (Figure S7.2a). The signals at 221 cm^{-1} (A_{1g}), 237 cm^{-1} (E_g), 284 cm^{-1} (E_g), 398 cm^{-1} (E_g), 489 cm^{-1} (A_{1g}), 601 cm^{-1} (E_g) and 649 cm^{-1} (E_u) can be assigned to hematite (α - Fe_2O_3) bands. Noticeably, neither β -FeOOH nor any other phases are visible below 10 min irradiation. The hematite spectrum starts to appear after 15 min and becomes gradually more pronounced with extended exposure time. To compare, the unfiltered laser beam immediately leads to the formation of hematite (Figure S7.2a, orange line). Corresponding micrographs recorded before and after the Raman measurement in Figures S7.2b – d show a dark spot occurring at the position where the laser beam was focused. This additionally confirms the structural change.

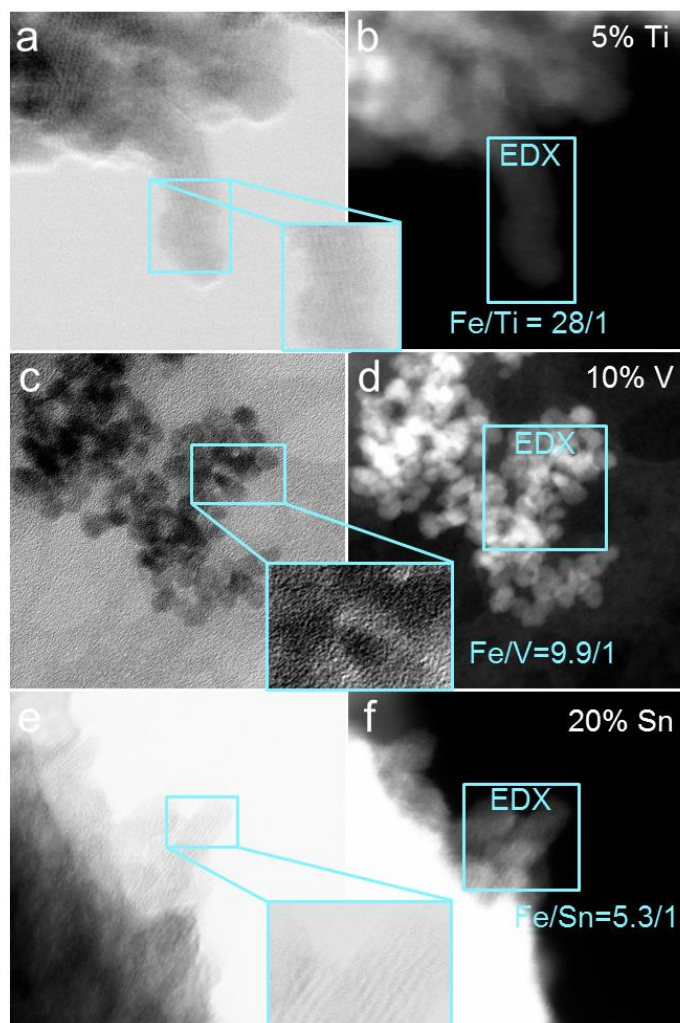


Figure S7.3 Single particle EDX analysis of the selected akaganeite nanoparticles (a, b) Ti5, (c, d) V10 and (e, f) Sn20. The marked range shows the respective area that was exposed to the EDX measurement. The numbers indicate the measured Fe/dopant ratios within the particles.

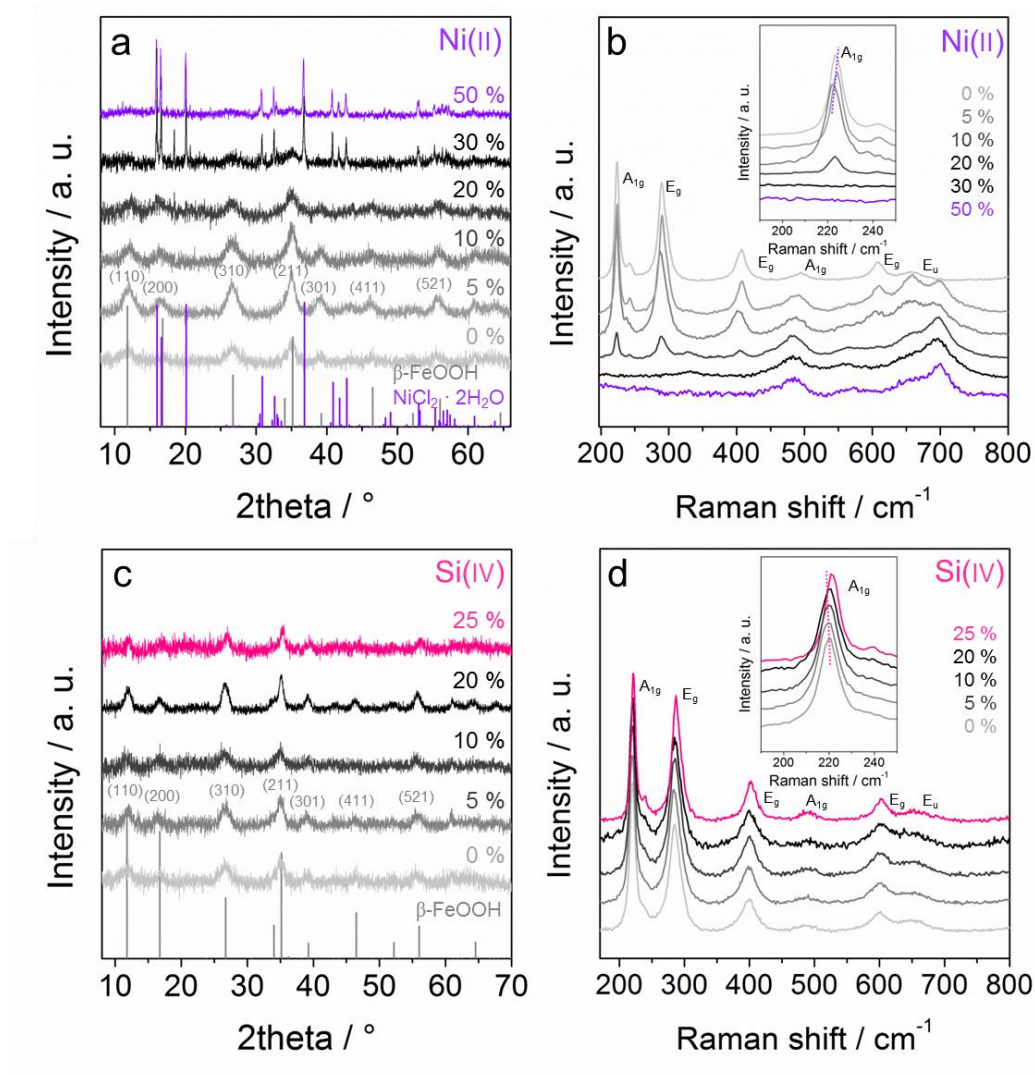


Figure S7.4 Structural analysis of Ni(II) and Si(IV) doped β -FeOOH nanocrystals. (a) XRD patterns and (b) Raman spectra of the Ni0 – Ni50 powders. The bands at 333 cm^{-1} (E_g), 484 cm^{-1} (T_{2g}), 573 cm^{-1} (T_{2g}), 661 cm^{-1} (E_g) and 701 cm^{-1} (A_{1g}) are characteristic for NiFe_2O_4 .¹ (c) XRD patterns and (d) Raman spectra of the Si0 – Si25 powders. The numbers indicate the respective dopant amounts in at%. β -FeOOH pattern ICDD card number 01-075-1594 (grey line). $\text{NiCl}_2 \cdot 2\text{H}_2\text{O}$ pattern ICDD card number 01-072-0044 (violet lines).

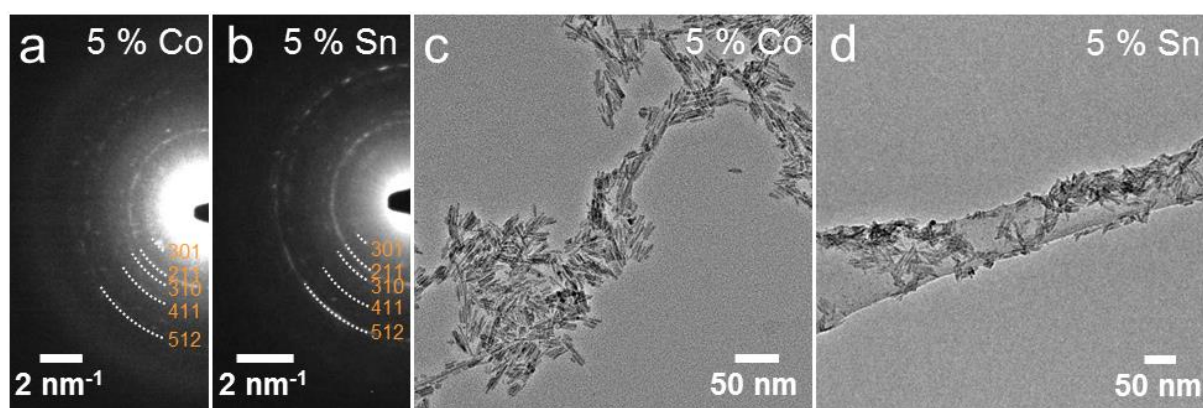


Figure S7.5 Electron diffraction (ED) and transmission electron microscopy (TEM) images of the samples (a, c) Co5 and (b, d) Sn5.

Figures S7.5a, c show electron diffraction (ED) patterns of the samples Co5 and Sn5. The corresponding d-spacings are 3.39 Å (301), 2.59 Å (211), 2.38 Å (310), 1.99 Å (411), 1.69 Å (512) for Co5 and 3.35 Å (301), 2.62 Å (211), 2.37 Å (310), 1.97 Å (411), 1.68 Å (512) for Sn5.

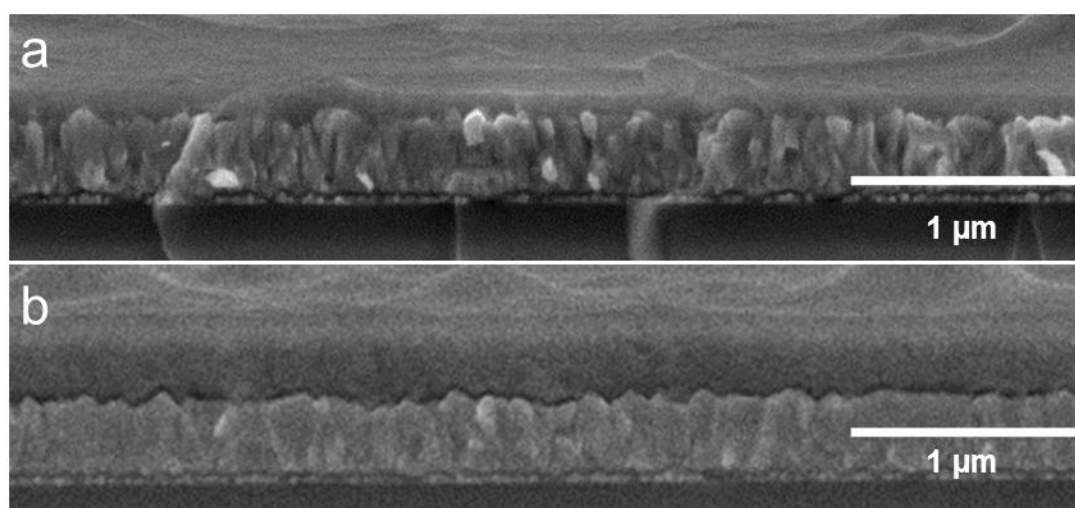


Figure S7.6 SEM images of β -FeOOH films prepared from H₂O/EtOH nanoparticle dispersions with the concentrations of (a) 2 mg mL⁻¹ and (b) 10 mg mL⁻¹.

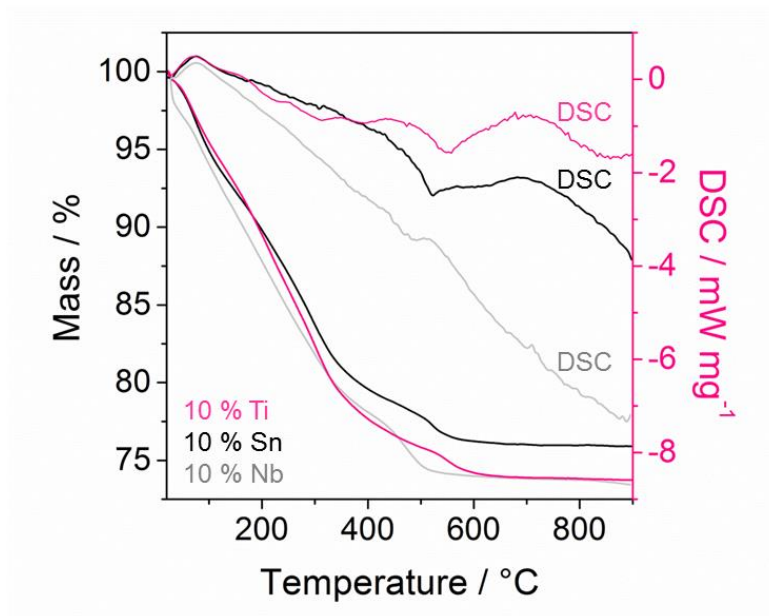


Figure S7.7 TGA and DSC curves of the samples Ti10 (pink), Sn10 (black) and Nb10 (grey).

Thermogravimetric analysis (TGA) and differential scanning calorimetry (DSC) curves of the samples Ti10, Sn10 and Nb10 in Figure S7.7 show several processes that are accompanied by changes in mass. The endothermic process with the mass loss of around 5 % at 100 °C corresponds to evaporation of adsorbed water and is visible for all samples that are stored in air. In the range between 100 and 400 °C all organic parts such as *tert*-butoxide residues are burned off with the greatest mass loss of around 20 %. The exothermic effects with only minor mass losses of 2 – 3 % between 480 and 600 °C are caused by the phase transition into hematite confirming the XRD results.

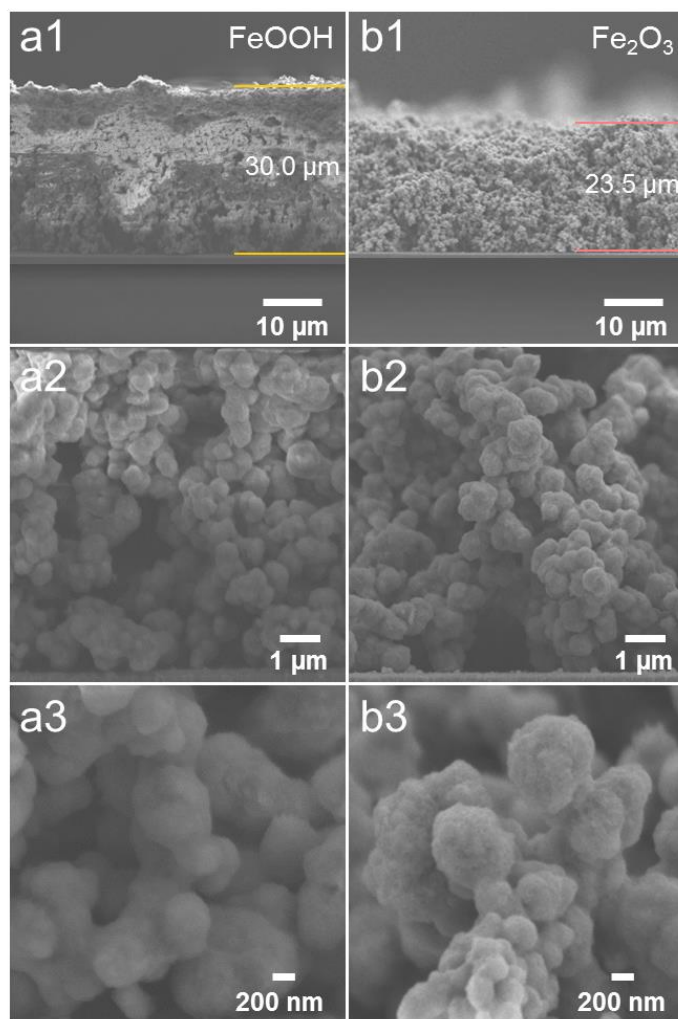


Figure S7.8 SEM images of a thick β -FeOOH film grown *in situ* for 2.5 h during the microwave reaction. (a, c, e) Different magnifications of the as-prepared β -FeOOH film. (b, d, f) Different magnifications of the film after annealing at 600 °C and phase transition to α -Fe₂O₃.

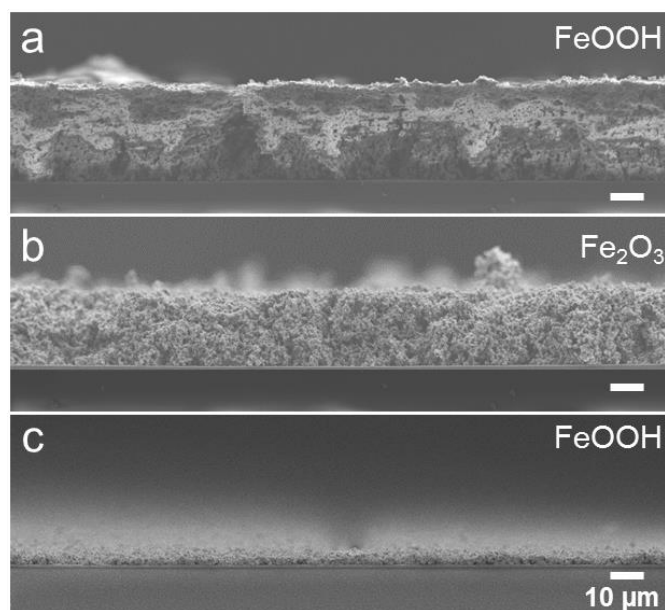


Figure S7.9 SEM images of as prepared β -FeOOH films grown *in situ* during the microwave reaction with the reaction time of (a) 2.5 h and (c) 1 h. (b) SEM image of the film grown *in situ* for 2.5 h after annealing at 600 °C and phase transition to α -Fe₂O₃. The scale bars correspond to the length of 10 μ m.

7.7.1 REFERENCES

1. Dixit, G.; Singh, J. P.; Srivastava, R.C.; Agrawal, H. M. Chaudhary, R. J. *Adv. Mater. Lett.* **2012**, 3, 21.

8 NANOCELLULOSE- ASSISTED FORMATION OF POROUS HEMATITE MORPHOLOGIES

This chapter is based on the following publication:

Alesja Ivanova*, Ksenia Fominykh*, Dina Fattakhova-Rohlfing, Patrick Zeller, Markus Döblinger and Thomas Bein *Inorg. Chem.* **2015**, *54*, 1129.

* these authors contributed equally

8.1 ABSTRACT

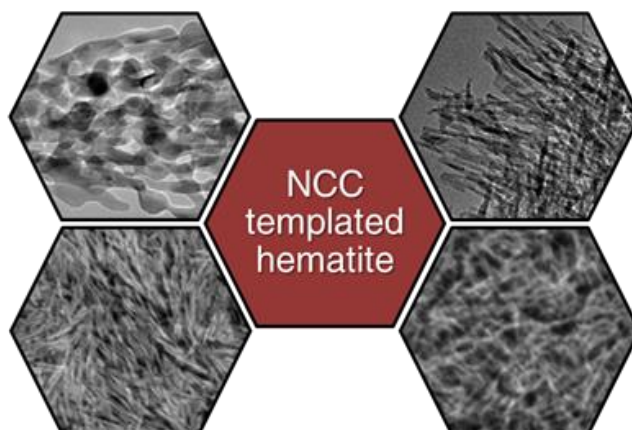


Figure 8.1 ToC image: variety of crystalline α -Fe₂O₃ (hematite) nanostructures with a well-defined anisotropic porosity is obtained *via* sol-gel transformations of molecular precursors in the confined space of self-organized cellulose nanocrystals (NCC) used as a shape-persistent template.

We report the formation of porous iron oxide (hematite) nanostructures *via* sol-gel transformations of molecular precursors in the confined space of self-organized nanocrystalline cellulose (NCC) used as a shape-persistent template. The obtained structures are highly porous α -Fe₂O₃ (hematite) morphologies with a well-defined anisotropic porosity. The character of the porous nanostructure depends on the iron salt used as precursor and the heat treatment. Moreover, a postsynthetic hydrothermal treatment of the NCC/iron salt composites strongly affects the crystal growth as well as the porous nanomorphology of the obtained hematite scaffolds. We demonstrate that the hydrothermal treatment alters the crystallization mechanism of the molecular iron precursors, which proceeds *via* the formation of anisotropic iron oxyhydroxide species. The nanocellulose templating technique established here enables the straightforward fabrication of a variety of mesoporous crystalline iron oxide scaffolds with defined porous structure and is particularly attractive for the processing of porous hematite films on different substrates.

8.2 INTRODUCTION

The combination of semiconducting properties with low cost, abundance and chemical stability makes iron oxides attractive materials for various energy conversion and storage applications. Among numerous iron oxide compounds, α -Fe₂O₃ (hematite) is the most studied material whose applications span from electrochemical energy storage and photoelectrochemical water splitting to photocatalytic degradation of air and water pollutants and gas sensing.¹⁻³ The performance of hematite in these applications critically depends upon mass transfer to the active surface sites, charge transfer at the interface, and charge and/or ion transport in the bulk. These processes are controlled to a large degree by the nanomorphology of iron oxide because of the role of interface-related processes caused by the large surface area, as well as the impact of the diminishing dimensions on its charge carrier and ion transport behavior. Because of the interest in nanostructured iron oxide, several strategies have already been developed for the fabrication of nano morphologies with optimized properties.⁴⁻⁶ Still, a major synthetic challenge is control over the structure on different length scales, from the organization of atoms in the crystalline structure to the macroscopic morphology, which strongly influence the performance of hematite in different applications.

Templated approaches based on sol-gel transformations of molecular precursors can provide a high level of control over the porous nanostructure by using objects with a well-defined shape and 3D organization to guide evolution of the structure and morphology. Mesoporous nanocrystalline iron oxide thin films with high surface area have been prepared by so called soft templating methods using supramolecular aggregates (micelles) of amphiphilic molecules.^{7,8} The practical benefits of soft templating include the straightforward formation of periodic porous structures based on the self-assembly processes, and the facile subsequent removal of the organic templates by thermal decomposition. However, the critical step in these transformations is crystallization of the inorganic scaffold, which often leads to collapse of the porous morphology due to uncontrolled crystal growth at elevated temperatures and requires a careful selection of the amphiphilic molecules and/or the processing conditions. Alternatively, hard-templating routes are advantageous regarding the formation of highly crystalline transition metal oxide morphologies with well-defined porosity.⁹⁻¹¹ Thermally stable and robust templates such as porous silica or alumina have been demonstrated to sustain the crystallization of porous transition-metal oxides, but these methods are less

suitable for the processing of porous coatings on different substrates because of the difficulties associated with the removal of the template under demanding conditions.

Nanocrystalline cellulose (NCC) extracted from natural cellulose sources^{12,13} is a promising biogenic template for the generation of porosity in inorganic oxides. Cellulose nanocrystals having anisotropic rodlike shape show a remarkable ability to self-organize and to form chiral nematic liquid crystalline phases.^{14,15} Owing to the rigidity and thermal stability of the cellulose nanocrystals, the NCC-based composites can sustain relatively high temperatures and provide fully crystalline metal oxide scaffolds with well-defined mesostructure, therefore combining the advantages of soft templating and shape-persistent hard templates.

Recent studies on the preparation of nanoscale iron oxide aided by cellulose have focused mainly on composite materials.¹⁶⁻²⁴ In these publications, cellulose of different origins acts as a supporting matrix for the formation of iron oxide and as a filler for the homogeneous distribution of presynthesized crystalline nanospecies. Other biomaterials have been shown to assist in the nanofabrication of iron oxide, such as silk,²⁵ chitosan,²⁶⁻²⁸ chitin,²⁹ proteins,³⁰ yeast cells³¹ and butterfly wings.³² A few publications describing the fabrication of porous hematite morphologies aided by sacrificial cellulose templating³³⁻³⁵ deal only with macroscopic cellulose-based objects such as wood, filter paper or fibers fabricated from regenerated cellulose. On the contrary, in our study we employ distinct nanosized cellulose species for the synthesis of porous hematite nanostructures. Recently, we have established the high potential of cellulose nanocrystals in the fabrication of porous titania thin films.³⁶ Herein we explore the suitability of this promising approach for the synthesis of iron oxide films. We show for the first time the direct formation of porous hematite thin films on different substrates by a nanocellulose-assisted templating method. We demonstrate several strategies to alter the scaffold morphology. In particular, we investigate the effect of iron oxide precursors and the calcination temperature on the film porosity and crystallinity. Furthermore, we reveal a striking effect of postsynthetic treatments on the crystallization of iron oxide in the nanocellulose matrix.

8.3 RESULTS AND DISCUSSION

For the fabrication of mesoporous iron oxide, aqueous dispersions of NCC were mixed with different iron salts acting as iron oxide precursors in the sol-gel process. As such, we used hydrates of iron(III) nitrate ($\text{Fe}(\text{NO}_3)_3 \cdot 9\text{H}_2\text{O}$), iron(III) chloride ($\text{FeCl}_3 \cdot 6\text{H}_2\text{O}$), and iron(II) chloride ($\text{FeCl}_2 \cdot 4\text{H}_2\text{O}$), which are perfectly soluble in the NCC dispersions without changes in their colloidal stability. Iron(III) salts color the opaque cellulose suspensions yellow, whereas the iron(II) chloride solution remains white. After dissolution, the precursor mixtures were processed to powders or films by drop casting on Teflon surfaces or spin-coating on different substrates (typically silicon wafers or fluorine-doped tin oxide, FTO), respectively. After drying, the composites were calcined in air at temperatures ranging from 300 °C to 600 °C to remove cellulose under formation of mesoporous iron oxide scaffolds.

Thermogravimetric analysis (TGA) of pure NCC reveals that it dehydrates in several subsequent steps in the temperature range from 200 °C to 500 °C^{37,38} and that it is completely decomposed at 500 °C. The Addition of iron salts leads to a decrease in the decomposition temperature, which depends on the type of precursor as demonstrated in Figures 8.2a1 – a3. According to the TGA measurements, the lowest decomposition temperature of ca. 290 °C was observed for the NCC/ $\text{Fe}(\text{NO}_3)_3 \cdot 9\text{H}_2\text{O}$ composite, which could be attributed to the oxidative character of the nitrate ions. The addition of iron(III) chloride leads to a rather small decrease in the decomposition temperature to ca. 450 °C, while in the iron(II) chloride containing composites NCC is combusted at about 400 °C.

In order to investigate the degradation behavior of the nanocellulose in thin films, we performed *in situ* X-ray diffraction (XRD) heating experiments on 1 μm thick composite films coated on silicon wafers. Figures 8.2b1 – b3 show a gradual reduction of the signals characteristic for native cellulose upon a temperature increase (the NCC signal assignment is shown in Figure S8.1 in the supporting information). Although the XRD results indicate complete degradation of crystalline cellulose at 250 °C, the optical appearance of the films calcined at this temperature implies the presence of template residues, as follows from the black coloring of the film (Figure S8.2d in the supporting information), which is consistent with the TGA revealing an incomplete decomposition of cellulose at 250 °C (Figure 8.2).

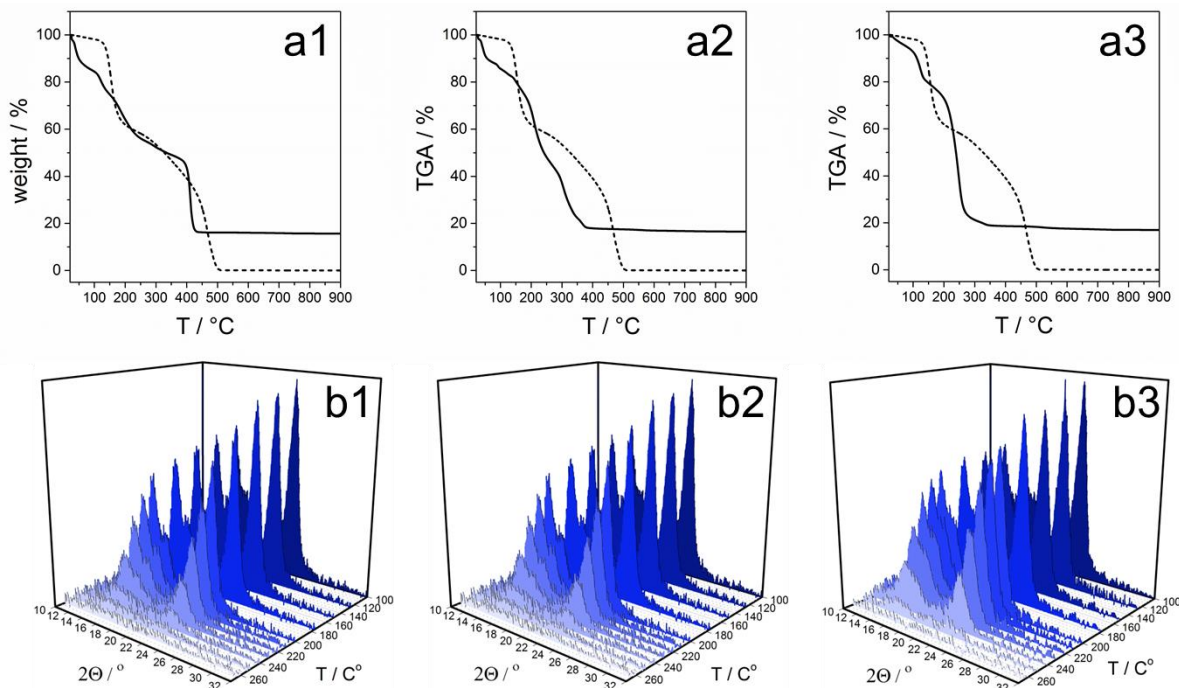


Figure 8.2 Degradation of NCC/iron oxide precursor composites containing different iron salts: $\text{FeCl}_3 \cdot 6\text{H}_2\text{O}$ (a1, b1), $\text{FeCl}_2 \cdot 4\text{H}_2\text{O}$ (a2, b2) and $\text{Fe}(\text{NO}_3)_3 \cdot 9\text{H}_2\text{O}$ (a3, b3). Top row (a1 – a3) TGA revealing mass loss of iron oxide precursor/NCC composites (black lines) compared to pristine NCC (dashed lines). The composites were dried at 35 °C prior to analysis and heated with a ramp of 2 °C min^{-1} . Bottom row (b1 – b3) *In-situ* XRD patterns obtained upon gradual heating of 1 μm iron oxide precursor/NCC composite films coated on silicon wafers.

The degradation studies demonstrate that calcination of composite films at 300 °C to 600 °C should be sufficient to remove NCC with the associated liberation of open pores. This is confirmed with scanning electron microscopy (SEM) images of the NCC-templated films, which demonstrate the formation of elongated slitlike pores characteristic for NCC-derived porous scaffolds, closely replicating the shape of the initial NCC (Figure 8.3). The mesoporous morphology obtained after calcination of the dried coatings is practically not influenced by the choice of iron precursors (SEM images in Figures 8.3 and S8.3 in the supporting information). The porous texture changes only slightly with increasing calcination temperature from 300 °C to 500 °C, corresponding to the stability range of NCC. However, calcination at 600 °C leads to significant crystal growth with the formation of wormlike disordered porous layers typically observed for different solution-processed hematite films (Figure 8.3d).

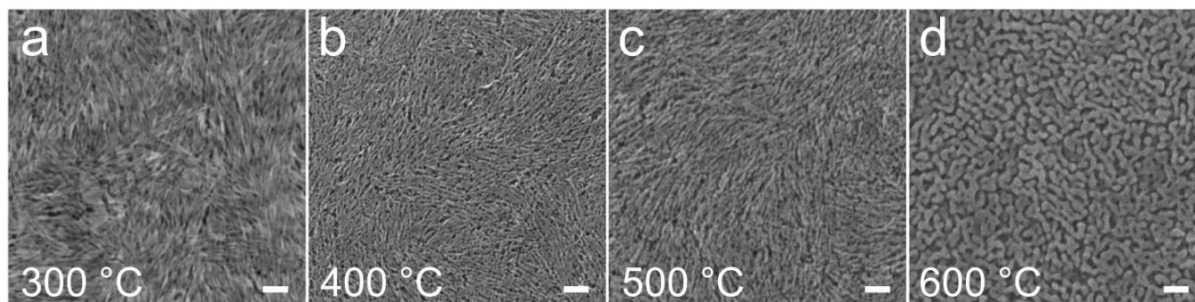


Figure 8.3 SEM top view images revealing the effect of the calcination temperature on the morphology of NCC-templated α -Fe₂O₃ thin films. The films were coated on silicon wafers from solutions containing NCC and FeCl₃·6H₂O and calcined at (a) 300 °C, (b) 400 °C, (c) 500 °C, and (d) 600 °C. The scale bars correspond to 100 nm.

Analysis by transmission electron microscopy (TEM) confirms the increase of the feature sizes for the NCC-templated film calcined at 600 °C compared to the one heated at 500 °C. The samples exhibit a highly porous structure and a crystalline morphology, as can be seen in the high-resolution and selected-area electron diffraction (SAED) images (Figures 8.4 and S8.4 in the supporting information). The determined d-spacing values are typical of hematite and agree very well with previous studies.³⁹

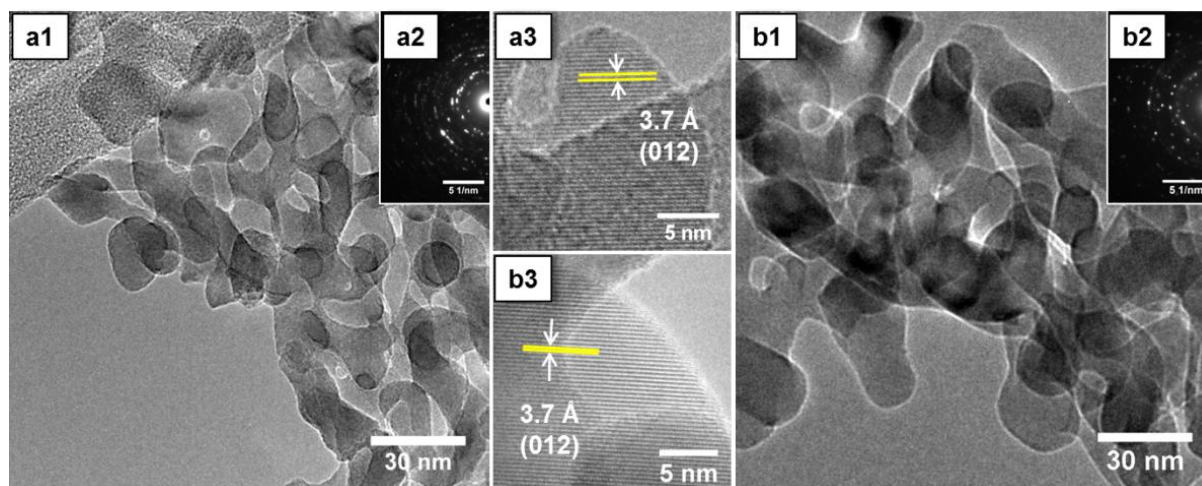


Figure 8.4 TEM images (a1, a3, b1, b3) and SAED patterns (a2, b2) of NCC-templated iron oxide thin films prepared from FeCl₂·4H₂O precursor solutions and calcined at (a) 500 °C and (b) 600 °C.

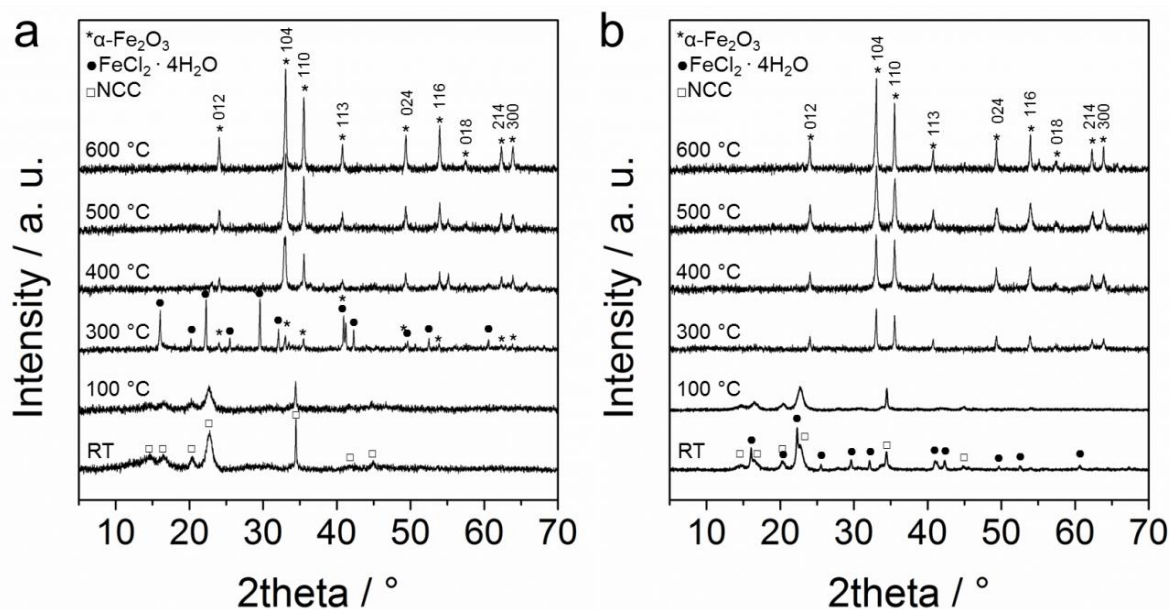


Figure 8.5 XRD patterns of NCC templated iron oxide free-standing films cast from FeCl₃·6H₂O (a) and FeCl₂·4H₂O (b) precursor solutions. The composites were dried overnight (assigned as room temperature (RT)) and then either heated at 100 °C overnight or calcined at 300 °C – 600 °C for 30 min. The assigned signals correspond to (□) native cellulose (ICDD pattern C00-003-0289), (•) iron(II) chloride tetrahydrate (ICDD pattern 00-016-0123) and (*) hematite (ICDD pattern 00-003-0289).

In order to study the temperature-induced formation of crystalline iron oxide in the presence of nanocellulose, we performed XRD measurements on cast free-standing composites. Figures 8.5 and S8.5a in the supporting information reveal formation of the α -Fe₂O₃ phase for all precursors at temperatures higher than 300 °C. Surprisingly, heating of the iron(III) chloride-NCC composite at 300 °C initially leads to the formation of hematite and iron(II) chloride, which could be due to a reaction of iron(III) chloride with NCC degradation products.

To modify the crystallization of hematite, the dried composite films were posttreated at 100 °C in high humidity, also known as delayed humidity treatment (DHT). This procedure can be considered as a hydrothermal treatment of the iron salts in the confined space of the prearranged NCC template rods. The XRD analysis reveals formation of a crystalline inorganic phase corresponding to crystalline iron oxyhydroxide (β -FeOOH, akaganeite) after DHT (Figure 8.6).

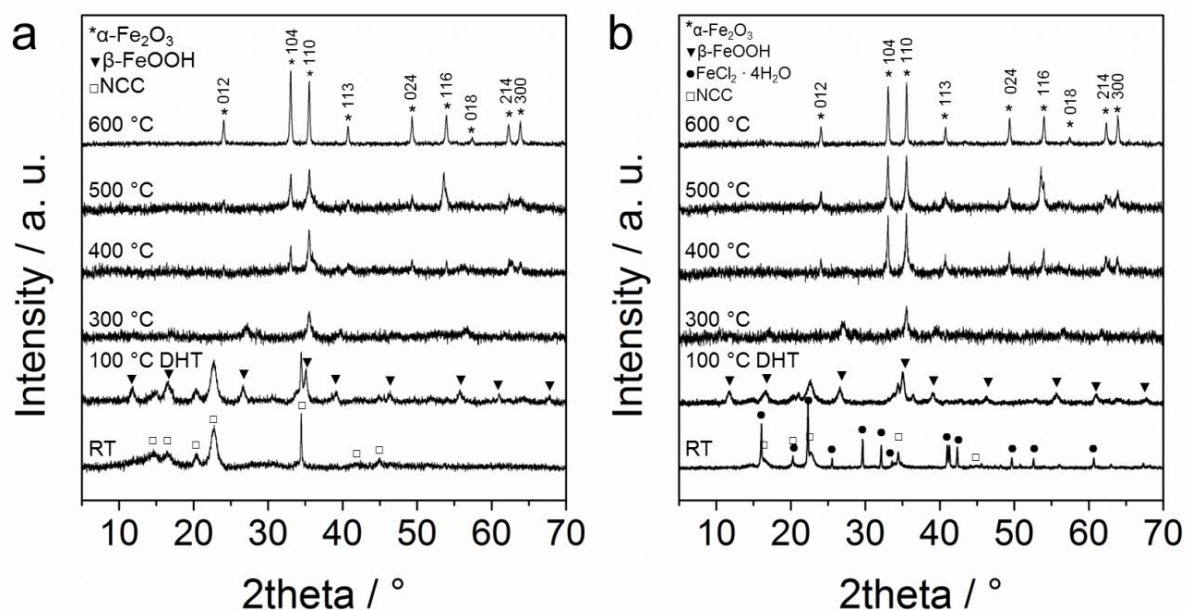


Figure 8.6 XRD patterns of NCC templated iron oxide free-standing films cast from $\text{FeCl}_3 \cdot 6\text{H}_2\text{O}$ (a) and $\text{FeCl}_2 \cdot 4\text{H}_2\text{O}$ (b) precursor solutions. The dried composites (assigned as RT) were postsynthetically treated overnight at 100 °C in high humidity (set to 85 % relative humidity at RT) and then calcined at 300 °C – 600 °C for 30 min. The assigned signals correspond to (\square) native cellulose (ICDD pattern 00-003-0289), (\bullet) iron(II) chloride tetrahydrate (ICDD pattern 00-016-0123), (\blacktriangledown) akaganeite (ICDD pattern 00-034-1266) and ($*$) hematite (ICDD pattern 00-033-0664).

We note that heating at 100 °C without hydrothermal treatment does not lead to formation of a crystalline phase (Figure 8.5). Our results imply that without the postsynthetic humidity treatment either amorphous iron oxide either directly transforms to the crystalline hematite or the intermediate phase is not stable and rapidly converts to the hematite. Moreover, we found that DHT facilitates crystallization of the oxyhydroxide species in the composite based on both iron(II) and iron(III) chlorides, although this is not the case for the nitrate hydrate precursor treated at the same conditions (Figure S8.5b in the supporting information). It has been previously shown that at certain conditions hydrolysis of iron chlorides proceeds through the formation of α and β -FeOOH oxyhydroxide phases prior to full conversion to α - Fe_2O_3 .^{40,41,42,43}

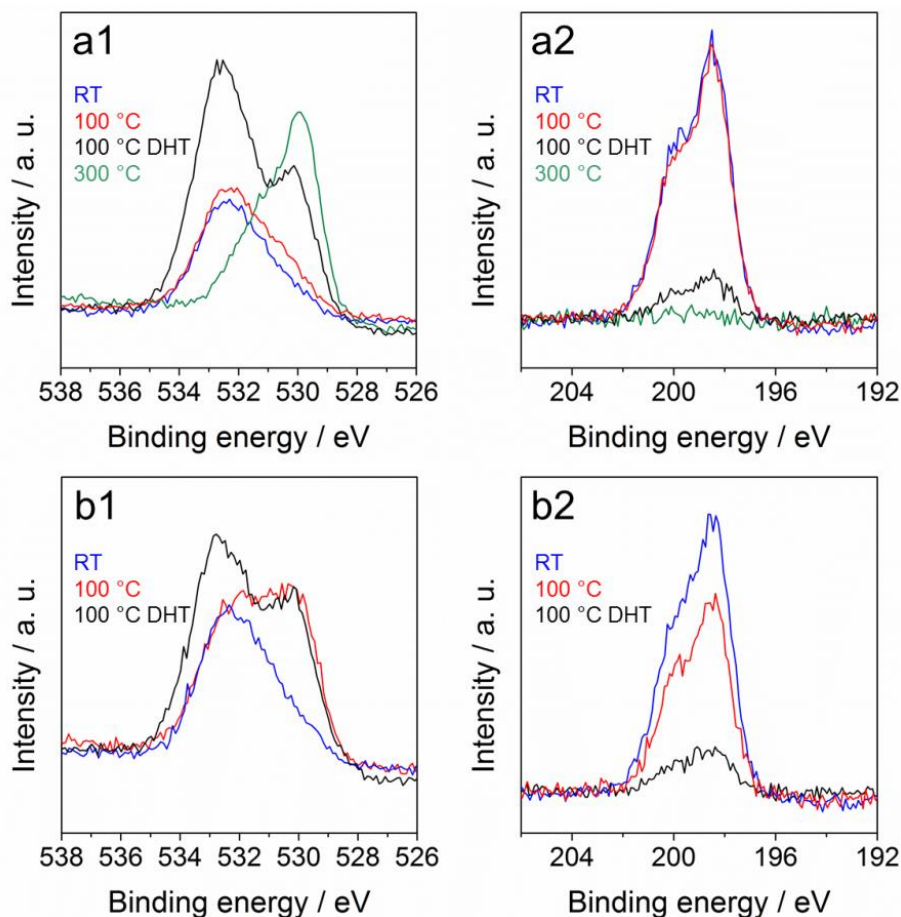


Figure 8.7 XPS spectra of O 1s (a1, b1) and Cl 2p (a2, b2) measured on iron chloride/NCC composite films coated on silicon wafers, resulting from $\text{FeCl}_3 \cdot 6\text{H}_2\text{O}$ (a1, a2) and $\text{FeCl}_2 \cdot 4\text{H}_2\text{O}$ (b1, b2) precursors and dried at different conditions: at RT, at 100 °C in humid air (assigned as 100 °C DHT) and at 100 °C and 300 °C in ambient humidity conditions.

To elucidate the effect of the postsynthetic treatment, the iron chloride/NCC composites were dried at different conditions and studied by X-ray photoelectron spectroscopy (XPS). Figures 8.7 and S8.6 in the supporting information show evolution of the peaks arising from oxygen, chlorine, iron and carbon depending on the film drying conditions. The most significant changes were observed for the oxygen and chlorine peaks shown in Figure 8.7. The oxygen peak shifts toward lower binding energies (Figure 8.7a1) with increasing temperature from RT to 300 °C, indicating the release of H_2O , degradation of cellulose and formation of iron species containing OH^- and O^{2-} (the fitting is shown in Figure S8.6a3 in the supporting information).^{44,45} In addition, chloride completely degrades at 300 °C (Figure 8.7a2). Interestingly, heating at 100 °C under hydrothermal conditions (DHT) leads to a significant decrease in the chloride contents, whereas after heating in air at the same

temperature the chloride is well-preserved (the black and red lines in Figure 8.7a2, respectively). This behavior indicates a higher degree of hydrolysis of iron chlorides because of the presence of water vapor, which is also consistent with the shape of the oxygen spectra recorded for the DHT samples. The black spectra in Figures 8.7a1, b1 demonstrate a doublet with a pronounced signal corresponding to water and cellulose at 532.5 eV, and a less intense peak at lower binding energies (530.1 eV) related to O^{2-} in iron oxide. The spectra point to hydration of cellulose and formation of oxygen bridges in the inorganic part of the composites. We found that the iron(II) chloride composite loses some chlorine already after ambient heating at 100 °C and contains iron oxide O^{2-} species, which was not the case for the iron(III) chloride sample (red spectra in Figures 8.7a2, b2 respectively). In conclusion, XPS analysis points to accelerated hydrolysis and nucleation of the crystalline phase due to DHT. Additionally, the increase of the signal at about 533 eV implies high contents of water in the samples, which may reduce shrinkage of the cellulose species due to swelling at high relative humidity.⁴⁶

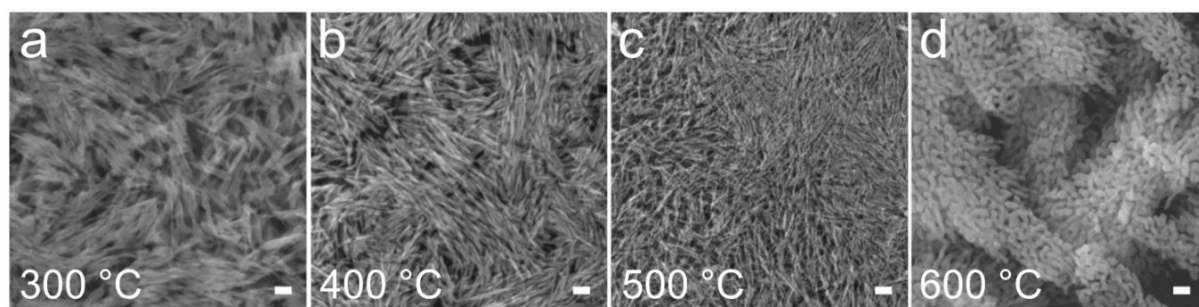


Figure 8.8 SEM top view images revealing the effect of the calcination temperature on the morphology of the NCC-templated α - Fe_2O_3 thin films postsynthetically treated in humid air at 100 °C prior to calcination at (a) 300 °C, (b) 400 °C, (c) 500 °C, and (d) 600 °C. The films were coated on silicon wafers from solutions containing NCC and $FeCl_2 \cdot 6H_2O$. The scale bars correspond to 100 nm.

Notably, we found that induced crystallization of iron oxyhydroxide during the postsynthetic treatment significantly affects the film morphologies after calcination as demonstrated in Figures 8.8 and S8.7 in the supporting information. DHT results in an anisotropic geometry of iron oxide species, which is especially pronounced for the films calcined at low temperatures of 300 – 400 °C (Figures 8.8a, b). However, thermal treatment at higher temperatures leads to

recrystallization of the nanorods to form intergrown roundly shaped species (Figure 8.8d). A more detailed investigation of the DHT effect on crystal formation is shown in Figure 8.9.

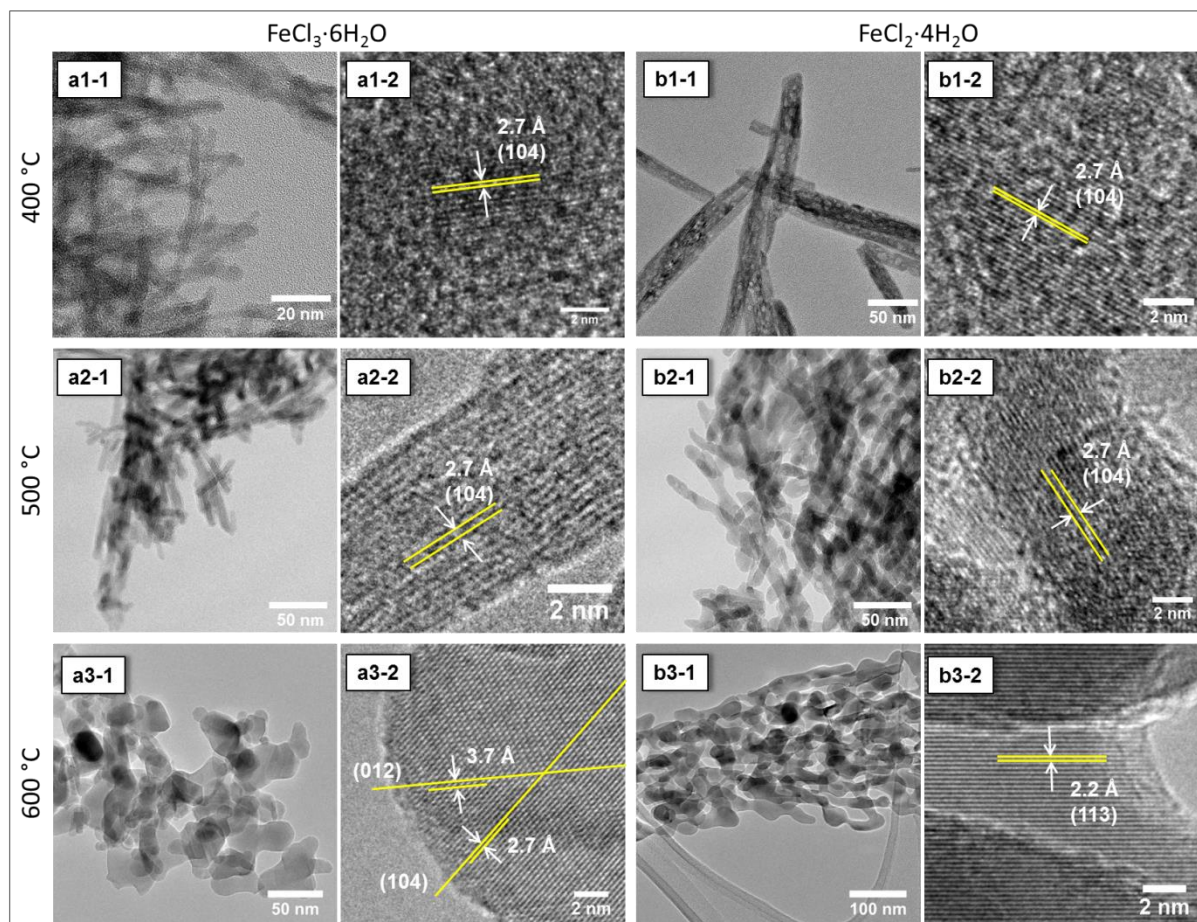


Figure 8.9 TEM images at low and high magnifications of iron oxide thin films prepared from iron chloride/NCC solutions coated on silicon wafer, obtained from $\text{FeCl}_3 \cdot 6\text{H}_2\text{O}$ (a) and $\text{FeCl}_2 \cdot 4\text{H}_2\text{O}$ (b) precursors. The composites were exposed to humidity treatment at 100°C and subsequently calcined at (a1, b1) 400°C , (a2, b2) 500°C , and (a3, b3) 600°C .

TEM analysis in Figure 8.9 reveals a similar trend in the crystallization pathway for both $\text{FeCl}_3 \cdot 6\text{H}_2\text{O}$ and $\text{FeCl}_2 \cdot 4\text{H}_2\text{O}$ precursors. Calcination at the moderate temperature of 400°C leads to the formation of crystalline species showing a pronounced anisotropic shape, with a length of around 55 nm and a width of around 5 nm (Figure 8.9a1-1). Additionally, the crystals obtained with $\text{FeCl}_2 \cdot 4\text{H}_2\text{O}$ (Figure 8.9b1-1) show a porous structure, which can be attributed to dehydration during the thermal conversion from $\beta\text{-FeOOH}$ to $\alpha\text{-Fe}_2\text{O}_3$.⁴⁷ At 500°C the elongated shape of the features is still present, although it is clearly visible that the particles start to recrystallize forming a polycrystalline network with the formation of

additional more spherically shaped species. The length of the rods is around 30 nm while the rod width remains approximately 5 nm. The lattice fringes of the elongated crystals correspond to (104) hematite planes, as can be seen in the high-resolution TEM images in Figure 8.9. At 600 °C the recrystallization step is more pronounced and the species have a nearly spherical geometry with a size of ca. 25 nm length and 20 nm width. Accordingly, the aspect ratio of the rods decreases from about 12.3 to 1.3 with increasing calcination temperature.

Iron(III) nitrate does not undergo oxyhydroxide-to-hematite transformation, therefore DHT does not have a pronounced effect on the NCC-templated hematite morphology (Figure S8.7 in the supporting information). We note that all obtained NCC-templated hematite scaffolds exhibit a rather similar specific surface area of about 65 m² g⁻¹ (Figure S8.8 in the supporting information).

8.4 CONCLUSIONS

We have established a facile method for the synthesis of crystalline and highly porous iron oxide thin films with various nanomorphologies by employing the biogenic template nanocellulose. Different iron salts, namely FeCl₃·6H₂O, FeCl₂·4H₂O and Fe(NO₃)₃·9H₂O can be successfully employed for the NCC-assisted synthesis. The nature of the calcination procedure of the NCC/iron oxide precursor composites has a strong influence on the morphology of the porous hematite films.

Furthermore, we show that a postsynthetic humidity treatment at elevated temperature drastically affects the morphology of the porous scaffolds prepared from FeCl₃·6H₂O and FeCl₂·4H₂O. Upon exposure to the humidity treatment at 100 °C, the crystallization of hematite proceeds through the formation of iron oxyhydroxide (β-FeOOH) species of highly anisotropic shape. Because of the shape-persistence of cellulose nanocrystals, the film homogeneity and porosity are well preserved despite the complex behavior of hematite crystallization. We show that a great variety of iron oxide networks can be achieved and the morphology of the films can be tuned by facile nanocellulose templating. The above synthesis approach is particularly advantageous for the fabrication of homogeneous porous coatings of iron oxide on different types of substrates.

8.5 EXPERIMENTAL SECTION

8.5.1 EXTRACTION OF CELLULOSE NANOCRYSTALS.

Nanocrystalline cellulose (NCC) was extracted from cotton linters CP20 (Peter Temming AG) by hydrolysis in sulfuric acid.⁴⁸ The cotton fibers were washed with water and dried at 60 °C. Then 64 % H₂SO₄ was added to the cotton fibers at a ratio of 1 mL of acid to 8.75 g of cellulose. The mixture was kept at RT for 25 min. Then it was heated at 55 °C for 45 min under vigorous stirring until large cellulose aggregates dissolved. Afterwards the suspension was 10-fold diluted with deionized water and stored overnight. The upper liquid phase was decanted and the NCC-rich lower phase was washed three times with water *via* repeated centrifugation at 47808 g relative centrifugal force (RFC) for 15 min. The last centrifugation step was performed at 70 g RFC for 10 min in order to sediment cellulose aggregates and to collect the suspension of finely dispersed NCC. Finally, the suspension was concentrated in a rotary evaporator to 8.15 wt% at pH 2.55.

8.5.2 PREPARATION OF PRECURSOR SOLUTIONS.

A total of 1.229 g of the above 8.15 wt% dispersion of cellulose crystals was added to 0.37 mmol of iron salt corresponding to 0.100, 0.0736 and 0.1495 g of FeCl₃·6H₂O, FeCl₂·4H₂O and Fe(NO₃)₃·9H₂O salts, respectively. The viscous mixture was vigorously stirred for about 2 min. Then 3.6 g of water was added in order to dilute the cellulose suspension and to dissolve the iron precursor. The precursor solutions contained concentrations of 0.076 M iron and 2 wt% NCC. The solutions were stirred for 2 h prior to film coating.

8.5.3 FILM PREPARATION

Free-standing films were cast from precursor solutions on a Teflon surface (5 g of a precursor solution on a 6 × 6 cm² area) and dried at 35 °C overnight prior to calcination. After calcination, pulverized cast films were analyzed by using XRD, nitrogen sorption measurements and TGA.

Thin films were deposited on a $1.5 \times 2.0 \text{ cm}^2$ silicon wafer or on $1.5 \times 2.5 \text{ cm}^2$ FTO glass by spin-coating a $100 \mu\text{L}$ precursor solution at 1500 rpm for 25 s followed by drying for 10 s with a heat gun set at $100 \text{ }^\circ\text{C}$. The spin-coating and drying cycles were repeated seven times to achieve ca. $1 \mu\text{m}$ film thickness of the composites for the XRD degradation experiments and for XPS analysis. For SEM imaging, two layers were coated on silicon wafers.

For DHT, the free-standing films or films coated on substrates were placed into a 2 L desiccator containing 80 mL of KCl saturated aqueous solution resulting in 85 % relative humidity at RT and kept in an oven at $100 \text{ }^\circ\text{C}$ overnight prior to calcination.

The free-standing films and thin films were heat-treated at $100 \text{ }^\circ\text{C}$ overnight, $300 \text{ }^\circ\text{C}$ for 30 min, $400 \text{ }^\circ\text{C}$ for 30 min and $600 \text{ }^\circ\text{C}$ for 30 min with a heating ramp of $3 \text{ }^\circ\text{C min}^{-1}$. Calcination at $500 \text{ }^\circ\text{C}$ was performed by using a $2 \text{ }^\circ\text{C min}^{-1}$ ramp with 2 h continuous heating steps at $100 \text{ }^\circ\text{C}$ and $360 \text{ }^\circ\text{C}$ and a final step at $500 \text{ }^\circ\text{C}$ for 30 min.

8.5.4 CHARACTERIZATION

TGA of the samples was performed on a Netzsch STA 440 C TG/DSC instrument (heating rate of $2 \text{ }^\circ\text{C min}^{-1}$ in a stream of synthetic air of about 25 mL min^{-1}).

XRD analysis of the free-standing films was performed on a STOE powder diffractometer in transmission geometry ($\text{Cu K}\alpha_1$, $\lambda = 1.5406 \text{ \AA}$) equipped with a position-sensitive Mythen 1K detector. XRD patterns were collected in a 2θ range from 5° to 70° with a step of 1° and fixed counting time of 45 s/ step. *In situ* XRD heating measurements of the films on silicon substrates were carried out in reflection mode (Bragg-Brentano) using a Bruker D8 Discover with Ni-filtered $\text{Cu K}\alpha$ radiation and a position-sensitive detector (LynxEye). The instrument was equipped with a heating stage operated by an Anton Paar TCU 200 temperature control unit. The films were heated with a ramp of $1 \text{ }^\circ\text{C s}^{-1}$ and 10 min of continuous heating at the set temperatures.

SEM images were obtained with a Jeol JSM-6500F scanning electron microscope equipped with a field emission gun operated at 5 kV. The films were prepared on silicon substrates and glued onto a sample holder with silver lacquer.

TEM analysis was performed with thin films removed from the substrate and deposited on a carbon-coated copper grid. Analysis was carried out on a FEI Titan 80-300 (S)TEM equipped with a field emission gun operated at 300 kV.

XPS analysis was performed with a VSW TA10 X-ray source, providing non-monochromatized Mg K α radiation, and a VSW HA100 hemispherical analyzer. The samples were cleaned before measurement by 15 min of Ar⁺ sputtering (1 kV and ~7 μ A). Peak shifts due to charging of the sample were corrected by setting the Cl 2p_{3/2} peak to 198.4 eV. The recorded elemental peaks were fitted with a Doniach-Sunjic line shape convoluted with a Gaussian and linear background subtraction.⁴⁹

The nitrogen sorption isotherms were obtained at -196 °C using a Quantachrome Autosorb-1. The specific surface area was determined with the Brunauer-Emmett-Teller method at $\frac{P}{P_0} = 0.05 - 0.2$.

8.6 REFERENCES

- (1) Sivula, K.; LeFormal, F.; Grätzel, M. *ChemSusChem* **2011**, *4*, 432.
- (2) Wu, C.; Yin, P.; Zhu, X.; OuYang, C.; Xie, Y. *J. Phys. Chem. B* **2006**, *110*, 17806.
- (3) Chen, J.; Xu, L.; Li, W.; Gou, X. *Adv. Mater.* **2005**, *17*, 582.
- (4) Sivula, K.; Zboril, R.; Le Formal, F.; Robert, R.; Weidenkaff, A.; Tucek, J.; Frydrych, J.; Grätzel, M. *J. Am. Chem. Soc.* **2010**, *132*, 7436.
- (5) Srivastava, D. N.; Perkas, N.; Gedanken, A.; Felner, I. *J. Phys. Chem. B* **2002**, *106*, 1878.
- (6) Mitra, A.; Vázquez-Vázquez, C.; López-Quintela, M. A.; Paul, B. K.; Bhaumik, A. *Micropor. Mesopor. Mat.* **2010**, *131*, 373.

8.6 REFERENCES

- (7) Brezesinski, T.; Groenewolt, M.; Antonietti, M.; Smarsly, B. *Angew. Chem. Int. Ed.* **2006**, *45*, 781.
- (8) Brezesinski, K.; Haetge, J.; Wang, J.; Mascotto, S.; Reitz, C.; Rein, A.; Tolbert, S. H.; Perlich, J.; Dunn, B.; Brezesinski, T. *Small* **2011**, *7*, 407.
- (9) Zhang, R.; Dai, H.; Du, Y.; Zhang, L.; Deng, J.; Xia, Y.; Zhao, Z.; Meng, X.; Liu, Y. *Inorg. Chem.* **2011**, *50*, 2534.
- (10) Jiao, F.; Harrison, A.; Jumas, J.-C.; Chadwick, A. V.; Kockelmann, W.; Bruce, P. G. *J. Am. Chem. Soc.* **2006**, *128*, 5468.
- (11) Lee, J.; Christopher Orilall, M.; Warren, S. C.; Kamperman, M.; DiSalvo, F. J.; Wiesner, U. *Nat. Mater.* **2008**, *7*, 222.
- (12) Klemm, D.; Kramer, F.; Moritz, S.; Lindström, T.; Ankerfors, M.; Gray, D.; Dorris, A. *Angew. Chem. Int. Ed.* **2011**, *50*, 5438.
- (13) Ranby, B. G. *Acta Chem. Scand.* **1949**, *3*, 649.
- (14) Beck-Candanedo, S.; Roman, M.; Gray, D. G. *Biomacromolecules* **2005**, *6*, 1048.
- (15) Kelly, J. A.; Giese, M.; Shopsowitz, K. E.; Hamad, W. Y.; MacLachlan, M. J. *Acc. Chem. Res.* **2014**, *47*, 1088.
- (16) Liu, S.; Luo, X.; Zhou, J. *Magnetic Responsive Cellulose Nanocomposites and Their Applications*, **2013**.
- (17) Ma, M.-G.; Zhu, J.-F.; Li, S.-M.; Jia, N.; Sun, R.-C. *Mat. Sci. Eng. C* **2012**, *32*, 1511.
-

- (18) Zhou, J.; Li, R.; Liu, S.; Li, Q.; Zhang, L.; Zhang, L.; Guan, J. *J. Appl. Polym. Sci.* **2009**, *111*, 2477.
- (19) Xiong, R.; Lu, C.; Wang, Y.; Zhou, Z.; Zhang, X. *J. Mater. Chem. A* **2013**, *1*, 14910.
- (20) Mahmoud, K. A.; Lam, E.; Hrapovic, S.; Luong, J. H. T. *ACS Appl. Mater. Interfaces* **2013**, *5*, 4978.
- (21) Yu, X.; Tong, S.; Ge, M.; Zuo, J.; Cao, C.; Song, W. *J. Mater. Chem. A* **2013**, *1*, 959.
- (22) Liu, S.; Tao, D.; Zhang, L. *Powder Technol.* **2012**, *217*, 502.
- (23) Rafi, M. M.; Ahmed, K. S.; Nazeer, K. P.; Siva Kumar, D.; Thamilselvan, M. *Appl. Nanosci.* **2014**, *1*.
- (24) Wu, Y.; Zhu, P.; Reddy, M. V.; Chowdari, B. V. R.; Ramakrishna, S. *ACS Appl. Mater. Interfaces* **2014**, *6*, 1951.
- (25) Fei, X.; Shao, Z.; Chen, X. *J. Mater. Chem. B* **2013**, *1*, 213.
- (26) Sreeram, K. J.; Nidhin, M.; Nair, B. U. *Colloid. Surface. B* **2009**, *71*, 260.
- (27) Singh, J.; Srivastava, M.; Dutta, J.; Dutta, P. K. *Int. J. Biol. Macromol.* **2011**, *48*, 170.
- (28) Chang, M.-Y.; Wang, W.-H.; Chung, Y.-C. *J. Mater. Chem.* **2011**, *21*, 4966.
- (29) Tang, H.; Zhou, W.; Lu, A.; Zhang, L. *J. Mater. Sci.* **2014**, *49*, 123.
- (30) Klem, M. T.; Young, M.; Douglas, T. *J. Mater. Chem.* **2010**, *20*, 65.
- (31) Zhou, W.; He, W.; Ma, J.; Wang, M.; Zhang, X.; Yan, S.; Tian, X.; Sun, X.; Han, X. *Mat. Sci. Eng. C* **2009**, *29*, 1893.
-

8.6 REFERENCES

- (32) Peng, W.; Zhu, S.; Wang, W.; Zhang, W.; Gu, J.; Hu, X.; Zhang, D.; Chen, Z. *Adv. Funct. Mater.* **2012**, *22*, 2072.
- (33) Liu, S.; Zhang, L.; Zhou, J.; Xiang, J.; Sun, J.; Guan, J. *Chem. Mater.* **2008**, *20*, 3623.
- (34) Ding, J.; Fan, T.; Zhang, D.; Saito, K.; Guo, Q. *Solid State Commun.* **2011**, *151*, 802.
- (35) Sadakane, M.; Kato, R.; Murayama, T.; Ueda, W. *Mater. Lett.* **2012**, *81*, 80.
- (36) Ivanova, A.; Fattakhova-Rohlfing, D.; Kayaalp, B. E.; Rathouský, J.; Bein, T. *J. Am. Chem. Soc.* **2014**, *136*, 5930.
- (37) Camarero Espinosa, S.; Kuhnt, T.; Foster, E. J.; Weder, C. *Biomacromolecules* **2013**, *14*, 1223.
- (38) Wang, N.; Ding, E.; Cheng, R. *Polymer* **2007**, *48*, 3486.
- (39) Swanson, H. E. *Standard X-ray diffraction powder patterns*; U.S. Dept. of Commerce, National Bureau of Standards U.S. G.P.O.: Washington, DC, **1953**.
- (40) Musić, S.; Krehula, S.; Popović, S. *Mater. Lett.* **2004**, *58*, 2640.
- (41) Chaudhari, N. K.; Yu, J.-S. *J. Phys. Chem. C* **2008**, *112*, 19957.
- (42) Wang, W.; Howe, J. Y.; Gu, B. *J. Phys. Chem. C* **2008**, *112*, 9203.
- (43) Xavier, A. M.; Ferreira, F. F.; Souza, F. L. *RSC Advances* **2014**, *4*, 17753.
- (44) McIntyre, N. S.; Zetaruk, D. G. *Anal. Chem.* **1977**, *49*, 1521.
- (45) Johansson, L.-S.; Campbell, J. M. *Surf. Interface Anal.* **2004**, *36*, 1018.
-

- (46) Aulin, C.; Ahola, S.; Josefsson, P.; Nishino, T.; Hirose, Y.; Österberg, M.; Wågberg, L. *Langmuir* **2009**, *25*, 7675.
- (47) Cui, X.; Liu, T.; Zhang, Z.; Wang, L.; Zuo, S.; Zhu, W. *Powder Technol.* **2014**, *266*, 113.
- (48) Dong, X. M.; Kimura, T.; Revol, J.-F.; Gray, D. G. *Langmuir* **1996**, *12*, 2076.
- (49) Doniach, S.; Sunjic, M. J. *Phys. C* **1970**, *3*, 285.

8.7 SUPPORTING INFORMATION

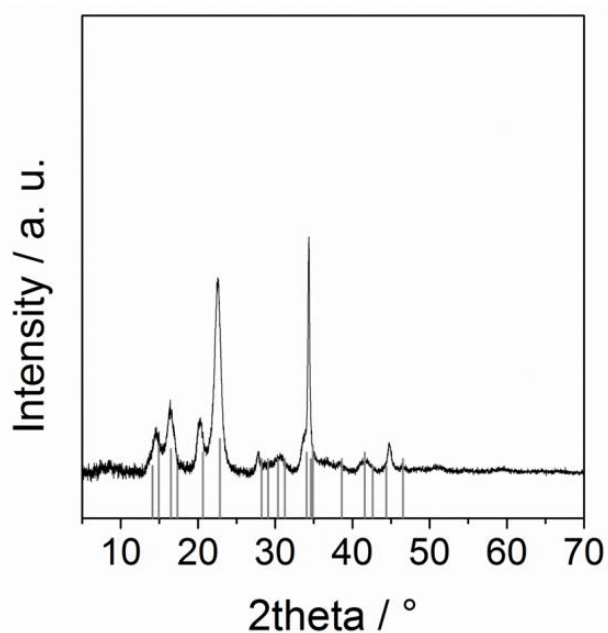


Figure S8.1 XRD pattern of an NCC free-standing film. The assigned signals correspond to native cellulose (ICDD pattern 00-003-0289).

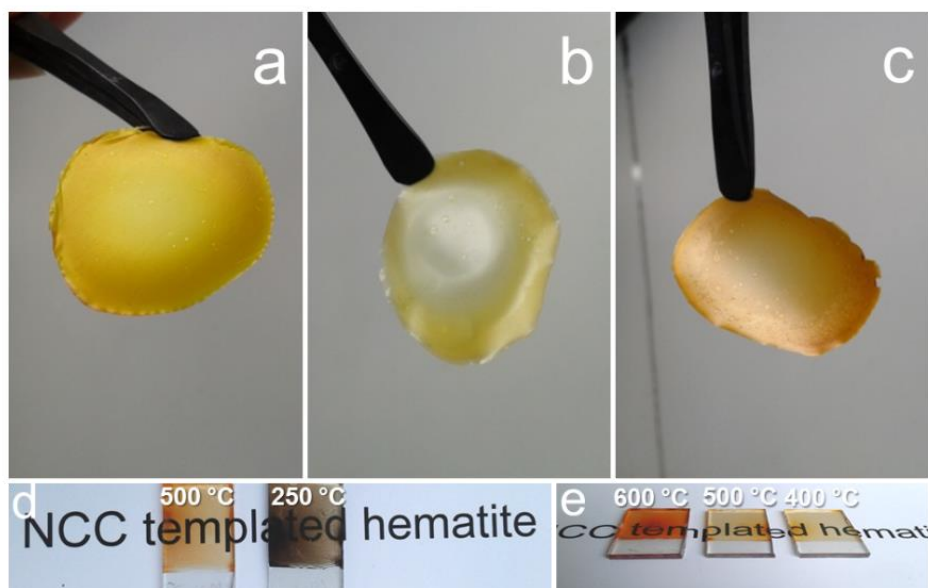


Figure S8.2 Photograph of free-standing nanocellulose-precursor composites prepared with (a) $\text{FeCl}_3 \cdot 6\text{H}_2\text{O}$, (b) $\text{FeCl}_2 \cdot 4\text{H}_2\text{O}$, and (c) $\text{Fe}(\text{NO}_3)_3 \cdot 9\text{H}_2\text{O}$ dried at 35°C . NCC/iron oxide precursor thin films coated on FTO glass from precursor solutions based on (d) $\text{FeCl}_3 \cdot 6\text{H}_2\text{O}$ and (e) $\text{Fe}(\text{NO}_3)_3 \cdot 9\text{H}_2\text{O}$ and calcined at different temperatures.

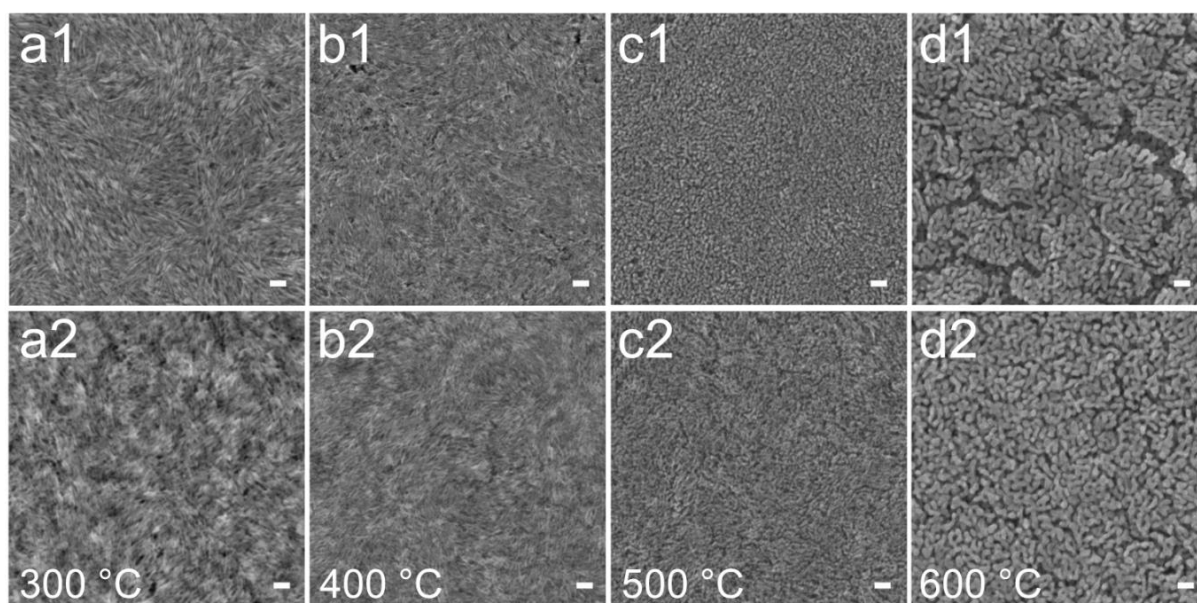


Figure S8.3 SEM top view images revealing the effect of the iron precursor and calcination temperature on the morphology of NCC-templated $\alpha\text{-Fe}_2\text{O}_3$ thin films. The films were prepared from precursor solutions containing $\text{FeCl}_2 \cdot 4\text{H}_2\text{O}$ (top row) or $\text{Fe}(\text{NO}_3)_3 \cdot 9\text{H}_2\text{O}$ (bottom row) and calcined at (a1, a2) 300°C , (b1, b2) 400°C , (c1, c2) 500°C and (d1, d2) 600°C . The scale bars correspond to 100 nm.

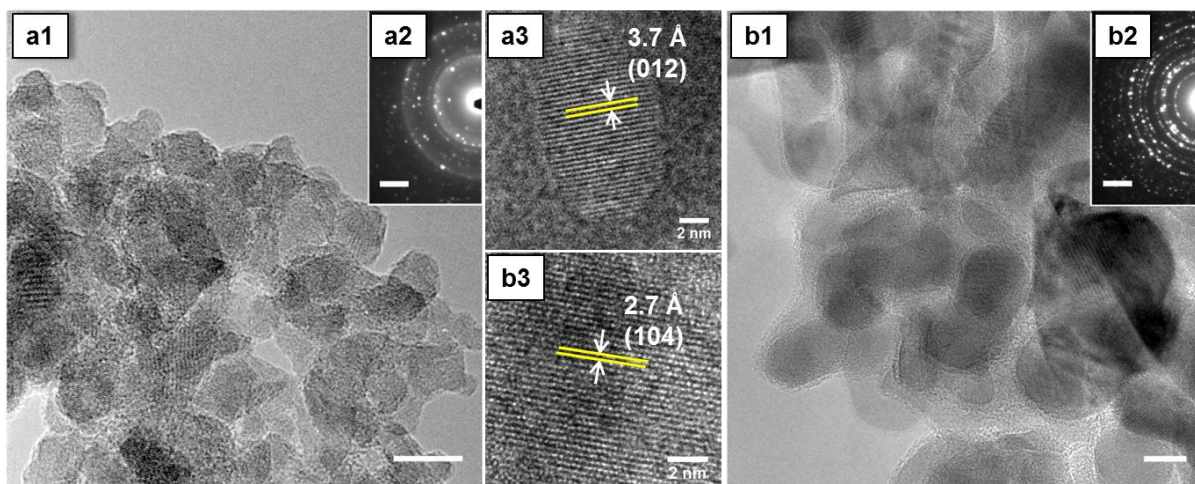


Figure S8.4 (a1, b1) TEM images (scale bars correspond to 10 nm), (a3, b3) high-resolution TEM images and (a2, b2) SAED patterns (scale bars correspond to 2.5 nm^{-1}) of NCC-templated iron oxide thin films prepared from $\text{FeCl}_3 \cdot 6\text{H}_2\text{O}$ precursor solutions and calcined at (a) 500 °C and (b) 600 °C.

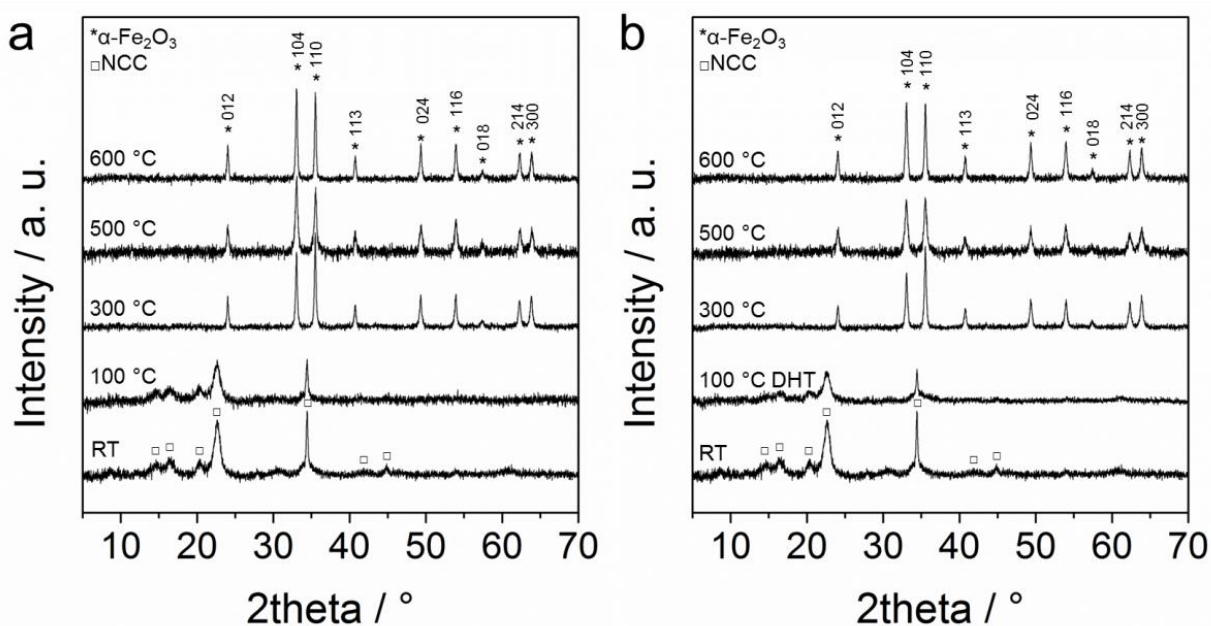


Figure S8.5 XRD patterns revealing the temperature-dependent development of phase composition of NCC/ $\text{Fe}(\text{NO}_3)_3 \cdot 9\text{H}_2\text{O}$ composites calcined at different temperatures (a) after drying at 35 °C (assigned as RT) and (b) after DHT treatment. The assigned signals correspond to (□) native cellulose (ICDD pattern 00-003-0289) and (*) hematite (ICDD pattern 00-033-0664).

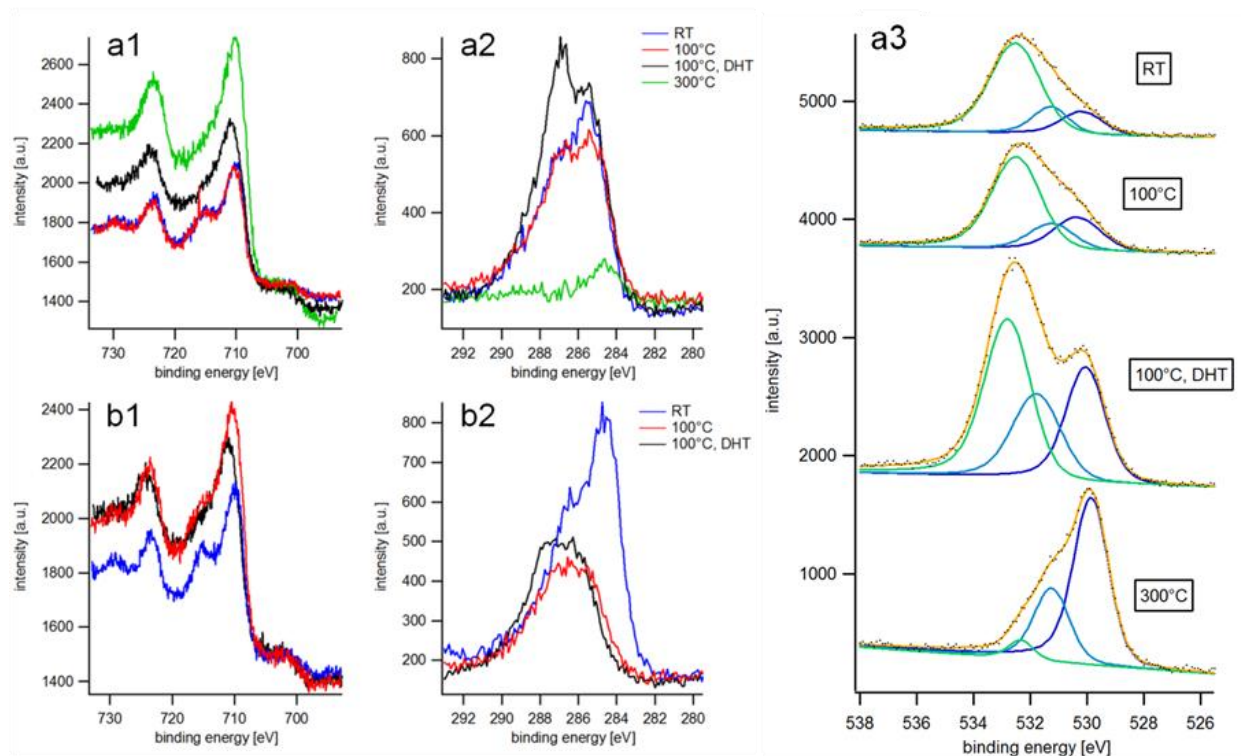


Figure S8.6 X-ray photoelectron spectra of iron chloride/NCC composite films coated from (a) $\text{FeCl}_3 \cdot 6\text{H}_2\text{O}$ and (b) $\text{FeCl}_2 \cdot 4\text{H}_2\text{O}$ precursors and dried at different conditions: at RT, 100°C at high humidity (100°C DHT), 100°C and 300°C at ambient humidity conditions. The spectra reveal the development of (a1, b1) Fe 2p, (a2, b2) C 1s and (a3) O 1s peaks. The points in figure a3 show the recorded oxygen spectra fitted with a Doniach-Sunjic line shape convoluted with Gaussian and linear background subtraction. The three peaks with maxima at 530.1 eV, 531.3 eV and 532.5 eV correspond to oxygen in iron oxide, iron hydroxide and water/cellulose, respectively. Spectra were taken using a Mg K_α source.

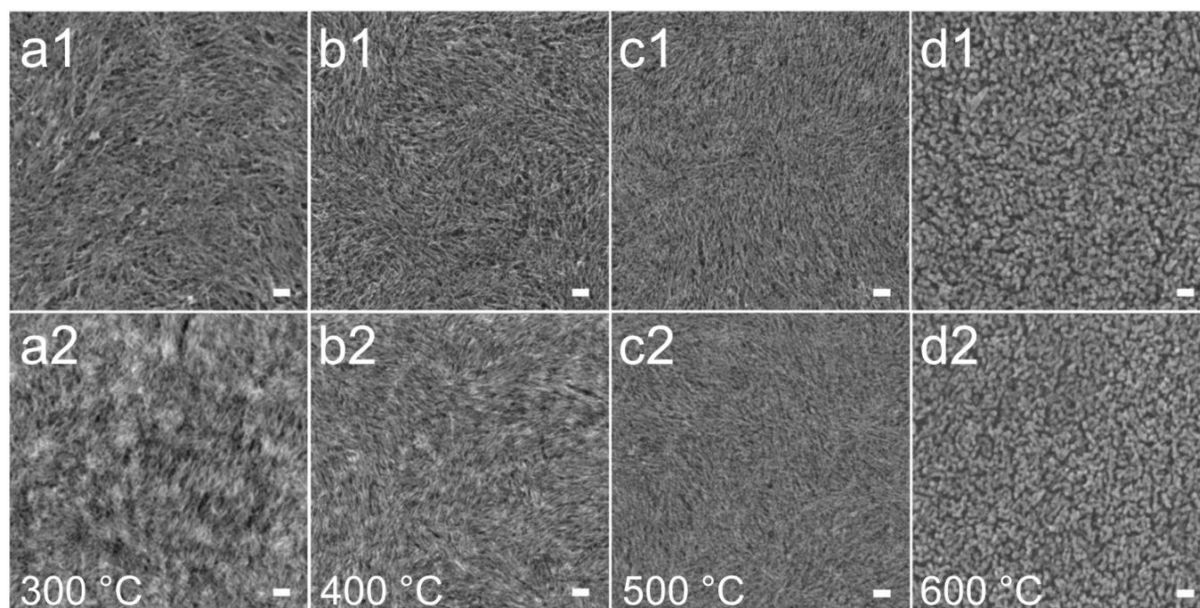


Figure S8.7 Top view SEM images of NCC-templated α - Fe_2O_3 thin films calcined at (a1, a2) 300 °C, (b1,b2) 400 °C, (c1,c2) 500 °C and (d1,d2) 600 °C after humidity treatment at 100 °C. The films were spin-coated on silicon wafers from aqueous precursor solutions containing NCC and $\text{FeCl}_3 \cdot 6\text{H}_2\text{O}$ (top row) or $\text{Fe}(\text{NO}_3)_3 \cdot 9\text{H}_2\text{O}$ (bottom row). The scale bars correspond to 100 nm.

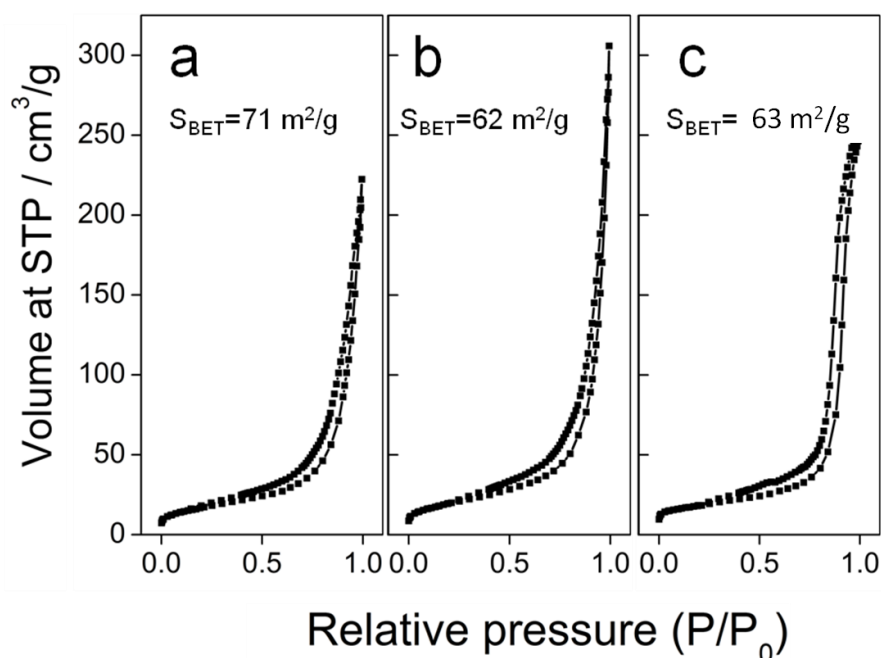


Figure S8.8 Nitrogen sorption isotherms measured on NCC-templated α - Fe_2O_3 powders after calcination at 500 °C. The samples were prepared from precursors containing NCC and (a) $\text{FeCl}_3 \cdot 6\text{H}_2\text{O}$, (b) $\text{FeCl}_2 \cdot 4\text{H}_2\text{O}$ and (c) $\text{Fe}(\text{NO}_3)_3 \cdot 9\text{H}_2\text{O}$.

9 CONCLUSION AND OUTLOOK

The main objective of this thesis was the development of nanostructuring concepts for efficient functional materials applied in electrochemical water splitting. Reducing the size of electrocatalysts to only a few nanometers provides an effective way to improve their electrochemical performance. The solvothermal reaction in *tert*-butanol developed in this project offers a great control over size and morphology of functional materials prepared as ultrasmall uniform nanoparticles. The nanoparticle synthesis allows for manipulating the defect chemistry and leads to an increased solubility of dopant atoms in the metal oxide crystal lattice resulting in unusual non-equilibrium compositions. The combination of crystallinity, dispersibility, unusual atomic compositions and presence of defects along with a greatly increased surface area due to the ultrasmall particle size are highly beneficial for electrocatalytic activity.

Using the *tert*-butanol route, nickel oxide based nanocrystals with 2–4 nm in diameter, uniform spherical shape and narrow size distribution were obtained. Phase pure NiO shown in chapter 3 was applied as electrocatalyst for the oxidation of water and demonstrated very high turnover frequencies of 0.293 s^{-1} at the overpotential of 300 mV, even outperforming expensive iridium oxide catalysts. The exceptionally high electrocatalytic activity in the oxygen evolution reaction is attributed to the partially oxidized surface resulting from the diminishing crystal size.

The catalytic performance in OER of the nickel oxide nanoparticles can be further enhanced by substitutional doping with Fe(III) ions, which is described in chapter 4. The doped particles reach a strikingly high maximum turnover frequency of 1.9 s^{-1} at 300 mV overpotential for 10 % Fe content. In contrast, the substitutional incorporation of Co(II) leads to enhanced performance in the hydrogen evolution reaction with growing Co content (chapter 5). Furthermore, the formation of non-equilibrium phases with unusually high miscibility of the elements is demonstrated for $\text{Ni}_x\text{Fe}_{1-x}\text{O}$ and $\text{Ni}_x\text{Co}_{1-x}\text{O}$, which we attribute to the kinetic control of the phase formation and a stabilizing effect of the nanoscale. Fe(III) could be substitutionally incorporated into the NiO lattice with up to 20 at% without losing structural integrity, whereas Co and Ni showed exceptionally high solubility in the whole composition range up to phase pure cobalt(II) oxide CoO. Noticeably, Fe, Ni, Co mixed phases usually do not show this behavior in the bulk, being able to incorporate only a few percent of the dopant without phase separation. Substitutional incorporation in case of $\text{Ni}_x\text{Fe}_{1-x}\text{O}$ was confirmed by the analysis of the atom arrangement in EXAFS, and $\text{Ni}_x\text{Co}_{1-x}\text{O}$ showed a distinct shift of the

electrode redox potential in CV curves with changing Co content, which was also supported by theoretical DFT calculations.

Moreover, ultrasmall nanoparticles of another stable cobalt oxide phase with spinel structure (Co_3O_4) were successfully prepared using the *tert*-butanol route. Due to their favorable dispersibility, the crystalline particles were efficiently distributed as co-catalysts on nanostructured Sn-enriched hematite films applied as photoanodes in the OER. This treatment led to a significant increase in photoelectrochemical water oxidation rates by up to 450 % and is associated with a reduction in electron/hole recombination processes (chapter 6).

Besides the compounds with cubic lattice symmetry described above, the *tert*-butanol reaction also allows for the fabrication of more complex monoclinic tunnel type structured metal oxides with an extremely small particle size (chapter 7). Thus, nanocrystals of akaganeite (β - FeOOH) were obtained in a microwave-assisted *tert*-butanol process. The particles can be doped by various metal ions in different oxidation states such as Co(II) , V(III) , Ti(IV) , Sn(IV) and Nb(V) . An extraordinary high doping level of up to 40 at% can be attributed to increased element solubility on the nanoscale. The dopants have a significant influence on the particle morphology ranging from 40 nm long nanorods with aspect ratios of around 9 to spherical nanoparticles with 4 nm in diameter. A remarkable feature of the nanosized akaganeite particles is their excellent dispersibility in water and ethanol without agglomeration. Colloidal nanoparticle dispersions can be coated on different substrates to give homogeneous thin films with tunable thickness. Furthermore, the nanostructured akaganeite films can also be prepared *in situ* during the solvothermal synthesis. The resulting films exhibit a unique morphology consisting of interconnected mesoporous spheres that are retained upon heating to 600 °C and phase transition to hematite (α - Fe_2O_3).

Another approach to produce a large variety of nanostructured iron oxides with tunable morphology was explored in a joint project with Alesja Ivanova (LMU) and is described in chapter 8. Crystalline and highly porous iron oxide films were prepared by employing different iron salts in combination with the biogenic template nanocrystalline cellulose (NCC). We could show the strong influence of the calcination procedure and additional post-synthetic humidity treatment at elevated temperatures on the nano-morphology of the porous hematite scaffolds. Interestingly, β - FeOOH with a highly anisotropic shape was found to be

one of the intermediate species during the calcination, confirming that preformed akaganeite nanoparticles are attractive candidates for the fabrication of hematite nanostructures.

In conclusion, we have developed successful nanostructuring strategies to enhance the efficiency of metal oxide based energy conversion materials. Future research may deal with the synthesis of other materials classes of electrocatalysts and novel multiple-metal oxide phases that possibly only exist at the nanoscale. The investigation of the newly synthesized structures may lead to the discovery of an electrocatalyst with even better performance than that of Fe/NiO. Since not only the catalytic properties of the materials can be tuned by the *tert*-butanol method but possibly also their optical, magnetic and electronic properties, the nanoparticles may be also applied in different other fields such as biomedicine, imaging or memory storage devices. Furthermore, the reaction mechanism of the *tert*-butanol synthesis as well as the surface chemistry of the resulting nanoparticles should be investigated in detail, to enhance our understanding and to be able to control their crystalline structure including lattice and surface defects.

10 PUBLICATIONS AND PRESENTATIONS

10.1 PUBLICATIONS

1. Nanoscale porous framework of lithium titanate for ultrafast lithium insertion

J. M. Feckl, K. Fominykh, M. Döblinger, D. Fattakhova-Rohlfing, T. Bein *Angew. Chem. Int. Ed.* **2012**, *51*, 7459.

2. Ultrasmall dispersible crystalline nickel oxide nanoparticles as high-performance catalysts for electrochemical water splitting

K. Fominykh*, J. M. Feckl*, J. Sicklinger, M. Döblinger, S. Böcklein, J. Ziegler, L. Peter, J. Rathousky, E.-W. Scheidt, T. Bein, D. Fattakhova-Rohlfing *Adv. Funct. Mater.* **2014**, *24*, 3123.

3. Macroporous indium tin oxide electrode layers as conducting substrates for immobilization of bulky electroactive guests

Y. Liu*, K. Peters*, B. Mandlmeier, A. Müller*, K. Fominykh, J. Rathousky, C. Scheu, D. Fattakhova-Rohlfing *Electrochim. Acta* **2014**, *140*, 108.

4. Nanocellulose-assisted formation of porous hematite morphologies

A. Ivanova*, K. Fominykh*, D. Fattakhova-Rohlfing, P. Zeller, M. Döblinger, T. Bein *Inorg. Chem* **2015**, *54*, 1129.

5. Ultrasmall dispersible crystalline Fe-doped nickel oxide nanoparticles as high performance catalysts for electrochemical water splitting

K. Fominykh, P. Chernev, I. Zaharieva, J. Sicklinger, G. Stefanic, M. Döblinger, A. Müller, A. Pokharel, S. Böcklein, C. Scheu, T. Bein, D. Fattakhova-Rohlfing *ACS nano* **2015**, *9*, 5180.

6. Ultrasmall Co_3O_4 nanoparticles strongly enhance solar water splitting on mesoporous hematite

J. M. Feckl*, H. K. Dunn*, P. M. Zehetmaier, A. Müller, S. R. Pendlebury, P. Zeller, K. Fominykh, F. Auras, M. Döblinger, J. R. Durrant, C. Scheu, L. Peter, D. Fattakhova-Rohlfing, T. Bein *Adv. Mater. Interfaces* **2015**, 2, 1500358.

7. Passivation of PbS Quantum Dot Surface with l-Glutathione in Solid-State Quantum-Dot-Sensitized Solar Cells

A. N. Jumabekov, N. Cordes, T. D. Siegler, P. Docampo, A. Ivanova, K. Fominykh, D. D. Medina, L. M. Peter, T. Bein *ACS Appl. Mater. Interfaces*, **2016**, 8, 4600.

8. Single Phase Doped Iron Oxyhydroxide Nanocrystals Incorporating Extraordinary High Amounts of Different Elements

K. Fominykh, D. Böhm, A. Folger, M. Döblinger, C. Scheu, T. Bein, D. Fattakhova-Rohlfing *Manuscript in preparation*

9. Rock Salt Ni/Co Oxides with Unusual Nanoscale-Stabilized Composition as Water Splitting Electrocatalysts

K. Fominykh, G. C. Tok, P. Zeller, H. Hajiyani, T. Miller, M. Döblinger, R. Pentcheva, T. Bein and D. Fattakhova-Rohlfing.

* these authors contributed equally

10.2 ORAL PRESENTATIONS

1. Ultrasmall metal oxide nanoparticles for energy conversion and storage

K. Fominykh, J. M. Feckl, T. Bein, D. Fattakhova-Rohlfing

E-MRS spring meeting, 2013, Strasbourg, France.

2. Nanostructured Oxide Electrodes for (Photo)electrochemical Water Oxidation and Catalysis

K. Fominykh, A. Müller, H. K. Dunn, H. Feckl, I. Kondofersky, C. Scheu, D. Fattakhova-Rohlfing, T. Bein

DFG SPP 1613 project meeting, 2013, Ellwangen, Germany.

3. Ultrasmall nickel oxide nanocrystals as highly efficient catalysts for electrochemical oxidation of water

K. Fominykh, J. M. Feckl, P. Zehetmaier, K. Peters, T. Bein, D. Fattakhova-Rohlfing

6th International FEZA Conference, 2014, Leipzig, Germany.

4. Nickel oxide based electrocatalysts for highly efficient electrochemical water oxidation

K. Fominykh, J. M. Feckl, J. Sicklinger, P. Zehetmaier, K. Peters, T. Bein, D. Fattakhova-Rohlfing

Electrochemistry conference, 2014, Mainz, Germany.

5. Highly efficient (Photo)electrocatalytic Water Oxidation on Ultrasmall Nickel Oxide and Cobalt oxide based Nanocrystals

K. Fominykh, P. Zeheitmaier, T. Bein, D. Fattakhova-Rohlfing

Solarfuel conference, 2015, Calvia, Mallorca, Spain.

6. Highly efficient Electrocatalytic Water Oxidation on Ultrasmall Nickel Oxide Nanocrystals

K. Fominykh, K. Peters, T. Bein, D. Fattakhova-Rohlfing

MRS Spring Meeting, 2015, San Francisco, USA.

10.3 POSTER PRESENTATIONS

1. Ultrasmall NiO, Fe-NiO and Co₃O₄ nanoparticles for water splitting

K. Fominykh, J. M. Feckl, T. Bein, D. Fattakhova-Rohlfing

CeNS Workshop "Nanosciences: Great Adventures on Small Scales", 2013, Venice, Italy.

2. Ultrasmall metal oxide nanoparticles for energy conversion and storage

K. Fominykh, J. M. Feckl, T. Bein, D. Fattakhova-Rohlfing

25. Deutsche Zeolith-Tagung, Hamburg, Germany.

3. Ultrasmall NiO and Co₃O₄ Nanoparticles for Water Splitting

K. Fominykh, J. M. Feckl, T. Bein, D. Fattakhova-Rohlfing

Symposium "Nanosystems for Solar Energy Conversion", 2013, Munich, Germany.

4. Solvothermal Synthesis of Ultrasmall Semiconducting Metal Oxide Nanoparticles

K. Fominykh, J. M. Feckl, T. Bein, D. Fattakhova-Rohlfing

Soltech Workshop, 2013, Kloster Banz, Germany.

5. Ultrasmall NiO and Co₃O₄ Nanoparticles for Water Splitting

K. Fominykh, J. M. Feckl, H. K. Dunn, T. Bein, D. Fattakhova-Rohlfing

DFG SPP 1613 project meeting, 2013, Ellwangen, Germany.

6. Ultrasmall dispersible crystalline nickel oxide nanoparticles as high performance catalysts for electrochemical water splitting

K. Fominykh, P. Zehetmaier, K. Peters, T. Bein, D. Fattakhova-Rohlfing

E-MRS spring meeting, 2014, Lille, France.

7. Nickel Oxide Based Nanoparticles as Highly Efficient Electrocatalysts for Water Splitting

K. Fominykh, J. Sicklinger, J. M. Feckl, P. Zehetmaier, K. Peters, T. Bein, D. Fattakhova-Rohlfing

Soltech Workshop, 2014, Wildbad Kreuth, Germany.